Alma Mater Studiorum – Università di Bologna

DOTTORATO DI RICERCA IN

INGEGNERIA CIVILE E AMBIENTALE

Ciclo XXVI

Settore Concorsuale di afferenza: 08/A1

Settore Scientifico disciplinare: ICAR/01

WAVE DRIVEN DEVICES FOR THE OXYGENATION OF BOTTOM LAYERS

Presentata da:

Alessandro Antonini

<table>
<tr><td align="center">Coordinatore Dottorato</td><td align="center">Relatore</td></tr>
<tr><td align="center">Chiar.mo Prof. Alberto Lamberti</td><td align="center">Chiar.mo Prof. Alberto Lamberti</td></tr>
</table>

Esame finale anno 2013-2014

ACKNOWLEDGMENTS

Questo capitolo della tesi esula notevolmente dagli altri e da tutto il resto del lavoro. In questa sezione vorrei ringraziare chi, in un modo o in un altro, mi è stato vicino e d'aiuto in questo percorso. Si tratta di parole e non di numeri o fenomeni fisici e vista la mia mancanza in questo ambito, così distante dall'ingegneria, spero che tutte le persone che non sono citate o ringraziate a dovere non se ne abbiano a male.

Sono passati tre anni, intensi ed entusiasmanti dove sono state poche le volte, se non forse nessuna, in cui è stato un peso per me alzarmi e andare a lavorare. E questo, credo, sia una cosa impagabile, con nessun tipo stipendio o alcuna posizione prestigiosa.

Per questo, il primo e più doveroso ringraziamento va al mio tutor, Professore Alberto Lamberti, che in un'estate di circa quattro anni fa si vide arrivare in ufficio uno sconosciuto che gli chiedeva di fargli da tutor durante il periodo di dottorato. Per la fiducia dimostrata, da quel giorno sino ad oggi, e per il continuo supporto in tutte le attività che ho portato avanti durante il dottorato, non posso che esprimergli la mia più totale gratitudine.

Una seconda importante figura di questo dottorato è stata la Professoressa Renata Archetti, che è stata presente ogni volta in cui ho avuto bisogno; rivolgendosi a me sempre con il sorriso. Vorrei rivolgerle un grazie particolare e doveroso per avermi coinvolto in numerose attività, dandomi la possibilità di lavorare con nuove persone e con altri gruppi di ricerca.

Un ringraziamento va poi alla Professoressa Nadia Pinardi, che ha reso possibile un periodo della mia vita che non potrò mai dimenticare, quello newyorkese. E' proprio durante quei sei mesi passati allo Stevens Institute of Technology che ho conosciuto delle persone stupende, che mi hanno accolto nel loro laboratorio con entusiasmo ed affetto. Per questo, un caloroso ringraziamento lo devo al Professor Alan Blumberg ed al Professor Len Imas che mi hanno messo a disposizione le loro conoscenze e le loro strutture. Inoltre, non posso che ringraziare anche i ragazzi dell'aula studenti al Davidson

ABSTRACT

Counteract one of the most urgent environmental issues in estuarine and coastal ecosystems as eutrophication, hypoxia and anoxia is a main goal for many countries around the world. According to the European Union, developing new projects to preserve native species, habitat and ecological and biological processes in coastal areas is a priority action sector for the Italian government.

This thesis discusses the design of a system to use wave energy to pump oxygen-rich surface water towards the bottom of the sea.

A simple device, called OXYFLUX, is proposed in a scale model and tested in a wave flume in order to validate its supposed theoretical functioning.

Once its effectiveness has been demonstrated, a overset mesh, CFD model has been developed and validated by means of the physical model results. Both numerical and physical results show how wave height affects the behavior of the device. Wave heights lower than about 0.5 m overtop the floater and fall into it. As the wave height increases, phase shift between water surface and vertical displacement of the device also increases its influence on the functioning mechanism. In these situations, with wave heights between 0.5 and 0.9 m, the downward flux is due to the higher head established in the water column inside the device respect to the outside wave field. Furthermore, as the wave height grows over 0.9 m, water flux inverts the direction thanks to depression caused by the wave crest pass over the floater. In this situation the wave crest goes over the float but does not go into it and it draws water from the bottom to the surface through the device pipe. By virtue of these results a new shape of the floater has been designed and tested in CFD model. Such new geometry is based on the already known Lazzari's profile and it aims to grab as much water as possible from the wave crest during the emergence of the floater from the wave field. Results coming from the new device are compared with the first ones in order to identify differences between the two shapes and their possible areas of application.

TABLE OF CONTENTS

LIST OF TABLES

LIST OF FIGURES

xiii

CHAPTER I: Introduction

A common worldwide problem: eutrophication and hypoxia

"No other environmental variable of such importance to estuarine and coastal ecosystems around the world has changed so drastically, in such a short period of time, as dissolved oxygen", [1].

Diaz started his work "Overview of Hypoxia around the World" with the above sentence, testifying how the problem of eutrophication of coastal zones is current and global for present society. The term eutrophication refers to an excessive enrichment of water by nutrients and its associated adverse biological effects,[2]. Cultural eutrophication, which results from human activity, may negatively affect marine ecosystems, increasing the occurrence of massive benthos and fish mortality, loss of diversity, poisoning episodes which can also cause human illness, and mucilage production [3], [4], [5] Eutrophication produces an excess of organic matter that fuels the development of hypoxia and anoxia when combined with water column stratification. Many ecosystems have reported some type of monotonic decline in dissolved oxygen levels through time with a strong correlation between human activities and a decline in declining dissolved oxygen.

Within the past 50 years eutrophication; the over enrichment of water by nutrients such as nitrogen and phosphorus, has emerged as one of the leading causes of water quality impairment. Selman identifies over 415 areas worldwide that are experiencing symptoms of eutrophication, highlighting the global scale of the problem. Recent coastal surveys of the United States and Europe have found that a staggering 78 % of the assessed continental U.S. coastal areas and approximately 65 % of Europe's Atlantic coasts show symptoms of eutrophication,[6], [7]. In other regions, the lack of reliable data hinders the assessment of coastal eutrophication. Nevertheless, trends in agricultural practices,

energy use, and population growth indicate that coastal eutrophication will be an ever-growing problem, [8].

Because of their geomorphology and circulation patterns, some marine systems have a greater tendency to develop hypoxic conditions. The basic features that make a system prone to hypoxia are low physical energy (tidal, currents, or wind) and large freshwater inputs. These features combine to form stratified or stable water masses near the bottom that become hypoxic when they are isolated from reoxygenation with surface waters. Better mixed or flushed systems do not have a tendency towards hypoxia.

What is the hypoxia

Oxygen is necessary to sustain the life of all fishes and invertebrates. In aquatic environments, oxygen from the atmosphere or from phytoplankton dissolves in the water and allows all animals to breathe, including those that swim or move about the sea bottom and those that have a sedentary life. Once dissolved into surface water, the normal condition for dissolved oxygen is to be mixed down into bottom layer waters. When the supply of oxygen to the bottom is cut off or the consumption rate exceeds resupply, oxygen concentration declines beyond the point that can sustain the life of most animals. This condition of low dissolved oxygen is known as hypoxia. The point at which various animals suffocate varies, but generally effects start to appear when oxygen concentration drops below 2 mg/l, [1]. For sea water, this is only about 18 % of air saturation. As a point of reference, air concentration is about 280 mg/l. Anoxia is the complete absence of oxygen. The two principal factors that lead to the development of hypoxia, are decreased water exchange between bottom water and oxygen-rich surface water, and decomposition of organic matter in the bottom water, which reduces oxygen levels. Both conditions must occur for hypoxia to develop and persist.

.

Consequence of the eutrophication

The rise in eutrophic and hypoxic events has been primarily attributed to the rapid increase in intensive agricultural practices, industrial activities and population growth, which together have increased nitrogen and phosphorus flows into the environment. Human activities have resulted in nearly doubling nitrogen and tripling phosphorus flows into the environment compared to natural values, [9]. By comparison, human activities have increased atmospheric concentrations of carbon dioxide, the gas primarily responsible for global warming, by approximately 32 % since the onset of the industrial age, [10].

Before nutrients and nitrogen in particular, are delivered to coastal ecosystems they pass through a variety of terrestrial and freshwater ecosystems, causing other environmental problems such as freshwater quality impairments, acid rain, the formation of greenhouse gases , significant impacts on food webs, and loss of biodiversity, [11].

Once nutrients reach coastal systems, they can trigger a number of responses within the ecosystem. The initial impact of the increase in nutrients is the excessive growth of phytoplankton, microalgae and macroalgae. This, in turn, can lead to other impacts such as:

- loss of subaquatic vegetation such as excessive phytoplankton, microalgae, and macroalgae growth which reduces light penetration;

- a change in species composition and biomass of the benthic (bottom-dwelling) aquatic community, eventually leading to a reduced diversity of species and the dominance of gelatinous organisms such as jellyfish;

- coral reef damage as increased nutrient levels promote algae growth over coral larvae. Coral growth is inhibited because algae outcompete coral larvae for available surfaces to grow on;

- shifts in the composition of phytoplankton species, creating favorable conditions for the development of nuisance, toxic, or otherwise harmful algal blooms;

- low dissolved oxygen and formation of hypoxic or "dead" zones (oxygen-depleted waters), which in turn can lead to the collapse of the ecosystem.

It is known that eutrophication diminishes the ability of coastal ecosystems to provide valuable ecosystem services such as tourism, recreation, the provision of fish and shellfish for local communities, sportfishing, and commercial fisheries. Furthermore, eutrophication can lead to reductions in local and regional biodiversity.

Currently nearly half of the world's population lives within 60 kilometers from coastal areas, with many communities relying directly on coastal ecosystems for their livelihoods, [12] This means that a significant portion of the world's population is vulnerable to the effects of eutrophication in their local coastal ecosystems.

Harmful Algal Blooms and Hypoxia.

Two of the most acute and commonly recognized symptoms of eutrophication are harmful algal blooms and hypoxia. Harmful algal blooms can cause the killing of fish, human illness through shellfish poisoning, and the death of marine mammals and shore birds. Harmful algal blooms are often referred to as "red tides" or "brown tides" because of the appearance of the water when these blooms occur. One red tide event, which occurred near Hong Kong in 1998, wiped out 90 percent of the entire stock of Hong Kong's fish farms and resulted in an estimated economic loss of $40 million USD, [13].

Hypoxia, which is considered to be the most severe symptom of eutrophication, has escalated dramatically over the past 50 years, increasing from about 10 documented cases

in 1960 to at least 169 in 2007[1],[14]. Hypoxia occurs when algae and other organisms die, sink to the bottom, and are then decomposed by bacteria using the available dissolved oxygen. Salinity and temperature differences between surface and subsurface waters lead to stratification, limiting oxygen replenishment from surface waters and creating conditions that can lead to the formation of a hypoxic or "dead" zone, [15].

Nutrients, eutrophication and hypoxia: an overview on the connections

The primary factor driving coastal eutrophication is an imbalance in the nitrogen cycle that can be directly linked to increased population, due either to urbanization in coastal areas or along rivers or to the development of agricultural activities. In many areas hypoxia follows from eutrophication, which results from the underlying nutrient problem. An examination of the distribution of hypoxic zones around the world showed that they were closely associated with developed watersheds or highly densely populated coastal areas that deliver large quantities of nutrients, the most important of which is nitrogen, to coastal seas,[16]. Agriculture and industry are regarded as the principal generators of nitrogen, even if, in the end increased population and rising living standards drive the need for industry and agriculture to produce. Atmospheric sources of nitrogen are also recognized as a significant contributor of nutrients in coastal areas, [17]. Nitrogen from fossil fuel combustion and volatilization from fertilizers and manure is released into the atmosphere and redeposited on land and in water by wind, snow, and rain.

---

[1]Hypoxia is generally defined as having a dissolved oxygen concentration of 2.0 milligrams per liter or less, [8] and [1].

The degenerative scenario linking nutrient additions to the formation of hypoxia via eutrophication, following an initial positive effect on fisheries, can be described as follow:

Excess nutrients lead to increased primary production, which represents new organic matter that is added to the ecosystem. Since shallow estuarine and coastal systems tend to be tightly coupled (benthic-pelagic coupling), much of this organic matter reaches the bottom. This increased primary productivity may also lead to increased fishery production, [18] At a certain point, however, the ecosystem's ability to maintain a balance in processing organic matter is exceeded. If physical dynamics permit stratification, hypoxic conditions develop. Initially, increased fishery production may offset any detrimental effects of hypoxia but, as eutrophication increases and hypoxia expands in duration and area, the fishery production base is affected and declines. The increasing input of anthropogenic nutrients to many coastal areas over the last several decades has been suggested as being the main contributor to the most recently declining trends in bottom water oxygen concentrations around the world. Many studies have demonstrated a correlation through time between population growth, increased nutrient discharges, increased primary production in coastal areas and increased occurrence of hypoxia and anoxia; an example might be the decline in oxygen concentration in the Gulf of Trieste in the last 25 years, [1]. . The direct connection between land and sea is best exemplified by the relationship between estuarine and coastal fishery production and land-derived nutrients. The most productive fishery zones around the world are always associated with significant inputs of either land (*runoff*) or deep oceanic (*upwelling*) derived nutrients. The basic nutrients carried by land runoff and oceanic upwelling are the essential elements that fuel primary production and that, through marine food webs, feed the species of economic importance. Problems begin when the nutrients entering the system exceed the capacity of the food chain to assimilate them. At first, increased nutrients lead to increased fishery production but, as organic matter production increases, changes occur in the food web leading to different endpoints. These changes are very predictable

and have been recognized in many marine ecosystems, Figure 1. Basically, a hypoxic zone is the secondary manifestation of the larger problem of excess nutrients, which leads to increased production of organic matter or eutrophication,[19]. When eutrophication combines with water column stratification, hypoxia results.
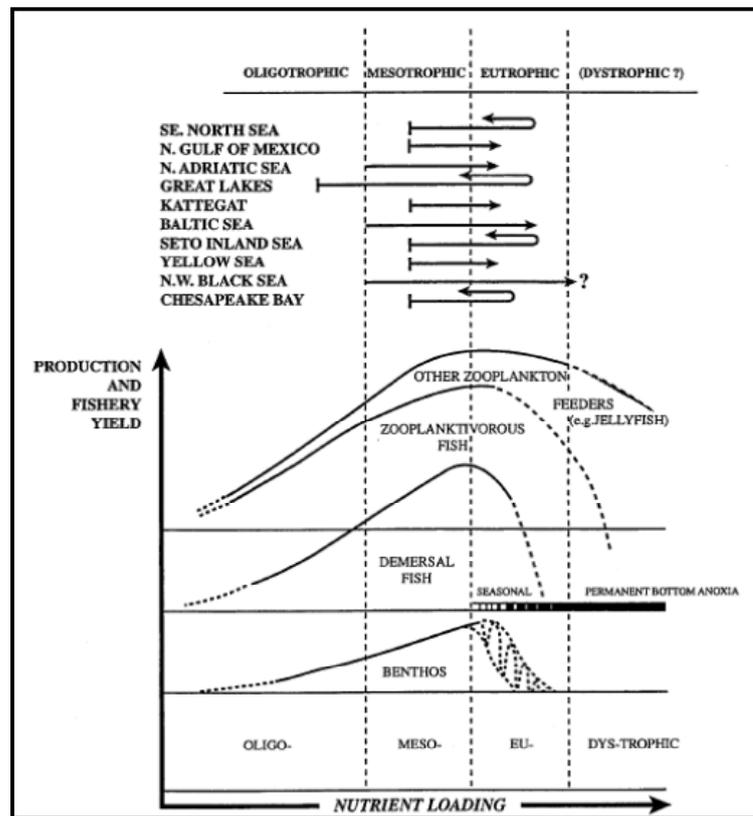
Figure 1: Comparative evaluation of fishery response to nutrients,[18].

Locations of global eutrophic and hypoxic areas

The latest results of a survey on eutrophic and hypoxic zones date back to 2008, when Selman et al. found 415 systems which presented problems related to eutrophication. Of these, 169 are documented hypoxic areas, 233 are areas of concern, and 13 are systems in

recovery. The advances in identifying and reporting eutrophic conditions will rapidly lead to the growth of the number of known areas. The first comprehensive list of hypoxic zones was compiled by Diaz and Rosenberg in 1995 [20] and identified 44 documented hypoxic areas, nearly one quarter of the hypoxic areas identified by Selman et al. twelve years later, [14]. The list of hypoxic areas assembled by Diaz was compiled from scientific literature and identified the majority of the documented hypoxic areas. However, the list did not include areas with suspected but not documented hypoxic events or systems that suffer from other impacts of eutrophication such as nuisance or harmful algal blooms, loss of subaquatic vegetation and changes in the structure of the benthic aquatic community. The supplementary list of hypoxic zones, shown in Figure 2, takes into account systems experiencing any symptoms of eutrophication, including but not limited to anoxia. The new zones are divided into:

- *documented hypoxic areas:* areas with scientific evidence that hypoxia was caused, at least in part, by nutrient overenrichment;

- *areas of concern:* systems that exhibit effects of eutrophication, such as elevated nutrient levels, elevated chlorophyll levels, harmful algal blooms, changes in the benthic community, damage to coral reefs and fish kills. These systems are impaired by nutrients and are possibly at risk of developing hypoxia;

- *systems in recovery:* areas that once exhibited low dissolved oxygen levels and hypoxia, but are now improving.
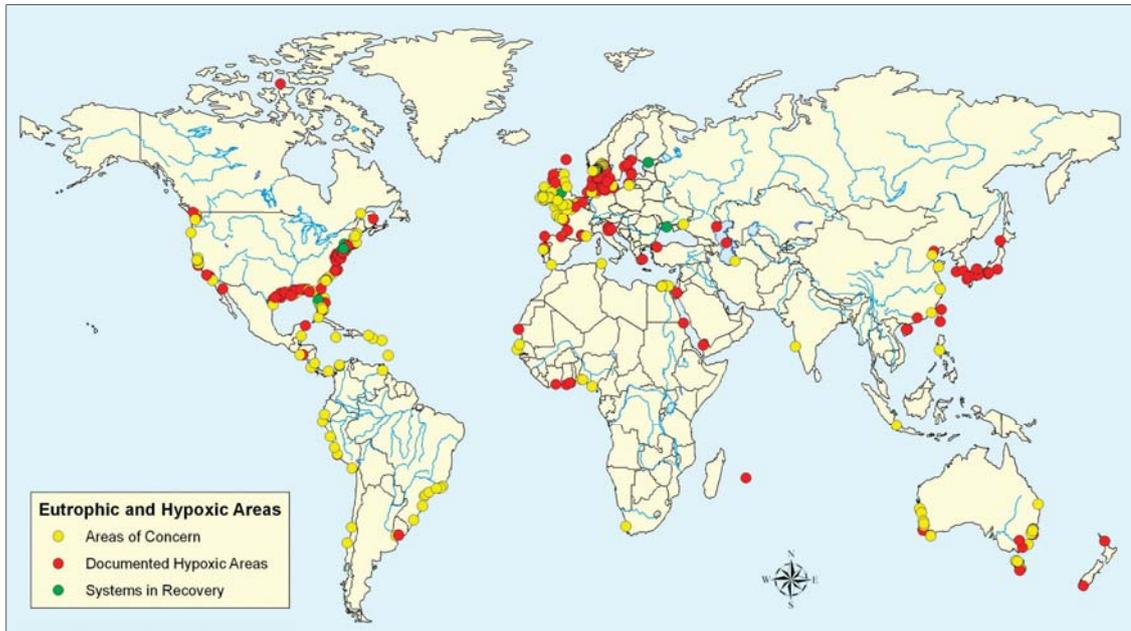
Figure 2: World hypoxic and eutrophic coastal areas, [8].

Wave Energy Converter, Strengths and weaknesses

History of the Ocean Wave Energy Converters

Energy from ocean waves is the most conspicuous form of ocean energy, possibly because of the often spectacular destructive effects of the waves. The waves are produced by wind action and are therefore an indirect form of solar energy, [21]. The opportunity of converting wave energy into usable energy has inspired numerous inventors: more than one thousand patents had been registered by 1980,[22] and the number has increased markedly since then. The earliest patent was filed in France in 1799 by a father and a son named Girard,[23].

Yoshio Masuda may be regarded as the father of modern wave energy technology, with his studies in Japan dating from the 1940s. He developed a navigation buoy powered by wave energy, equipped with an air turbine, which was in fact what was later named a

(floating) oscillating water column (OWC). These buoys have been commercialized in Japan since 1965, [24]. In 1976 Masuda promoted the construction of a much larger device: a barge, named Kaimei, which was used as a floating testing platform housing several OWCs equipped with different types of air turbines, [25]. Probably because this was done at an early stage, when the theoretical knowledge on wave energy absorption was at its beginning, the power output levels achieved in the Kaimei testing program were not a great success. Masuda realized that converting wave energy to pneumatic energy with the Kaimei project was quite unsatisfactory and conceived a different geometry for a floating OWC: the Backward Bent Duct Buoy (BBDB). In the BBDB, the OWC duct is bent backwards from the incident wave direction, (Figure 3), which was found to be advantageous when compared to the frontward facing duct version,[26]. In this way, the length of the water column could be made sufficiently large enough for resonance to be achieved, while keeping the draught of the floating structure within acceptable limits. The BBDB converter was studied (including model testing) in several countries (Japan, China, Denmark, Korea, Ireland) and was used to power about one thousand navigation buoys in Japan and China,[27], [28].

In 1974, a paper published by Stephen Salter,[29] became a landmark and brought wave energy to the attention of the international scientific community. In 1975 the British Government started an important research and development program in wave energy,[21], followed shortly afterwards by the Norwegian Government. In Norway the activity resulted in the construction of two full-sized shoreline prototypes near Bergen in 1985. In the following years, up until the early 1990's, the activity in Europe remained mainly at an academic level; the most visible achievement being a small OWC shoreline prototype deployed on the island of Islay, Scotland,[30]. At about the same time, two OWC prototypes were constructed in Asia: a converter integrated into a breakwater at the port of Sakata, Japan,[31] and a bottom-standing plant at Trivandrum, India,[32].

In 1991 the situation in Europe was dramatically changed by the decision made by the European Commission of including wave energy in their R&D program on renewable

10

energies. The first projects started in 1992. Since then, about thirty projects on wave energy were funded by the European Commission involving a large number of teams in Europe,[21]. In the last few years, interest in wave energy has been growing in northern America, involving national and regional administrations, research institutes and companies, and giving rise to frequent meetings and conferences on ocean energy, [33], [34].
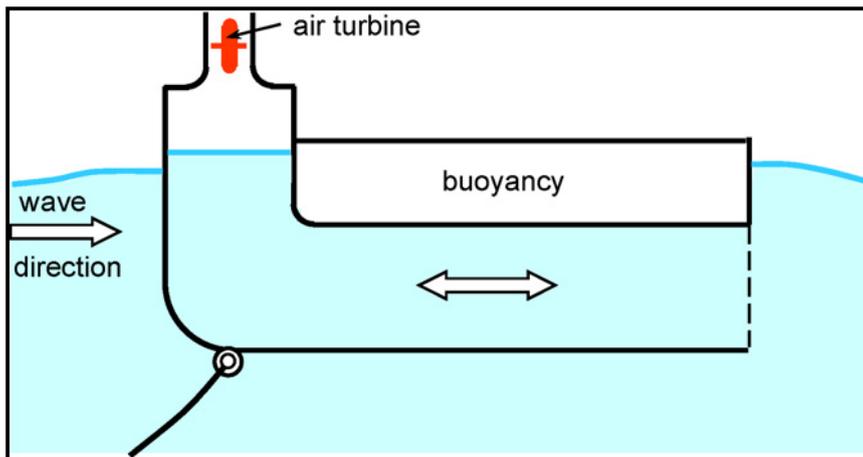
Figure 3: Schematic representation of Backward Bent Duct Buoy, [21].

Strengths and weaknesses of the Wave Energy Converter

The development of wave energy converter devices is characterized by numerous inventions. Since the first patent on wave energy,[23], a great number of ideas to harness the energy of waves has been conceived; however, only few of them have succeeded in being tested in the sea.

Nowadays developing wave energy converters is no longer a privilege of virtuous and wealthy Nations. Even if it does not still represent a safe business, obtaining energy from waves allows for the creation of new jobs and the production of clean energy characterized by a low environmental footprint. Wave energy is a concentrated and

readily available energy source, unlike fossil fuels which, in some places in the world, are running out just as quickly as people can discover them. Unlike ethanol, a corn product, wave energy is not limited by seasons and it does not need any kind of intervention from man,[35]. It is close to densely populated areas and is well distributed around the globe and it has a very low visual impact. Moreover, wave energy can be predicted with good accuracy and is more constant than wind energy, [36].

Nevertheless, the road ahead for the realization of efficient wave energy converters is beset with difficulties, particularly related to testing in real seas, due to the characteristics of ocean waves and to the related costs. Contrary to many other WECs, the system has to be tested in real seas on a certain prototype scale. Sea trials are generally more complicated and expensive than laboratory testing [37]. The deployment also requires suitable weather windows and specific vessels. Above all, the prototype has to be designed to survive extreme events and to operate in harsh environments, despite being a test plant. The extreme conditions at the deployment location, although being infrequent, dictate the structural design of the WECs and mooring systems, which are also directly linked to the overall investment. All these factors strongly affect project costs. Many failures in this sector, (like mooring breakages and WECs getting stranded before an audience) are retained and emphasized by the public and other stakeholders. On the other hand, one of the biggest success stories of the sector must be recalled. There are about three hundred OWCs navigational buoys functioning around the world in places where battery changing, lighting a 60 W bulb and driving a flashing unit, as designed by Commander Yoshio Masuda, is inconvenient [34].

Concerning the environmental impacts, the problems due to WECs are probably few, and mostly unknown. Some stakeholders' concerns regard the negative impacts on fisheries or marine mammal migration, with marine life risking getting entangled in cables. Apart from wildlife conservation and site specific environmental issues other recommendations for suitable sites for wave energy converters include: avoidance of shipping lanes, avoidance of areas of military importance, and marine archaeological sites. Other

potential conflicts include areas intended for mining or for the dredging of sand and gravel. Further restrictions on the placement of WECs comes from existing pipelines and cables, although most likely on a smaller scale. Already existing offshore activities limit future establishments, including offshore wind power parks, oil and gas fields,[38]. Wave power converters are less likely to interfere with recreational activities such as leisure boats, since parks may be placed far off the coast, [36]. Although the techniques are generally not very well developed yet, it is likely that wave power will become at least as important as wind and hydropower are today,[39].

CHAPTER II: Literature Survey

Adriatic Sea Conditions

The Adriatic Sea is an elongated basin, with its major axis oriented in a northwest - southeast direction, located in the central Mediterranean, between the Italian peninsula and the Balkans.
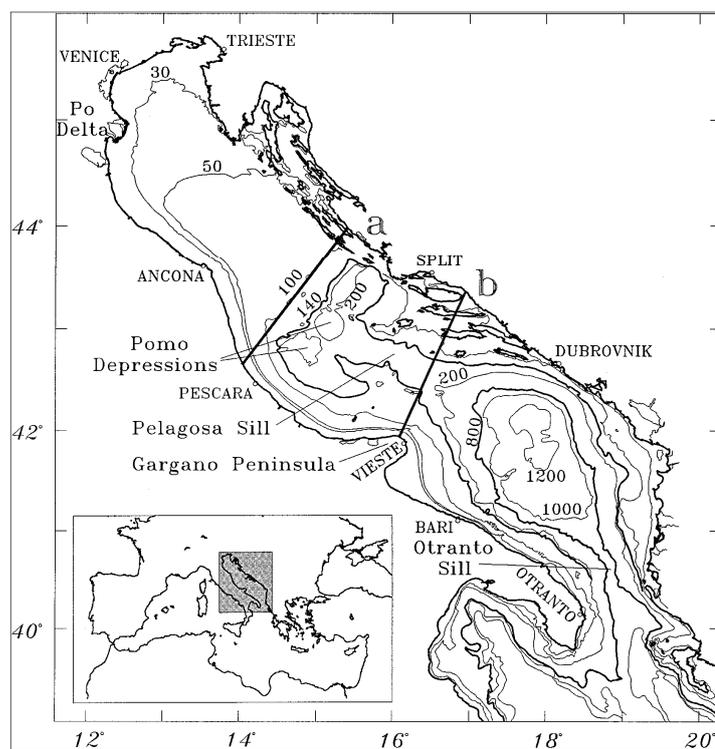
Figure 4: Adriatic Sea coastline an topography, [40].

Its northern section is very shallow and gently sloping, with an average bottom depth of about 35 m. Middle Adriatic average depth is 140 m, with the two Pomo Depressions reaching 260 m. The southern section is characterized by a wide depression more than 1200 m deep. The water exchange with the Mediterranean Sea takes place through the

Otranto Channel, whose sill is 800 m deep. The eastern coast is characterized by rocky shores and cliffs, whereas the western coast is flat and mostly sandy. A large number of rivers discharge into the basin, with significant influence on the circulation, particularly relevant being the Po River in the northern basin, and the ensemble of the Albanian rivers in the southern basin,[40].

The structure and the seasonal variability of the Adriatic general circulation is synthesized in Fig. 5. At the surface the winter general circulation is composed only of the Northern and Southern Adriatic current (NAd and SAd) segments and the flow field is very different from all other seasons. The general circulation is dominated by temperature and salinity compensation effects. It can be speculated that the barotropic, wind-induced transport and circulation is probably a major component of the general circulation during winter. This can also be estimated by looking at the seasonal water mass properties [40], where during winter and throughout the basin vertical temperature and salinity profiles become practically uniform with depth. Spring–Summer surface flow field is characterized by the appearance of western current segments (W-Mad and W-SAd) and the two major cyclonic gyres of the Adriatic circulation. It can be argued that the seasonal vertical stratification in the basin triggers the appearance at the surface of gyres and an intensification of boundary currents, more generally of eddies and jets, probably as a result of baroclinic-barotropic nonlinear instabilities in the basin,[41].
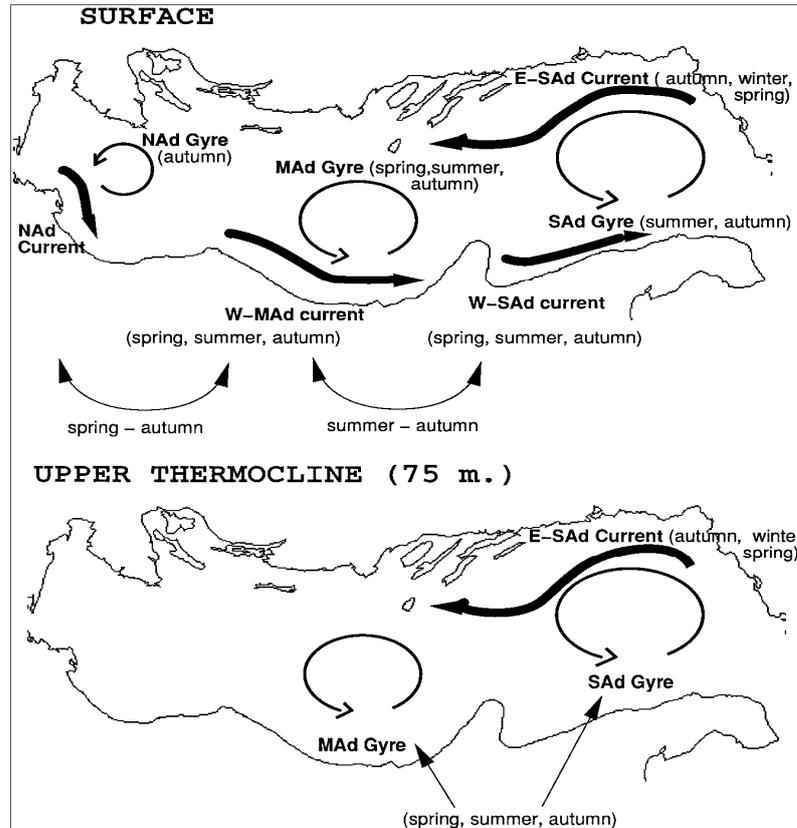
Figure 5: Adriatic Sea general circulations,[41].

During summer currents occur on smaller spatial scales and the E-SAd current weakens. Autumn conditions are characterized by the maximum spatial coherence of the general circulation structure. In fact, there are three cyclonic gyres, a continuous western Adriatic boundary current, connected between the three subbasins, and an intense SAd current. As known from [40], this season is characterized by maximum middle levantine intermediate water entrance and spreading from Otranto, a well-defined surface mixed layer and maximum warming of the subsurface layers of the northern Adriatic.

Anoxia in the northern Adriatic

The northern Adriatic is a shallow basin characterized by a cyclonic circulation and by the inputs of many rivers; Po and Adige contribute to the most of the total freshwater input. Anthropogenic nutrient loads coming from rivers flowing into the north-western

16

Adriatic Sea have considerably increased during the late 20th century, especially between 1968 and 1980,[42]. A major fraction of the productivity in surface waters reaches the sea floor [43] and anoxic or near anoxic events frequently occur in bottom waters, especially during late summer and autumn as a consequence of high downward of organic fluxes, microbial decay and thermal stratification,[44], [45], [46]. High concentrations of particulate organic matter are present in the north west Adriatic due to the combined effects of terrestrial suspended matter input and primary productivity, which depends highly upon nutrient load discharged by rivers, [47]. Consequently, massive diatom and dinoflagellate blooms and "red tides" (sometimes associated with toxicity episodes) are well known along the northwestern Adriatic coast,[5]. In the Adriatic basin, a trophic gradient increasing from east to west is present. In the western side of the basin, particulate organic matter (POM) reaches higher concentrations, especially in proximity of the deltas of Adige and Po,[48]. The POM, diffusing through the water column, represents an important source of energy for the benthic system and through the degrading processes contributes to the decrease of oxygen content in the bottom waters. In coastal environments, the flux of settling particles is influenced by river discharge, physical and chemical reactions at the fresh-salt water interface, primary and secondary production and water circulation, [49]. The downward flux of particulate organic matter in the shallow northern Adriatic basin is relevant both for the sinking and recycling of nutrients and for the oxygen consumption at the bottom, which often causes local hypoxia in the coastal belt and occasionally may lead to basin scale hypoxia events, when general circulation and wave intensity are reduced.

Water mass structure: temperature, salinity, dissolved oxygen and stratification of the North Adriatic Sea

The shallow northern Adriatic Sea is characterized by marked seasonal and long-term fluctuations of oceanographic and biological conditions, mainly due to atmospheric

forcing, freshwater discharges, variable intrusion of high salinity waters, and a very variable and complex circulation,[50], [51]. Due to intense heat losses Fig.6, at the air–sea interface, the water column of the offshore North Adriatic is well mixed during late autumn and winter.
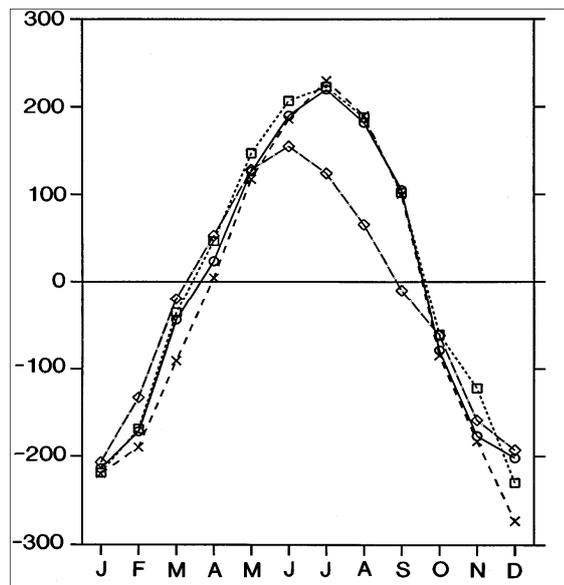
Figure 6: Monthly mean heat flux at the surface (W/m^2), estimations based on 4 different datasets,[40].

Water mass exchange between northern and central Adriatic is at its maximum during this period, characterized by a prevailing cyclonic circulation, and by northward currents in the eastern part and southward currents along the western coast, [51]. During spring dense water generally remains in the bottom layer in northernmost areas and as a vein along the western side of the entire region. During spring and summer, semi-enclosed circulation patterns prevail in the region, and thermal stratification gradually increases and reaches its maximum in August as a result of heat accumulation in the upper layers, [52]. In these conditions freshened surface waters, formed along the western coast, are generally advected eastward to the Istrian coast, so significantly increasing the stratification of the water column.

Particular freshwater discharge dynamics in spring and summer, characterized by relevant peaks of short duration, may play an important role for the development of the mucilage phenomenon, particularly in conditions of reduced water dynamics, [4],[53]. This phenomenon is characterized by the formation of macro-aggregates of different shapes and dimensions in the upper water column of the entire northern Adriatic.

Temperature and Salinity

Figure 7, shows the climatological medium profiles for temperature and salinity obtained for the entire Adriatic Sea. In the northern Adriatic the entire water column exhibits an evident seasonal thermal cycle. A well-developed thermocline is present in spring and summer down to 30-m depth, whereas a significant cooling begins close to the surface in autumn when the bottom temperature reaches its maximum value, probably due to increased vertical mixing and intrusion of middle Adriatic waters.
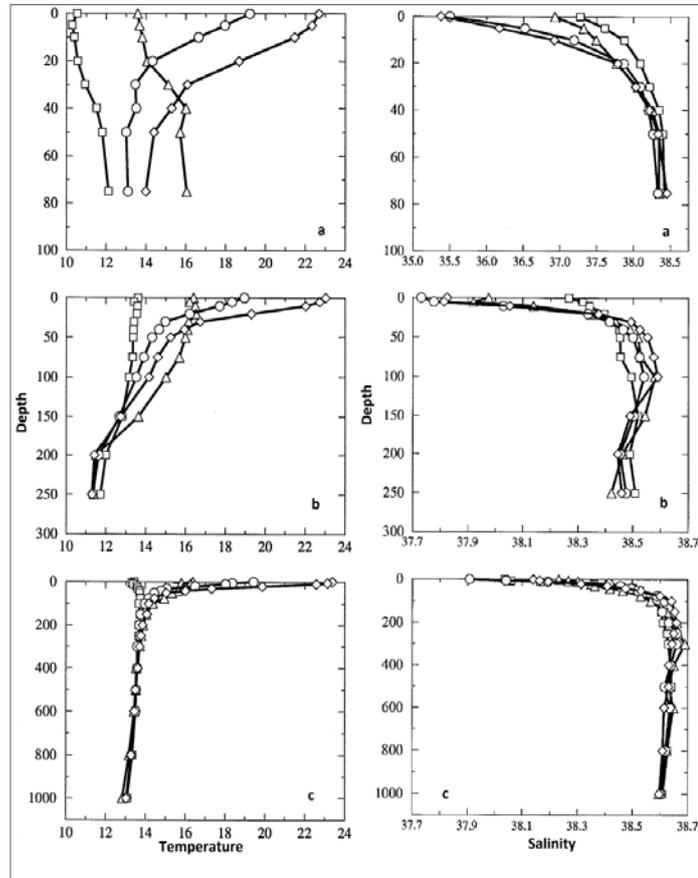
Figure 7: Seasonal climatological profile of Adriatic, a) Northern Adriatic, b) Middle Adriatic, c) Southern Adriatic. The variables represent are Temperature, °C, (left); and Salinity, ppm, (right). Spring ○, summer ◇, autumn △, winter □, [40].

The cooling of the whole water column only occurs in winter; in this season temperature generally increases down to the bottom, but the water column stability is preserved due to an associated increase of salinity at depth. The effects of freshwater input can be clearly seen in spring and summer due to the increased runoff and the increased water column stratification, [41].

Dissolved oxygen

Except for its northern part, the Adriatic Sea is a well-oxygenated basin. The dissolved oxygen profiles show that in the warmer seasons a relatively low concentration layer is present just near the sea surface, due to oxygen equilibration with the atmosphere,[40]. In

the northern Adriatic it can be noticed that the average oxygen profiles have a qualitatively different shape of with respect to middle and southern Adriatic conditions. The northern Adriatic can be subdivided in two sub regions, the first corresponding to areas shallower than 50 m, Figure 8a and Figure 8b, and the second corresponding to the remaining part Figure 8c.
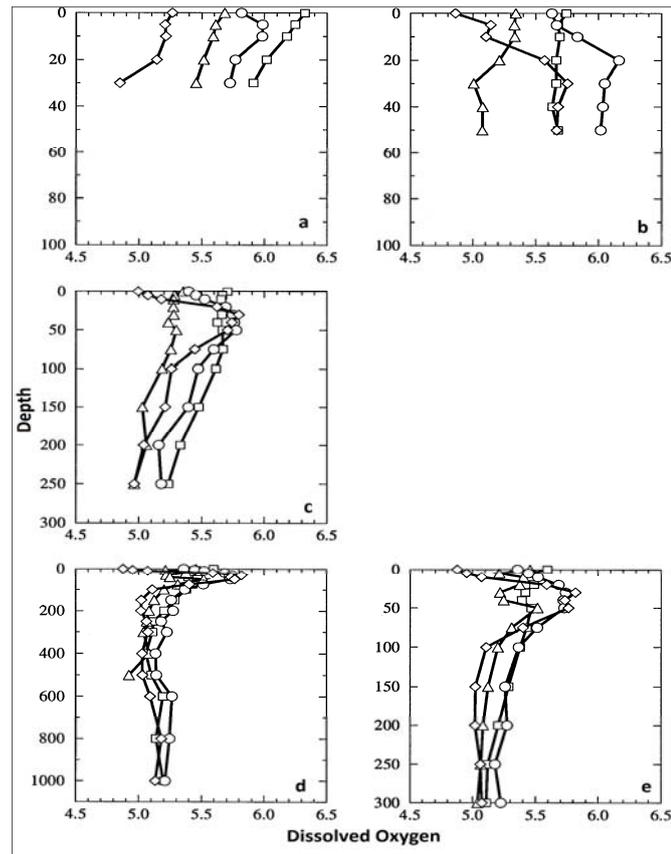
Figure 8: Seasonal climatological profile of Adriatic: a) Northern Adriatic shallower or equal to 50 m, b) northern Adriatic deeper than 50 m, c) middle Adriatic, d) southern Adriatic max depth, e) southern Adriatic shallower or equal to 300 m. Dissolved oxygen (ml/l). Spring ◯, summer ◇, autumn △, winter ☐ , [40].

The average value of dissolved oxygen in the Adriatic basin is approximately 5.5 ml/l. The parameter wich has been used to describe the variability of the dissolved oxygen is standard deviation (STD). Lowest variability of dissolved oxygen appears near the bottom in autumn (STD equal to 0.1 ml/l) and summer (STD equal to 0.4 ml/l), while the

highest STD value occurs at the surface with values of 0.5 - 0.6 ml/l in all seasons except for summer, when the highest STD of 0.9 ml/l is found at a depth of 30 m, [40].

In this chapter an overview on the climatological water mass and dissolved oxygen structure is proposed. The whole Adriatic basin can be divided in three main sectors: northern, the shallowest; middle, the transitional area; southern zone, the deepest and the interface with the Ionian Sea. Each of them is characterized by its own profiles of temperature, salinity and dissolved oxygen level. No differences can be found for the water surface characteristics between the three areas. All of them are sensible to the seasonal climatological cycle, presenting the highest values of temperature during summer and the deepest level of column agitation during winter. At the surface salt balance is largely affected by river runoffs, especially during spring and summer.

Wave climate of North Adriatic

Leder in 1998 [54] was the first to investigate the characteristic wave climate of the northern Adriatic Sea from measured data. His study was aimed to identify the monthly significant wave height through Gumbel distribution fitted on data measured in the offshore part of the northern Adriatic Sea from the platforms Panon and Labin, Figure 9.
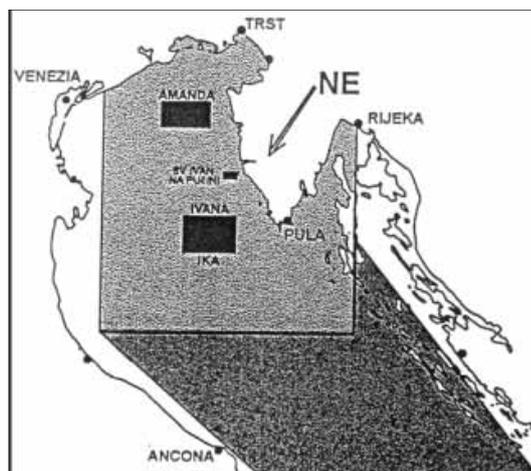
Figure 9: Locations of the platform Panon and Labin, [54].

Monthly extreme values were available for a ten year period (1978–1986 and 1992). The absolute maximum significant wave height measured in those 10 years was 6.58 m recorded during a storm in December 1979. The wave height of 10.2 m was measured during that storm, being the second highest measured wave in the Adriatic Sea. The largest individual wave height recorded so far in the Adriatic Sea reads 10.8 m. The wave was measured in the Northern Adriatic in February 1986 during a storm with a significant wave height of 6.16 m. The theoretical prediction of the most probable extreme significant wave height in 20 and 100 years by [54], reads 7.20 and 8.57 m, respectively, Table 1. It should be mentioned that another study has been conducted,[55], but, since it was based on data collected by observations from merchant ships, which are better suited to the analysis of seagoing ships comparing to the data from the fixed measurement stations,[56],[57] it will not be considered.

Table 1: Average monthly and annual wave power significant wave heights (m), Tr return period (years), [58].

Tr	Jan	Feb	Mar	Apr	May	Jun	Jul	Aug	Sep	Oct	Nov	Dic	Annual
5	4.44	4.06	3.18	2.76	2.57	2.53	2.90	4.06	4.08	3.84	4.22	4.78	5.97
10	5.05	4.91	3.65	3.09	2.98	2.90	3.34	4.84	4.78	4.44	4.70	5.36	6.60
20	5.64	5.71	4.09	3.40	3.38	3.26	3.76	5.58	5.46	5.01	5.17	5.92	7.20
50	6.39	6.76	4.67	3.81	3.89	3.73	4.31	6.55	6.33	5.75	5.77	6.64	7.98
100	6.96	7.54	5.11	4.11	4.27	4.08	4.72	7.27	6.98	6.31	6.22	7.19	8.57

Such values were calculated in order to identify the extreme events, with the aim to develop an helpful tool for people working in activities related with this area of the Adriatic. Hypoxia develops during period of stable stratification, when the waves are not strong enough to break this layer. Thus extreme waves are not indicators for events related to the anoxia, but they can give an idea of the low wave power in the North Adriatic (compared with other extreme wave climates).

Vicinanza in [58], used the available data recorded by the Italian Buoy Network (IWN), [59], that is active since July 1998, to characterize wave power around Italian coasts. IWN offshore wave measurements are available for 15 different sites highlighted in Fig. 9, but for the present study only results coming from buoy 15 are relevant. From 1989 up to about 2002, each wave buoy collected 30 minutes of wave measurements every three hours but in presence of wave heights greater than 1.5m the measurements were continuous. From 2002 wave measurements have always been continuous and wave characteristics parameters refer to 30 minutes time intervals.
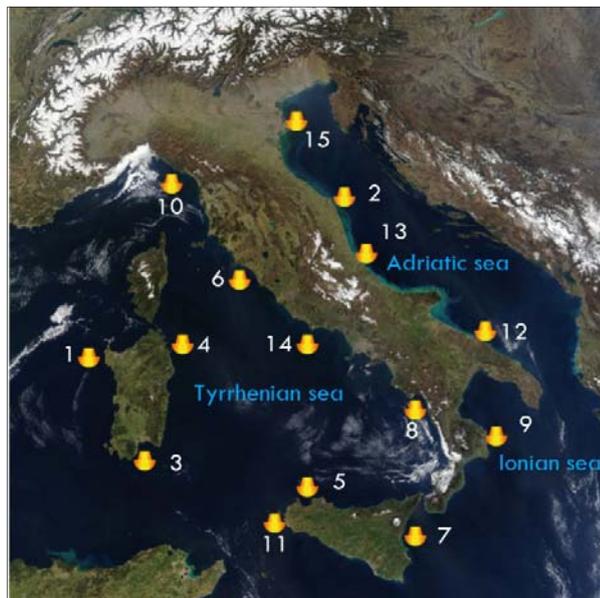
Figure 10: Location of the IWN buoys, [58].

In [58] Vicinanza identified the average monthly and annual value of offshore wave power for the Adriatic Sea. It can be argue that the Adriatic has the lowest energetic level, with peak of low level of agitation in its northern area. Table 2 shows the entire dataset identified by Vicinanza and, as expected, during summer a generalized trend of low values of monthly averaged value is recognized. Results coming from buoy 15,

related to June, July and August, report 1.2, 0.6 and 0.9 kW/m respectively; even buoy 2 shows low wave power for the same period (0.5, 0.7 and 0.7).

Table 2: Average monthly and annual wave power (kw/m), [58].

Buoy	Jan	Feb	Mar	Apr	May	Jun	Jul	Aug	Sep	Oct	Nov	Dic	Annual
1	12.4	13.4	10.2	10.8	5.9	4.1	4.3	3.7	6.2	7.5	14.8	15.4	9.1
2	2.7	1.2	2.2	1.2	0.7	0.5	0.7	0.7	1.6	1.9	4.5	3.8	1.8
3	1.8	0.9	1	2	na	na	0.6	0.4	0.7	1.4	3.5	2.9	1.5
4	1.9	2.3	2.7	3.3	1.3	0.6	0.6	1	1.6	1.1	5.5	7.3	2.4
5	6.1	6.5	5.5	2.9	2.1	1.4	1.4	2.2	2.7	1.2	4.8	9.9	3.9
6	3.7	5.1	3.4	3.4	2.4	0.9	0.9	2.4	1	2.7	2.1	6.7	2.9
7	3.1	2.9	3.1	2	1.2	0.5	0.4	0.4	1	1.7	2.8	3.7	1.9
8	4.3	4.7	4.5	3.3	2	1.1	1	1	1.6	1.6	4	5.1	2.9
9	5	4.3	3.8	2.9	1.3	0.5	0.5	0.5	1.4	2.7	4.8	6.7	2.9
10	4	4.9	3.8	3.9	2	2	1.9	1.9	3.1	4	5.3	4.9	3.5
11	7.2	7.3	5.6	6.7	2.9	1.8	1.4	1.5	2.6	3.5	7	9.4	4.7
12	3.6	3.4	3.2	1.7	1	0.7	1	0.9	1.1	1.8	2.5	3.7	2.1
13	3.3	2.9	2.7	1.6	0.8	0.7	0.7	0.6	1	1.4	2.8	4.3	1.9
14	4.8	4.9	3.8	4.2	2.1	1.4	1.8	1.8	3	3	6.6	6.9	3.7
15	1.7	4.3	2.7	1.2	1.3	1.2	0.6	0.9	1.7	1.4	1.7	na	1.7

Monthly and annual values of wave power are good indicators of the global wave climate; Table 2 presents annual wave power values below 2 kw/m only for the buoys along the Adriatic coast and Catania coast.

The northern Adriatic is one of the most delicate environmental in the entire Mediterranean Sea and its dynamic seems to be independent from the middle and southern Adriatic,[40]. However, it shows its influence on the other two regions through the North Adriatic deep water. Its large river runoff brings a great amount of nutrient that, when combined with summer wave climate and strong vertical stratification, produces the ideal environment to develop hypoxia or anoxia. This work focus is to develop a device especially designed for summer wave climate in seas like North Adriatic; the declared aim does not represent a restriction, since the device will be able to work in all the Seas that, always more frequently, exhibit symptoms of eutrophication and hypoxia. Seas characterized by these phenomena show, during hypoxic or anoxic events, a wave climate that presents different steepness and direction but its heights are of the same order of magnitude of the northern Adriatic Sea; between, completely flat sea and 0.40 m.

Wave Overtopping

Research on wave overtopping of coastal structures has been the subject of numerous investigations over the past 50 years. Since then overtopping prediction tools for typical sea defense structures have continuously been refined. The term wave overtopping is used here to refer to the process where waves hit a sloped structure, run up the slope and eventually, if the crest level of the slope is lower than the highest run-up level, overtop the structure, Figure 11.

Figure 11: Wave overtopping of the Wave Dragon prototype,[60].

The discharge from wave overtopping is thus defined as overtopping volume (m^3) per time (s) and structure width (m). The reason for predicting overtopping of structures is to design better structures to protect human lives and significant structures against the violent force of the surrounding sea. Typically, rubble mound or vertical wall breakwaters have been used for the protection of harbors and dikes and offshore breakwaters have been used for the protection of beaches and land. All these structures are designed to avoid the risk of overtopping or at least to reduce it to a minimum, since overtopping can lead either to functional or structural failure of structures.

The research described in this thesis has a slightly different target; in fact it is aimed to use wave energy to pump water from the surface to the bottom with a simple and economical device able to catch even waves characterized by a low level of energy and convert the overtopping discharge into a downward flux. Economical or energetic fields are not concerned in the present study; the only purpose of this work is to improve the quality of deep water.

Wave overtopping studies: present knowledge

A number of different methods are available to predict overtopping of particular structures under given wave conditions and water levels. Each method has its strengths and weaknesses under different circumstances. In theory, analytical methods can be used to relate the driving process and the structure to the response through equations based directly on a knowledge of the physics of the process. It is however extremely rare for the structures, the waves and the overtopping process to all be well-controlled and known so that an analytical method can give reliable predictions. Other methods are based on the use of measured overtopping from model tests and field measurements. They can use the neural network tool trained using a test, [61]. The last method is based on physical modelling and it consists in testing a scale model with correctly scaled wave conditions. Usually, such models may be built in a scale typically ranging between 1:20 to 1:60. Physical models can be used to measure many different aspects of overtopping such as wave-by-wave volumes, overtopping velocities and depths. Past physical investigations on the wave overtopping of marine structures highlighted that the discharge does not depend only on environmental condition such as wave height, wave period and level but also on the geometrical layout and on the material of the structure, [62], [63]. A lot of investigations have been conducted but none of them has been able to describe all the possible situations. The most common and reliable way of investigation is the physical modelling. Such type of investigation aims to identify an empirical relationship between

environmental conditions, geometrical layout and material properties of the structure and the overtopping discharge. Several formulas have been produced, since the first study conducted by Owen, [64] in 1980. The research was aimed to investigate the overtopping over a specific classes of coastal frameworks that included impermeable and smooth, rough and straight and bermed sloped structures. In his work Owen determined the first experimental method to quantify the overtopping flow rate. The formula was an exponential equation that gave as a result a dimensionless value of the overtopping discharge and the input was a dimensionless parameter dependent by the free board of the breakwater. Since 1980 ten new equations have been proposed, but all of them were based on the same exponential structure of the Owen's formula, [65], [66], [67], [68],[69], [70],[71], [72], [73], [62]. In order to clarify the status of the present knowledge Burcharth wrote in 2000 a comprehensive overview on overtopping of coastal structures, [74], where more details on some of the prediction formulae are available. Douglass, in 1986 [75], reviewed and compared a number of methods for estimating irregular wave overtopping discharges. He concluded that overtopping discharges calculated using empirically derived equations can only be considered within a factor of the actual overtopping discharge. The abovementioned methods deal with overtopping of coastal defense structures and so the typical crest freeboards are relatively high and the overtopping discharges low. Under such conditions overtopping discharge depends on relatively few and relatively large overtopping events. That means that the overtopping discharge becomes very sensitive to the stochastic nature of irregular waves. It must be expected that uncertainty in estimating the overtopping discharge are going to be reduced if the crest freeboard is reduced, since more waves are able to overtop the structure.

Before Kofoed 2002 [62], all available the studies and researches aimed to estimate the overtopping discharge for a ground-based structures. The advent of floating overtopping wave energy converters required more accurate equations that can take into account how the level of buoyancy affects the water flow over the structure. In his research Kofoed made large series of laboratory tests in order to incorporated some correction factors

related to slope angle, crest free board, draft, slope shape and shape of guiding walls into the expression proposed by Van der Meer 1995, [70].
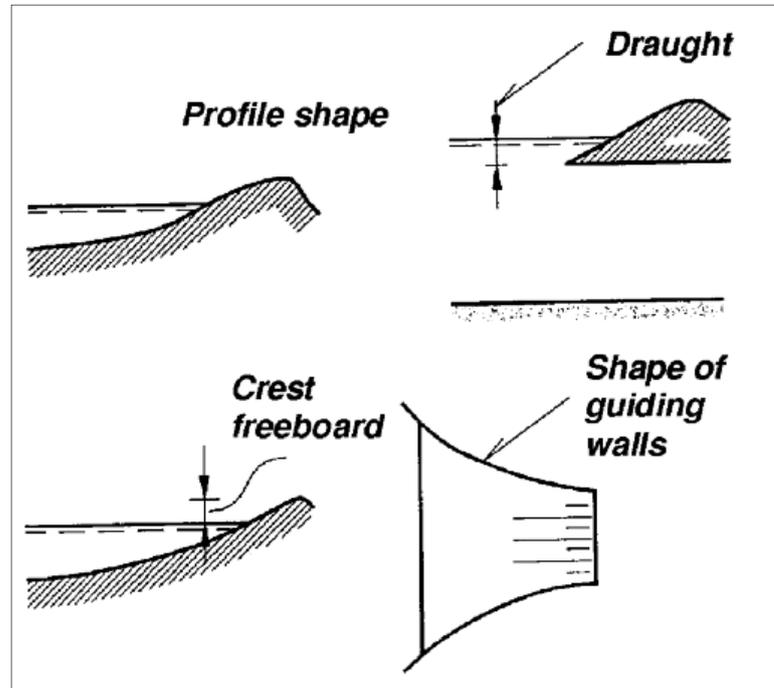
Figure 12: Parameters investigated by Kofoed,[62].

The results of the new equation proposed by Kofoed fitted experimental data very well, R^2 (square of the Pearson product moment correlation coefficient) increases from 0.75 (van der Meer's equation) to 0.97 (Kofoeed's equation, below).

$$\frac{q}{\lambda_\alpha \cdot \lambda_{dr} \cdot \lambda_s \cdot \sqrt{g \cdot H_s^3}} = 0.2 \cdot e^{-2.6 \cdot \frac{R_c}{H_s} \cdot \frac{1}{\gamma_r \cdot \gamma_b \cdot \gamma_h \cdot \gamma_\beta}} \qquad (1)$$

Where λ_a, λ_{dr} and λ_s are defined by Kofoed and γ_r, γ_b, γ_h and γ_β are defined by Van der Meer, 1995, [70].

Influence of slope angle

Completed test series by Kofoed, with varying slope angle shows that the average overtopping discharge is slightly dependent an α. Introduced corrector factor λ_α was identified in order to take into account this dependency, its equation is:

$$\lambda_\alpha = cos^\beta \cdot (\alpha - \alpha_m) \qquad (2)$$

where α_m is the optimal slope angle, equal to 30° and β is a coefficient equal to 3, both values are identified by best fit. Equation 2 is formulated so that the result is for optimal slope angle and it decreases when difference between optimal and actual slope angle increases. The correction factor λ_α for the device here investigated is equal to 0.989, with a slope angle of 25.4°, see Appendix A for the calculus.
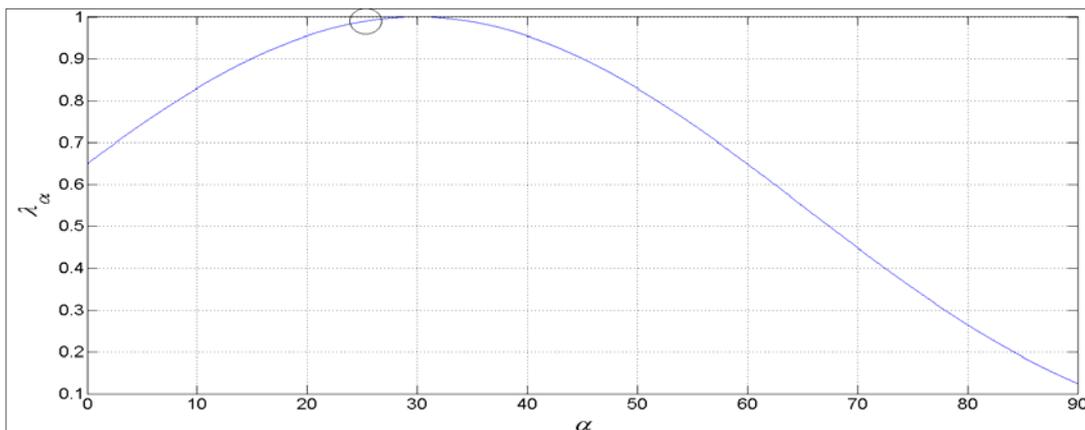
Figure 13: λ_α as a function of the slope angle. Value for tested shape in present work is black circle.

Influence of draft

Conducted test series by Kofoed with varying draft shows results strongly affected by this parameter. In order to take into account this dependency the coefficient proposed is:

$$\lambda_{dr} = 1 - k \cdot \frac{sinh\left(2 \cdot k_p \cdot d \cdot \left(1 - \frac{d}{d_r}\right)\right) + 2 \cdot k_p \cdot d \cdot \left(1 - \frac{d}{d_r}\right)}{sinh(2 \cdot k_p \cdot d) + 2 \cdot k_p \cdot d} \qquad (3)$$

where k_p is the wave number based on L_p and k is a coefficient controlling the degree of influence of the limited draft. k is equal to 0.4 by nest fit. The expression taking the dependency of the draft into account is based on the ratio between the time averaged amount of energy flux integrated from the draft up to the surface $E_{f,dr}$ and the time averaged amount of energy flux integrated from the seabed up to the surface $E_{f,d}$.

$$\frac{E_{f,dr}}{E_{f,d}} = \frac{\int_{-dr}^{0} p^+ \cdot u \, dz}{\int_{-d}^{0} p^+ \cdot u \, dz} = 1 - \frac{sinh\left(2 \cdot k \cdot d \cdot \left(1 - \frac{d_r}{d}\right)\right) + 2 \cdot k \cdot d \cdot \left(1 - \frac{d_r}{d}\right)}{sinh(2 \cdot k \cdot d) + 2 \cdot k \cdot d} \qquad (4)$$
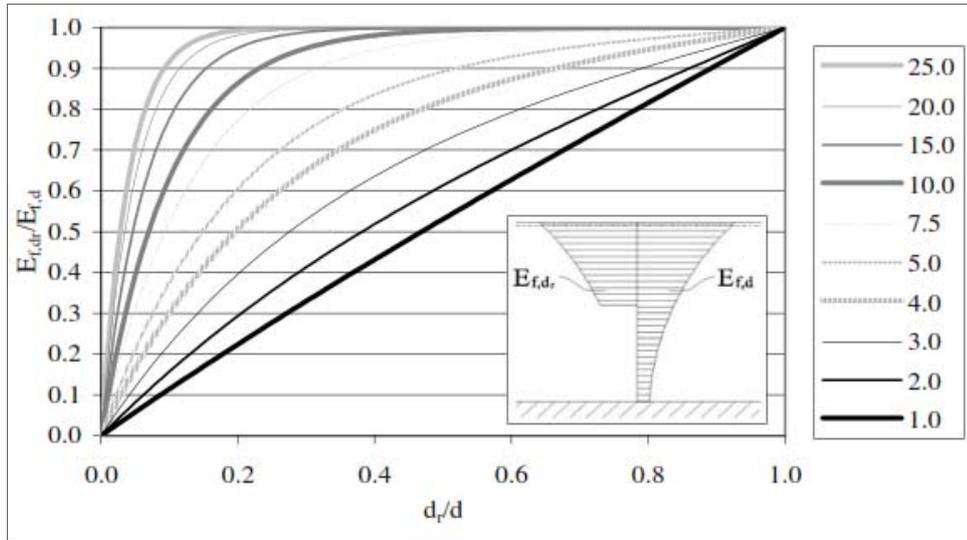
Figure 14: Ratio described by equation 4 as a function of the relative draft, [62].

To derive equation 3 linear wave theory has been used; this implies a limitation that leads to a not exact description of the overtopping phenomena.

The correction factor λ_{dr} for the device here investigated is equal to 0.8101 for a draft equal to 0.37 m and a freeboard crest of 0.11 m.
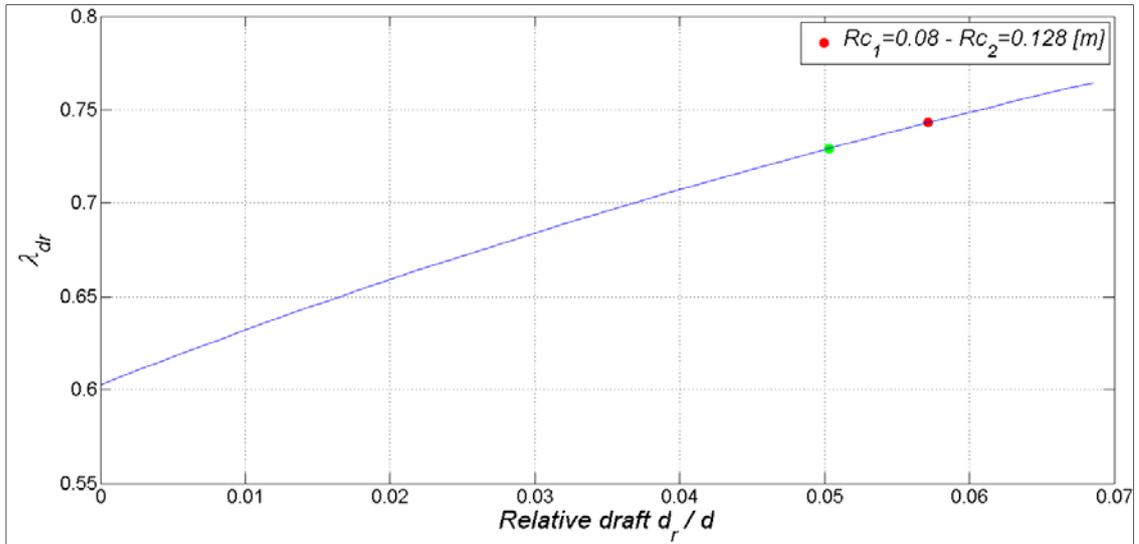
Figure 15: λ_{dr} as a function of the relative draft. Two freeboard levels for wave state T (H=0.48 m and T=2.88 sec).

Influence of dimensionless freeboard parameter (R)

Kofoed identified that for values of dimensionless freeboard (R) larger than 0.75 the equation given in [70], fit the data very well, but when the R decries from 0.75 to 0 some discrepancies appear between the predicted values and the observed values. In order to increase the degree of description of the phenomena parameter proposed by Van der Meer was modified as follow:

$$\lambda_s = \begin{cases} 0.4 \cdot \sin\left(\frac{2\cdot\pi}{3} \cdot R\right) + 0.6 & for\ R < 0.75 \\ 1 & for\ R \geq 0.75 \end{cases} \tag{5}$$

32
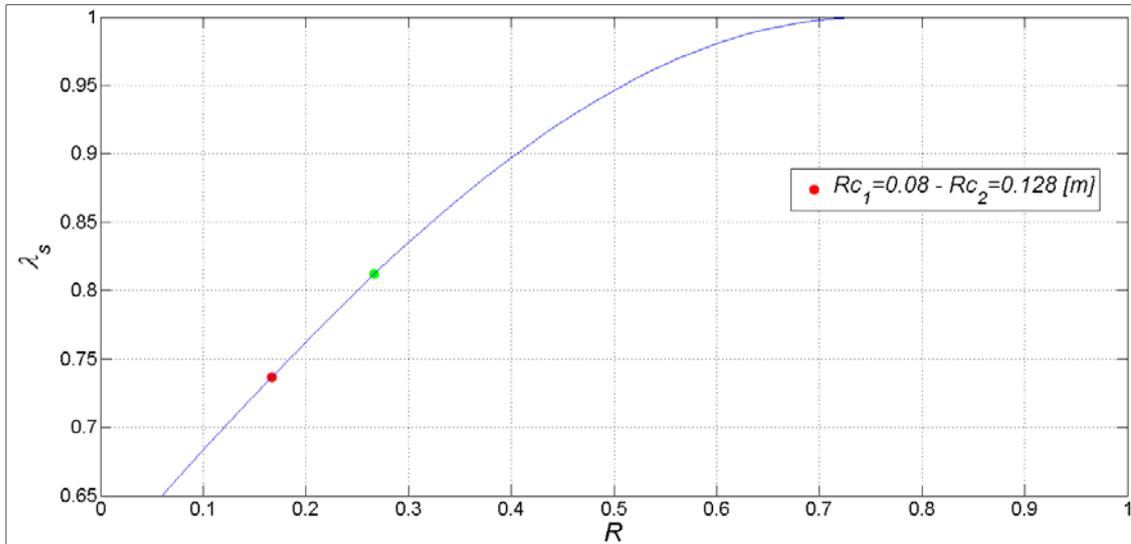
Figure 16: λ_s as a function of dimensionless freeboard parameter (R_c/H_s). Two freeboard levels for wave state T (H=0.48 m and T=2.88 sec).

Coefficients γ_r, γ_b, γ_h are introduced to take into account the influence of a berm, shallow foreshore, roughness and angle of wave attack respectively. All these coefficients are worth between 0.5 - 1.0 meaning that when maximizing overtopping the coefficients should be 1.0, which is the case of no berm, no shallow foreshore, smooth slope (no roughness and impermeable) and head-on wave. This will be the case of the current study.

In the current study Kofoed's equation is used to estimate the overtopping discharge over the device under investigation *OXYFLUX,* Figure 17.
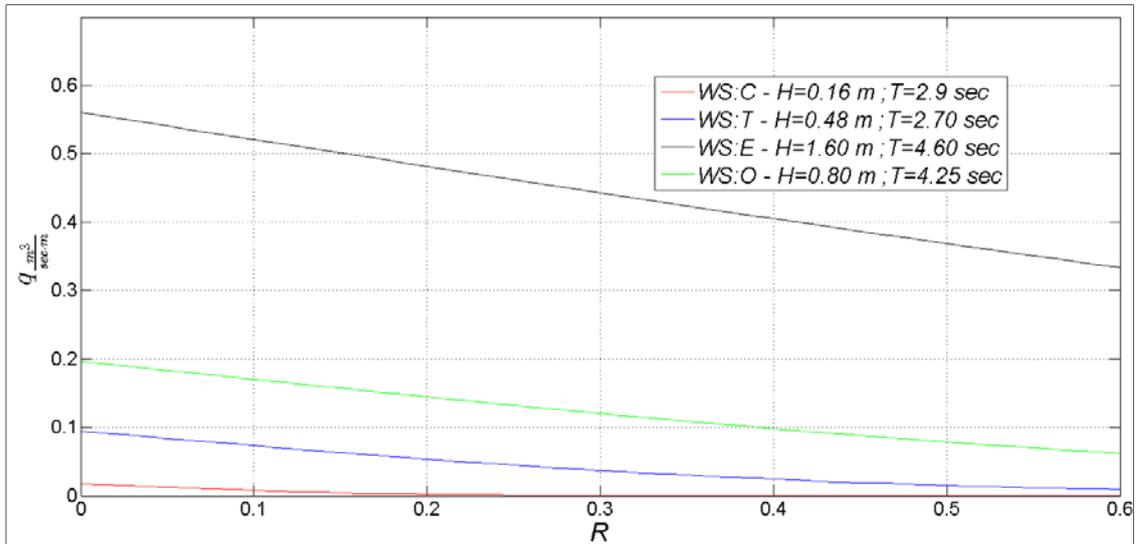
Figure 17: q [m^3/m/sec] as a function of dimensionless freeboard parameter (R$_c$/H$_s$). Results for OXYFLUX, wave climate of Northern Adriatic Sea

Wave energy as a propellant for sea water pump

Within the past 50 years two different ideas have been proposed for water pumps suitable to the ocean and both of them have been built and tested to work under environmental conditions. The first method, chronologically speaking, is the perpetual salt fountain that is based on the fact that both temperature and salinity affect the density of seawater and that heat can be conducted through a metal pipe whereas salt cannot. This idea attracted a brief interest only in the 1950s [76] but its origin probably goes back to about 100 years before, [77]. In the regions of the ocean, where warm salty water overlies cold fresh water (e.g. some areas of the tropics and subtropics) such that overall static stability in the vertical direction is maintained, a metal pipe is placed in a vertical position so that it bridges these two water types. The system is primed by moving some water upward inside the pipe. Heat will diffuse into the rising water in the pipe through its conducting metal walls but the impermeability of the pipe will prevent any salt from diffusing in. Thus the water in the pipe will become less dense than the environment at the same depth

34

and will continue to rise upward under positive buoyancy. This is the perpetual salt fountain, which was first tried in the North Atlantic in 1971 using a 1000 m flexible plastic tube, though with unconvincing results, [78]. However, recent results in 2002 in the North Pacific have been more encouraging,[79]. The salt fountain can be reversible since a downward push on the water would make it flow downward. Since diffusion is what drives the fountain, the time-scale of this type of pump is a diffusion time-scale, which is expected to be relatively long, compared to a wave period, for example, while the flow velocity is anticipated to be relatively weak. In a different sense the salt fountain is not reversible because it does not work if a layer of cold fresh water overlies a layer of warm salty water, as occurs in the Mediterranean and in some high latitude regions (e.g. Norwegian fjords),[80].

A second method is represented by Isaacs's idea, dated in 1976. The basic principle is simple: a length of tubing attached to a surface buoy, with a one-way valve at the bottom can be extended below the eutrophic zone to act as a conduit for deep water. The vertical motion of the ocean forces the attached valve to open on the down slope of a wave and close on the upslope, thus generating upward movement of deep water to the surface ocean,[81], [82].

A third new type of wave water pump was proposed by Kenyon in 2007. The concept is mechanically simpler than the Isaacs's pump, because it involves no valves at all and has a considerably faster pumping rate than the salt fountain method. Furthermore, this wave pump does not need to be primed to get started unlike the salt fountain. Kenyon proposed to utilize the pressure gradient established inside a strictly rigid, impermeable pipe oriented vertically and submerged in the ocean near the surface. Tube's lower end had to be located at, or below the depth of wave influence, where the fluid motion and pressure variations due to the surface waves are negligibly small compared to those at the surface. The upper end of the pipe had to be placed just below the lowest anticipated level of the wave troughs in the region of the most active part of the wave field. Kenyon suggested 15 m below mean sea level could be a reasonable value, taken into account that a 30 m wave

height is possible but it is a very rare occurrence. Once the tube is positioned, water will immediately begin to flow upward inside the pipe and it will continue to do so as long as surface waves move, no reasons lead to think that the flow needs to be primed, as soon as the gradient is established along the pipe fluid will move upward, according with,[80]. Kenyon's idea is based on taking advantage of two natural principles, the first is Bernoulli's principle and the second is the exponential decay of the wave motion with increasing depth. Particle motion due to the wave moves across the top opening of the pipe, causing relatively low pressure compared to the, essentially, constant and higher pressure at the bottom end of the pipe. The pressure difference along the pipe causes the fluid to flow consistently upward. In the numerical example given by Kenyon the maximum vertical velocity of the wave pump is predicted to be about 3.5 cm/sec when the pipe radius is 3 cm, the length of the pipe was half a wavelength and the average wave steepness was about 1/100, [80]. That rate was an order of magnitude greater than the one quoted by Maruyama, [79], of 2.45 mm/sec for the salt fountain with a pipe radius of 15 cm.

More recently a fourth type of device aimed to pump water has been analyzed by several authors. The aim of those studies was to find mechanism to pump water downward through the stratified water column. Two major purpose lead such new technologies; the first is the extraction of clean energy from wave motion,[83] , and the second, which also the purpose of the present thesis, is to pump well oxygenated surface water to the bottom, where oxygen is required, [84], [85], [86], [87]. Concerning with the second of the two reasons, it is not a surprise that both the devices investigated in those woks are born in countries where eutrophication and anoxia are common, like Italia's northern Adriatic coasts and Sweden's south-eastern Baltic coasts, according to [40] and [85].

Overtopping wave energy converters

In this work only a few overtopping wave energy converters have been studied. Among them, the Wave Dragon, [62],[88], is the most practical and pioneering model. It consists

of two wave reflectors, a reservoir and several hydro turbines. The wave reflectors direct the incoming waves towards a ramp, and overtopping water is collected in a reservoir above sea level. Low-head hydro turbines generate power by using the hydraulic head of the stored water. The Wave Dragon is a floating converter that can be placed in offshore areas with a mooring line, Figure 18.

Figure 18: The Wave Dragon pilot plant (scale 1:4.5) in Nissum Bredning, Denmark, [89].

A different conception of overtopping wave energy converter is the Seawave Slot-Cone Generator (SSG), Figure 19. It consists of multiple reservoirs and a multi-stage turbine, which results in a higher overall efficiency compared to a single stage one, Figure 20, [90], [91], [92].

Figure 19: The SSG pilot plant in the Island of Kvitsøy, Norge, [90].
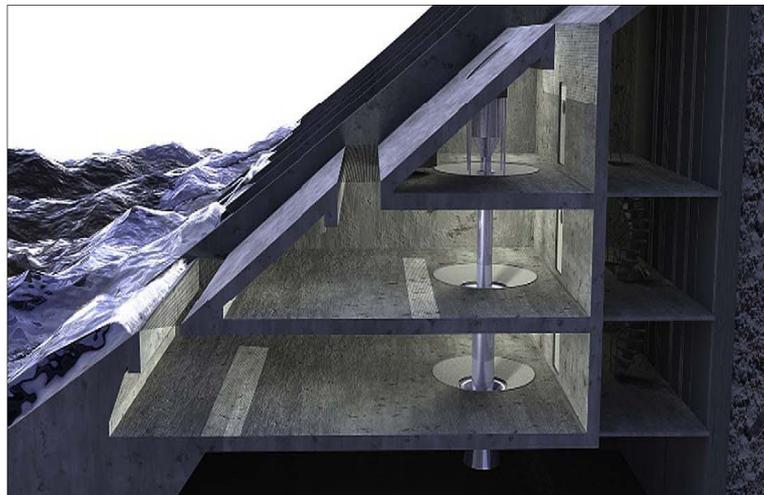
Figure 20: Lateral section of a three-levels SSG device with Multi-stage Turbine, [90].

A different kind of device is the so called spiral-reef overtopping wave energy converter. Such device is a fixed circular-shaped structure. Consequently, the converter's performance is not affected by the direction of the incoming waves. The device is composed of a sloped ramp, an inner reservoir and a substructure. The substructure can be a mono-pile type or jacket type. Guide-vanes are attached on the ramp to reinforce wave overtopping. Overtopping water is accumulated in the reservoir and then drained out through a center hole.

Figure 21: Spiral-reef overtopping wave energy converter, [83].

All these devices have been investigated both numerically and physically. From the numerical point of view commercial CFD software like STAR-CCM+ [93] , FLUENT [94] or FLOW 3D [83] have been used to describe the non linear phenomena acting on the devices. For simpler shapes or when the viscosity is negligible software like WAMIT or AQWA have been used to investigate the hydrodynamic behavior and the hydrodynamic parameters, such as added mass, radiation damping and wave induced force. Physical models are well consolidated, both for fixed and floating structures. The overtopping volume can be measured by means of different instruments. Wave overtopping over the Wave Dragon was widely described by Kofoed in [62]. He used a complex but accurate measuring system based on two reservoirs, a pump and a water level gauge. Between the slope and the reservoir there was a perforated damping wall to reduce the amount of turbulence on the water surface in the reservoir since it can intefere with the water level measurements. The water level gauge and the pump were connected to a PC monitoring and recording water levels in reservoir. Every time a preset maximum water level was reached the pump was activated for a fixed time period and the pumped volume of water was estimated thank to the pump. After data from simulations were collected, Kofoed calculated the overtopping discharge time series by mean of differentiation. The signal from the water level gauge was corrected by adding a section

of the water level time series measured during the calibration of the pump at the time where the pump is emptying the reservoir. Measuring the different overtopping discharges for each level of the Seawave Slot-cone Generator (SSG), needed a more complex method, even if similar to the one described before. Each reservoir was connected to a tank behind the structure where the collected overtopping water was measured using water elevation gauges and calibrated pumps,[95], [96].

Devices to counteract oxygen depletion

So far only two different types of device aimed to counteract hypoxia or anoxia, have been investigated. The paternity of the idea to use floating breakwaters to oxygenate the anoxic bottoms and the deep water can be attributed to an independent nonprofit organization called O_2 gruppen, [97]. They proposed, Figure 22, the Wave Energized Baltic Aeration Pump (*WEBAP*), [85], [86], [87].
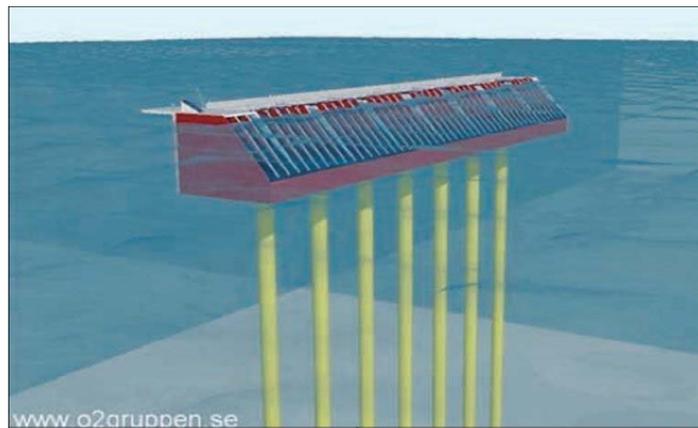
Figure 22: An artist's conception of a wave pump,[97].

This new idea has been considered by the European Union and financed with a Life+ project of one million Euro,[98]. The project started with Carstens's master thesis [85], in which he investigated the design aspects of the device and possible sites where a scale prototype could be installed. Carstens analyzed, analytically, the predictable overtopping discharge by means of Kofoed's formula and USACE standard,[99]. He proposed two different locations for pilot plant, Kanholmsfjärden and Söder Möjafjärd, which are two

connected bays located in the Stockholm archipelago. Second in chronological order, and subject of the present work is the *OXYFLUX,* that will be largely discuses in the following chapters.

The physical principle of the WEBAP, is not so different from the device investigated in the present document. A floating breakwater is supposed to collect incoming waves into a reservoir inside the breakwater. The stored water, after overtopping the ramp leading to the reservoir, will be at a higher level than mean water level and therefore will have a potential energy. The driving head of the overtopping water temporarily stored in the reservoir induce the water to flow out through a long vertical pipe that ends close to the bottom of the sea. Margheritini studied the WEBAP device by means of physical models developed at the University of Aalborg. She was concentrated on finding the proof of concept of the device, estimating the displacements of the floating body and the mooring force under the action of extreme waves and estimating the overtopping discharge thorough the Kofoed's formula.
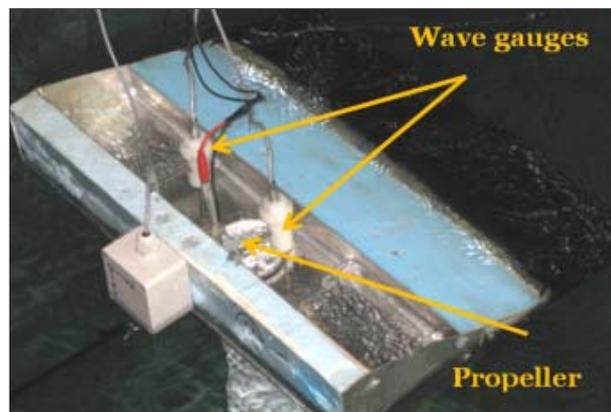
Figure 23:WEBAP physical model,[87].

Margheritini tried to measure the downward water velocity by means of a propeller posed inside the reservoir but high level of agitation, large displacement, and the impossibility to identify the direction of rotation of the propeller made this method of measurement

unreliable. Investigation on the physical model of the OXYFLUX will not take into account this procedure.

After 2010, when Margheritini made her studies, the demonstration plants were constructed, transported and installed at the defined locations, i.e. Hanö bay outside the shoreline of Simrishamn and Kanholmsfjärden/Möja Söderfjärd in the outer Stockholm Archipelago. The pilot plants were then tested for three years together with extensive monitoring and sampling of water and sediments in and around the pumps.
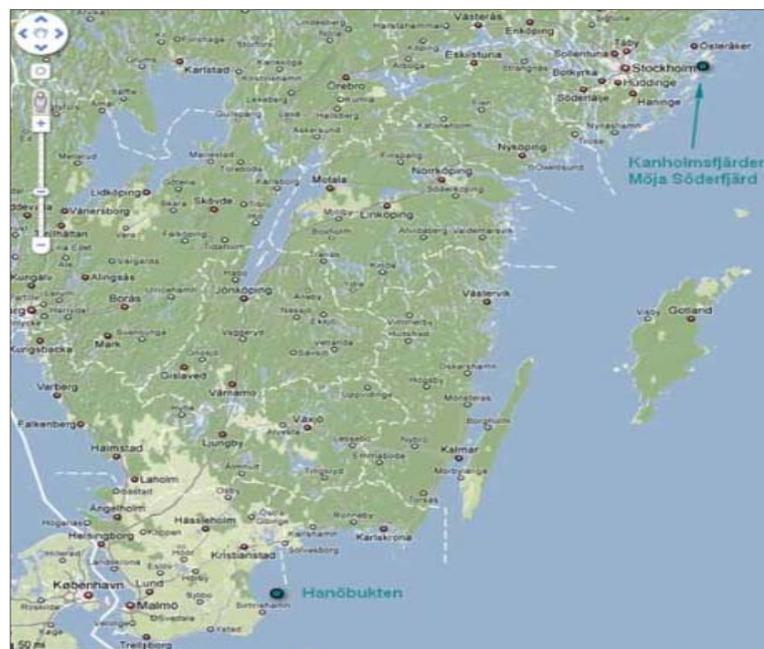
Figure 24:WEBAP pilot plan locations,[87].

On 31st Dicember 2012, WEBAP-LIFE project ended and the results were published in the web site of project [100]. The principal parameters that have been monitored are dissolved oxygen in the bottom water and phosphorus released from sea sediments because of the lack of oxygen.

Baresel in the project's final report argues how the expected positive environmental impact occurred in the pilot plant location, [101]. Indeed around the lower end of the

devices low level of phosphorus in the sediment were recognized. In the project's final report it has been highlighted how, on the basis of environmental impact and total cost assessment the WEBAP represent the most sustainable and cost-efficient system.
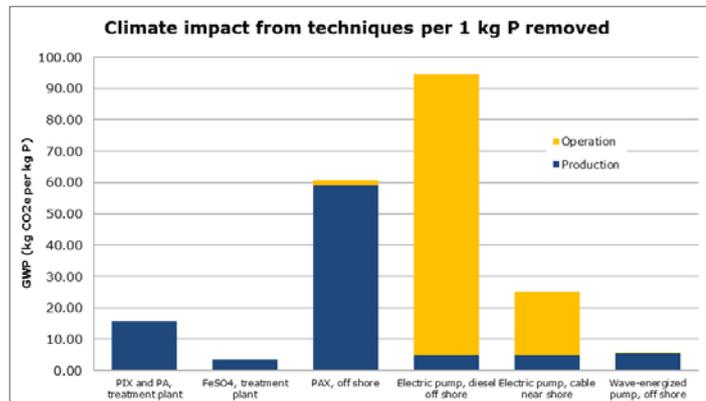
Figure 25:Comparison of environmental footprint for different technologies aimed to remove phosphorus in Baltic Sea,[101].
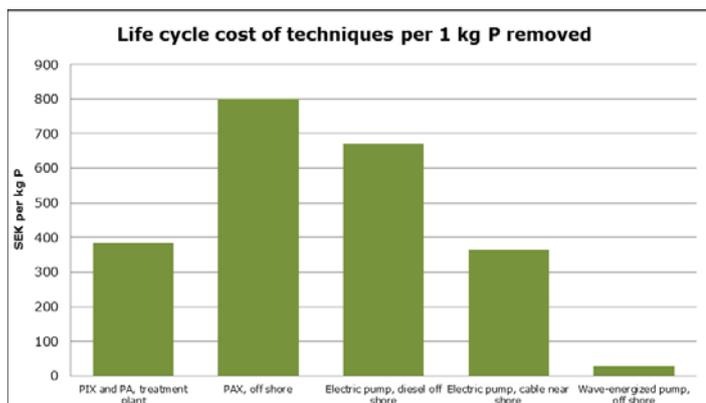
Figure 26:Comparison of costs for different technologies aimed to remove phosphorus in Baltic Sea,[101].

Purpose of the study

In light of the outlined state of development of WECs and the state of the environmental health of the Northern Adriatic Sea, the author has carried out a design of a device able to counteract oxygen depletion at the bottom sea layers as a PhD project at the Department

of Civil, Chemical, Environmental and Material Engineering (DICAM), University of Bologna, (UNIBO). This work aims to provide a new type of device able to pump well-oxygenated surface water to the bottom, where in many cases, oxygen is consumed by the large oxidization activity due to the abnormal quantity of sedimented organic matter. The study has investigated how different geometric parameters such the shape of the floaters, its structures (flexible or rigid), the crest freeboard and mooring systems affect the amount of the downward water flux, highlighting a possible application in the Northern Adriatic Sea. This has been achieved through studies of the literature, theoretical considerations, model tests in two different wave tanks and numerical modelling of the floating device. By using model tests the reliability of the idea was pointed out and the influence of several parameters (geometrical and not) were recognized. The displacements of the devices have been measured and so the variation in the downward flux over time since the latter is influenced by the displacement of the devices. While the numerical modelling has been used to investigate performance of new floater shape, after the validation by means of results comparison between physical and numerical analysis.

It is expected that the findings of this study will be useful for developing new devices to counteract oxygen depletion on the bottom layers as well as helpful for all public authorities involved in managing eutrophic, hypoxic and anoxic coastal areas.

CHAPTER III: Development of the device *OXYFLUX*

The first idea to oxygenate the anoxic bottom of the sea by using wave energy originated from an independent nonprofit organization called O_2-Groupen [97] which proposed a floating breakwater able to catch water from waves and to convert its potential energy to create a downward water flux in a tube. This device was designed to be used in the Baltic Sea and it has large dimensions since it is a breakwater. Due to its working mechanism, characterized by having a principal wave direction and a by the need for a relatively high minimum wave height in order to work, this device is not suitable for the Adriatic Sea, since the Adriatic's summer wave climate and its medium depth are smaller than the Baltic's ones.

A second idea to counteract oxygen depletion and excessive algal blooms in the Baltic Sea has been made by Stigebrandt and Gustafsson in 2007 [102] and it is called the halocline ventilation by mid-water mixing. The idea is to mimic the natural mixing processes observed during periods of high internal mixing, and to increase both the transport of oxygen-rich water to the deep areas and to mix the layers around the

halocline pumping water between the depth of 50-125 meters. This is expected both to increase oxygen levels in deep water and decrease phosphorus concentrations due to decreased leaking from bottom sediment and phosphorus binding when more aerobic conditions occur. The hypothesis is that this would lead to better conditions in deep water, giving benthic animals, deep-water living and reproducing fish possibilities to recover, and contributing to the decrease of algal blooms during the summer months, thanks to lower P concentrations in the surface waters, [85].

In this thesis a device able to induce aeration taking advantage of wave energy during the summer along the Northern Adriatic coasts has been designed and tested. The idea is based on the abovementioned systems, but OXYFLUX will be characterized by an operational range of wave height suitable to obtain a water column mix just with a minimum wave height of .20 m and by not needing a main wave direction. The most important aspect of this new technology is the absence of any moving or electro-mechanic parts. The decision to exclude these components comes from the observed failures of the WEC's, as the main problems derived from the inability of movable parts to endure open sea environmental conditions, Figure 27.
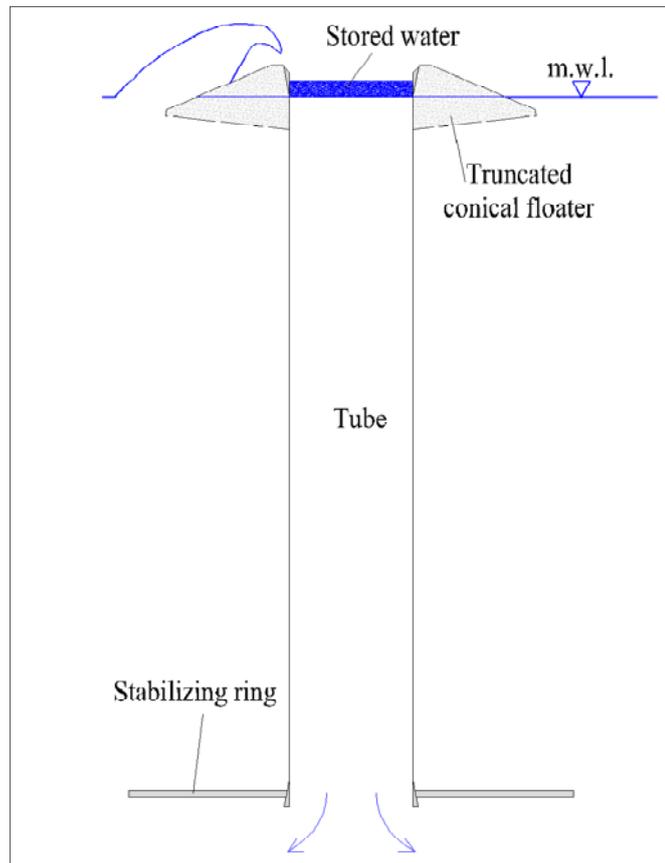
Figure 27: Schematic representation of OXYFLUX's pumping mechanism.

Proof of concept

The physical principle on which the investigated device "*OXYFLUX*" is based, is the capacity to enhance vertical mixing processes and to induce aeration of deep water by pumping oxygen-rich surface water downward at a desired depth around the halocline. Its operating mechanism is based on wave overtopping. The floater will collect incoming waves into a reservoir floating on the sea. Water overtopping yields a higher hydraulic head in the reservoir, which in turn induces a downward water flux, Figure 27. OXYFLUX is developed to be used with a minimum depth of 5 m, such a restriction is mainly due to the motion of water particles. Since the device uses only the vertical

displacement induced by waves on water particles, the more the depth decreases, the more the vertical water displacement decreases, and so the capability of the floater to collect water in its floater. It can be argued that there should not be a maximum depth as long as wave conditions are able to generate a required head.

Required head

Just like every fluid flux in a tube, so the water flux generated by the OXYFLUX needs a head capable of inducing water column motion. The evaluation of this quantity is made on the basis that the required head must overcome two main components. A long pipe like the one that will be used for OXYFLUX is characterized by significant head losses due to its length and roughness, as well as inlet and outlet ones, furthermore the issue of the different water density along the vertical water column must also be taken into account. Density gradient is affected by two main environmental parameters such as salinity and the temperature of the water column. In this work, reference values of the summer vertical profile of salinity and temperature of the Northern Adriatic [40] have been used to calculate final density distribution by means of UNESCO's algorithms,[103] and so the minimum hydraulic head to overcome the density difference, Figure 28.

Table 3: Average Summer density anomaly in North Adriatic, [46].

Depth (m)	Dnsity ($\sigma_t = \rho - 1000$)
0	26.076
8.5	26.155
14	26.547
23.5	27.53
33.5	28.238
40	28.459
50	28.675
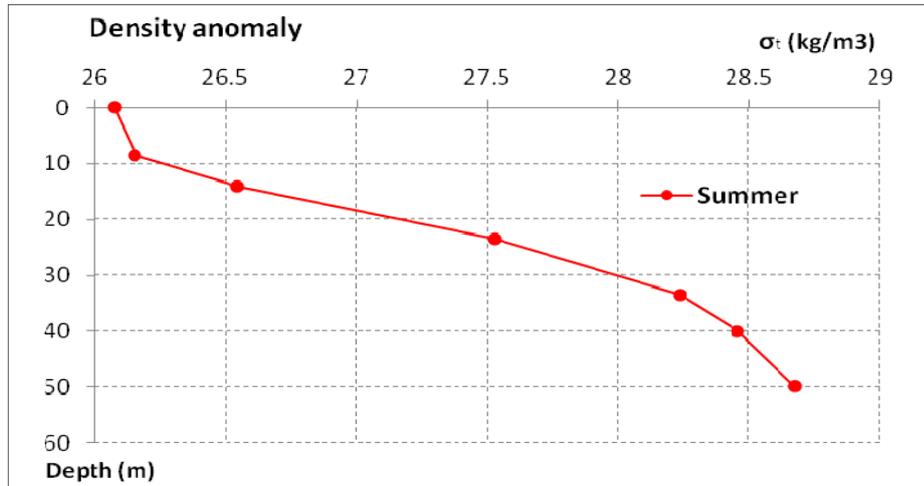
Figure 28: Summer density anomaly in North Adriatic, [46].

From Figure 28 a consistent gradient after 8.5 m depth it can be noted. This study takes into account a depth range from 0 to 10 m since OXYFLUX is designed to work only in shallow waters in the southern area of the mouth of the Po river, where hypoxia generally develops, as highlighted by the chlorophyll concentration in Figure 29.
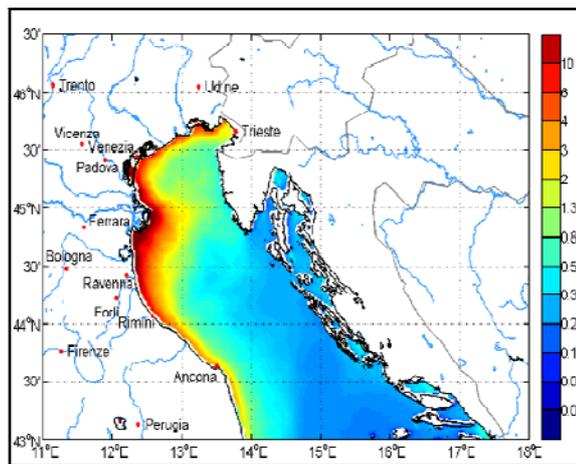
Figure 29: Average value of chlorophyll for August in years 1997-2004, [46].

The minimum head to overcome the density difference (Δh_ρ) has been calculated by means of the application of Kelvin's circulation theorem [104], in the sense that the water column inside the device has been considered to be made up of only lighter surface water

pushed downward by the wanted minimum head. This phenomenon has been modeled as a circular integral on a closed path from the surface to the desired depth in which one vertical branch of the path is characterized by a surface density and the other by the density profile shown in Figure 28 , eq *(6)*.

$$\Delta h_\rho = \frac{\sum_1^n(\rho_i \cdot l_i) - \rho_1 \cdot L}{\rho_1} \qquad\qquad (6)$$

Where ρ_i is the density of the "i" layer, l_i is the length of the "i" layer, equal to 0.01 m , ρ_1 is the water density at the surface, equal to 1026.10 kg/m³ and L is the desired depth to reach.

Distributed and concentrated pressure drops have been calculated by means of the classical Chezy formula in which two tubes have been evaluated in two different states. Distributed losses have been evaluated through the Gauckler-Strickler coefficients, the values of 120 m$^{1/3}$/sec and 60 m$^{1/3}$/sec [105] have been selected for the new and used tube, respectively, Figure 30, Figure 31, Figure 32, Figure 33.
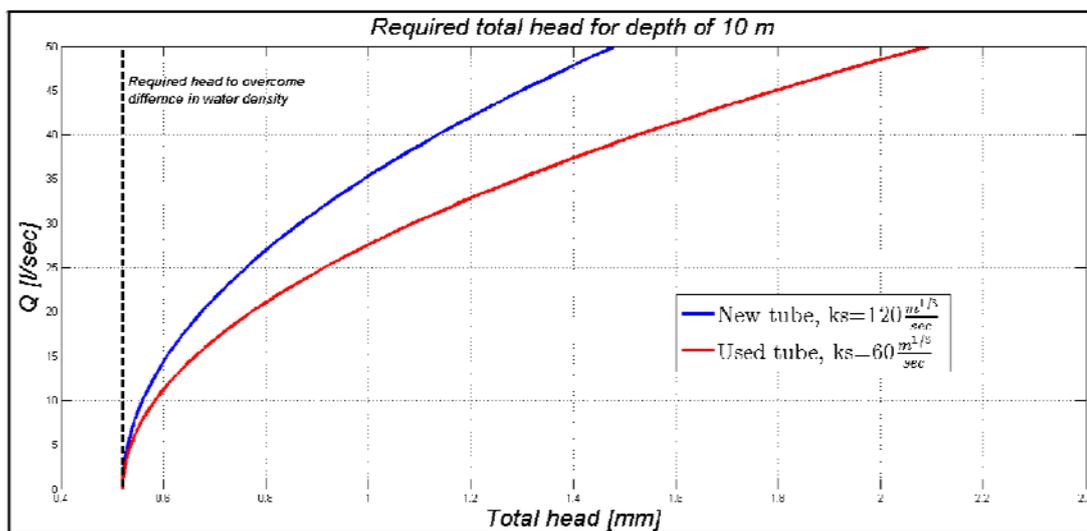
Figure 30: : Device capacity for 10 m of water column for different heads and material conditions.
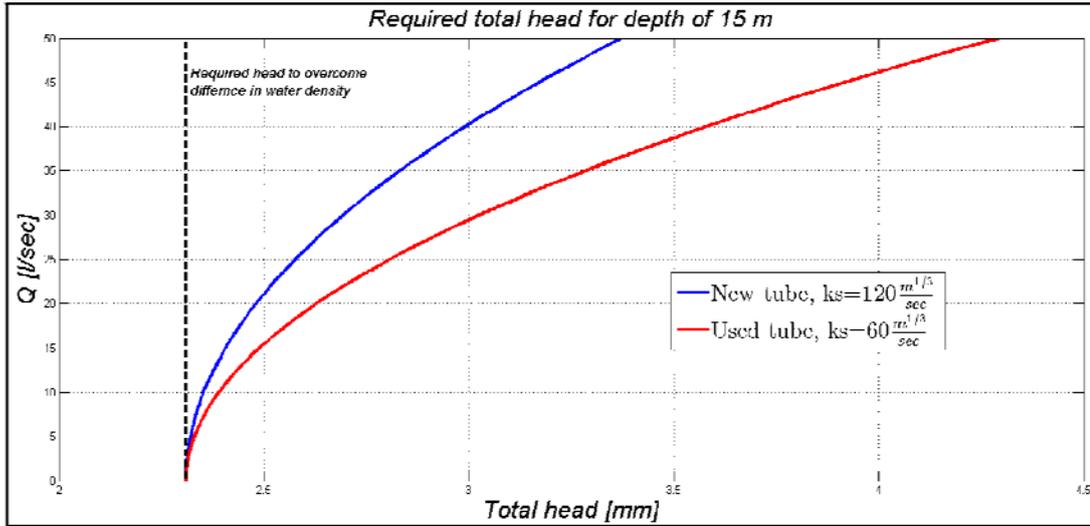
Figure 31: Device capacity for 15 m of water column for different heads and material conditions.
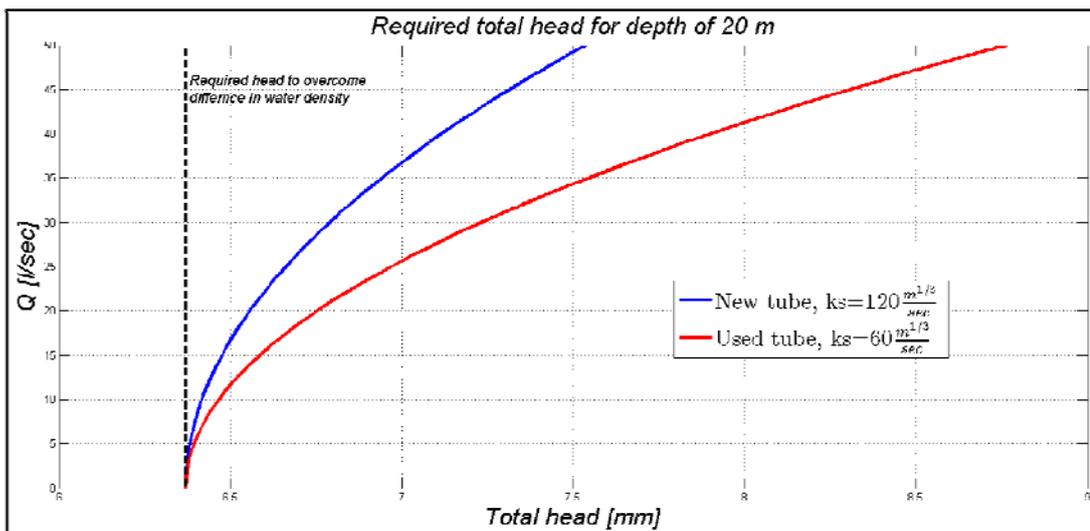
Figure 32: Device capacity for 20 m of water column for different heads and material conditions.
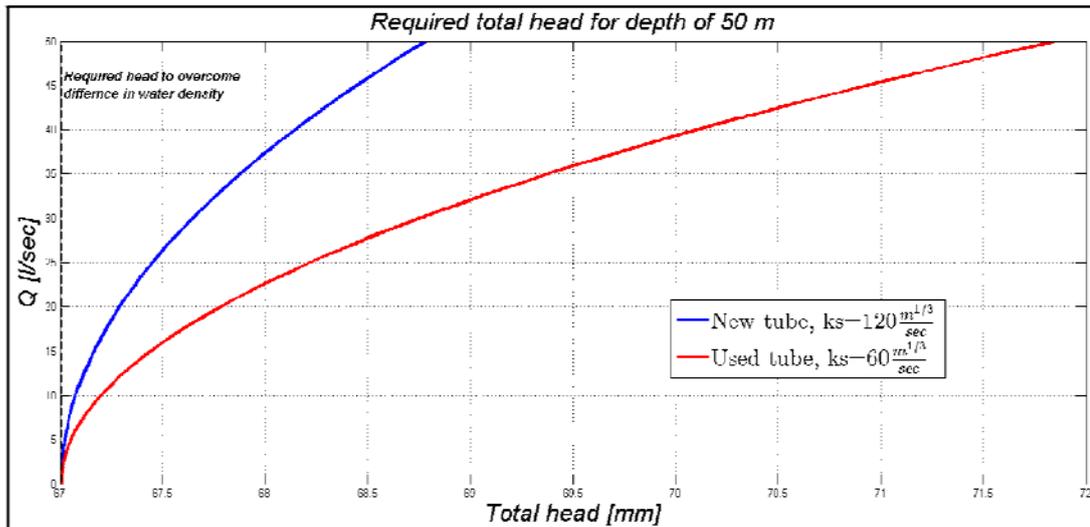
Figure 33: Device capacity for 50 m of water column for different heads and material conditions.

The required head is easily obtainable with the modest wave heights developed during the summer along the coasts of any Seas, since there is always a minimum agitation of the free surface due to the breeze.

Construction of the model

Three main parts constitute *OXYFLUX,* and each of them has a precise function. Below their functions will be discussed as well as the way in which they have been made. Buoyancy of the whole structure is entrusted to a truncated-conical floater, which as well as keeping the structure afloat also collects the water from overtopping. The connection with the bottom, where a stabilizing ring is mounted, is guaranteed by means of a tube made of plexiglas or nylon.

Both the materials have been tested during preliminary tests. Due to problems in the measurement of the velocity of the water flux the idea of a tube made of nylon has been abandoned.

All the models presented in this thesis were made using the machinery of the Hydraulic Laboratory of the University of Bologna.

The following paragraphs focus on the design and realization of the physical scaled model, therefore lengths, masses and forces will be expressed in millimeters [mm], grams [g] and Newton [N] respectively. Physical model tests were carried out according to Froude's law on a scale ratio of 1:16, Table 4.

Table 4: Froude scale law

Variable	λ
Length	16
Area	256
Volume	4096
Time	4
Velocity	4
Force	4096
Power	16384
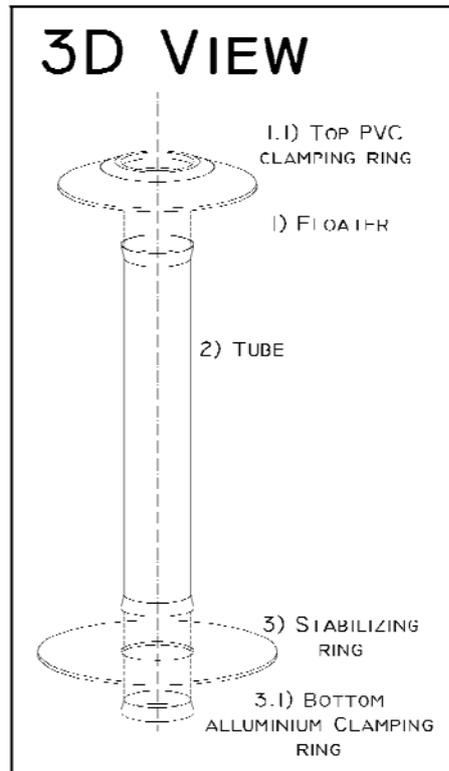
Figure 34: Components of OXYFLUX model.

Floater

In order to maximize the overtopping discharge, particular attention has been taken in the design of the slope angle of the floater. Kofoed [62], identified the optimal slope angle to maximize the overtopping discharge for a linear structure ramp as 30°. In this work the slope angle has been kept as close as possible to this value. A plate of 200 x 200 x 50 mm of closed polystyrene cells has been modeled by means of a lathe and used as a floater. The selection of adequate materials assumes primary importance in order to realize a model able to be tested for a long period of time in water without running into trouble due to the absorption of water by the floater. Furthermore the material of the floater must guarantee an appropriate level of free-board crest. The selected material has a specific weight of 490 N/m^3.

The result of the manufacturing process is a truncated conical shape with a volume of 227191.00 mm^3, corresponding to a weight of 0.11 N. Its maximum diameter is equal to 150 mm while its height is 25.00 mm. The top of the floater was completed with a PVC ring aimed to define precisely the free-board crest and to clamp the flexible tube; the PVC ring has a height of 5.00 mm. The hole in the center is directly connected to the outlet side and it has a diameter of 50.00 mm. See Appendix A for all the details of the structure.
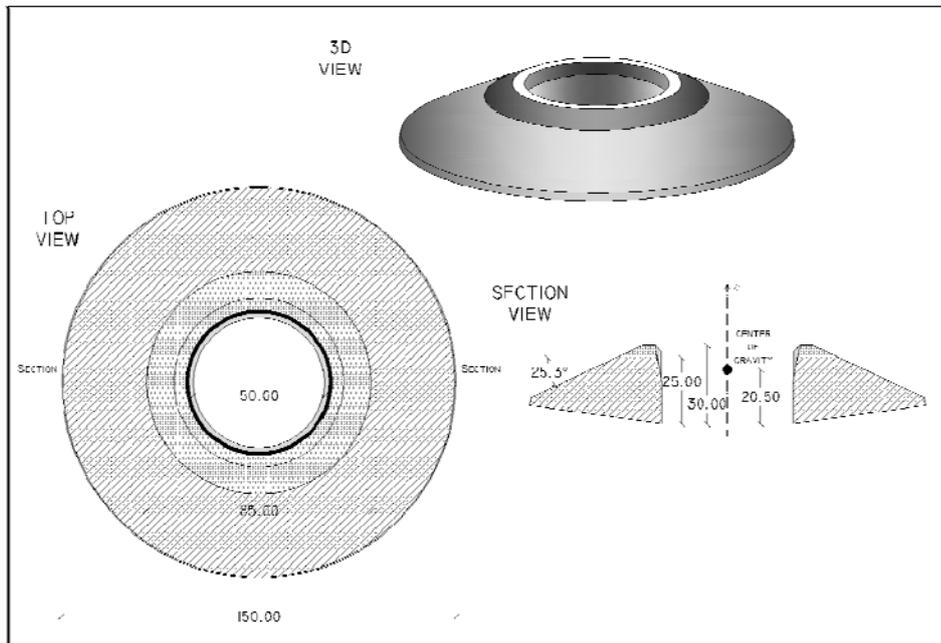
Figure 35: Details of the floater, all lengths are in mm.

Table 5: Hydrodynamics parameters of the floater.

Floater			
Center of gravity (respect z, mm)	Radii of Gyration [mm]		Mass moment of inertia (respect Center of gravity) [mm^2·g]
	R_{xx}	35.5	39395
20.5	R_{yy}	35.5	39395
	R_{zz}	48.5	1516

Tube

The tube connects the floater, where the water is stored, to the bottom, where the water flows out from the device. It has been made with two different materials: a nylon layer and plexiglas. They were realized by means of a lathe and heat welding respectively. The mass of the tube is 1.15 N for the rigid device and 0.35 N for the flexible one. The internal diameter has been kept equal to 50.00 mm. A rigid structure aimed to support the DOP transducer, Figure 36, has been installed inside the tube.
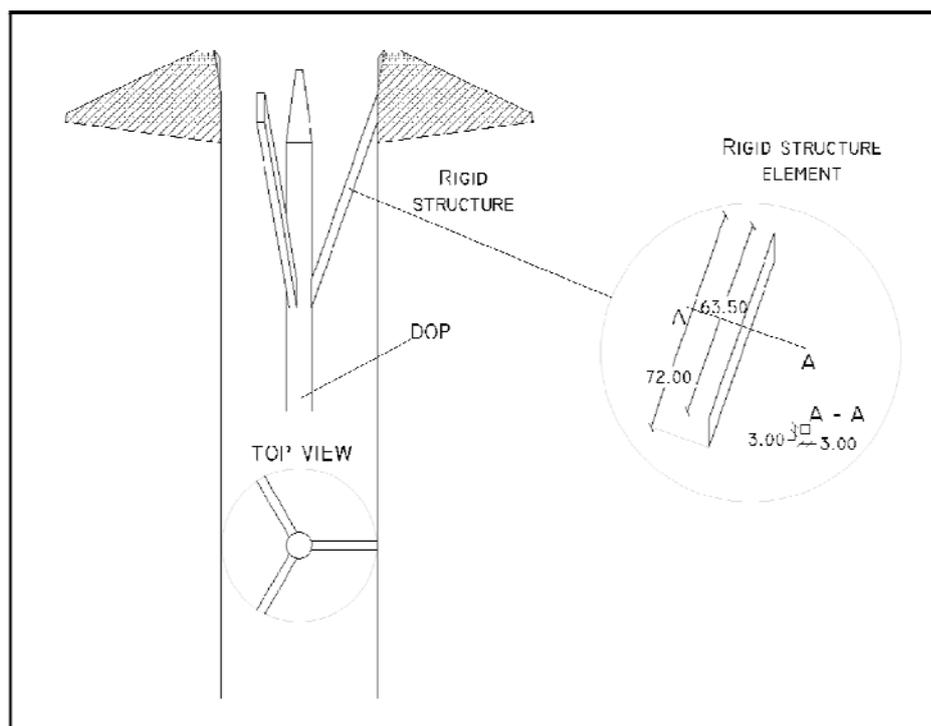
Figure 36: Details of the tube and of the support for the DOP transducer, all lengths are in mm.

Stabilizing ring

The function of this component is to dampen the heave motion in order to let the wave crest overtop the floater. The stabilizing ring is made of aluminum and was realized by

means of a lathe in the laboratory. It is 3.00 mm thick, its diameter is 180.00 mm and its weight is 1.88 N. The diameter has been calculated in order to guarantee a dragging force equal to or larger than the maximum buoyancy force acting on the entire structure, which is equal to 0.50 N. The drag force has been estimated assuming that the plate moving in accordance with the surface and considering, the depth of the stabilizing ring, a vertical velocity is calculated according to the linear distribution of the particles velocity. Such a method was used at the beginning of the design procedure in order to estimate the size that the ring should be. A wave height of 18.00 mm has been hypothesized and a period of 0.75 sec (in real scale H=0.30 m – T=3.00 sec) capable of generating a vertical velocity of 79.00 mm/sec and 8.00 mm/sec respectively, for the surface and the ring depth.
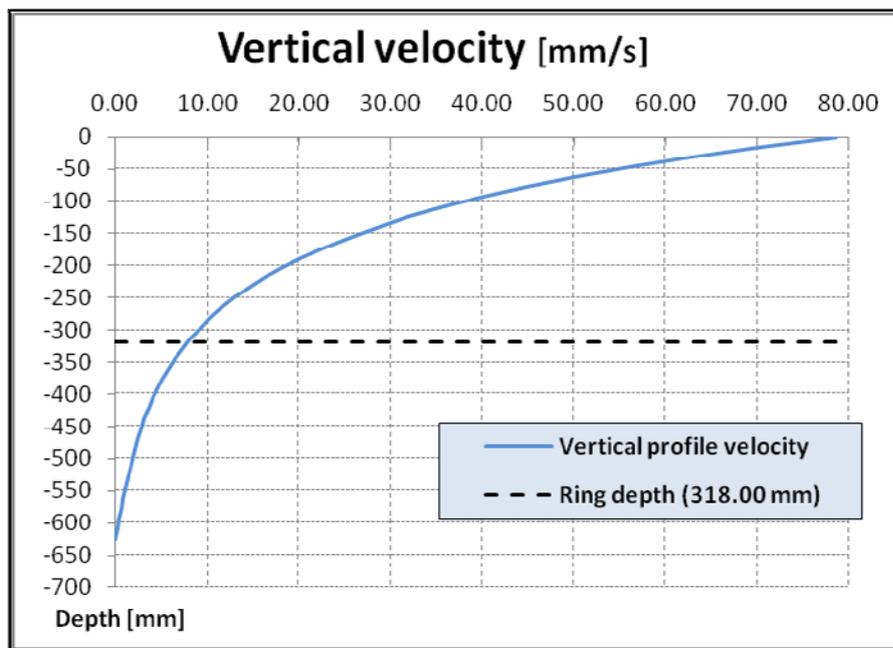
Figure 37: Vertical velocity profile for H=18.00 mm – T=0.75 sec. and h=400.00 mm.

$$F_{drag} = \frac{1}{2} \cdot \rho \cdot C_d \cdot v^2 \cdot A = 0.74 \, N \qquad\qquad (7)$$

Where ρ is the fresh water density, equal to 997.561 kg/m^3, C_d is the drag coefficient, equal to 1.28 as is suggested in [106], [107] for a flat plate perpendicular to the flow direction, v is the relative vertical velocity between the surface and water at the ring depth and A is the frontal area of the ring.
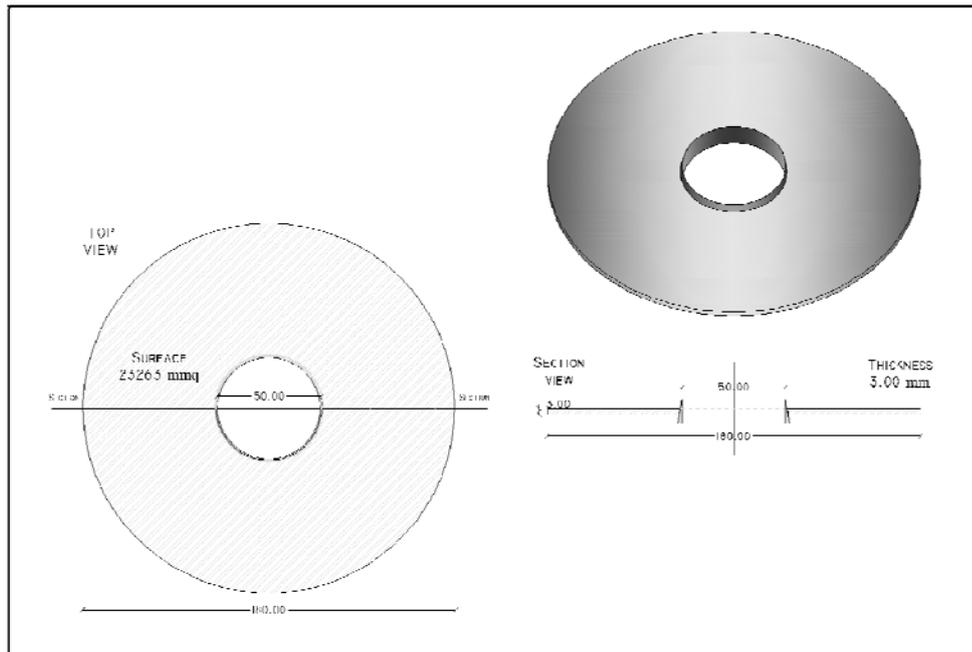
Figure 38: Details of stabilizing ring, all lengths in mm.

The three components of the OXYFLUX model were then assembled. Its total length is equal to 335.00 mm (from the top of the floater to the stabilizing ring), the position of the center of gravity is largely affected by the difference in density of the components, and it is located 267.00 mm below mean water level when the device is at rest i.e. 69.00 mm above the lowest surface of the stabilizing ring, Figure 40. Such a position for the center of gravity, below the center of buoyancy, was chosen in order to improve the stability of the device under the action of waves. The total weight of the model is 3.17 N while the maximum buoyancy force is 3.39 N ensuring a buoyancy reserve force of 0.22 N, 7 % of the total buoyancy force. 3.17 N corresponds to a free-board crest equal to 7.00 mm (*real scale 0.11 m*), Figure 39. Such a buoyancy reserve was chosen in order to guarantee, (*in*

the real sea environment) floatation of the device also after inevitable weight gain due to biofouling growth, that has to be taken into account for structures immersed in sea water.
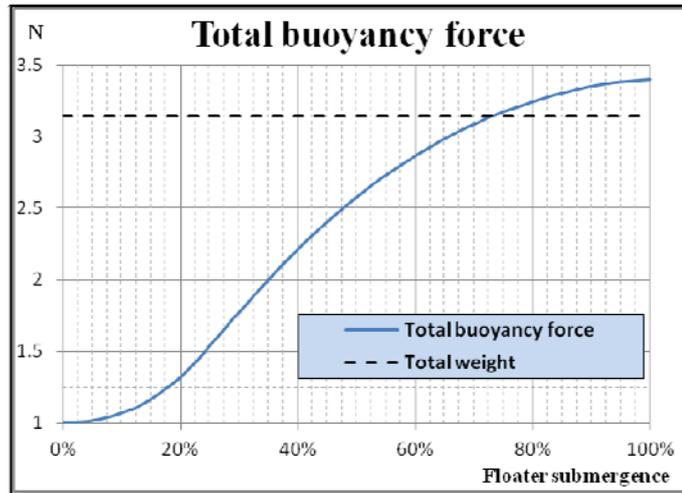
Figure 39: Total buoyancy force vs floater submergence.
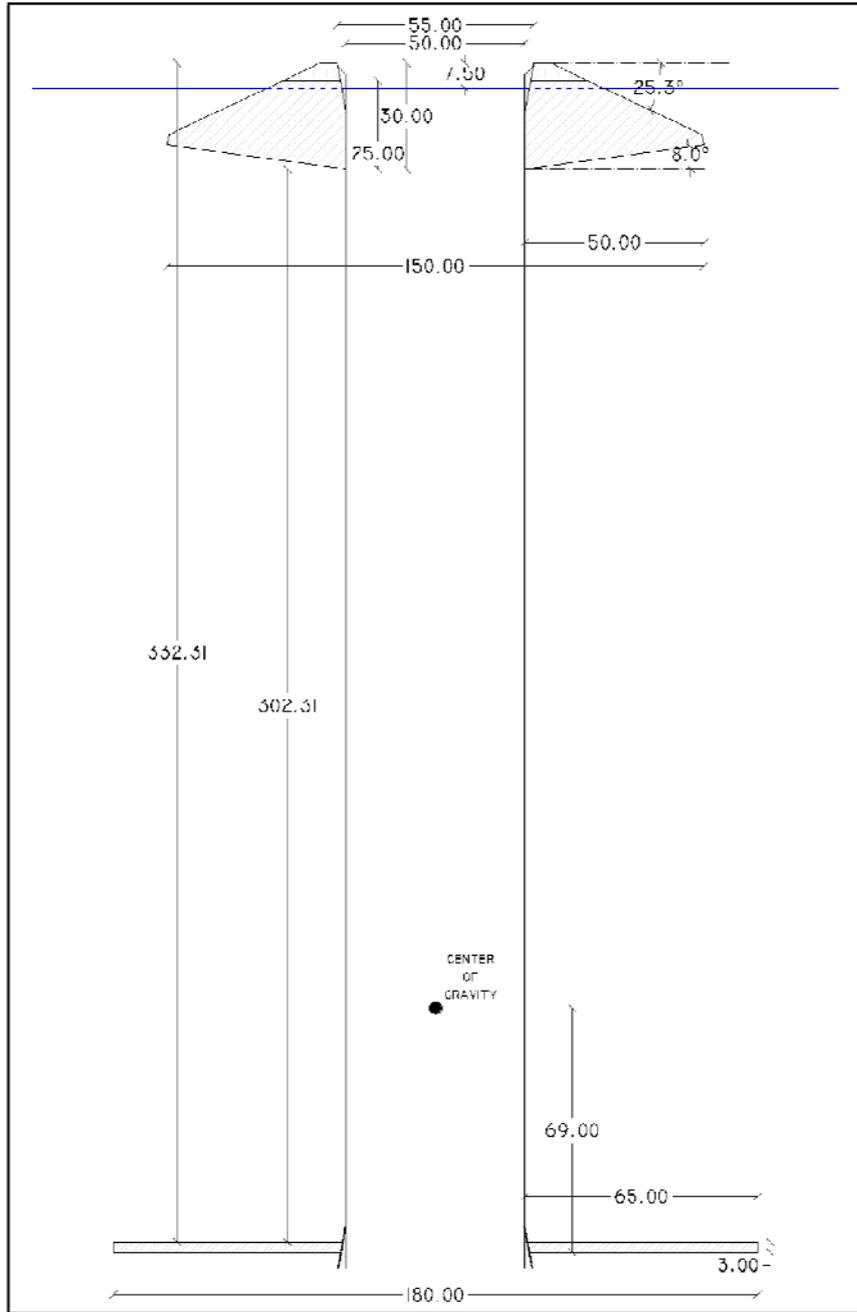
Figure 40: Final design of the tested physical model.
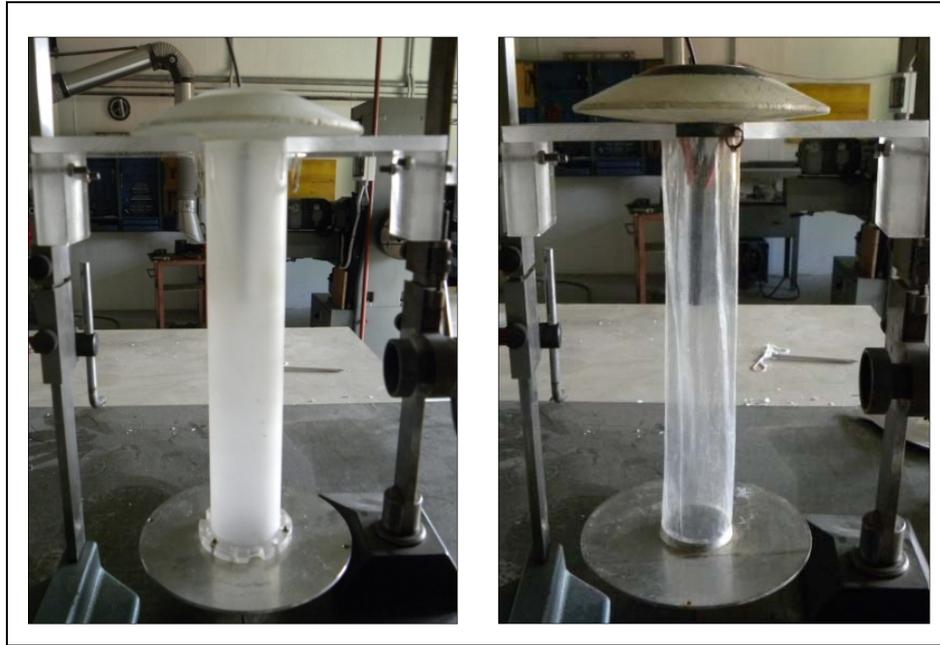
Figure 41: OXYFLUX physical models.

All details of the physical model can be seen in Appendix A

CHAPTER IV: Physical investigation

The conditions for the physical tests performed on the OXYFLUX model are described In this chapter. The model test setup and the results, as well as the measuring methods, are then presented. The tests examine two different aspects: the displacement of the floating device and the velocity of the generated water flux. Some characteristics of the device are also investigated: crest freeboard, the structure (flexible or rigid) and the mooring system. By means of free oscillation tests, the hydrodynamic parameters of the devices are also estimated. In this chapter the reliability of the OXYFLUX is investigated for the first time. The performance of the device is described for 49 sea states ranging between 1,25 to 5,50 % of the design wave steepness

Parameters investigated

Device's structures

Two different types of structures have been investigated difference of which consists in the material the tube is made of. A series of preliminary tests have been carried out with a flexible (F) and a rigid (R) tube in order to identify the influence of the structural characteristics on the operating mechanism. The rigid tube was made with Plexiglas while the flexible one was made with a nylon layer. The flexible structure aimed to minimize the transmitted force between the tube and the float. The rigid tube was created by means of a lathe from a plastic parallelepiped Figure 42, and the flexible one from a common plastic bag. The flexible one required thermal welding between the two extremes of the layer. In order to obtain the required diameter, a mechanism to weld the plastic has been developed, Figure 43. The float has the same shape and dimensions regardless of the material of the tube, Figure 41. The flexible version of the device will be rejected after the physical investigation because it is unsuitable to allow the measurement of the velocity of the water flux in the tube.

Figure 42: Realization of the rigid tube at the Hydraulic Laboratory of University of Bologna..
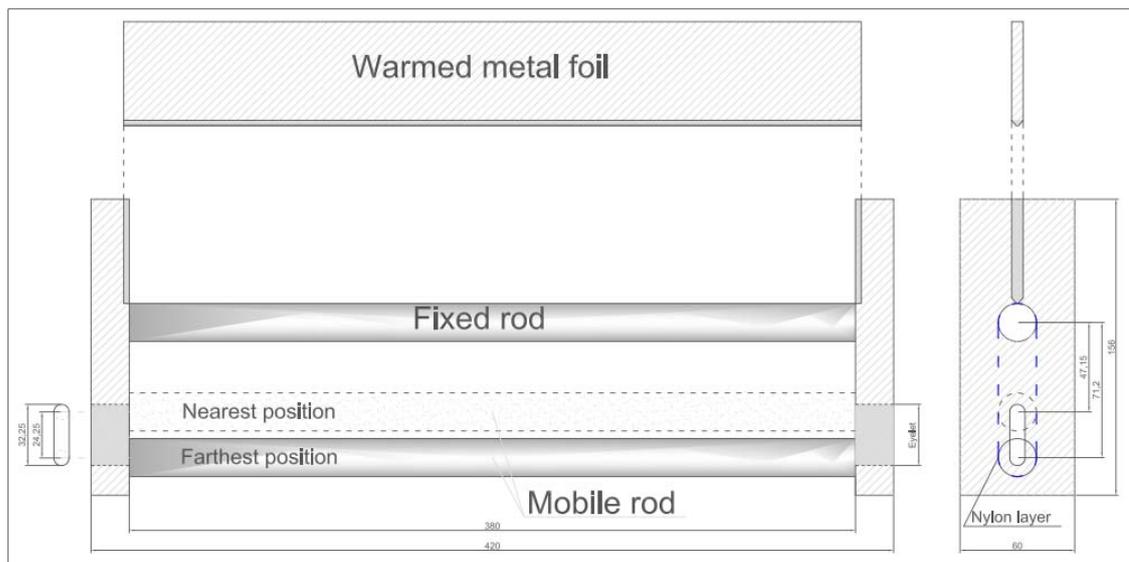
Figure 43: The mechanism used to weld nylon layer.

Modification of the mooring system

Two mooring systems are investigated. The first one is made of four chains (CH) attached to the bottom of the floater and fixed with four anchors; the chains are 1.25 m long (almost three times the water depth 0.40 m) and are characterized by a linear density equal to 27.5 g/m in Froude similitude 1:16. The second system is made with two pre-tensioned nylon cables (CA) attached to the bottom part of the floater and 1.15 m long, Figure 44.
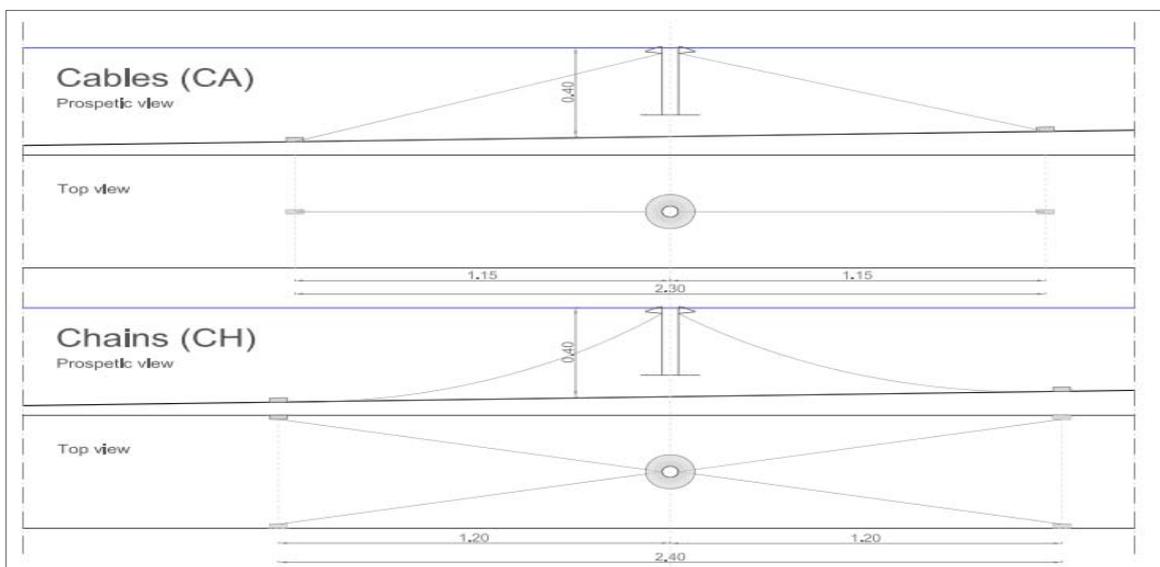
Figure 44: Schematic view of the mooring disposition.

The positions of the small lead anchors were checked after each test, and it was confirmed that they had not been moved by the device during the tests. The main function of the mooring lines is to counteract the slow drift force and to maintain the floater in its dynamic equilibrium position.

Modification of the crest freeboard

Hypoxic areas commonly develop during summer, when agitation level is scarce and waves and currents are not strong enough to break vertical stratification. Starting from

these considerations, the device has been designed with a low crest freeboard in order to catch water from waves with a height of 0.20 m or even lower. Two values of crest freeboard (R_c) are investigated in the physical model scaled 1:16, 5.00 mm (F_1) and 7.00 (F_2) mm, Figure 45.
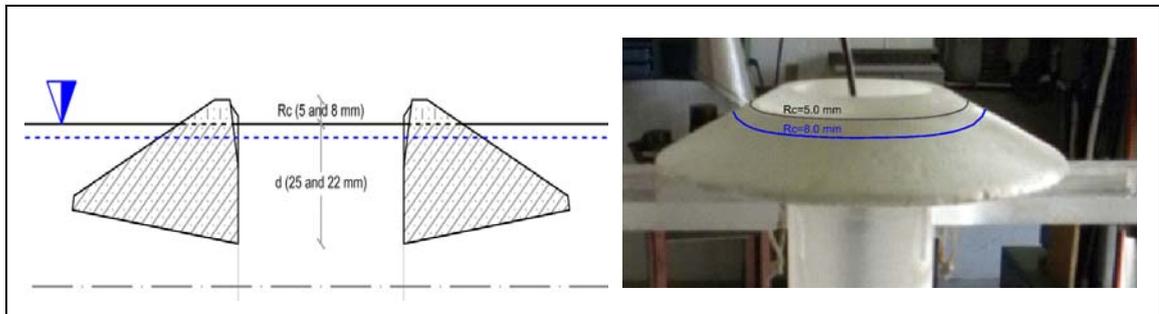
Figure 45: Schematic representation of the two values of crest freeboard (left) and particular of the physical model (right).

During the tests, both values have been imposed by changing the relative distance between the anchor and the device. Little displacements of one anchor (5 mm) allowed to vary crest freeboard and to obtain the required values.

Laboratory set-up

The tests were carried out in the wave flume at the Hydraulic Laboratory of the University of Bologna (LIDR). The wave flume has a length of 15.0 m, a width of 0.50 and maximum depth of 0.70 m.
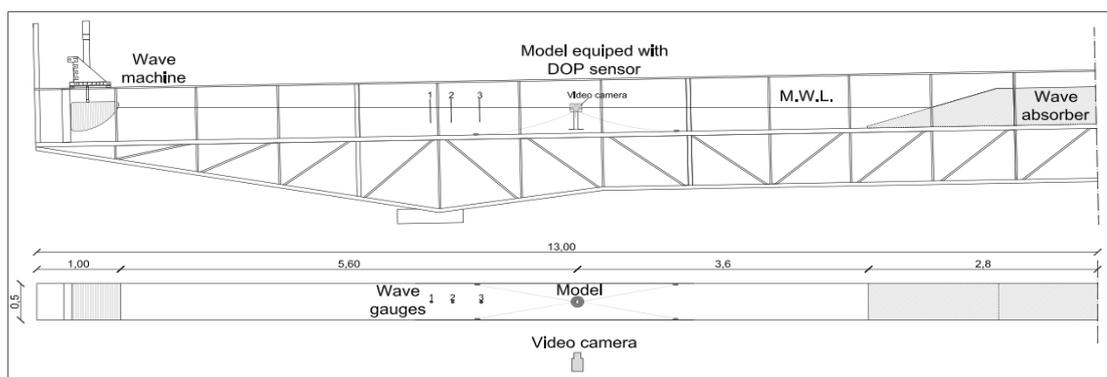
Figure 46: Test set-up, values in meters. Longitudinal (top) and horizontal (bottom) sections.

65

Figure 46 shows the test set-up. A vertical piston-type wave paddle generates waves at one end of the wave flume, while a passive wave absorber is installed at the other end. The scaled model is positioned in the middle section of the flume. The water depth varies between 0.52 m and 0.33 m and at the location of the model it has been kept equal to 0.40 m. The slope is fixed at 2 %, in order to have a better control of the waves to which the tested model is exposed, reducing reflection from the passive absorber.

Three resistance type wave-gauges with a sampling frequency of 1000 Hz are installed on the axis of the flume in front of the model to measure the incident and reflected waves. The mutual distances between the gauges and the device are the following:

- Gauge 1 and gauge 2, 0,20 m;
- Gauge 2 and gauge 3, 0,55 m;
- Gauge 3 and the device, 1,65 m.

This particular disposition of the gauges allows the method developed by Zelt and Skjelbreia in 1992[103] to be used for the separation of incident and reflected waves, Figure 47. The incident wave time series calculated using the Zelt method is then applied to further wave analysis. Time domain analysis of the incident wave in front of the device are conducted for every test. The results of such process are used to identify medium wave heights (H_m) and period (T_m) by means of zero up crossing.
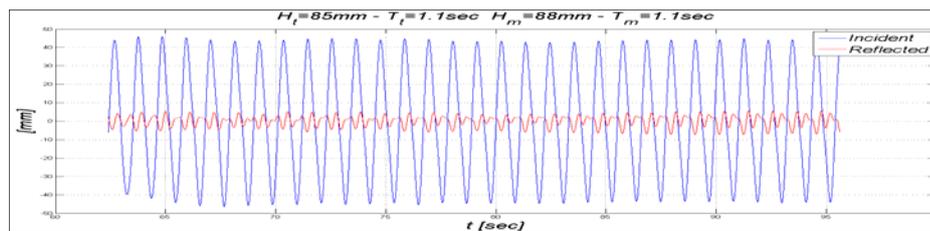
Figure 47: Example of reflection analysis.

Table 6: Results of reflection analysis for 49 tested wave state, (subscripts *t, m_i, m_r* indicate *target, medium incident, medium reflected*)

WAVE CODE	Target values (scale 1:16)					Reflection analysis results						
	H_t [mm]	T_t [sec]	L_t [mm]	C_t [mm/s]	S_t	H_{m_i}	T_{m_i}	H_{m_r}	T_{m_r}	H_t/H_{m_i}	H_{m_r}/H_{m_i}	s
1	15.00	0.80	987.06	1233.83	1.5%	10.88	0.8	0.739	0.676	1.38	0.07	1.1%
2	15.00	0.85	1104.53	1299.45	1.4%	11.95	0.85	0.97	0.738	1.26	0.08	1.1%
3	20.00	0.85	1104.53	1299.45	1.8%	16.11	0.85	1.094	0.761	1.24	0.07	1.5%
4	25.00	0.90	1223.80	1359.78	2.0%	21.67	0.9	0.682	0.665	1.15	0.03	1.8%
5	30.00	0.90	1223.80	1359.78	2.5%	26.07	0.9	0.756	0.651	1.15	0.03	2.1%
6	35.00	0.90	1223.80	1359.78	2.9%	30.59	0.9	1.024	0.872	1.14	0.03	2.5%
7	40.00	0.90	1223.80	1359.78	3.3%	35.19	0.9	1.287	0.769	1.14	0.04	2.9%
8	45.00	0.90	1223.80	1359.78	3.7%	39.84	0.9	1.552	0.769	1.13	0.04	3.3%
9	50.00	0.90	1223.80	1359.78	4.1%	44.37	0.9	1.625	0.768	1.13	0.04	3.6%
10	30.00	0.95	1343.80	1414.53	2.2%	27.29	0.95	1.969	0.791	1.10	0.07	2.0%
11	35.00	1.00	1463.78	1463.78	2.4%	33.69	1	1.797	0.579	1.04	0.05	2.3%
12	40.00	1.00	1463.78	1463.78	2.7%	38.58	1	1.618	0.568	1.04	0.04	2.6%
13	45.00	1.00	1463.78	1463.78	3.1%	43.41	1	2.604	0.568	1.04	0.06	3.0%
14	50.00	1.00	1463.78	1463.78	3.4%	48.2	1	2.632	0.548	1.04	0.05	3.3%
15	55.00	1.00	1463.78	1463.78	3.8%	52.93	1	2.366	0.559	1.04	0.04	3.6%
16	60.00	1.00	1463.78	1463.78	4.1%	57.82	1	2.889	0.51	1.04	0.05	3.9%
17	40.00	1.05	1583.25	1507.86	2.5%	39.79	1.05	1.743	0.554	1.01	0.04	2.5%
18	45.00	1.10	1701.91	1547.19	2.6%	44.33	1.1	1.994	0.844	1.02	0.04	2.6%
19	50.00	1.10	1701.91	1547.19	2.9%	49.44	1.1	2.587	0.801	1.01	0.05	2.9%
20	60.00	1.10	1701.91	1547.19	3.5%	59.41	1.1	3.23	0.551	1.01	0.05	3.5%
21	65.00	1.10	1701.91	1547.19	3.8%	64.55	1.1	3.735	0.551	1.01	0.06	3.8%
22	70.00	1.10	1701.91	1547.19	4.1%	69.92	1.1	3.73	0.552	1.00	0.05	4.1%
23	75.00	1.10	1701.91	1547.19	4.4%	75.63	1.1	4.451	0.551	0.99	0.06	4.4%
24	80.00	1.10	1701.91	1547.19	4.7%	81.1	1.1	3.49	0.552	0.99	0.04	4.8%
25	85.00	1.10	1701.91	1547.19	5.0%	85.09	1.1	4.243	0.552	1.00	0.05	5.0%
26	90.00	1.10	1701.91	1547.19	5.3%	89.4	1.1	3.922	0.55	1.01	0.04	5.3%
27	50.00	1.15	1819.60	1582.26	2.7%	50.96	1.15	1.853	0.944	0.98	0.04	2.8%
28	55.00	1.20	1936.25	1613.54	2.8%	56.01	1.2	2.049	0.612	0.98	0.04	2.9%
29	60.00	1.20	1936.25	1613.54	3.1%	61.5	1.2	2.581	0.602	0.98	0.04	3.2%
30	60.00	1.25	2051.87	1641.49	2.9%	63.54	1.25	2.546	1.08	0.94	0.04	3.1%
31	65.00	1.30	2166.47	1666.51	3.0%	69.91	1.3	2.65	0.661	0.93	0.04	3.2%
32	70.00	1.30	2166.47	1666.51	3.2%	75.2	1.3	3.176	0.653	0.93	0.04	3.5%
33	75.00	1.30	2166.47	1666.51	3.5%	80.65	1.3	2.884	0.836	0.93	0.04	3.7%
34	80.00	1.30	2166.47	1666.51	3.7%	86.21	1.3	4.219	0.651	0.93	0.05	4.0%
35	15.00	0.70	762.90	1089.86	2.0%	8.104	0.7	0.852	0.696	1.85	0.11	1.1%
36	20.00	0.70	762.90	1089.86	2.6%	10.75	0.7	1.233	0.673	1.86	0.11	1.4%
37	25.00	0.70	762.90	1089.86	3.3%	13.53	0.7	1.662	0.697	1.85	0.12	1.8%
38	30.00	0.70	762.90	1089.86	3.9%	16.39	0.7	2.07	0.697	1.83	0.13	2.1%
39	35.00	0.70	762.90	1089.86	4.6%	19.24	0.7	2.371	0.698	1.82	0.12	2.5%
40	40.00	0.70	762.90	1089.86	5.2%	21.99	0.7	2.615	0.697	1.82	0.12	2.9%
41	15.00	0.75	872.70	1163.60	1.7%	10.25	0.75	0.522	0.684	1.46	0.05	1.2%
42	20.00	0.75	872.70	1163.60	2.3%	13.45	0.75	0.908	0.531	1.49	0.07	1.5%
43	25.00	0.75	872.70	1163.60	2.9%	16.98	0.75	1.041	0.506	1.47	0.06	1.9%
44	30.00	0.75	872.70	1163.60	3.4%	20.32	0.75	0.965	0.661	1.48	0.05	2.3%
45	35.00	0.75	872.70	1163.60	4.0%	23.85	0.75	1.131	0.753	1.47	0.05	2.7%
C	10.00	0.72	806.18	1119.69	1.2%	6.66	0.72	0.48	0.56	1.50	0.07	0.8%
T	30.00	0.68	720.55	1059.63	4.2%	18.28	0.68	0.75	0.48	1.64	0.04	2.5%
E	100.00	1.15	1819.60	1582.26	5.5%	99.06	1.15	6.588	0.597	1.01	0.07	5.4%
O	50.00	1.06	1607.06	1516.09	3.1%	52.00	1.06	3.07	0.53	0.96	0.06	3.2%
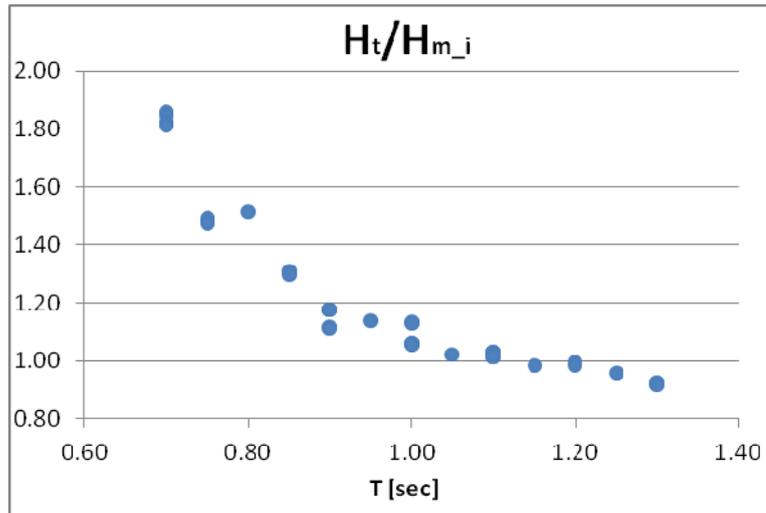
Figure 48: Ratio between the target wave height (H_t) and the incident wave height (H_{m_i})
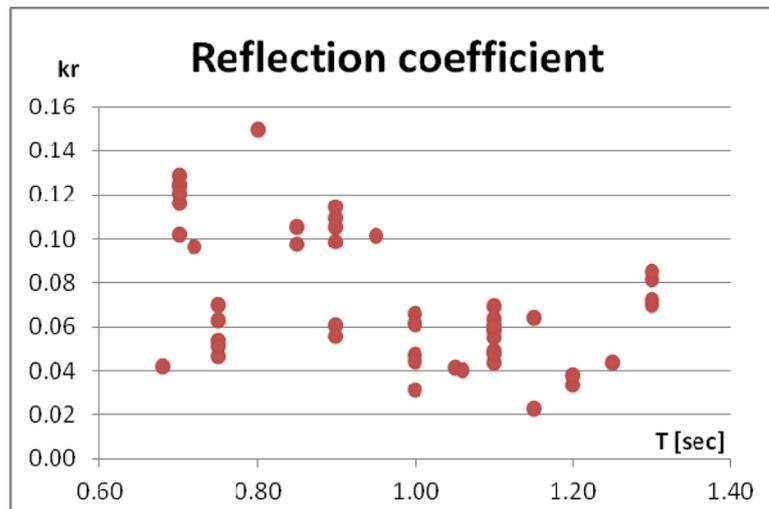
Figure 49: Reflection coefficients (H_r/H_{m_i})

As it can be seen in Figure 48, slight deviations occurred during the tests. The biggest deviations correspond to the smallest period, due to the fact that small waves with periods below 0.8 – 0.85 sec. are inaccurately generated by the facilities of the laboratory. Reflection analysis results show highest values of the reflection coefficients (k_r), in correspondence to the smallest periods, Figure 49. Although slight deviations between recorded (H_{m_i}) and target (H_t) values occur, target wave conditions are obtained satisfactorily.

Measurement of the displacement

It is important to identify the dynamic behavior of the floating body in order to know the displacements of the device. This kind of information assumes high importance in the design of a OXYFLUXs farm for real sea application. From this point of view it is important to identify the maximum displacements of a single device in order to know the mutual distance between it and other devices and structures positioned nearby so that it does not hit any of them. This kind of investigation, in the present thesis, has been conducted by means of image processing analysis. The advantages of this technique are related to the low costs of the procedure; in fact the only hardware needed is a commercial digital video camera and a standard computer in which Matlab 2012a or a successive version has to be installed. The techniques to perform precise and reliable measurements of the environment by the use of images are called videometrics [104]; among other advantages, they are normally nonintrusive, so that their effect on the environment tends to be minimum or nil.

Image processing procedure

Computer vision systems are artificial systems that can obtain information from images, [105]. The image data may take on many formats, such as a photograph, a video sequence, views from multiple cameras, etc. The present system uses images from a digital video camera and a set of processing algorithms; the camera records a video sequence of the flume section of interest at a rate of 30 frames per second, then in non real-time condition, the algorithms process the images to determine the position of the device. The investigation has been conducted with two different methods, both based on non real-time approaches. In the first method, used only for the preliminary tests, the user has to manually identify the two extreme points of the investigated floating body and water surface, while in the second one, by means of a set of algorithms, identification of the dynamic of the floating body is made by tracking, frame by frame, the position of a marker for each time step. When using video images for measurement purposes, there are

a number of issues to take into account: first, lens distortion and 3D–2D projection and second, in case of certain video cameras and of moving objects, interlacing. Lens distortion is an optical error that causes an object to be magnified differently depending on its position in the image; a collateral effect is that straight lines in the real world may appear curved on the image plane, [106]. The 3D–2D projection refers to the computation of distances in a 3D ("real") scene from its projection into a 2D image. The procedure used to overcome these issues is based on the Tsai camera calibration method [106], in the sense that it provides correspondences between points in the image and points in space. To avoid lens aberration problems, rectification methods usually resort to an image of a template with equidistant marks; pixels are moved from their location on the original image to that in the final image based on the proximity of the four nearest points in the template [107]. In this work, the process is simplified by identifying a conversion factor (pixel/mm). The system takes as inputs one image of the template and through its physical dimensions it finds the scale. Another issue to address when using video frames for measuring purposes is interlacing, which affects video images of fast-moving objects taken with non-progressive scanning video cameras. Interlacing was corrected by averaging the two fields that make up a single frame, [108].

Both methods; the semi manual and the automatic one are based on the hypothesis that the movements of the floating bodies are 2D, i.e. the device must move only in the vertical plane passing for the midpoint of the flume.

Semi manual approach

The first method is described here. Such a method was used at the beginning of the research, when the tests were carried out with the Northern Adriatic's wave climate. The approach requires a long time for the analysis of displacements, since it requires, for each time step, manual identification of the variable to describe. The method consists in decomposing the registration in single frames that are analyzed on by one. For each frame, several points on the figure have to be identified. After detecting the extremes of

the floater (blue dots Figure 52 - Figure 51 - Figure 50), by means of optical identification, a dashed line joining their centers is drawn by the system. Its midpoint (green dot Figure 52 - Figure 51 - Figure 50), gives the position of the float in the image.
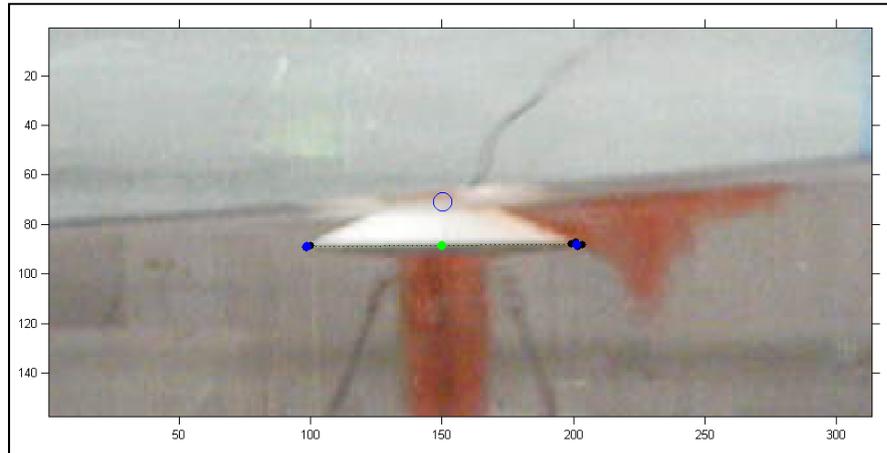
Figure 50: Identification of mean value for the extremes of the floater (mean value blue dot single optical detection black dots) and for water surface position (blue circle).

In order to avoid errors due to the imprecision of the optical method, the coordinates of the final point are calculated considering the mean value of 4 observed points for each interested extreme, Figure 51.
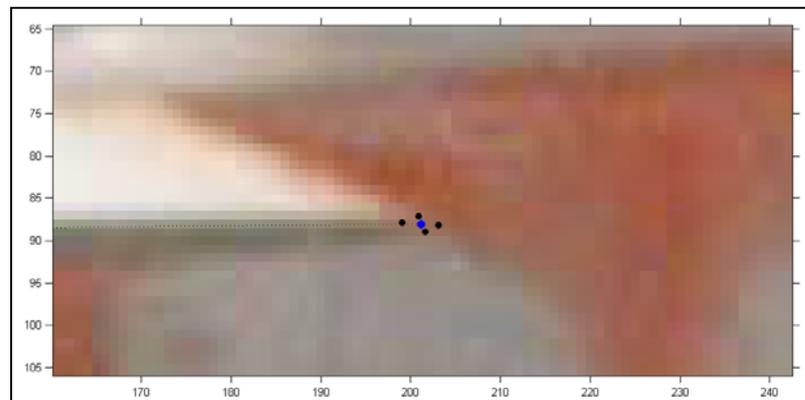
Figure 51: Identification of mean values for the extremes of the floater (mean value blue dot, single optical detection black dots) and for water surface position (blue circle).
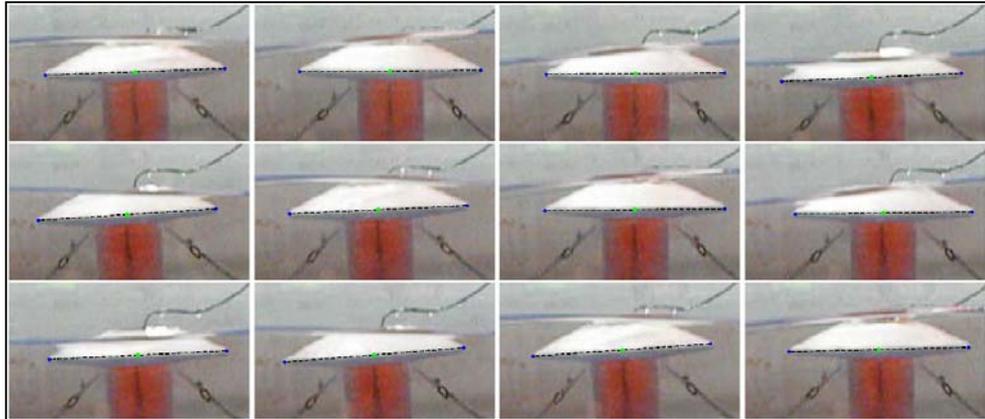
Figure 52: Sequence of analyzed frames, [84].

The results coming from this procedure are a series of points in the space and time domain. Once the displacement of the device has been estimated, its mean elliptical trajectory can be fitted onto the experimental data.
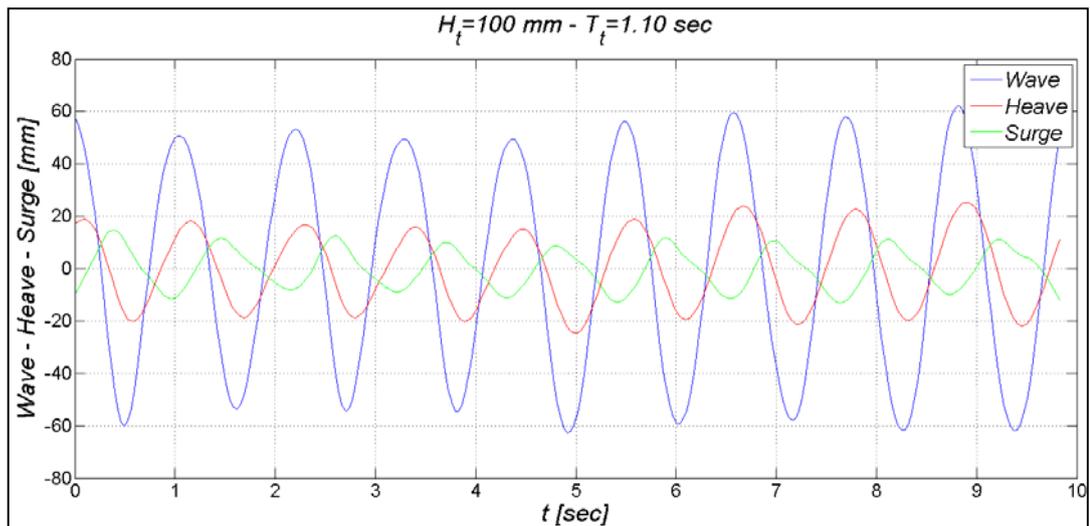
Figure 53: Time series measured example
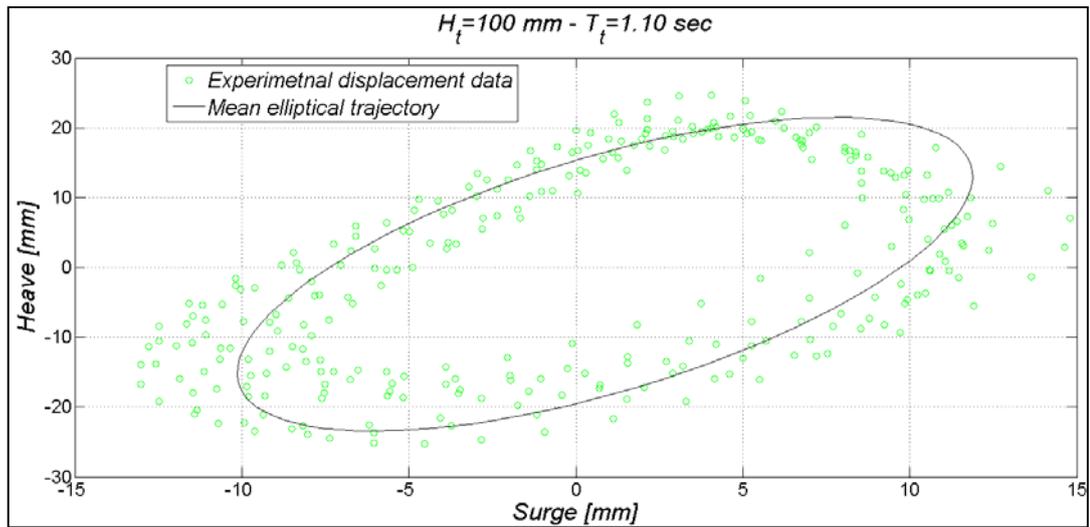
Figure 54: Time series measured example

Motion analysis is used to estimate the submergence of the floater during the wave cycle and its influence on the pumping mechanism: at each wave cycle, the position of free surface elevation (blue line) and the floater vertical displacements (red line) are compared (Figure 55, Figure 56). The medium value of submergence for each wave state is then evaluated over the sampled wave periods.
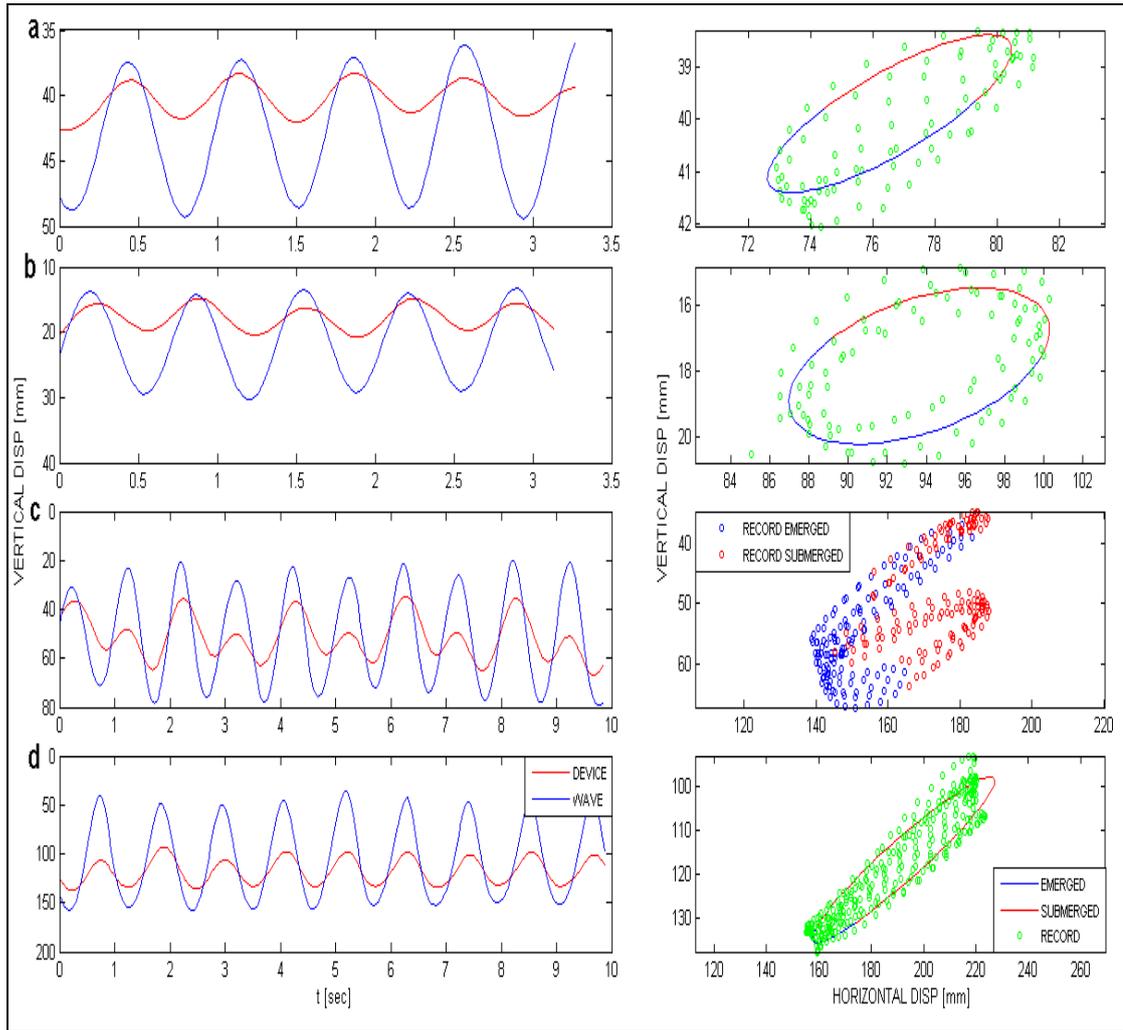
Figure 55: Rigid device moored with chains: wave state C (a), wave state T (b), wave state O (c), wave state E (d) , (measurements are in mm).
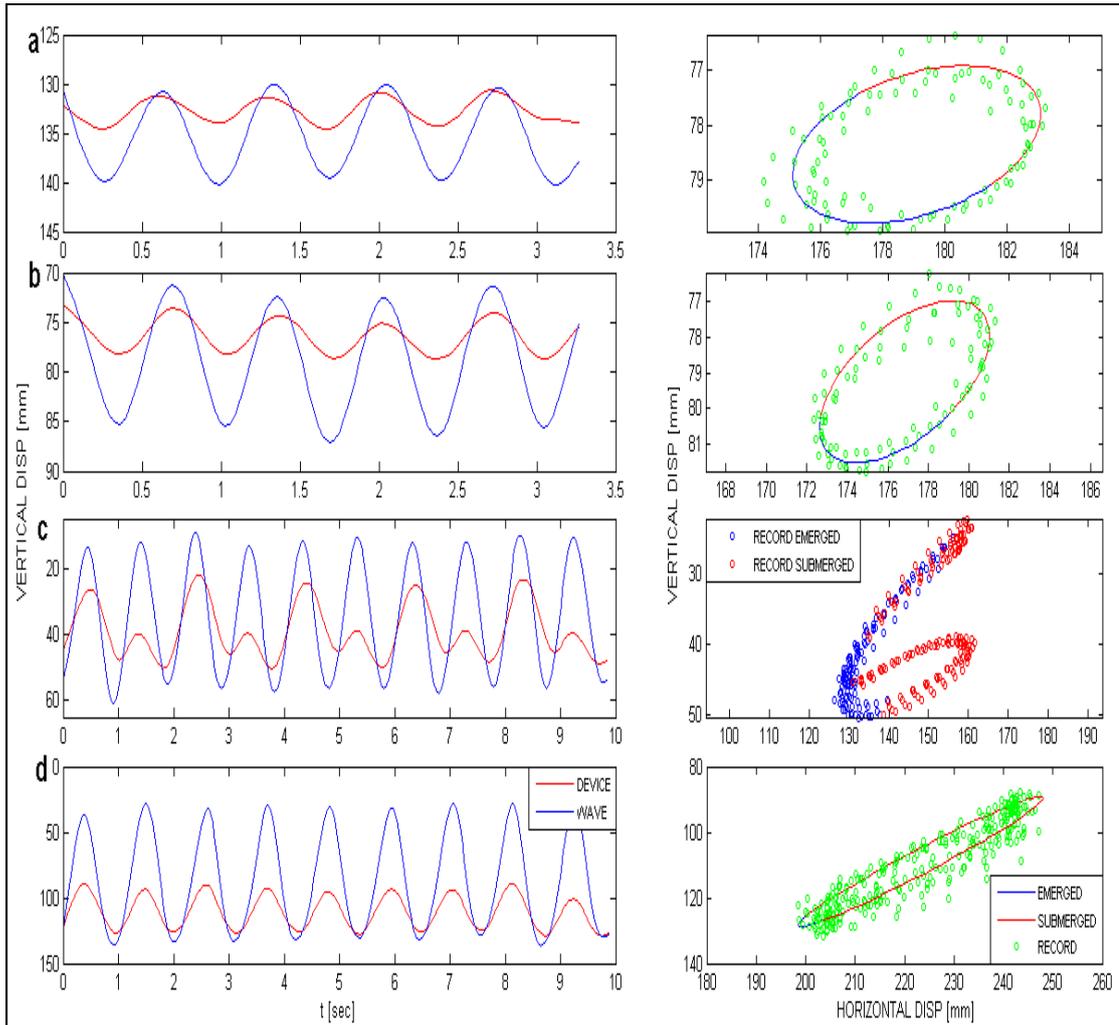
Figure 56: Flexible device moored with chains: wave state C (a), wave state T (b), wave state O (c),wave state E (d), (measurements are in mm).

For both the rigid and the flexible device, the tests performed with waves C, T, and E show the same frequency response for the incoming wave and the device displacement. For both the devices the exception can be observed with wave O. In the spectral analysis reported in Figure 57, two main frequency peaks are identified: the first corresponding to the wave period (i.e., 1 s) and the second (i.e., 2 s) correlated with the solicitation of the natural frequency of the device. The nonlinear response of the devices explains why the spatial trajectory of the device motion does not fit the elliptical shape.
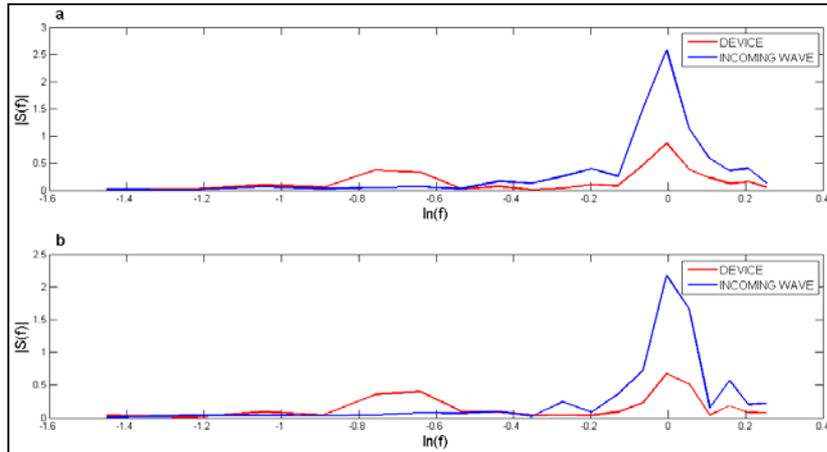
Figure 57: Energy spectrum for heave motion, wave state O. Rigid (a), Flexible (b).

All results showed in this paragraph were quantified just for the preliminary tests.

Automatic approach

This system uses images from a digital video camera and a set of processing algorithms to measure the displacement of a marker drawn on the device surface. For each frame the procedure has the following steps:

− Frames cropping;
− Averaging the two fields that make up a new single frame.
− Conversion of cropped frames from RGB to grayscale image;
− Intensity adjustment of cropped frame;
− Complement of the cropped frames;
− Morphological opening and closing of the cropped frame;
− Conversion of the cropped frame to binary image by thresholding;
− Identification of the medium conversion factor (mm/pixel);
− Centroid identification for the white area in binary image;
− Storage centroid coordinates (pixel) in a new variable;
− Conversion of the coordinates from pixel to length, (i.e. mm).

This procedure is not a real time system since the video camera used may not be connected to the PC, so its functioning can be extended to real time with an appropriate hardware. All the records are read by a Matlab procedure once the files are downloaded on the internal PC memory. The strength of this method consists in its cheapness and easiness of installation procedures. The whole procedure has been developed by means of a Matlab Image Processing Toolbox.

Cropping the frames requires the recognition of the area of interest inside the whole frame. Such an operation was carried out by mean of a description of the area given by the user dragging the cursor over the image, Figure 58. This step has to be repeated for each tests series that has to be analyzed, since the position of the video camera and the distance between the camera and the model is supposed to remain the same during the entire tests session.
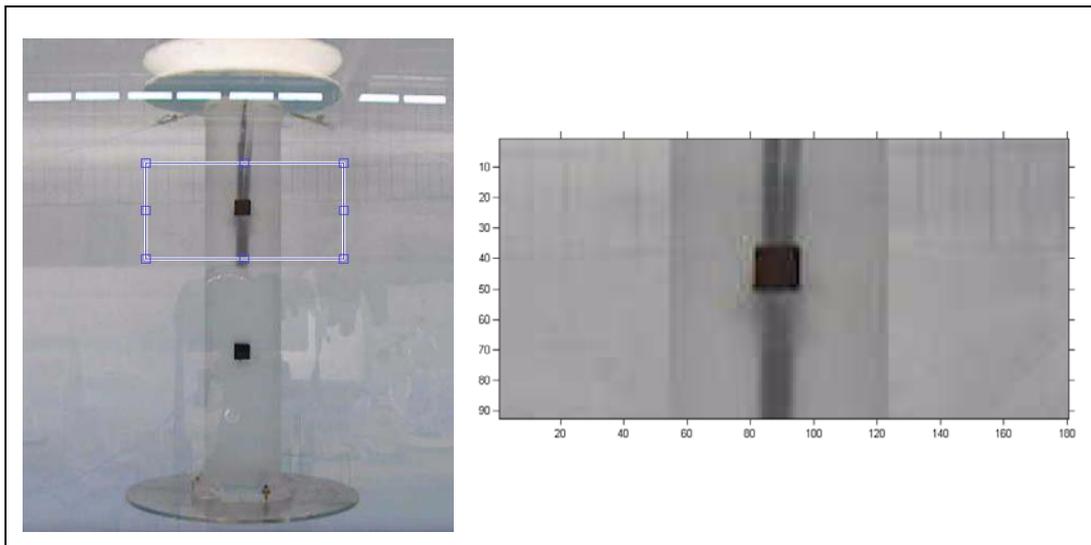
Figure 58: Manual identification of the region of interest (left), zoom on the selected area (right).

Once the region of interest has been selected, the image processing cycle starts the procedures to improve the quality of the image and to finally convert the picture into binary code in order to extract the center of the mass of the white stain in the picture, Figure 63. Image enhancement techniques are used to improve an image, where term "improve" can sometimes be used in an objective manner (e.g., increase the signal-to-

noise ratio), and sometimes in a subjective manner (e.g., make certain features easier to be seen by modifying colors or intensities). The aim, in this instance, is to increase the contrast between the black marker and rest of the image as much as possible; the first step is the conversion of the region of interest from an RGB image to a gray scale image. Such a conversion is required to allow the next step, which consists in the adjustment of the intensity of the image. Intensity adjustment is an image enhancement technique that maps the intensity values of an image to a new range. To illustrate this feature, Figure 59 shows a low-contrast cropped frame with its histogram; the histogram shows how all the intensity values are gathered in the center of the range. In Figure 59, which shows the same cropped frame after intensity adjustment, all the intensity values shift towards higher values leaving a peak in correspondence to frequency equal to zero representing the black stain of the marker, thus maximizing the contrast between the marker and the rest of the image.
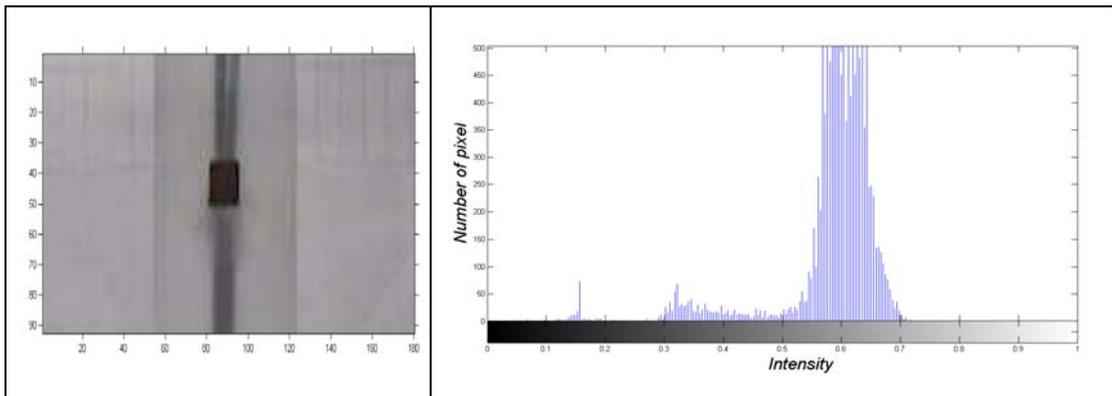
Figure 59: Zoom on selected area of interest before intensity adjustment (left) and its intensity histogram (right).
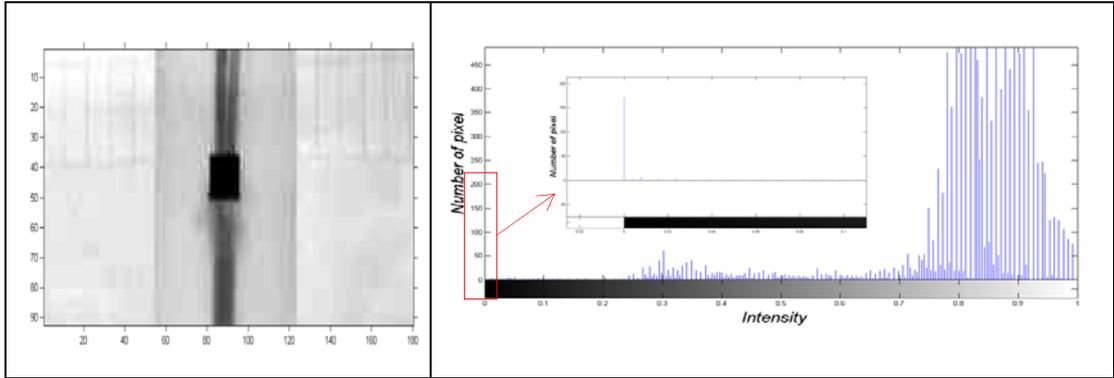
Figure 60: Zoom on selected area of interest after intensity adjustment (left) and its intensity histogram (right).

The fourth step of the procedure consists in calculating the complement of the elaborated image. In the complement of an intensity image, each pixel value is subtracted from the maximum pixel value supported by the class (i.e. 1.00) and the difference is used as the pixel value in the output image. In the output image, dark areas become lighter and light areas become darker, Figure 61. Such a procedure is required in order to select a proper area during the conversion of the image in binary.
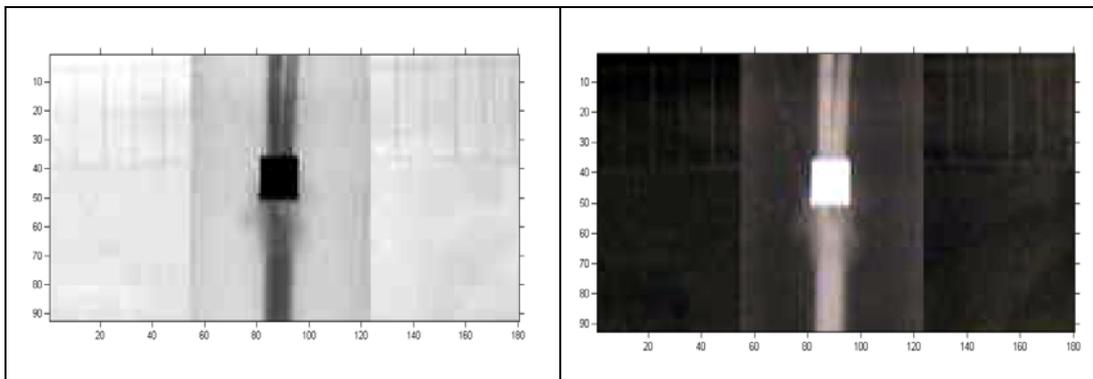
Figure 61: Original image (left), complement (right).

As can be seen in Figure 61, some inaccuracies on the definition of the edges of the marker still remain, like the presence of the DOP in the background. To remove inaccuracies on the edges and objects that do not represent the investigated shape, a morphological opening and closing of the complement image is done. Morphological opening of image A (i.e. image that as to be analyzed) by structuring element B is defined as $A \circ B = (A \ominus B) \oplus B$ while, similarly morphological closing is defined as $A \cdot B =$

$(A \oplus B) \ominus B$, [108]. The opening procedure aims to completely remove those regions of an object that cannot contain the structuring element, to smooth the object contours and to break the thin connection and thin protrusion but it can also be used, for gray scales images, to compensate for non-uniform background illumination. The closing procedure tends to smooth the contours of objects, to join narrow breaks and to fill long thin gulfs and holes that are smaller than the structuring element. In this algorithm, the opening and closing procedures are used in combination with smooth images and to remove noises. Since the key to performing an effective morphological operation is picking a good structuring element, the definition of this element is derived from several tests. The results illustrated in Figure 62 lead to the choice of a squared structuring element with a dimension of 12 x 12 pixels. The dimensions of the marker edges are, on average, 15 pixels, and they are vertical and horizontal, so the squared structuring elements seems to be the most appropriate choice.
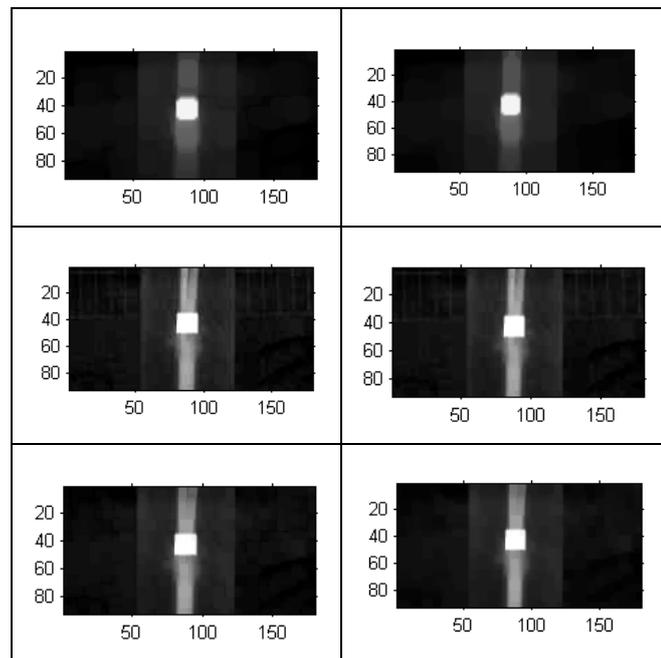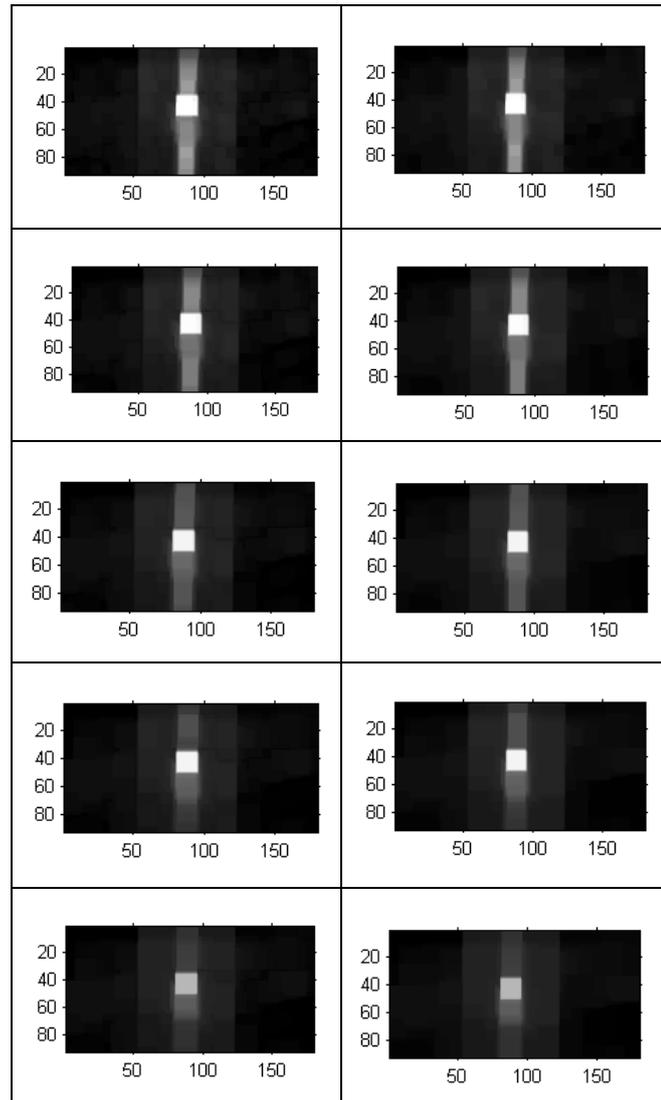
Figure 62: Comparison of the effects of morphological opening (left) and closing (right), with different structuring element, (*disk length 7 (1), square length 2 (2), square length 5 (3), square length 8 (4), square length 10 (5), square length 12 (6), square length 13 (7), square length 14 (8)*)

The main process in the algorithms is the conversion of the image from gray scale to binary. Such an operation replaces all the pixels in the input image with a luminance greater than a selected level with value 1 (white) and replaces all the other pixels with value 0 (black). The issue is the recognition of the right threshold. Common values have been tested for all the series of tests, obtaining no good results. Finally, a different

threshold for each tests series has been chosen in order to take into account the variation of illumination during the day.
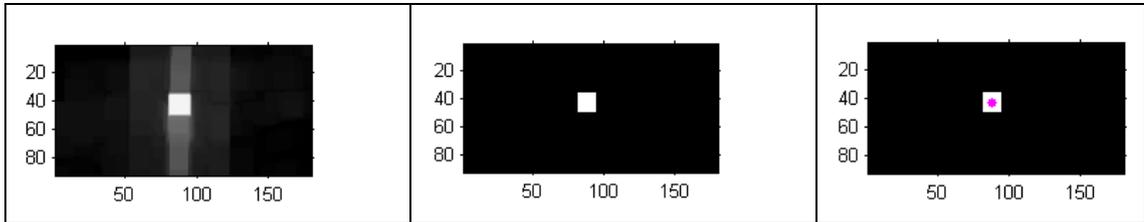
Figure 63: Sequence of the last two steps of the algorithm: conversion of the image in binary and identification of the center of mass of the marker.

Once the frame has been converted, through Matlab's function "region props" it is easy to identify the center of the mass and the edge lengths of the white stain. The marker was sketched on the external surface of the tube with squared shape with sides equal to 11 mm. For each frame the system identifies the length of the marker's edges, compares their values with those identified in the region of interest and calculates the medium conversion factor to convert the image from pixel to mm.

This procedure is only reliable under the hypothesis of strictly rigid body structure and of a plane motion. The automatic procedure proved to be a powerful tool during the analysis operation. Its relative velocity, compared with the manual one, allowed to analyze 49 tests in a half hour.

Results

Calm water tests: hydrodynamic parameters

During calm water tests the device is displaced and released in the water. From the resulting motions, the logarithmic decrement, as a measure of the decay rate, is determined. These tests were performed on both rigid and flexible devices and the cables and chains mooring systems. An additional test without the mooring system, was also performed in order to evaluate its influence. It must be noted that this experimental method masks the frequency dependence of both added mass and damping coefficients. Hence, the values of the coefficients will be approximated.

For the purpose of this study, a linearized form of the equation of motion is preferred, as suggested in [109]. In eq. *(8)* the viscous damping is represented by the equivalent linear viscous damping coefficient. The relation between the linear and nonlinear damping coefficients is established by assuming that the nonlinear motion is approximately sinusoidal. The resulting linear motions, produced by the tests, is predicted by the following homogeneous equation eq. *(8)*: Where a_{wz}, b_{rz}, b_{vz}, are the hydrodynamic parameters of the devices, which represent added mass, radiation damping and equivalent linear viscous damping coefficients, respectively, while A_{wp} represents the waterplane area when the device is at rest.   The solution of the homogeneous equation, under the initial condition $z_{(0)}=Z_0$ is:

$$(m + a_{wz}) \cdot \frac{d^2z}{d^2t} + (b_{rz} + b_{vz}) \cdot \frac{dz}{dt} + \rho \cdot g \cdot A_{wp} \cdot z = 0 \qquad (8)$$

where ω_{dz} is the damped natural circular frequency of the decay motion and is related to the natural frequency through the following relation:

$$\omega_{dz} = \omega_{nz} \cdot \sqrt{(1 - \Delta_z^2)} \qquad (9)$$
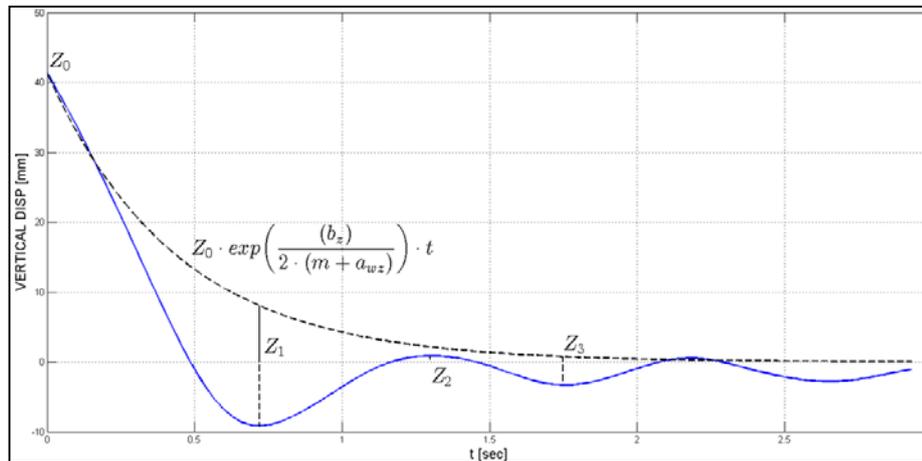
Figure 64: Time response of a freely floating damped heaving unmoored

The time-dependent amplitude of the motion is then:

$$|Z_{max}(t_j)| \equiv Z_j = Z_0 \cdot \exp\left(-\frac{b_{rz}+b_{vc}}{2(m+a_{wz})}\right) \cdot t_j \equiv Z_0 \cdot exp\left(-\Delta_z \cdot \omega_{nz} \cdot t_j\right) \qquad (10)$$

where t_j is the time corresponding to a maximum displacement, Figure 64.

In eq. (9) and eq. (10) quantity Δ_z is defined as damping ratio and it can be expressed as the ratio between total and critical damping coefficients:

$$\Delta_z = \frac{b_z}{b_{cz}} = \frac{b_{rz}+b_{vz}}{2\sqrt{\rho \cdot g \cdot A_{wp}(m+a_{wz})}} \qquad (11)$$

The aim of the calm water tests is to measure consecutive amplitudes. Eq. (10) relates two successive amplitudes, and the exponent of the last term is called logarithmic decrement eq. (12).

$$\frac{Z_j}{Z_{j+1}} = exp\left(-\Delta_z \cdot \omega_{nz} \cdot (t_j - t_{j+1})\right) = exp\left(\pi \cdot \frac{\Delta_z}{(1-\Delta_z^2)}\right) \qquad (12)$$

$$\ln\left(\frac{Z_j}{Z_{j+1}}\right) = \pi \cdot \frac{\Delta_z}{\sqrt{(1-\Delta_z^2)}} \qquad (13)$$

From Eq. (13) Δ_z is then calculated:

$$\Delta_z = \frac{b_z}{b_{cr}} = \frac{\ln\left(\frac{Z_j}{Z_{j+1}}\right)}{\sqrt{\pi^2 + \left[\ln\left(\frac{Z_j}{Z_{j+1}}\right)\right]^2}} \qquad (14)$$

By measuring two consecutive amplitudes of the damped heaving motion, we can then determine the value of the combined damping coefficient, b_z:

$$b_z = \Delta_z \cdot b_{cr} = \Delta_z \cdot 2\sqrt{\rho \cdot g \cdot A_{wp}(m+a_{wz})} \qquad (15)$$

where the added mass is calculated by:

$$a_{wz} = \frac{\rho \cdot g \cdot A_{wp}}{\omega_{nz}^2} - m \qquad (16)$$
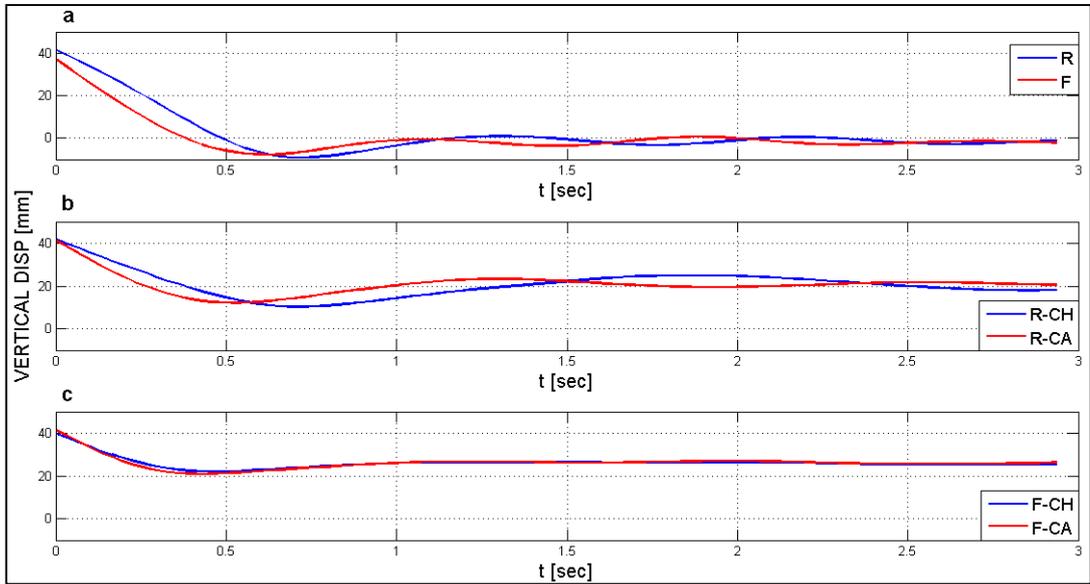
Figure 65: alm water test results: unmoored (a), rigid device moored (chains and cables) (b), flexible device moored (chains and cables) (c)
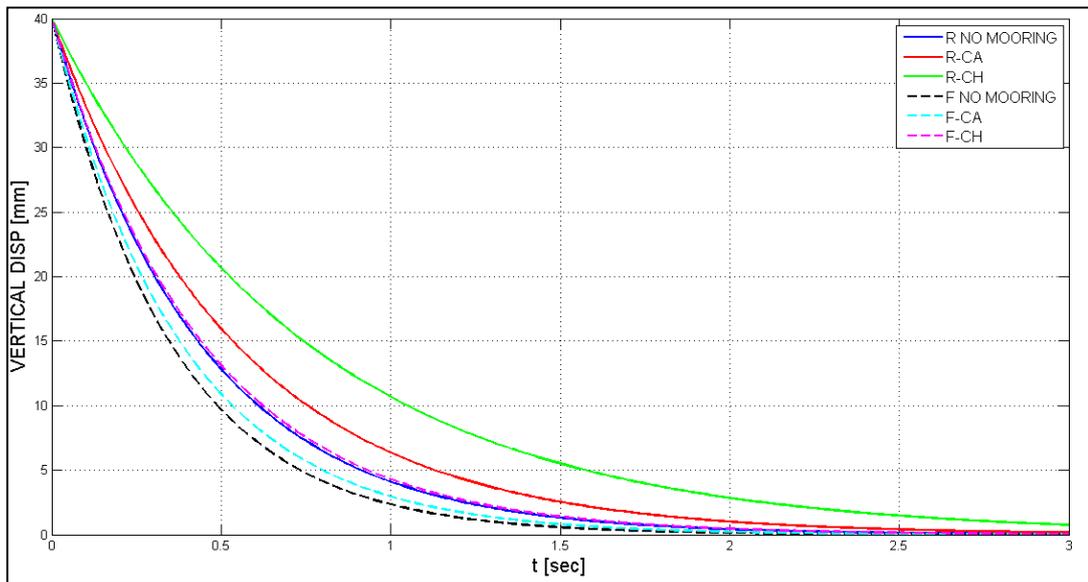
Figure 66: Comparison of the damping coefficients, peaks envelope

The heave is almost unaffected by the mooring system for both devices; the natural period presents no relevant variations with the mooring systems. The flexible device

shows an evident second natural period, which could be explained by the mechanical characteristics of the device. The flexible duct is less massive and more compliant than the rigid duct and cannot contrast compression. The compliance of the duct generates more degrees of freedom and a second natural period. The nonlinear elastic behavior highly affects the resultant free oscillations.

Table 7: Hydrodynamic parameters

Test	Natural period [sec]	Damping [N· sec/m]	Added mass [kg]	Added mass coef.	Ratio critical damping
R	1.00	10.44	1.95	4.79	0.36
R-CH	1.15	6.63	2.05	5.04	0.22
R-CA	1.10	8.83	2.00	4.91	0.30
F	0.95	12.42	1.84	4.52	0.45
F-CH	1.00	10.70	1.90	4.54	0.37
F-CA	0.97	11.76	1.85	4.67	0.42

Motion analysis

Motion analysis is used to estimate the submergence of the floater during the wave cycle and its influence on the pumping mechanism: at each wave cycle, the position of the free surface elevation and the displacement floater are compared. The average value of the submergence for each wave state is then evaluated over 10 sample wave periods. The experimental response amplitude operator (RAO) is evaluated by means of time domain analysis. The procedure calculates, for each wave cycle, the amplitude of the motion in heave and surge of the body and then determines, as a final result, the ratio between the median of the calculated values and the incident wave. In the following paragraph the complete series of results coming from the analysis of the dynamic behavior for 49 wave

states will be presented. The physical tests will be proposed only for the rigid device. This decision comes out after the preliminary tests carried out under the action of the North Adriatic Sea's wave climate. The preliminary tests highlighted some problems in the measurement of velocity and displacements for the flexible device, therefore the full analysis of the device behavior will be conducted and proposed only for the rigid one with a crest freeboard of 7 mm equivalent to 0.11 m in real scale.

The tests without a mooring system have been carried out in order to identify a freely floating behavior of the device. Results coming from such tests will be helpful to demonstrate the influence of the mooring system on the dynamic response of the floater. These tests were completed in the high-speed towing tank of Davidson Laboratory at Stevens Institute of Technology; they were based on the measure of the elongation of a magnetic wire rolled into a spiral. The obtained measurements took into account both heave and surge mode, and gave as results a combination of the two. Therefore in order to compare these results with those coming from the single mode motion analysis heave and surge responses need to be combined.

Figure 67: Facilities at Davidson Laboratory

Figure 68: Displacements measuring method at Davidson Laboratory
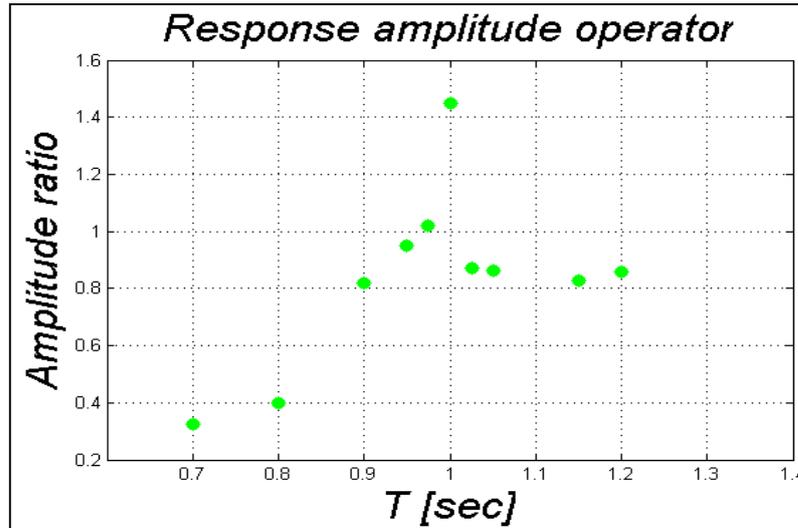
Figure 69: Experimental RAO for rigid device with no mooring system
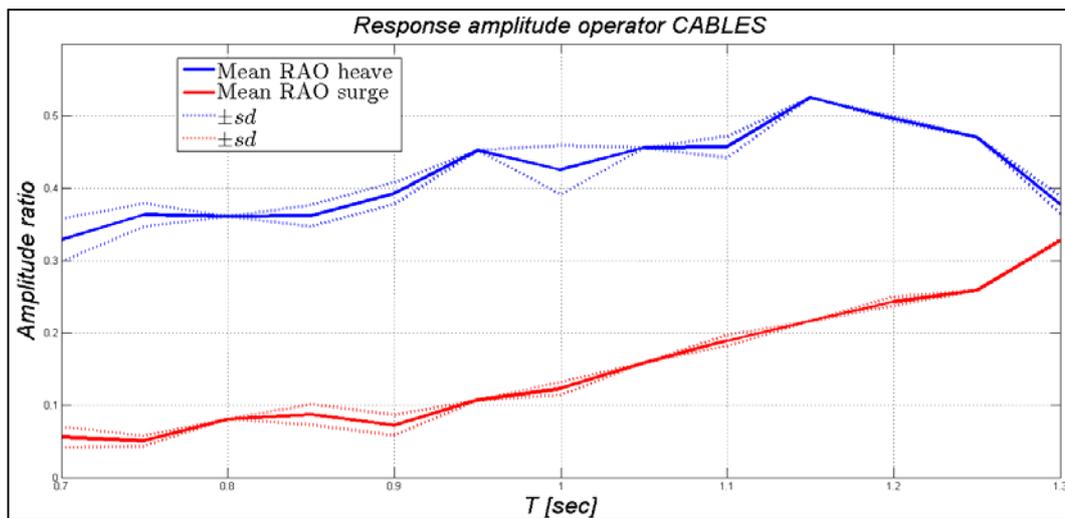
Figure 70: Experimental Response Amplitude Operator (RAO) for rigid device moored with cables; dotted lines indicate standard deviation. They appear only in correspondence to some period, since different wave heights have been tested only for selected wave periods.

Figure 70 and Figure 75 show good correspondence with the results coming from calm water tests. Resonant periods for OXYFLUX moored with cables (CA) and chains (CH) are equal to 1.15 and 1.05 sec, respectively. Such values are reasonably greater than the resonant periods calculated by means of the calm water tests with no mooring system

since the presence of the additional mass due to the mooring lines increases the natural period of whole structure.

Cables (Figure 70), largely affect the dynamic response of the floater. The heave peak (blue line Figure 70) relative to the resonant period (1.15 sec) is less pronounced as compared to the heave peak for the chains system, Figure 75), while the surge mode is completely damped by the mooring line. Surge shows an increasing trend according to horizontal water particle displacement growth. No resonant period seems to be reached for surge mode during the period of the tests with the device moored with cables.
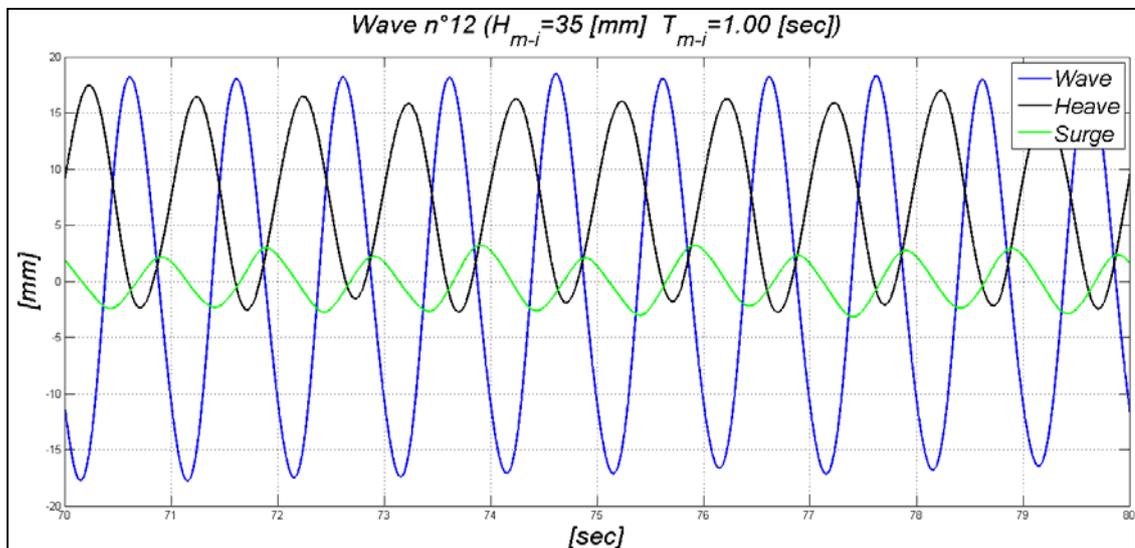
Figure 71: Example of measured time series, Wave n°12

Non linear effects due to the elastic cables affect the shape of the signal, and are mainly caused by the drag acting along the cables. Both heave and surge mode show higher values of steepness than the wave signal; furthermore surge mode asymmetry can be noticed inside the wave cycle, Figure 71. The more the wave grows, the more the non linear effects affect the response. As wave height increases, relative velocity between water particles and the device also increases. Such phenomenon interests the cables and the stabilizing ring at the bottom of the tube, generating a flow separation at the ring corners and then dampening the vertical displacement by means of viscous dissipation,

Figure 72. Less energetic wave states show near linear behavior in virtue of the lower water particle velocities values,, Figure 74.

Figure 72: Eddy formation at the stabilizing ring, wave trough (left), wave crest (right)
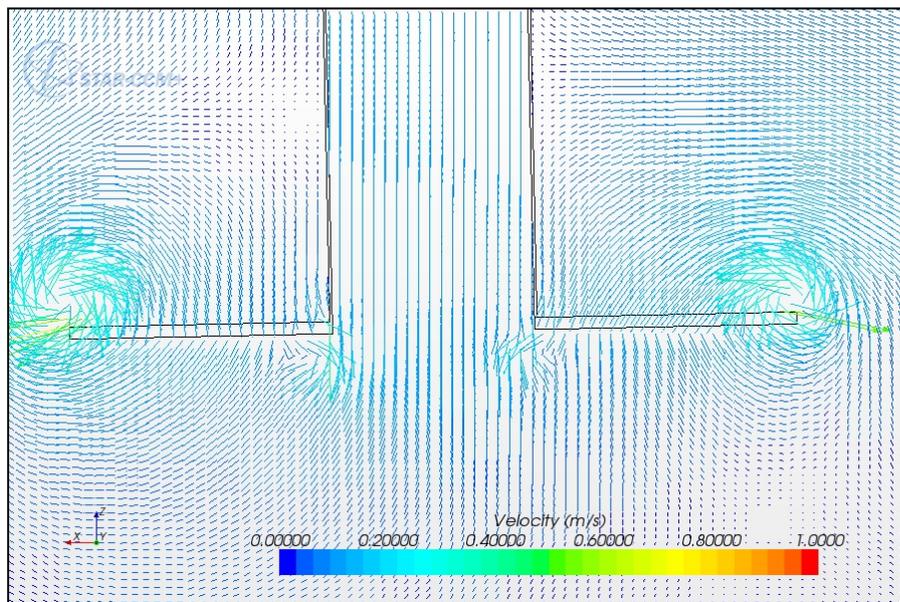
Figure 73: Eddy formation at the stabilizing ring from numerical model.
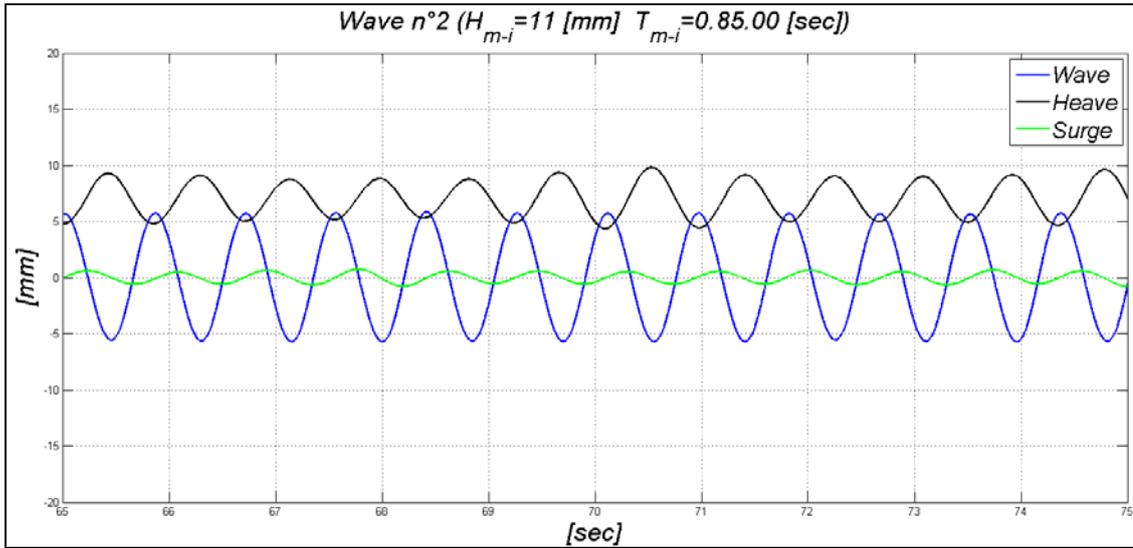
Figure 74: Example of measured time series, Wave n°2
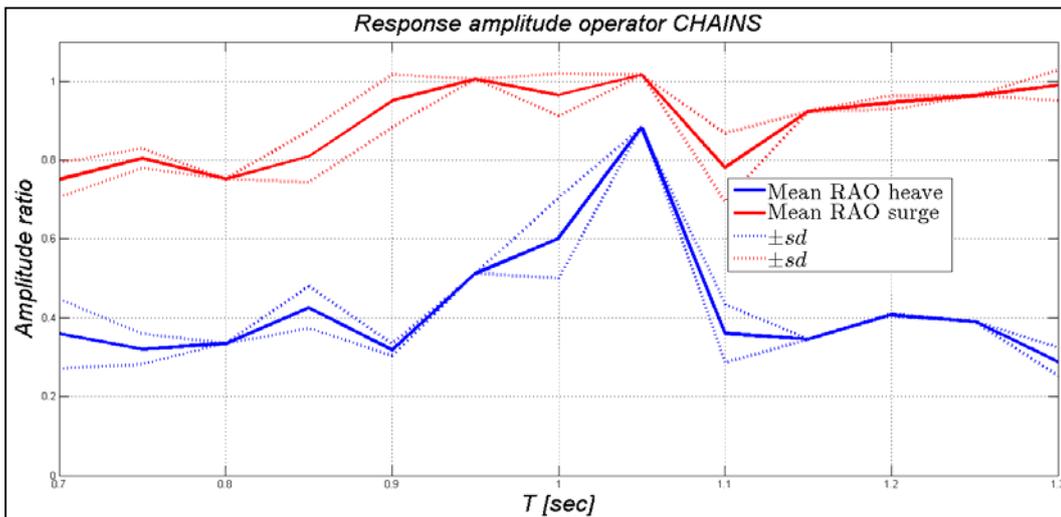
Figure 75: Experimental Response Amplitude Operator (RAO) for rigid device moored with chains; dotted lines indicate standard deviation. They appear only in correspondence to some period, since different wave heights have been tested only for selected wave periods.

Comparing Figure 75 with Figure 70 it is evident how the chain mooring system allows the motion of the device more than the cables mooring system. Heave response presents a clear peak relative to the solicitation of the natural period which is approximately equal to 1.05 sec, while for the surge mode it can be noticed that chains allow the floater to ride the waves much better than the cables since the RAO shows higher values of response;

92

for the values of the period between 0.9 and 1.05 sec the response of where the floater oscillates near 1. In the following, a tool similar to the response amplitude operator will be used to describe the dynamic response of the floater even if the device shows large non linear effects in its behavior. Such effects are taken into account showing the standard deviation from the mean value of response to estimate the non linearity. The dotted lines correspond to the standard deviation (sd); they are present only in correspondence with some periods since not all the periods have been tested with different wave heights. The trend of standard deviation highlights the non linear response of the floater for both mooring systems.
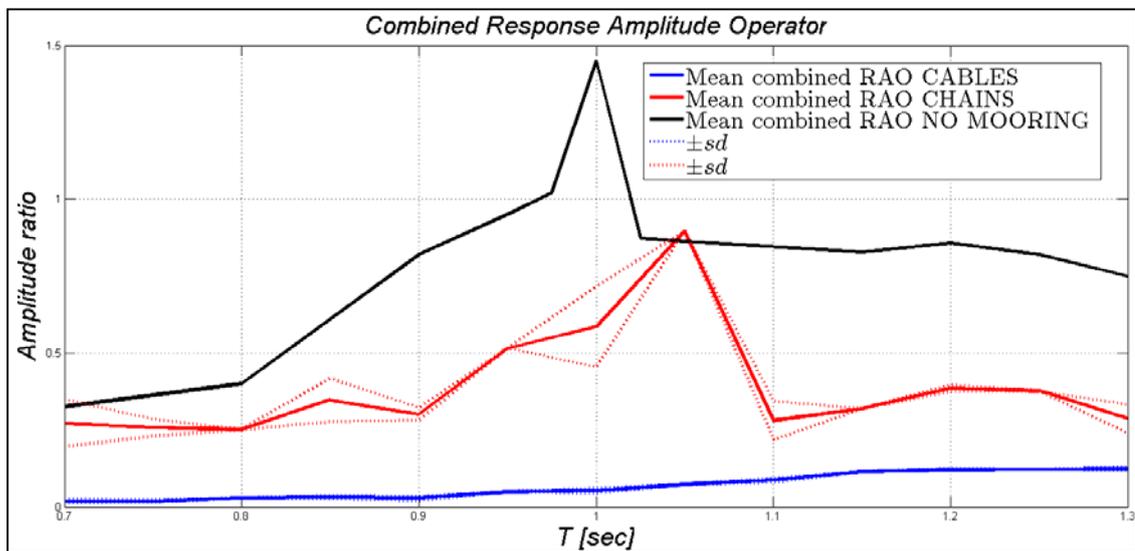
Figure 76: Comparison between experimental Response Amplitude Operator (RAO) for the rigid device; dotted lines indicate standard deviation. They appear only in correspondence to some points since multiple wave heights have been tested only for selected wave periods.

In Figure 76 the comparison with the combined RAO is shown. The combined RAO was calculated by taking into account the surge and heave components of the motion. As can be expected resonance shifts toward higher values of period for moored device in virtue of its increased mass due to the mooring lines. The most relevant effect due to the chain is shown in Figure 77.
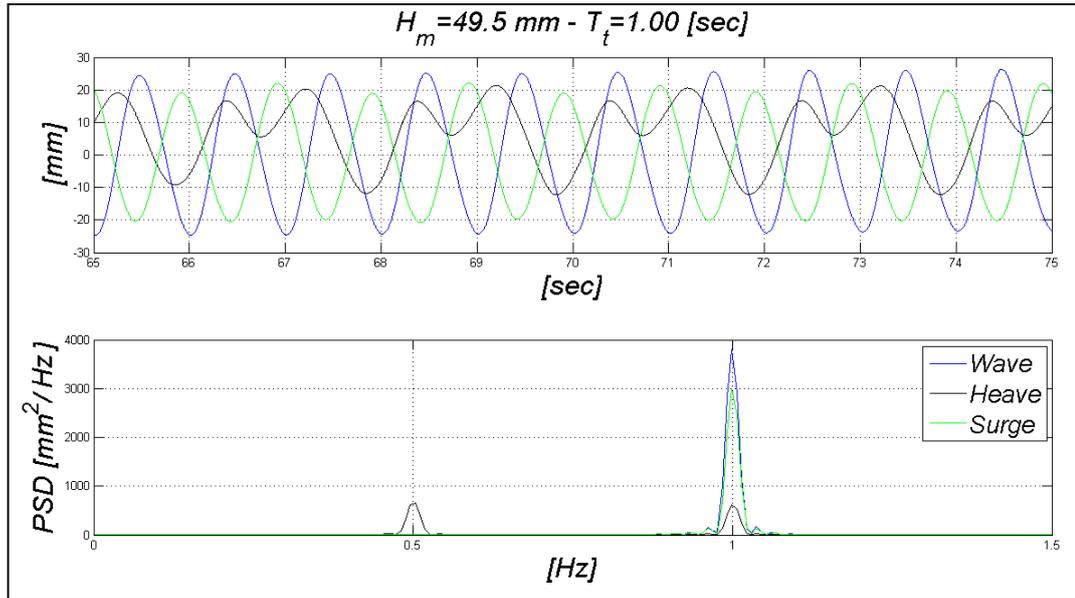
Figure 77: Example of measured time series and relative spectral analysis for chains moored device; the non linear behavior of the device is highlighted for wave n° 14 in heave mode.

Another parameter investigated is the average submergence of the floater during the wave cycle. This parameter is strongly affected by the mooring system. Elastic cables dampen the possible displacements resulting in asymptotic tendency of the submergence to reach 100 % during the wave cycle as the wave period increases, while chains allow the body to move with the water particle, resulting in an asymptotic value of 50%, as shown in Figure 79.
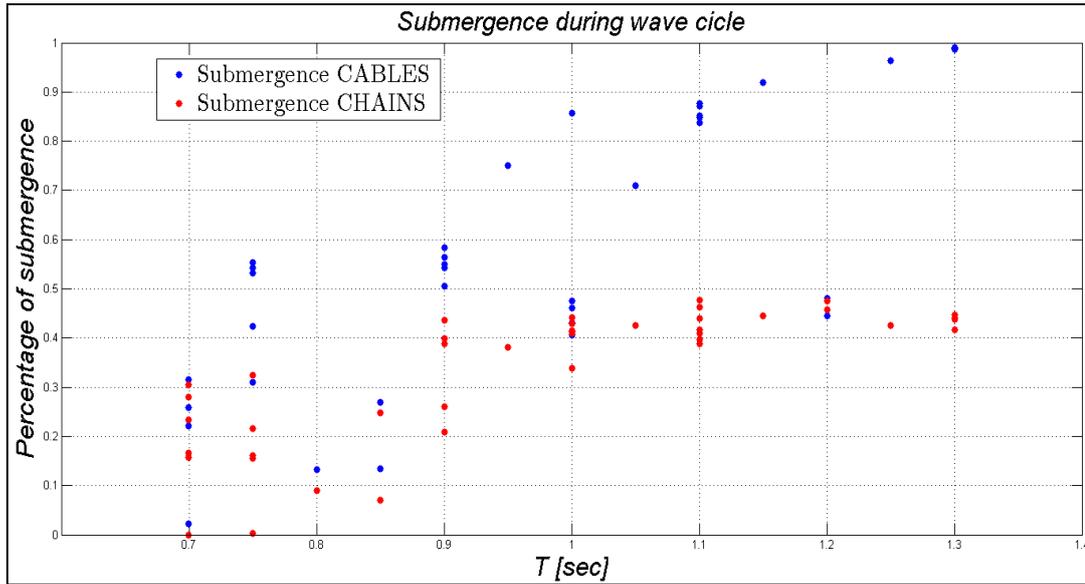
Figure 78: Submergence of the floater during wave cycle (%) vs wave period.

Water velocity measurements

Ultrasound Doppler velocimetry was originally applied in the medical field and dates back to the late 40's. The first use of ultrasound for medical diagnosis came about in 1949 with attempts to obtain ultrasonographic cross-sectional imaging. In 1954, H. P. Kalmus [111], described how flow velocity in fluids could be determined by measuring the phase difference between an upstream and downstream ultrasonic wave. Baker and H. F. Stegall [112] presented the first Doppler instrument intended for transcutaneous measurement of blood flow velocity in man using the continuous wave Doppler principle. Approximately five years later, pulsed Doppler instruments were introduced, allowing blood flow velocity measurements at predetermined depths. The use of pulsed emissions has extended this technique to other fields and has opened the way to new measuring techniques in fluid dynamics. Takeda [113] subsequently extended this method to non-medical flow measurements and developed a monitoring system for the velocity profile measurement of general fluids. The method itself was found to be quite useful for

measuring the flow of a fluid and in the end, through years of use, has gradually become accepted as a tool to study the physics and engineering of fluid flow, [114]. The working principle of pulsed ultrasound Doppler velocimetry is to detect and process many ultrasonic echoes issued from pulses reflected by micro particles contained in a flowing liquid. A single transducer emits the ultrasonic pulses and receives the echoes. By sampling the incoming echoes at the same time relative to the emission of the pulses, the variation of the positions of scatterers are measured and therefore their velocities. The measurement of the time lapse between the emission of ultrasonic bursts and the reception of the pulse (echo generated by particles flowing in the liquid) gives the position of the particles. By measuring the Doppler frequency in the echo as a function of time shifts of these particles, a velocity profile after few ultrasonic emissions is obtained [115].

The used key features of Signal Processing's DOP2000 velocimeter

The Emitting Frequency

In the choice of an emitting frequency the following four factors are crucial. First of all, the desired position of the sampling volume is important, especially when dealing with small channels. The emitting frequency contributes to the definition of the axial and lateral dimension of the sampling volume. Since this dimension is linked to the duration of the burst, for a defined number of wave cycles in the burst, a higher emitting frequency will give a better resolution. Besides the sampling volume size, attenuation of the ultrasonic signal is an important factor to be taken into account in the choice of an emitting frequency. The attenuation of ultrasonic waves depends on their frequencies. Low frequencies are less attenuated than high frequencies. Moreover, the maximum measurable velocity, which is inversely proportional to the emitting frequency, and the energy backscattered by particles depend on the ultrasonic frequency. In this study the

chosen emitting frequency is equal to 4 MHz since the only usable transducer was a 4 MHz instrument. This restriction is due to the characteristic dimensions of the transducer. The instrument had to be installed inside the tube of the device (diameter equal to 50 mm), then its diameter had to be small enough so as to not disturb the flow inside. The selected apparatus has a diameter of 8.8 mm, the smallest available. It can be argued that the effects of the instrument on the flow at a distance from its bottom surface equal to more than five times the diameter of the device can be neglected, and the measured velocity should be unaffected by the DOP.

Pulse repetition frequency

Pulse repetition frequency determines the maximum measurable depth as well as the maximum Doppler frequency and therefore the maximum velocity which can be measured unambiguously. The choice of the pulse repetition frequency should be based on the velocity values that have to be measured and not on the depth that has to be reached. The best way to select a correct value is to start with a high value and reduce this value until at least 50 percent of the velocity scale is covered. The desired analyzed depth can then be adapted by changing the resolution, the position of the first gate or the number of gates. In this research the emitting frequency is identified considering the maximum velocity range to measure. Such velocity is calculated according to the linear wave theory for the most energetic simulated wave, Figure 79. The selected emitting frequency has been chosen as equal to 2202 Hz, corresponding to a maximum investigated depth of 334 mm from the transducer.
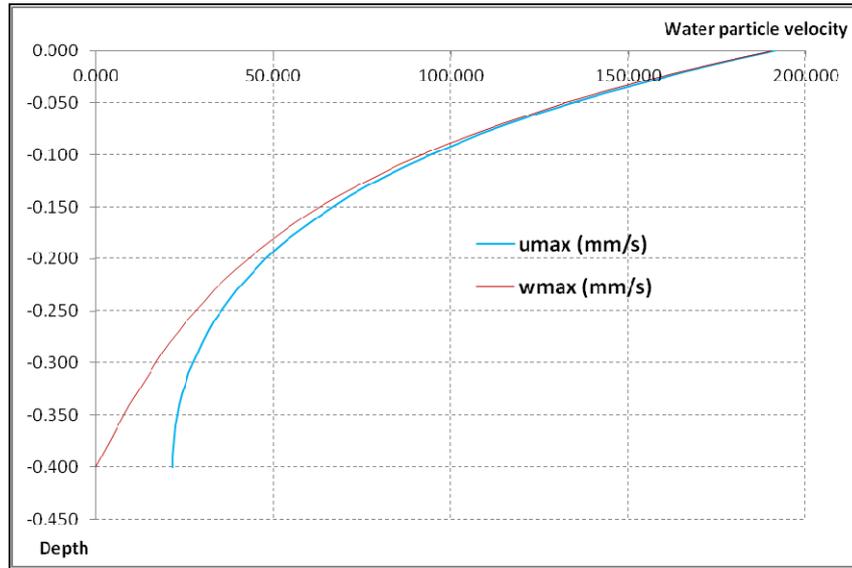
Figure 79: Water particles velocity according linear wave theory for wave state 34

Wall effect, position of the first gate and saturation effect

In order to determine the velocity profile in a correct manner, the position of the first gate should be chosen carefully so that the wall effect and saturation are decreased. The measured portion of each sample volume is located in the center of the sample. When part of the sample volume is located inside the channel wall, this position will not reflect the actual measuring position given by the instrument (wall effect). In the following, the position of the first gate will be set so that the sampling volume begins ideally right after 5 times the transducer's diameter in order to exclude the effects of the wake caused by the sensor and the turbulence caused by overtopping. The position of the first gate is based on the position of the center of the first sample volume which depends on the emitted ultrasonic burst length, the speed of sound in the media located between the transducer face and the first gate and the starting depth that can be set in the instrument. When the first gates are close to the surface of the transducer, the burst duration and the ringing of the piezoelectric ceramic do not allow any measurement in these gates due to a saturation of the receiver (saturation effect). The saturation region can be visualized in the display

of the received echoes, where the level echoes of the gates located at the depths near the surface of the transducer stretch over the entire scale. The position of the first measurable gate therefore depends on the emitting frequency, the burst length, the geometry of the experimental setup, the emitted power and the amplification level. The starting depth chosen in the instrument is the distance between the transducer face and the center of the first gate. For the purposes of the present study the position for the first gate was kept equal to 43 mm from the emitted bottom surface of the DOP.

Burst length

The length of the emitted burst affects the sampling volume. The bandwidth of the electronic receiving unit in the ultrasonic instrument is fixed, but the number of cycles contained in the emitted ultrasonic burst can be changed. The length of the emitted burst depends on the selected emitting frequency and on the speed of sound in the medium. The value of this parameter was selected as equal to 4 ultrasonic wave cycles. The length of the used burst is equal to 1.48 mm, according to the hypothesis that the speed of sound in water is equal to 1480 m/sec, the emitting frequency is equal to 4 MHz and wave length is equal to 0.37 mm.

Resolution

In ultrasonic instruments, the resolution is defined as the distance between the centers of adjacent sampling volumes. In ultrasonic Doppler velocimetry, the shape and lateral size of sampling volumes (measured perpendicularly to the ultrasonic beam axis) are defined by the geometry of the ultrasonic beam. The longitudinal size of the sampling volumes on the other hand is defined by burst length. The borders of the sampling volumes are not well defined since the levels of the ultrasonic echoes increase and decrease "slowly" due to the finite bandwidth of the receiver. Whenever possible, a value for the spatial filter matching the resolution should be selected to achieve an optimum signal to noise ratio. Physical tests were completed using a resolution set to 0.74 mm and a relative spatial filter fixed on 0.78 mm.

Number of gates

The number of gates that can be measured depends on the selected pulse repetition frequency, the position of the first gate and the selected resolution. An upper limit can be fixed to ensure a better display of velocity profiles, especially when low pulse repetition values are selected. The position of the first gate and the number of gates define the measuring range and, therefore, the analyzed depth. In the present investigation 140 gates were used to identify water velocity inside the tube corresponding to a range between 43 and 146 mm from the transducer. Medium simultaneous values are calculated for 140 measurements obtaining a sinusoidal trend, Figure 80.
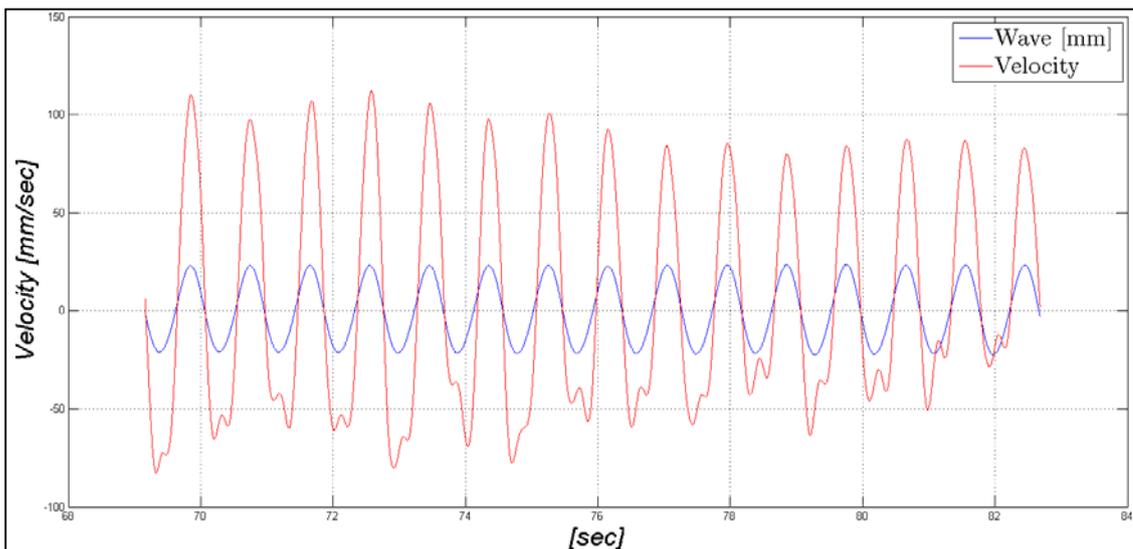
Figure 80: Velocity values time series, wave n° 9.

Emitting Power and Sensitivity

Emitted ultrasonic power has to be selected in order to receive enough backscattered energy from the particles and to avoid saturation in the receiver stage of the instrument as much as possible. High emitting power should be avoided since it induces more ringing in the transducer and more dissipated energy. Therefore it is generally better to increase the amplification (time gain control) instead of increasing the emitting power.

Nevertheless, a too high level of amplification can also induce saturation in the receiver stage of the instrument, which can lead to wrong measurements. The algorithm used to measure the Doppler frequency computes the mean frequency of the Doppler spectrum. When Doppler energy decreases, the mean value becomes more and more random due to the noise included in the spectrum. In order to avoid the appearance of random values in the measurement, the instrument also computes the level of Doppler energy received and allows the user to cancel the computation of the Doppler frequency if the level of the Doppler energy is below a value defined by the user. In this case the canceled values are replaced by zero values. The sensitivity parameter contains five different values, which define the level below which the computation is canceled. The sensitivity parameter can be used to obtain information on the quality of the measured values. Both parameters discussed in this section were set on the highest values during the tests.

Number of Emissions Per Profile

The measurement of the Doppler frequencies is based on the correlation that exists between different emissions. Since each emission can be considered as a particular realization of a random process, more samples are available which reduce the variance of estimated quantity. The algorithm used to estimate the Doppler frequency is based on the assumption that the particles that generate the echoes during the measurement of the Doppler frequency remain inside the ultrasonic beam and their velocities are constant. For low velocities in steady flows this assumption is valid, but for transient ones, characterized by high velocities (as in this study), a compromise between the quality of the estimation (minimum variance) and the measuring time has to be accepted. The number of emissions per profile should be selected in accordance with the type of flow investigated and with the width of the ultrasonic beam. For low velocities in steady flows, a high number of emission will decrease the variance and therefore should be selected. For high velocities in unstationary flows this number should be adapted to the degree of variation of the velocities versus time. This number was set as equal to 128 emission per profile.

101

Profiles to record

In pulsed ultrasound Doppler velocimetry measurements, a certain number of instantaneous velocity profiles are used to calculate the mean velocity profile. Possible velocity fluctuations, caused by the recirculation of the backward facing step at high Reynolds-numbers (as in the present research), may lead to small differences between different instantaneous profiles and therefore to a statistical error. Therefore, it is necessary to determine a mean velocity profile on the base of enough instantaneous velocity profiles; this parameter was set equal to five contemporarily profiles. Furthermore the final result of the present method is the mean velocity value of 15 wave cycles. Such procedure allows to identify single representative value of velocity for each tested wave state. An important step in the analysis is the choice of the instance when the signal should be cut. Velocity values have a sinusoidal trend, therefore the mean value must be calculated on integer times of the wave period in order to make negligible relative velocity between transducer and water flux due to the movement and not to the wave overtopping.
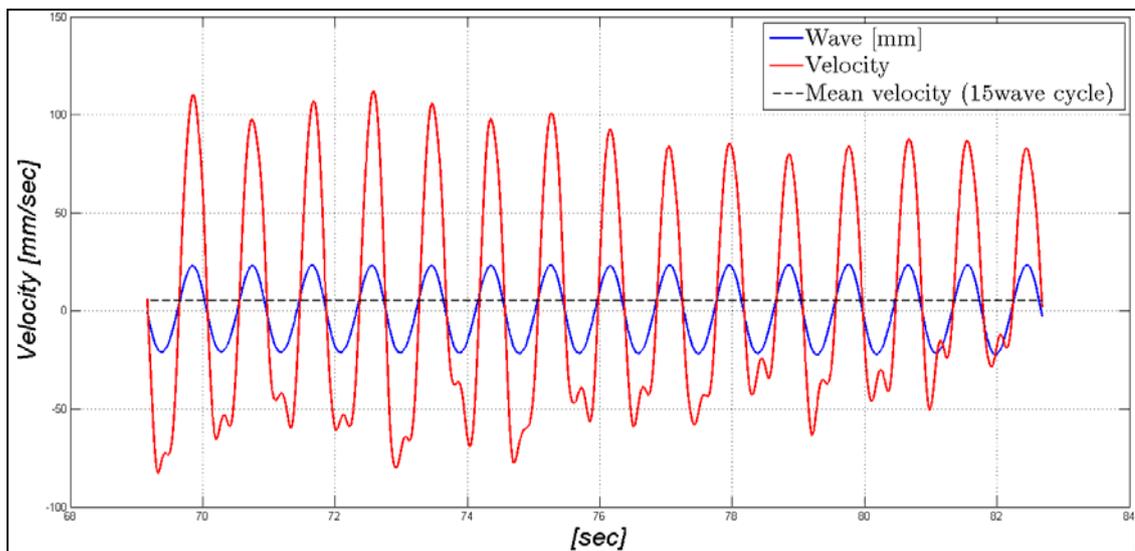
Figure 81: Velocity values time series, wave n° 9.

Measurement set-up

In this study, a commercially available pulsed ultrasound Doppler velocimetry system (DOP 2000) manufactured by Signal Processing S.A., Switzerland, is used to measure downward water velocity in the experimental setup described above. The basic function of pulsed ultrasonic Doppler velocimetry is to measure the Doppler shift frequency and time delay between emission and reception of ultrasound scattered back by small particles which are moving with the fluid. In water, natural particle contamination usually generates enough significant echo signals. If not, particles have to be added in a process called seeding. The most important parameter during the selection of the seeding material is the size of the scatterer, because the amount of energy reflected by the scatterer and its angular distribution depends primarily on the ratio between particle size and ultrasonic wavelength. The tests series analyzed in the present document were accomplished in a flume filled with water coming from the aqueduct, therefore there were not enough particles. Powder of titanium dioxide was added to the water in order to have sufficient seeding. Titanium dioxide (TiO_2) is a naturally found oxide of titanium, its most important application areas are paints and varnishes as well as paper and plastics. Its characteristic gravity is equal to 3970 kg/m^3 [116] and its primary particle size (d_{50}) varies from some nm to tens of μm. Titanium dioxide has been chosen according to Longo [117], who already used it in his experiment aimed at investigating turbulence flow structures in wind generated gravity waves.

Results

The DOP sensor was installed along the pipe axis of the physical model at a distance of approximately equal to 150 mm from the top of the floater. The measurements start at 195 mm below mean water level and end at 296 mm below mean water. The connection

between the probe and the structure of the floater was developed by means of a rigid structure made in the machinery and inherently moving with the device, Figure 83.
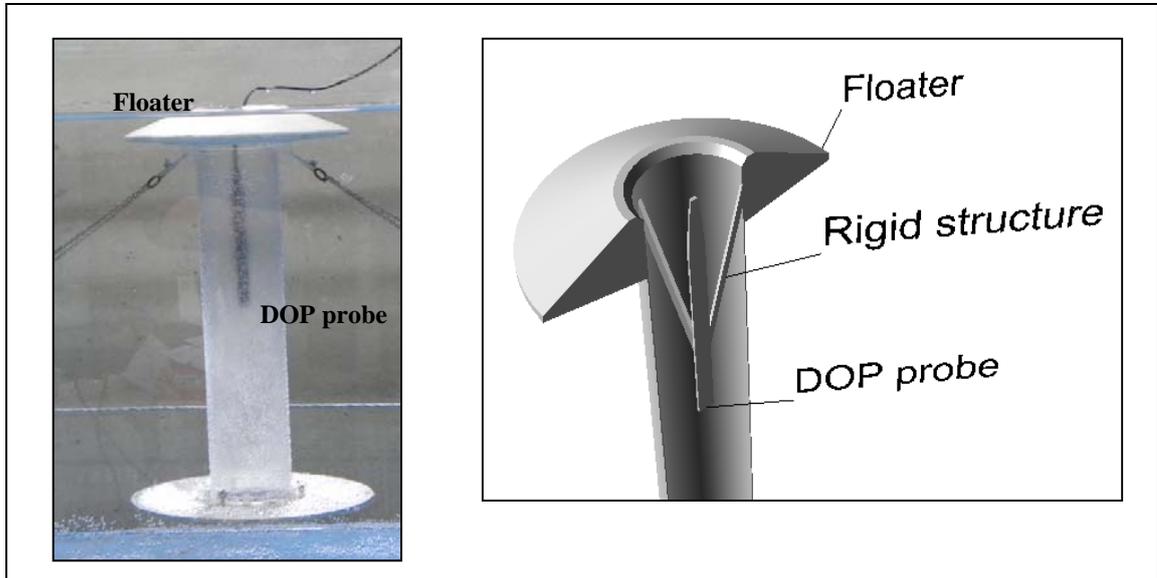
Figure 82: OXYFLUX during a physical test, only the probe and floater are visible (left), cad view of a section of the device with DOP (right).

A sampling frequency equal to 14.40 Hz is imposed. The DOP data allows to calculate average velocity at each point of the measured profile for the whole duration of the signal or for just a single wave cycle. The sensor inherently moves with the floater; the relative velocity between the device and the water inside the tube is negligible since mean velocity is calculated on a multiple of the wave cycle. This method used to estimate flux velocity inside the duct was found to be not robust enough for the highest waves acting on the flexible device, since the sensor is linked to the floater but not to the flexible duct; hence, the emitted beam may sometimes measure velocity outside the duct, Figure 83.
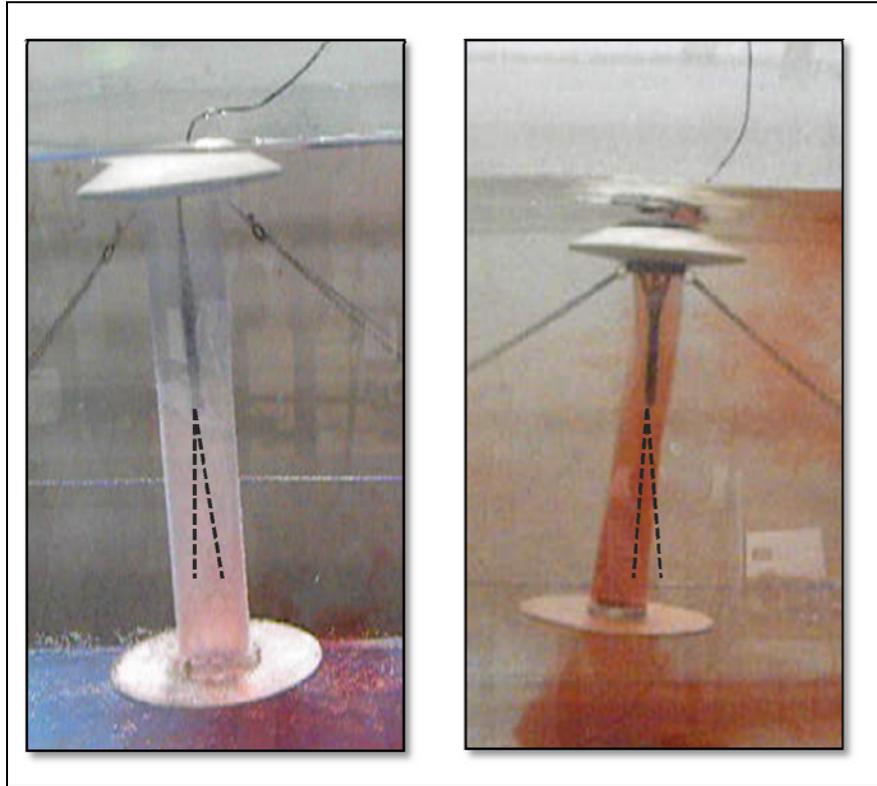
Figure 83: Problems relative to the measurements with the flexible structure (right), rigid structure (left).

In order to have the same temporal reference system the ultrasonic Doppler velocimeter was triggered with the acquisition of the wave signal and the camera. Results are given in a table format in which each column is the time series at the single point of measurement (i.e. each 0.74 mm) while each row is an instantaneous profile along the whole tube for the entire set of measuring gates.

For the purpose of the present study each tested wave state has been characterized by a single value of velocity identifying three main operating ranges determined by two threshold values of wave heights. As can be noticed from Figure 84 the three fields are identified by means of wave height thresholds. Such values distinguish *Field 1* for wave heights smaller than 3.00 mm in Froude similitude 1:16 (*real scale 0.05 m*) where no overtopping occurs, *Field 2* for wave heights between 3.00 mm and 48.00 mm (*real scale 0.77 m*) where overtopping of incoming wave generates downward flow for higher head

of the water column inside the device with respect to the surrounding wave field and *Field 3* for wave heights between 48.00 mm and 100.00 mm (*real scale 1.60 m*) where water flux reverses its direction and the water flows from the bottom to the surface. Such behavior is mainly due to the depression generated by the wave crest as it goes over the floater but not into it.
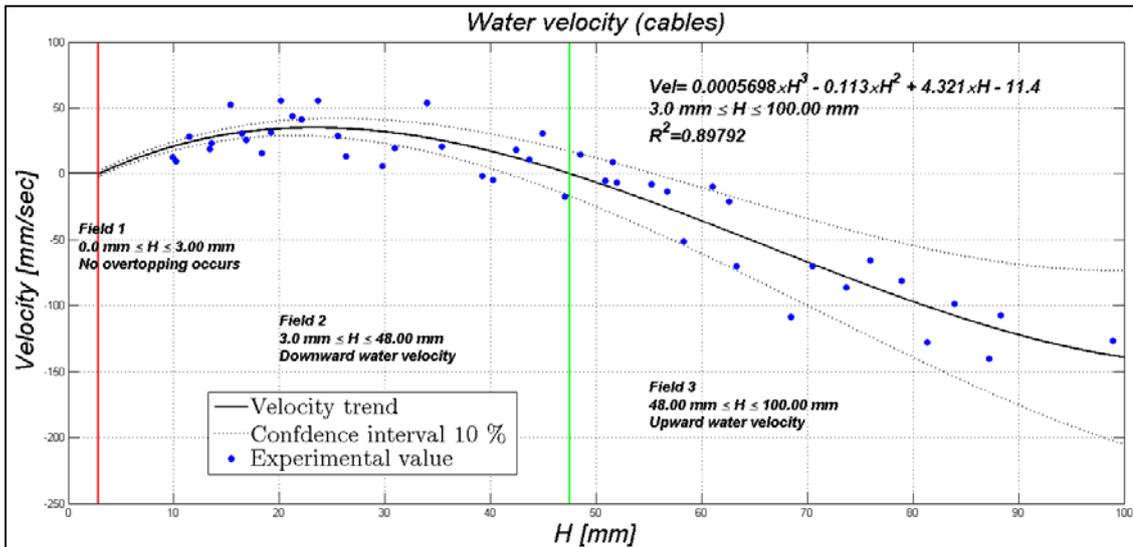
Figure 84: Vertical water velocity vs. incident wave height, (positive values represent downward water velocities), device moored with cables.
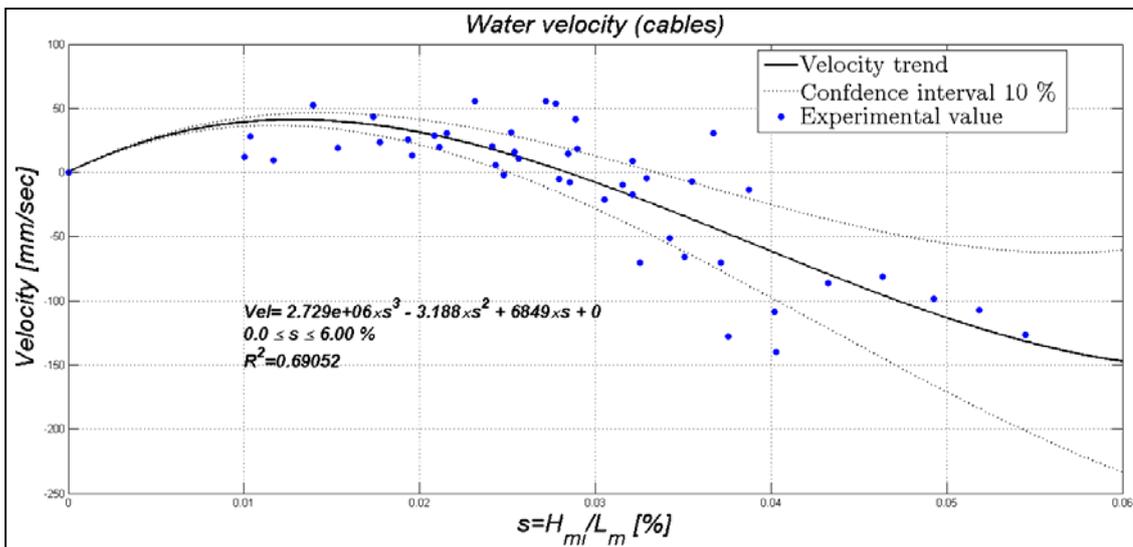
Figure 85: Vertical water velocity vs. wave steepness, (positive values represent downward water velocities), device moored with cables.
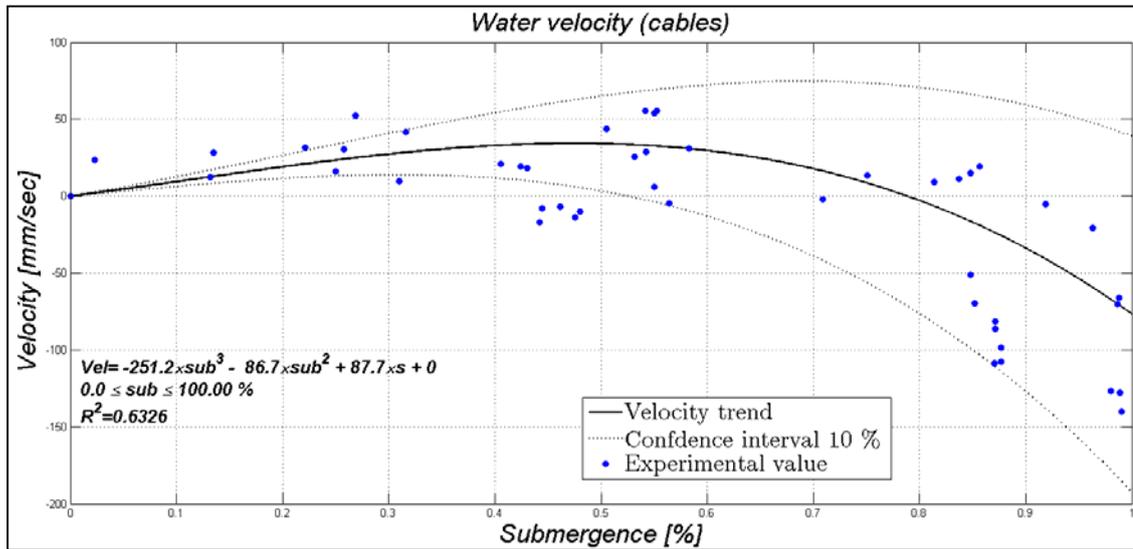
Figure 86: Vertical water velocity vs. average submergence level during the wave cycle, (positive values represent downward water velocities), device moored with cables.

Comparing R^2 values for the investigated parameters it can be argued that wave height is the environmental variable that better describes the pumping mechanism.

Each mooring configuration presents a different pumping mechanism; the chain mooring system allows the floater to freely ride the waves and then increases the minimum threshold value to allow overtopping of the floater. Both threshold values increase but the same trend can be recognized even for this mooring system. In Figure 87 the three fields are distinguished as: *Field 1* for wave heights smaller than 12.00 mm in Froude similitude 1:16 (*real scale 0.19 m*) where no overtopping occurs, *Field 2* for wave heights between 12.00 mm and 62.00 mm (*real scale 0.99 m*) where overtopping of incoming waves generates a downward flow for higher head of the water column inside the device with respect to the surrounding wave field and *Field 3* for wave heights

between 62.00 mm and 100.00 mm (*real scale 1.60 m*) where water flux reverses its direction and the water flows from the bottom to the surface.
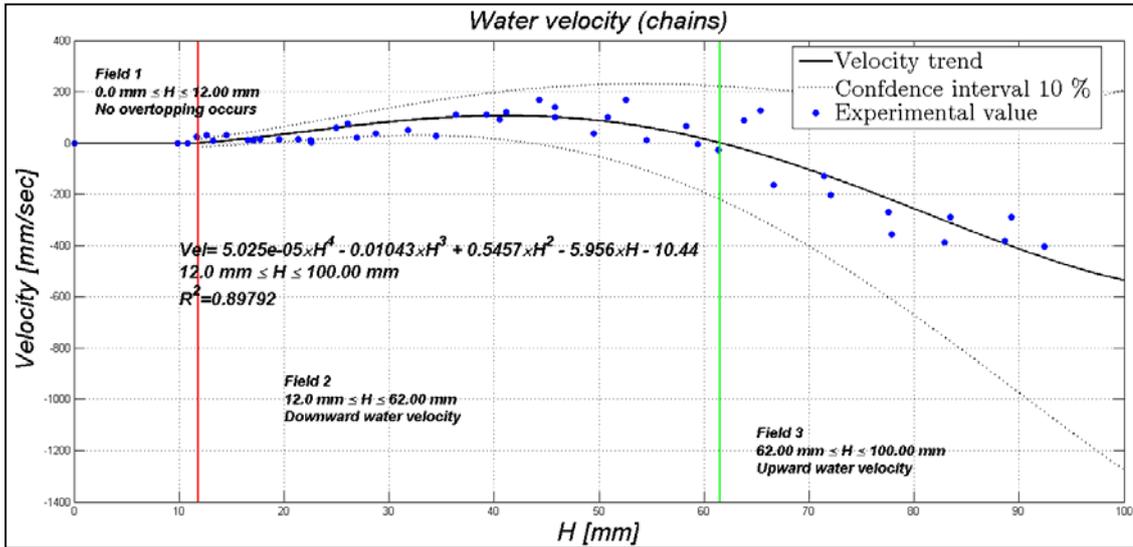
Figure 87: Vertical water velocity vs. incident wave height, (positive values represent downward water velocities), device moored with chains.
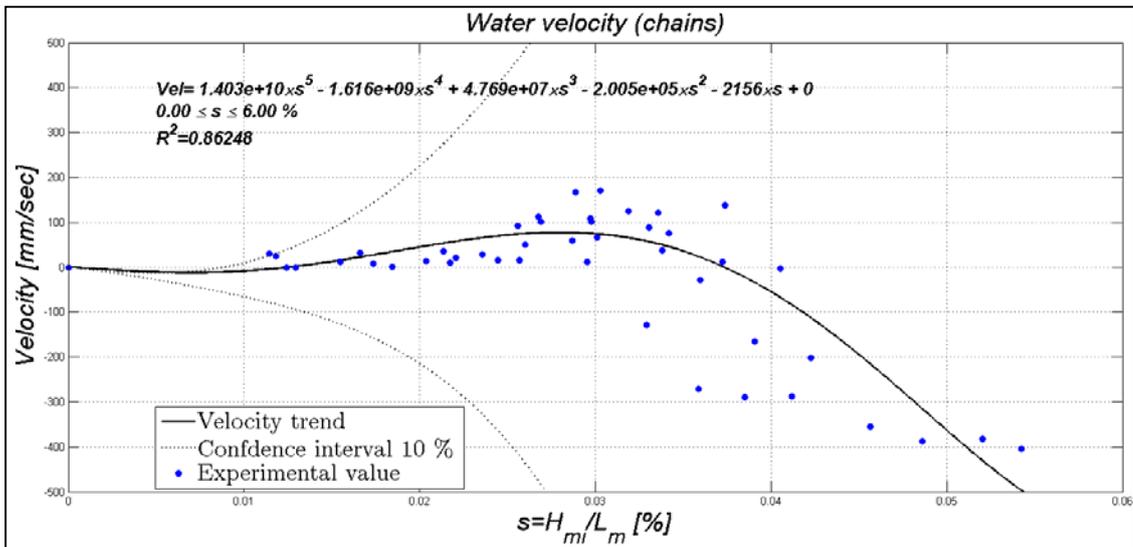
Figure 88: Vertical water velocity vs. wave steepness, (positive values represent downward water velocities), device moored with chains.
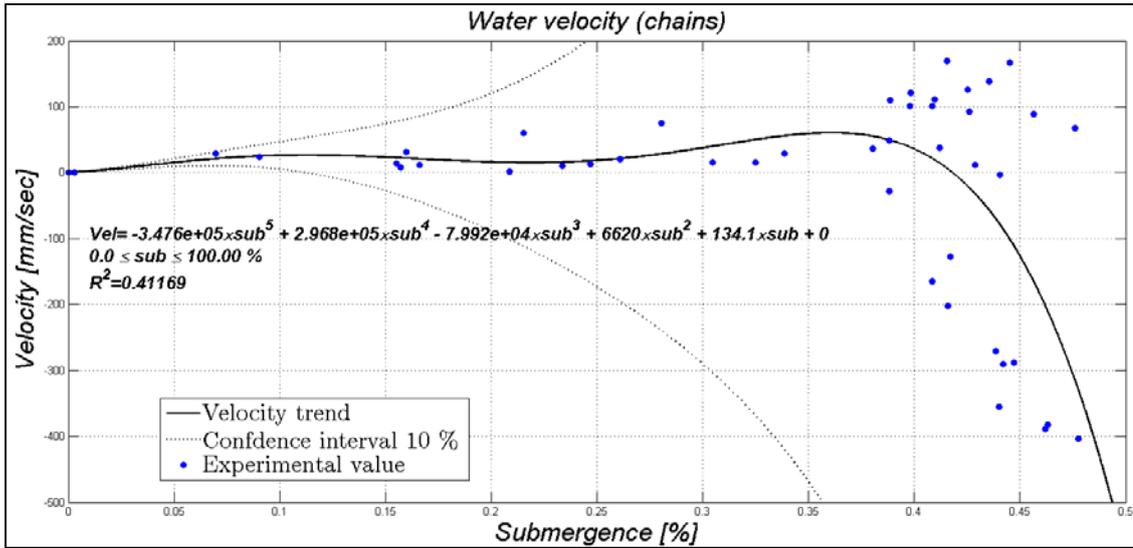
Figure 89: Vertical water velocity vs. medium submergence level during the wave cycle, (positive values represent downward water velocities), device moored with chains.

In Figure 87, Figure 88, Figure 89 water velocity results are proposed for the device moored with chains; from the values of R^2 it is clear that suitable equations for these results are harder to identify. Figure 90 clarifies the differences in the pumping mechanism for the two mooring systems. Chains let the device ride the waves generating a higher value of velocity that can be reached only for wave heights greater than 12.00 mm (*real scale 0.19 m*). Since the aim of the device is to induce downward vertical water flux during the summer season, when strong vertical stratification shows its effects and wave energy is generally reduced, a lower value of the first threshold should be preferred in order to guarantee constant flux during all kind of wave states.
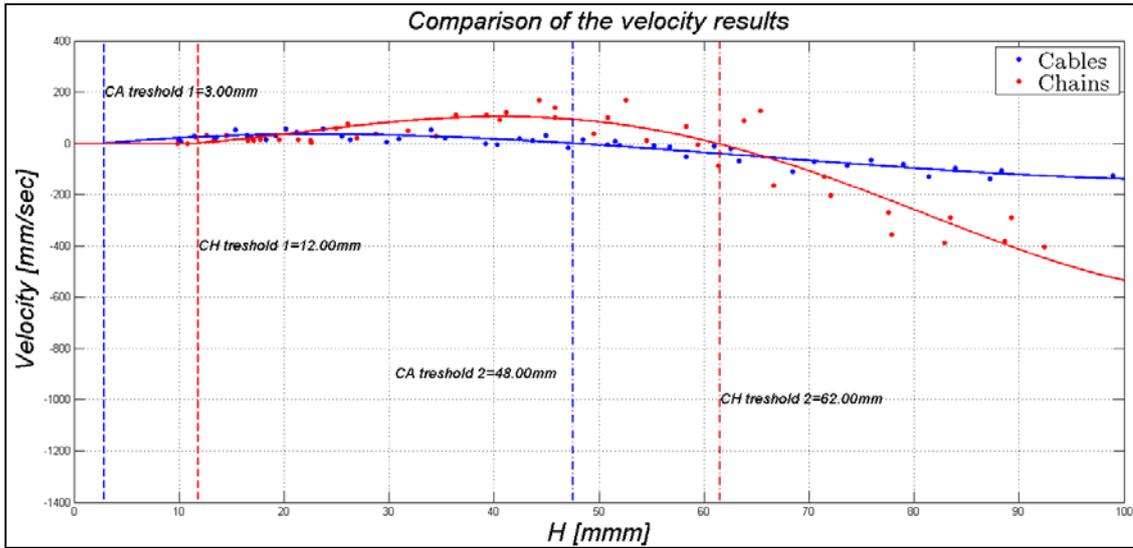
Figure 90: Comparison of water velocity results and fitting for the two mooring systems.

CHAPTER V: Numerical investigation

Numerical study of wave-structure interaction is a wide field of research; at the present day three main approaches are known and broadly used. The methods of investigation can be distinguished between empirical, potential flow based, and CFD based,[110]. Empirical approaches, such as Morrison's equation, can be used to estimate the force acting on a pile. Since the method is fully empirical it depends on flow coefficients that have to be estimated from measurements and they are not generally valid for all flow regimes. Morrison's equation can correctly estimate the forces only if applied to compact bodies and it cannot provide a complete description of the pressure acting on them,[111].

A general overview of potential flow based methods is presented by Newman [112]; such methods allow a more realistic representation of the fluid flow than Morrison's equation. These codes discretize the model into panels and calculate pressure and velocity potential for each of them. Potential flow methods are based on a simplification of the Navier-Stokes equations that consists in assuming non-viscous and non-rotational incompressible fluid flow. Such hypothesis make them efficient for linear, weakly non-linear, and viscous negligible wave structure interaction problems.

For highly non-linear phenomena as, wave breaking, green water, violent body motion and important viscous flow Computational Fluid Dynamic (CFD) should be used. Remaining within the CFD category two different methods of calculus can be identified. The Eulerian method uses a mesh to describe the fluid flow, and it solves the Navier-Stokes equation for each mesh element. The Lagrangian method, models the interaction between particles representing the fluid instead of using a mesh. The main advantage of CFD methods is that in principle they are valid for all flow regimes in off-shore engineering. The second advantage of CFD methods is that the simulation does not need to be scaled as it is necessary for the physical model. Unfortunately they often need to be validated against tests conducted on scaled models due to the lack of full scale data. CFD

methods have been widely used to model the complex nonlinear hydrodynamic interaction between waves and floating bodies, including several types of WEC's, [113], [114], [83].

The OXYFLUX exhibits a complex hydrodynamics. The description of its operating principles involves the interaction between wave and floating part, the submerged parts (in particular the stabilizing ring), and wave overtopping. This implies non linear effects that cannot be modeled without CFD techniques. In the present thesis I used the commercial CFD code STAR-CCM+, [115] to investigate the nonlinear effects of the interaction between regular waves and OXYFLUX device on the pumping mechanism. Below, the principal basis on which the software works, basic flow equation and discretization schemes are described in order to give a brief illustration of the whole software.

Governing equation

Basic equations for the present problem are Navier-Stokes equations, which discretized on a 3D mesh are solved by the CFD solver in order to calculate the velocity and the pressure in the flow field. The integral form of the Navier-Stokes include continuity and momentum equation which can be written in integral form as eq. *(17)* and eq. *(18)*, respectively, [116].

$$\frac{\partial}{\partial t} \int_V \rho \cdot dV + \int_A \rho \cdot (\boldsymbol{v} - \boldsymbol{v_g}) \cdot da = 0 \qquad\qquad (17)$$

$$\frac{\partial}{\partial t} \int_V \rho \cdot \boldsymbol{v} \cdot dV + \int_A \rho \cdot \boldsymbol{v} \otimes (\boldsymbol{v} - \boldsymbol{v_g}) \cdot d\boldsymbol{a} = \int_A (\boldsymbol{T} - p\boldsymbol{I}) \cdot d\boldsymbol{a} + \int_V \boldsymbol{f} \cdot dV \qquad (18)$$

Where ρ is the fluid density, V is the cell volume bounded by the closed surface A, **v** is the velocity vector, $\mathbf{v_g}$ is the grid velocity vector, t is the time, **T** is the viscous stress tensor, and **f** is the vector of all body force terms. Viscous stress tensor for turbulent flow is defined as the sum of the laminar and turbulent stress tensors, and under Bussinesq approximation is defined as:

$$T_l = \mu \cdot \left[\nabla \boldsymbol{v} + \nabla \boldsymbol{v}^T - \frac{2}{3} \cdot (\nabla \cdot \boldsymbol{v}) \cdot \boldsymbol{I}\right] \qquad (19)$$

$$T_t = \mu_t \cdot (\nabla \boldsymbol{v} + \nabla \boldsymbol{v}^T) - \frac{2}{3}(\mu_t \nabla \cdot \boldsymbol{v} + \rho \cdot k) \cdot \boldsymbol{I} \qquad (20)$$

$$T = T_l + T_t = \mu_{eff} \cdot \left[\nabla \boldsymbol{v} + \nabla \boldsymbol{v}^T - \frac{2}{3} \cdot (\nabla \cdot \boldsymbol{v}) \cdot \boldsymbol{I}\right] \qquad (21)$$

Where μ is the laminar viscosity, μ_t is the turbulent viscosity, μ_{eff} is the effective viscosity defined as the sum of laminar and turbulent viscosity and k is the turbulent kinetic energy, [115]. In STAR-CCM+ additional transport equations for scalar quantities are solved for μ_t to be derived by means of eddy viscosity model based on Reynolds-Averaged Navier Stokes approach. In this research K-Omega model has been used to evaluate the magnitude of the viscous force on the OXYFLUX structure.

Discretization: Finite Volume Method (FVM)

In this thesis a Finite Volume Method (*FVM*) to discretize the previous equations is used. Such method expects the solution domain, like the numerical wave tank and the structure of the device, to be subdivided into a finite number of discrete volumes called control volumes (CVs). The integral form of Navier Stokes equations is applied to each CV in order to calculate the values of the variables at its center node. Summing all the equations for all the CVs the global conservation equation can be obtained, since surface integrals over inner CV faces cancel. The final result is a set of linear algebraic equations with the total number of unknowns equal to the number of cells in the grid that it is solved by means of the well known segregated, interactive scheme SIMPLE, [117].

Discrete form of momentum equation

Appling eq. *(18)* to a cell-centered control volume for cell-0, one obtains the following discrete equation for the transport of velocity, [93]:

$$\frac{\partial}{\partial t}(\rho \cdot \boldsymbol{v} \cdot V)_0 + \sum_f \left[\boldsymbol{v} \cdot \rho \cdot (\boldsymbol{v} - \boldsymbol{v_g}) \cdot \boldsymbol{a}\right]_f = \sum_f \left[(\boldsymbol{T} - p \cdot \boldsymbol{I}) \cdot \boldsymbol{a}\right]_f \qquad (22)$$

The discrete equation for each velocity component may be expressed implicitly as a linear system of equation. Evaluating the stress tensor **T** requires to calculate the velocity tensor gradient at the face f, $\nabla \mathbf{v}_f$.

$$\boldsymbol{v} \otimes \boldsymbol{\alpha} + \overline{\nabla} \boldsymbol{v}_f - (\overline{\nabla} \boldsymbol{v}_f \cdot \boldsymbol{ds}) \otimes \boldsymbol{\alpha} \qquad (23)$$

$$\text{Where: } \nabla \boldsymbol{v}_f = \boldsymbol{v}_1 - \boldsymbol{v}_0 \,, \overline{\nabla} \boldsymbol{v}_f = \frac{\Delta v_1 - \Delta v_0}{2} \text{ and } \boldsymbol{\alpha} = \frac{\boldsymbol{a}}{\boldsymbol{a} \cdot \boldsymbol{ds}} \qquad (24)$$

$\Delta \mathbf{v}_1$ and $\Delta \mathbf{v}_0$ are the velocity gradient tensors at cells 1 and 0.

Each boundary condition available in STAR-CCM+ has its own method to calculate **T** that also depends on the simulated flow regime, (laminar or turbulent), more information are available in [93].

Discrete form of continuity equation

Discretization of the continuity equation in STAR-CCM+ is done according the following, [93]:

$$\sum_f \dot{m}_f = \sum_f \left(\dot{m}_f^* + \dot{m}_f'\right) = 0 \qquad (25)$$

The uncorrected mass flow rate $(\dot{m}_f^*)$ is computed after the discrete momentum equation have been solved according the following expression:

$$\dot{m}_f^* = \rho_f \cdot \left[\boldsymbol{a} \cdot \left(\frac{v_0^* + v_1^*}{2}\right) - G_f\right] - \Upsilon_f \qquad (26)$$

$\boldsymbol{v}_0^*$ and $\boldsymbol{v}_1^*$ are the cell velocities after the discrete momentum equation has been solved.

G_f is the grid flux and Y_f is the Rhie-and-Chow-type dissipation at the face; the fully developed equation of the grid flux and Rhie-and-Chow-type dissipation can be found in [93],[116], [118]. Mass flow correction term $(\dot{m}_f')$ is calculated by means of the following equation, [93]:

$$\dot{m}_f' = Q_f \cdot (p_0' - p_1') + \frac{\dot{m}_f^*}{\rho_f} \cdot \left(\frac{\partial p}{\partial \rho}\right)_T \cdot p_{upwind}' \tag{27}$$

where p_0' and p_1' are the pressure cell corrections and p_{upwind}' is given by:

$$p_{upwind}' = \begin{cases} p_0' \ if \ \dot{m}_f^* > 0 \\ p_1' \ if \ \dot{m}_f^* < 0 \end{cases} \tag{28}$$

then, the discrete pressure correction is obtained from eq. *(25)* and eq. *(28)* in coefficients form as below:

$$a_p p_p' + \sum_n a_n p_n' = r \tag{29}$$

Where r is the residual equal to the net mass flow into the cell

$$r = -\sum_f \dot{m}_f^* \tag{30}$$

For the boundary faces two different conditions can be identified.

The first one is relative to boundary faces with specified velocity, such as wall, symmetry and inlet boundary, in which the value of face mass flow predictor $(\dot{m}_f^*)$ is directly calculated from the imposed velocity. In such case the Neumann condition is used for the pressure correction and the mass flux corrections are zero.

The second one is relative to the boundary with specified pressure, such as stagnation inlet and pressure outlet, in which the pressure corrections are not zero.

SIMPLE Solver Algorithm

In STAR-CCM+ SIMPLE algorithm is used to control the overall solution. Simple method is an iterative solver that couples continuity and momentum equations. The summarization of such algorithm can be outlined as follow, [93]:

1. Set the boundary conditions;
2. Compute the reconstruction gradients of velocity and pressure;
3. Compute the velocity and pressure gradients;
4. Solve the discretized momentum equation. This creates the intermediate velocity field, $\mathbf{v}^*$;
5. Compute the uncorrected mass fluxes at faces, $\dot{m}_f^*$;
6. Solve the pressure correction equation. This produces a value of the pressure correction, p' for each cell;
7. Update the pressure field:

$$p^{n+1} = p^n + \omega_p \cdot p',$$

   where ω_p is the under-relaxation factor for pressure;
8. Update the boundary pressure corrections, p_b';
9. Correct the face mass fluxes:

$$\dot{m}_f^{n+1} = \dot{m}_f^* + \dot{m}_f';$$

10. Correct the velocity cells:

$$\boldsymbol{v}^{n+1} = \boldsymbol{v}^* - \frac{V \cdot \nabla p'}{a_p^V};$$

   where $\nabla p'$ is the gradient of the pressure corrections, $\boldsymbol{a}_p^V$ is the vector of central coefficients for the discretized linear system representing the velocity equation and V is the volume cell;
11. Update density due to pressure changes;
12. Free all temporary storage.

The application of the previously described finite volume discretization schemes to Navier Stokes equations will result in the coefficients of the linear equation system that needs to be solved implicitly.

Multigrid Methods

Algebraic multigrid methods solve iteratively the discrete linear system originated from the discretization method described above.

$$A \cdot x = b \qquad\qquad (31)$$

where $\mathbf{A}$ is the coefficients matrix, $\mathbf{x}$ is the unknowns vector (i.e. true solution of system) and $\mathbf{b}$ represents the residuals vector for each cell. Typically $\mathbf{A}$ matrix is sparse. Direct methods such as Gauss elimination or LU decomposition on such systems are costly, since the triangular factors of the sparse matrices are not sparse. It is therefore preferable to use an iterative method, such as the one used in the present research by means of STAR-CCM+.

The general principle behind iterative methods is that, given an approximate solution of the system $\mathbf{x}^k$, a better approximation $\mathbf{x}^{k+1}$ is sought. The process is repeated until the solution is found. If the system in eq. *(31)* is solved through the iterative method we can obtain an intermediate solution $\mathbf{y}$ after a non specified number of iterations that does not satisfy eq. *(31)*.

$$A \cdot y = b - r \qquad\qquad (32)$$

An error vector can be introduced as the difference between the true solution and the intermediate one, so that, subtracting eq. *(32)* from the initial system eq. *(31)* it gives the relationship between the residual vector and the error vector, eq. *(35)*, [116].

$$e = x - y \qquad\qquad\qquad (33)$$

$$A \cdot e = r \qquad\qquad\qquad (34)$$

The residual vector can be calculated using the iteration process by substituting solution in eq. (32), [116]; then the system in its iterative form can be written as:

$$e^k = T \cdot e^{k-1} + c \qquad\qquad\qquad (35)$$

where matrix **T** depends on chosen iteration method, i.e. the Jacobi method or Gauss-Seidel method with or without relaxation, [119].

It has been established that the solution error has components within the range of wave lengths that are multiples of the mesh size. Iteration methods cause rapid reduction of error components from short wave lengths up to a few multiples of the mesh size. Coarser mesh presents its longest possible wavelengths of error relative to the short wave length range of mesh and hence all error components reduce rapidly. On the finer meshes, the longest error wave lengths cannot be eliminated as they fall outside the short-wave length range for which decay is rapid, [119]. Multigrid methods are designed to exploit these inherent differences of the error behavior and use iteration on meshes of different size through the following steps:

1. Agglomerate cells to form coarse grid levels;
2. Transfer the residual from a fine level to a coarser level, (known as restriction);
3. Transfer the correction from a coarse level back to a finer, (known as prolongation);

Multigrid algorithms can be divided into two types: geometric and algebraic.

Geometric multigrid uses the grid geometry and the discrete equation at the coarse level to obtain the linear system that has to be solved on that level. Algebraic multigrid derives a coarse level system without any reference to the underlying grid geometry or discrete

equations. The coarse-grid equations are derived from arithmetic combinations of the fine-grid coefficients. Since it is not always straightforward to obtain suitable discrete equations on coarse levels, algebraic multigrid (AMG) is at an advantage. Therefore, it is used for the solution of all linear systems in the present investigation. AMG solver in STAR-CCM+ has two cycling strategies: fixed and flexible. For systems that are not very stiff, it is more economical to use flexible cycles. Instead of following a regular pattern, multigrid cycles are applied on the basis of the reduction that is witnessed in residuals. This means that in flexible strategy residuals are constantly monitored and if the residuals exceed a given threshold, the solution will continue on a coarser level. On the other hand, if residuals on a given level are lower than a specific tolerance, the solution moves to a finer level.

Multiphase Methods

Multiphase flow is a term that refers to the flow and to the interaction of several phases within the same system where distinct interfaces exist between the phases. Multiphase flows can be classified into two categories:

- Dispersed flows, such as bubbly, droplet, and particle flows;
- Stratified flows, such as free surface flows, or annular film flow in pipes.

STAR-CCM+ provides five distinct models to meet the requirements of these two categories of flow: Lagrangian Multiphase, Multiphase Segregated Flow, Volume of Fluid (VOF), Discrete Element Model (DEM) and Fluid Film. For the purpose of the present thesis a VOF method is used. The Volume of Fluid (VOF) model is suitable for systems containing two or more immiscible fluid phases, where each phase constitutes a large structure within the system (such as typical free surface flows). This approach captures the movement of the interface between the fluid phases, [93].

VOF Multiphase Model

Volume Of Fluid method is a tool capable to simulate the flow of several immiscible fluids on numerical grids and to resolve the interface between the phases of the mixture. The main advantage of such method is that it does not need to model inter-face interaction, then it is computationally very advantageous. This model is based on the assumption that all phases share velocity and pressure. Thanks to its numerical efficiency, the model is suited for simulations of flows where each phase constitutes a large structure, with a relatively small total contact area between phases. The spatial distribution of each phase at a given time is defined in terms of a variable that is called the volume fraction, α. A method to calculate such distributions is to solve a transport equation for the phase volume fraction. The method uses the STAR-CCM+ Segregated Flow model. The description ot the VOF model assumes that all immiscible fluid phases present in a control volume share velocity, pressure, and temperature fields. Therefore, the same set of basic governing equations describing momentum, mass, and energy transport in a single-phase flow is solved. The equations are solved for an equivalent fluid whose physical properties are calculated as functions of the physical properties of its constituent phases and their volume fractions,[93].

$$\rho = \sum_i \rho_i \cdot \alpha_i \qquad (36)$$

where α_i is defined as $\alpha_i = \frac{V_i}{V}$ and ρ_i and V_i are the density and the volume of the ith phase for each cell. For the case of a two fluid mixture such as air and water mixture, which is what this thesis is dealing with, it will have,[116]:

$$\rho = \rho_1 \cdot \alpha_1 + \rho_2 \cdot \alpha_2 = \rho_1 \cdot \alpha_1 + \rho_2 \cdot (1 - \alpha_1) \qquad (37)$$

The conservation equation that describes the transport of volume fractions is:

$$\frac{d}{dt}\left(\int_V \alpha_i \cdot dV\right) + \int_A \alpha_i \cdot (v - v_g) \cdot da = 0 \qquad (38)$$

The discretization of the transport equation, eq. *(38)*, needs special attentions because values of α_i are bounded between 0 and 1, then the regions with partially filled cells should be as small as possible, [120]. Discretization of the convective term in eq. *(38)* is critical. First-order upwind scheme smears the interface too much and introduces artificial mixing of two fluids, then for the simulation here proposed a second order discretization in time has been used.

Three main factors should be taken into account in the discretization process. The first is the permitted value of α_i, that has to be ensured so that the scheme does not generate overshoots or undershoots. Secondly it must be ensured that the convective flux out of one CV does not transport more fluid than what is available in the donor cell and finally it must be taken into account the interface orientation and local Courant number, [120]. For the simulation conducted in this study local Courant number at the surface was monitored during the simulation and kept smaller than the unit, Figure 91.
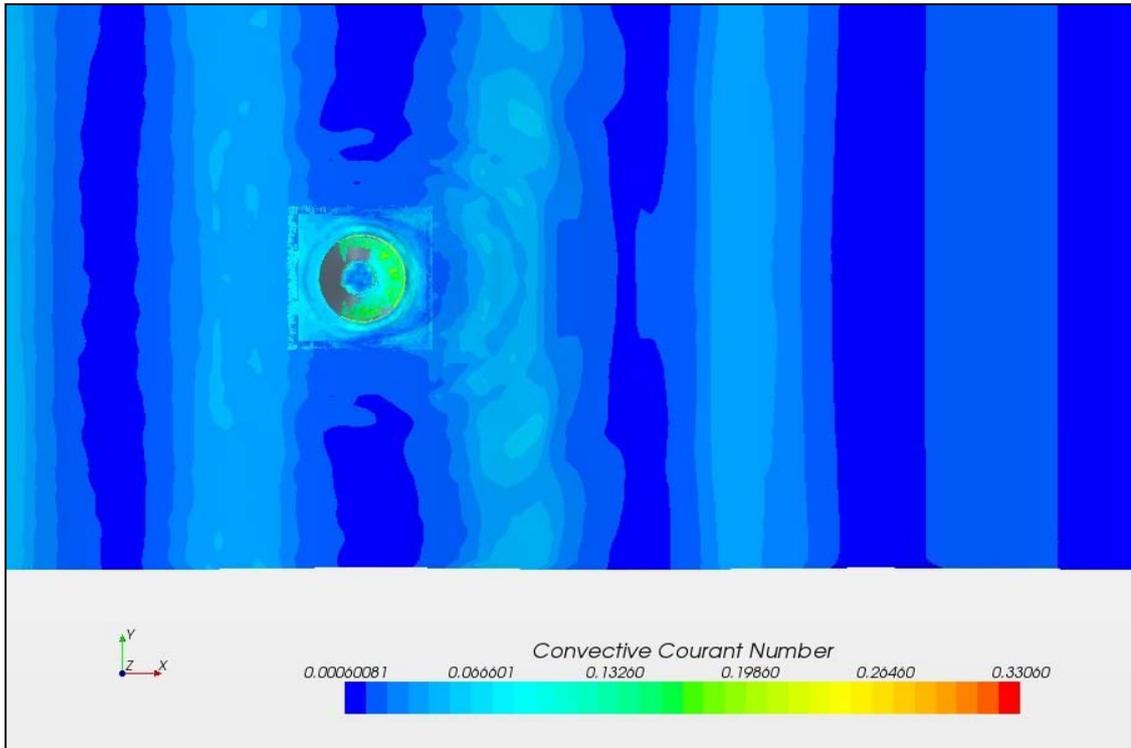
Figure 91: Monitoring of local Courant Number at the surface.

STAR-CCM+ presents two schemes to capture the free surface, the normalized variable diagram proposed by Leonard, [121], and High-Resolution Interface Capturing. Both methods are used according to the Courant number at the interface, more detail are available at [93].

Turbulence model

In STAR-CCM+ additional transport equation for scalar quantities are solved so that μ_t is derived by means of eddy viscosity model based on Reynolds-Averaged Navier Stokes approach. In this research K-Omega model has been used to provide closure of the governing equation. Three basic approaches are available in STAR-CCM+, models that provide closure of the governing equation. They are Reynolds-Averaged Navier-Stokes

(RANS) equations, Large eddy simulation (LES) and Detached eddy simulation (DES). The LES and DES approaches are commonly used to simulate flow in which the resolution of small time and length scales are justified. Such approaches are computationally more expensive than RANS approach. This study is based on the RANS approach, using a two equation closure model to evaluate the magnitude of the viscous force acting on the OXYFLUX structure. STAR-CCM+ offers two different approaches to model the Reynolds stress tensor in terms of mean flow quantities, and hence provides closure of the governing equations. These methods are Eddy viscosity model, which involves K-Epsilon, K-Omega and Spalart-Allmaras models, and Reynolds stress transport model. Eddy viscosity models use the concept of a turbulent viscosity to model the Reynolds stress tensor as a function of mean flow quantities. The K-Omega model is a two-equation model. The transport equations that are solved are for the turbulent kinetic energy k and a quantity, ω defined as the specific dissipation rate, that is, the dissipation rate per unit turbulent kinetic energy, [93], [122]. One advantage of the K-Omega model is its improved performance for boundary layers under adverse pressure gradients. Second significant advantage is that it may be applied throughout the boundary layer, including the viscous region, without further modification. Furthermore, the standard K-Omega model can be used in this mode without requiring the computation of wall distance. The biggest disadvantage of the K-Omega model, in its original form, is that boundary layer computations are sensitive to the values of ω in the free stream. This translates into extreme sensitivity to inlet boundary conditions for internal flows. Such problem has been addressed by Menter [123], who recognized that the transport equation from the standard K-Epsilon model could be transformed into an ω transport equation by means of variable substitution. The transformed equation looks similar to the one in the standard K-Omega model, but adds an additional non-conservative cross-diffusion term containing the dot product. Inclusion of this term in the transport equation potentially makes the K-Omega model give identical results to the K-Epsilon model. Menter suggested using a blending function that would include the cross-diffusion term far from walls, but not near the wall. This approach effectively blends a K-Epsilon model in the

far-field with a K-Omega model near the wall. Menter also introduced a modification to the linear constitutive equation and dubbed the model containing this modification the SST (*shear-stress transport*) K-Omega model, [123]. The SST model has seen applications in the marine and ocean application, where viscous flows need to be resolved and turbulence models need to be applied throughout the boundary layer,[124], [120], [125]. For the above reason it can be argued that the most suitable turbulence model for this investigation is the SST K-Omega model.

Response calculation

The dynamic behavior of the OXYFLUX during the simulation is described by the equation of motion:

$$m \cdot \boldsymbol{a} = \boldsymbol{F} \tag{39}$$

$$\boldsymbol{I}_g \cdot \boldsymbol{a}_\Omega = \boldsymbol{M} \tag{40}$$

where m is the mass of the total body, $\boldsymbol{a}$ is the acceleration vector for the translation, $\boldsymbol{\Omega}$ is the angular velocity and $\boldsymbol{a}_\Omega$ is the angular acceleration, $\boldsymbol{I}_g$ is the inertial tensor, $\mathbf{M}$ and $\mathbf{F}$ are the total moment and force acting on the body. The resultant forces and moments acting on the rigid body are obtained from the fluid pressure and shear forces acting on each boundary face of the body.

The similarity of the device here investigated with a point absorber wave energy converter described in [124], [126], can lead to compare the overtopping discharge to the produced energy. Furthermore, also the dynamic motion of the OXYFLUX and its shape can be compared with those of a point absorber wave energy converter. In these two works, [124], [126] the effect of the mooring system on the power extraction performance is neglected, so, also in this study it is not considered. Considering also the pitch mode guarantees a more realistic modelling, since the overtopping mouth change its capacity to capture water with its orientation.

124

Modelling of the wave driven device with STAR-CCM+

The numerical study here proposed was conducted using two different mesh techniques approaches:

- *fixed mesh*, the entire mesh moves itself according with the motion of the rigid body;
- *overset mesh or "chimera" mesh*, the discretized computational domain is divided in several different meshes that overlap each other in an arbitrary manner. For this modeling two meshes have been used; a smaller and finer mesh is used to follow the rigid body motion and describe the hydrodynamic around the body while a second larger and coarser mesh is used to discretize the background fluid domain.

Both methods will be described below, pointing the focus on the problems occurred with the fixed mesh and explaining in detail the advantages and the results coming from the overset modelling, that has been chosen to be the final technique to describe the functioning of the OXYFLUX.

In the RANS simulations, the whole structural design has been considered, taking into account also the support for the DOP transducer and the transducer used in the physical modelling and the supporting jacket used to connect the tube to the reaction ring in the model scale 1:16.
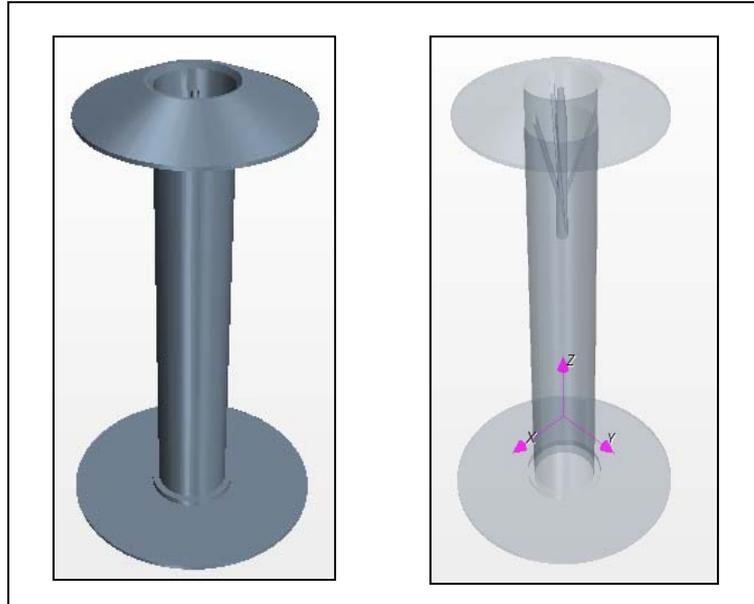
Figure 92: Geometry input used for the simulations and location of the center of gravity.

All the simulations were completed considering a real scale geometry, so the device presents a length equal to 5.30 m (from top of the floater to the bottom of the ring). Width and thickness of the floater are equal to 2.40 and 0.48 m respectively, while the reaction ring has a width and a thickness equal to 2.88 and 0.048 m. The mass of the full scale model is 1323.00 kg, its center of gravity is located 4.27 m below the mean free surface and inertial moments with respect to it are equal to 20226.00 $m^2 \cdot kg$ for axis x and y and 980.00 $m^2 \cdot kg$ for axis z.

Parameters of the solver

In this paragraph the parameters of the solver used during the simulation will be described. Such configuration will be the same for both the used meshes.

STAR-CCM+ was configured to model the dynamic motion and the overtopping phenomena occurring on the OXYFLUX's floater. The building the CFD model involves selecting mesh resolution, simulation algorithm, boundary condition including air-water interface properties, turbulent model and some tools able to catch particular phenomena

126

which in the physical model are hardly measurable. In this work a tool like a non physical interface was added to the OXYFLUX model in order to measure the mass flow over it and then measure the overtopping flow. In addition to testing the ability of the numerical model to replicate the experimental data, the CFD simulation had the secondary objective of determining the best model setup to achieve most accurate simulation results. In this context several 3D models with different mesh sizes and time steps are tested. Simulations are completed as isothermal. STAR-CCM+'s multiphase segregated flow model is used to separate governing equations for both water and air. The Segregated Flow solver controls the solution update for the Segregated Flow model according to the SIMPLE algorithm, [127]. It controls two additional solvers: velocity solver and pressure solver. The velocity solver controls the under-relaxation factor and algebraic multigrid parameters for the momentum equations. More specifically, it solves the discretized momentum equation to obtain the intermediate velocity field. The pressure solver controls the under-relaxation factor and algebraic multigrid parameters for the pressure correction equation. More specifically, it solves the discrete equation for pressure correction, and updates the pressure field, [93]. Water is modeled as an incompressible fluid with a density equal to 997.561 kg/m^3 (*STAR-CCM+ default value*) while air is modelled as an incompressible ideal gas with a density equal to 1.18415 kg/m^3 (*STAR-CCM+ default value*). The volume of Fluid (VOF) model in STAR-CCM+ is used to model air and water free surface interactions. The VOF model is used to setup the multiphase domain. The domain is initialized into water and air section with the free surface set in order to have the same freeboard crest measured in the experiments. STAR-CCM+ currently allows to define five types of waves: flat, first order, fifth order, superposition of first order waves, and irregular waves. This model automatically sets up functions to be used as boundary conditions that will update while the wave moves. For VOF solver the second order discretization scheme is used to discretize the convection equation described above. For temporal discretization solver the second order implicit scheme is used. The number of internal iteration for these simulations is chosen to be

equal to 10, in order to reach the convergence for each time step before going to next time step.

Table 8: Solver configuration for all simulations.

Solver	Parameter	Value/Scheme	Cycle type
Implicit Unsteady	Temporal discretization	2nd order	"
Segregated Flow	Under Relaxation Factor velocity	0.8	Flex cycle
	Under Relaxation Factor pressure	0.2	F cycle
Segregated VOF	Under Relaxation Factor	0.9	V cycle
K-Omega	Under Relaxation Factor turbulence	0.8	Flex cycle
	Under Relaxation Factor turbulent viscosity	1.0	"

All the simulations are conducted by means of the available facilities of the Hydraulic Laboratory of the University of Bologna. The machine consists of a dual socket/six-core 2.00 GHz Intel processor, with 64 GB of memory shared by all twelve cores. Even with such facilities, the high computational intensity of CFD modeling demands an efficient model setup to ensure manageable run time. For the final mesh with 0.8 million elements, it took about 7 days on 12 cores to complete 10 wave periods of time.

Solution convergence

Numerical analysis here presented uses an iterative process to compute the solution. For each iteration, values of the residual are given; they indicate how well the governing equations, for each solver quantity, are being satisfied numerically. Such quantity can be used as a mean to estimate how the solution converges. Products from residuals are not necessarily interesting engineering variables such as force or pressure. A convergence can be considered good when all residuals are steady and/or drop by some order of magnitude. However, if initial conditions match perfectly for solution, residuals may drop only slightly, and stay leveled throughout the simulation, [128].
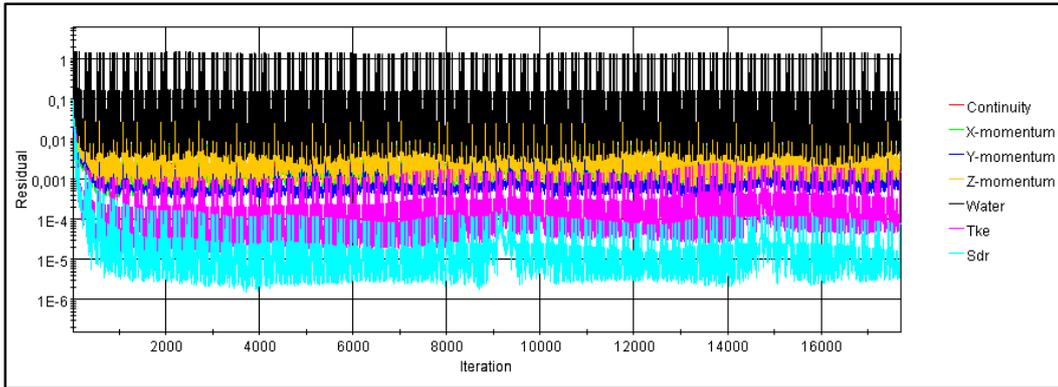
Figure 93: Residual for all solver quantities .

The convergence of the coupling between the RANS simulation and the dynamics of the body was reached at each time step.

Fixed mesh technique

The simplest type of mesh motion strategy is to displace the fluid mesh as if it was a rigid body. This is the simplest type of mesh motion strategy available in STAR-CCM+. In this case all the cells maintain their shape and the description of the mesh motion is from a displacement vector and Euler angles. In Dynamic Fluid Body Interaction (*DFBI*), the position of the grid is determined by solving the equations of the assumed rigid structure, and the fluid transport equations automatically account for motion of the grid.

Domain and boundary conditions

The set of simulations here described was conducted taking advantage from the symmetry section placed along the *x-z* plane, then the following dimensions will refer to half the domain as shown in Figure 94. Computational domain was 112.00 m long (-75.00 $\leq x \leq$ 37.00), 15.00 m wide (-15.00 $\leq y \leq$ 0.00) and 57.00 m high (-32.00 $\leq z \leq$ 25.00). Selected length of the domain should guarantee the required distance in order to have unperturbed wave field at the pressure outlet boundary. The seabed was given at

32.00 m below mean water surface, and a 1st order wave velocity profile was specified at the up-wave, lateral, top and bottom boundary. The pressure outlet was implemented at the down wave boundary, and a symmetry boundary was placed along the x–z plane to reduce the size of the problem, Figure 96. An additional artificial interface is generated at the top of the floater in order to measure flow and velocity of overtopping water, Figure 95.
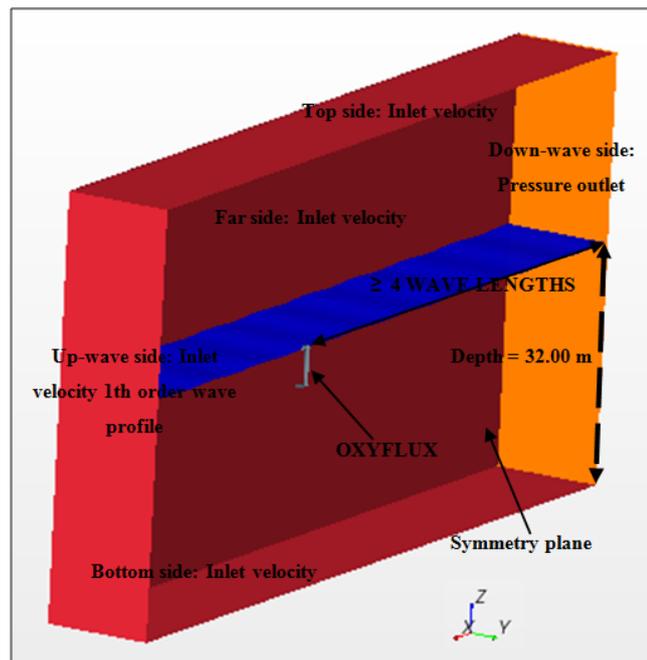
Figure 94: Domain and boundary conditions.
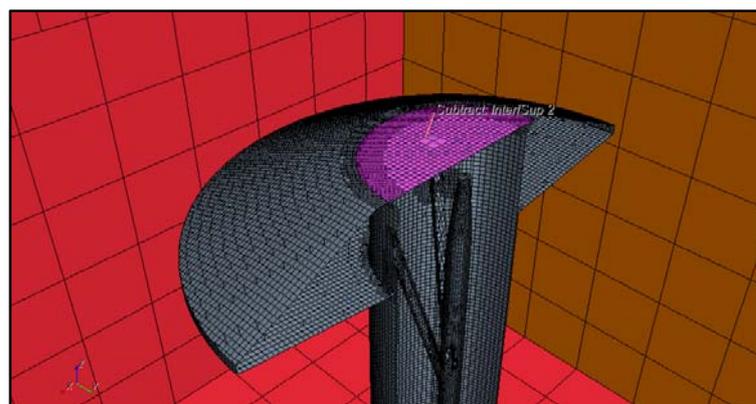
Figure 95: Generated interface at the top of the floater.
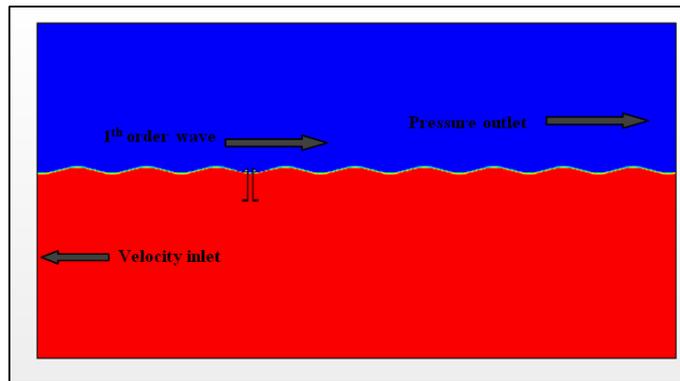
Figure 96: Section view of the domain.

Four boundary conditions have been used to describe the fluid field at the bounds of the domain. They involve wall, velocity inlet, pressure outlet and symmetry plane condition. Wall boundary condition represents an impenetrable, no-slip condition for viscous flow simulation. For no-slip walls, tangential velocity is explicitly set either to zero (for the case of no wall motion) or to a specified value while pressure at the boundary is extrapolated from the adjacent cell using reconstruction gradients. A velocity inlet boundary represents the inlet of the domain at which the flow velocity is known; in this investigation it represents the wave maker of the numerical wave flume, where the inlet face velocity vector is specified directly according to the required wave profile. The boundary face pressure is extrapolated from the adjacent cell using reconstruction gradients. A pressure outlet boundary is a flow outlet boundary at which pressure is specified. The boundary face velocity is extrapolated from the interior using reconstruction gradients, while boundary pressure can have two different calculation methods. If inflow occurs, pressure is defined by the follow equation:

$$p = p_{specified} - \frac{1}{2} \cdot \rho \cdot |v_n|^2 \qquad\qquad (41)$$

else boundary pressure is kept equal to the specified one. A symmetry plane boundary represents an imaginary plane of symmetry in the simulation. The solution that is obtained with a symmetry plane boundary is identical to the solution that would be obtained by mirroring the mesh around the symmetry plane. The shear stress at a symmetry boundary is zero. The face value of velocity is computed by extrapolating the parallel component of velocity in the adjacent cell using reconstruction gradients. The boundary face pressure is extrapolated from the adjacent cell using reconstruction gradients. All boundary conditions mentioned above involve some specified values, constant or variable during the simulation; these values are given to the model by means of field function. Such functions are automatically developed during the selection of the physical model.

Mesh and time step selection

The volume mesh in CFD simulation is the mathematical description of the space (or geometry) of the problem being solved, [93]. Selecting a suitable type and size of the mesh can largely affect computational requirements, accuracy and convergence rate of the solution.
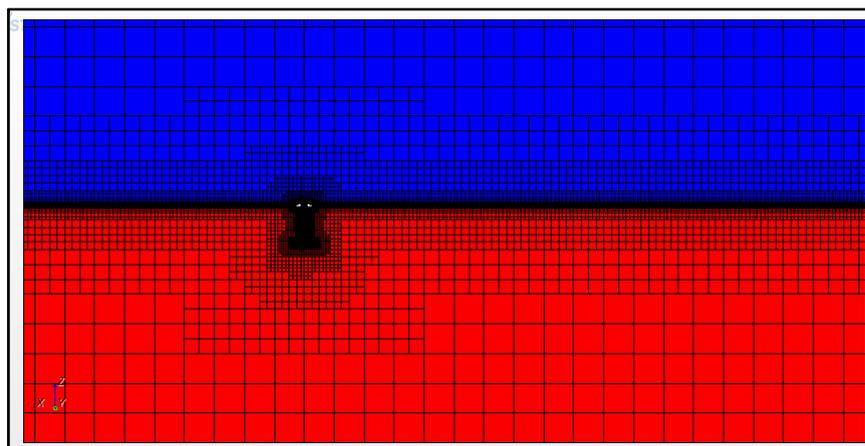
Figure 97: Section view of the volumetric mesh.

The meshes were created using the STAR-CCM+ grid generation utility. Figure 97 shows the grid resolution around the OXYFLUX model. The grid resolution was finer near the free surface and around the OXYFLUX to capture both the wave dynamics and the details of the flow around the device. In addition, prism-layer cells were placed along the OXYFLUX surface, Figure 99. Such layer of cells near the body surface is responsible of generating the grid that is used to solve the closure problem. Relatively coarse mesh was used near boundaries; the lower part of the boundary layer, namely the viscous sub-layer and part of the buffer, is not resolved. The centre point (P) of the wall-adjacent cell is placed inside the buffer or logarithmic layer and the flow parameters are modelled by blended wall functions[2], [93], [129]. Typically, during simulations, y^{+}[3] values of the wall-adjacent cell between 5 and 300 are recognized so that P is located in the buffer or logarithmic region. A all-y^{+} wall treatment is used in order to not impose a more sever wall treatment, like high-y^{+} wall treatment and then solve both buffer and logarithmic layer. The all y^{+} wall treatment is an hybrid model. It provides a more realistic modeling than either the low-Re or the high-Re treatments, when the wall-cell centroid falls in the buffer region. This treatment uses damping functions for the source terms in the transport equation, but the source terms of the model in the wall cell are modified using the blended wall laws.

---

[2] Wall function is the set of mathematical relations that are used to obtain the boundary conditions for the continuum equations. It is assumed that the turbulence model is valid only outside the viscous region of the boundary layer, and the viscous-affected region of the boundary layer is not resolved, it is assumed also that the centroid of the near-wall cell lies within the buffer or logarithmic region of the boundary layer. The blended wall laws are intended to represent the buffer layer by appropriately blending the viscous sub-layer and logarithmic regions, [94], [142].

[3] y^{+} is a non-dimensional number, determining whether the influences in wall-adjacent cells are laminar or turbulent, hence indicating the part of the turbulent boundary layer that it resolves. It is defined as, $y^{+} = \frac{u_{*} \cdot y}{\nu}$ where u_{*} is the friction velocity at the wall-adjacent cell, y is the distance at the wall-adjacent cell and ν is the kinematic viscosity. Generally it can be argued that, [150]:

$y^{+} \leq 5$ wall-adjacent cell is in the viscous sub-layer ;
$5 < y^{+} \leq 30$ wall-adjacent cell is in the buffer region;
$y^{+} \geq 30$ wall-adjacent cell is in the logarithmic region.
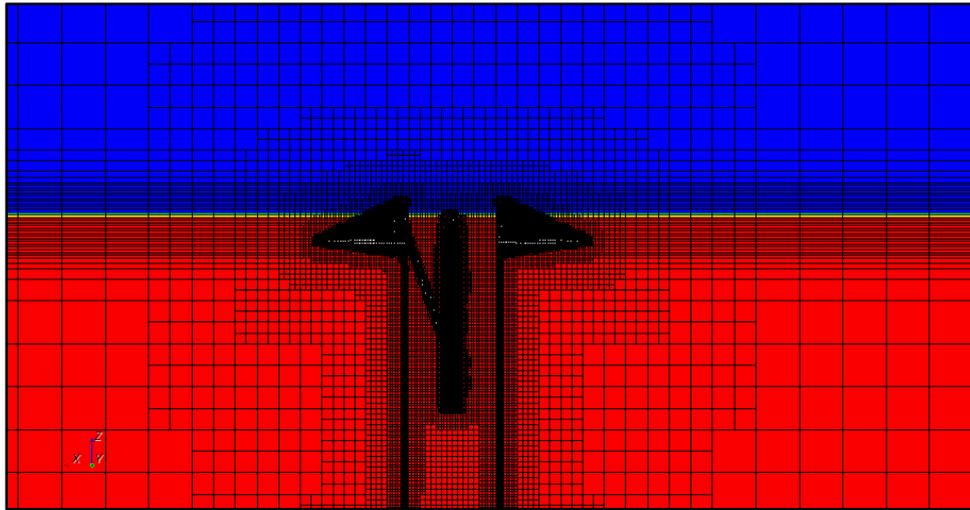
Figure 98: Section view of the volumetric mesh, thinner mesh layer between the free surface.
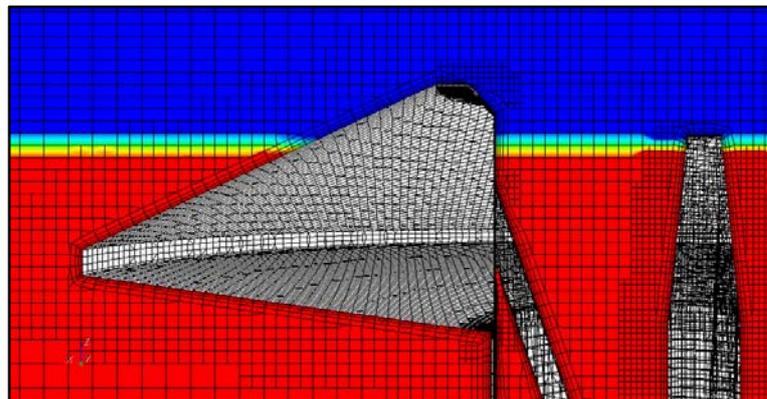
Figure 99: Section view of the volumetric mesh, boundary layer.

In the mesh generation the grid size Δx (in the wave propagation direction) was determined by the incident wavelength λ, and the grid size Δz (in the vertical direction) near the free surface was adjusted according to the wave height, H.

Grid resolution near the free surface was chosen with dimensions of Δx=λ/30 and Δz= H/10. Yi-Hsiang [124] proposed Δx≤ λ/80 and Δz≤ λ/20 but, since this mesh technique presents some problems due to wave reflection by the pressure outlet boundary, the effects of the grid dimension and the sensitivity to the grid parameters were not investigated differently from what it will be done for the following mesh technique

presented in thesis. Then, values of Δx= λ/30 and Δz= H/10 were considered acceptable to obtain preliminary results. The total number of cells used in this class of simulation to discretize the domain ranges around 977825. To keep Courant number small in oreder to preserve numerical stability, a small time step of T/315 was utilized in the study, where T was the incident wave period.

Results

The series of numerical simulations that will be described in this section are related to the preliminary investigation, since this technique is largely affected by the reflection generated at the pressure outlet. This reflection is mainly due to a couple of factor: the first, is that the wave field is perturbed by the device motion also at distance equal to four wave lengths. The second, and more relevant, is that free surface interface at the outlet and inlet boundary is solved by unsuitable grid part, since the whole mesh follows the rotation of the body. Also for small values of pitch angle the simulation showed important effects due to reflection. In Figure 100 it is clear how the pitch motion can affect resolution at the domain's boundaries. The more the outlet and inlet boundaries are far from the device, the more the rotation of the mesh brings to numerical diffusion at the boundary extreme due to the unsuitable grid size used.
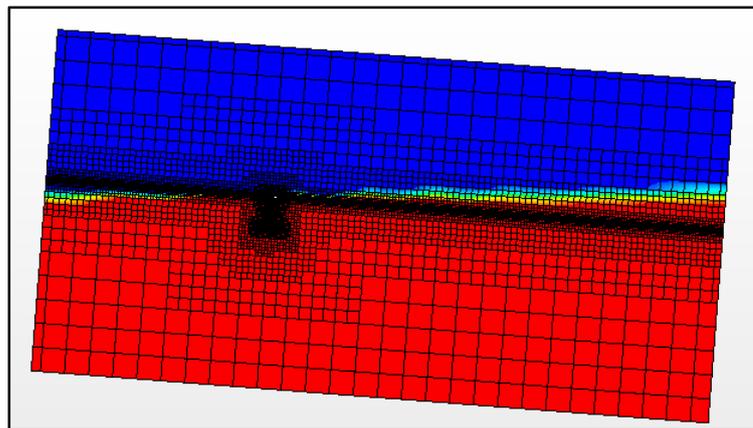
Figure 100:Problem due to the mesh rotation.

For the above mentioned reasons results coming from these simulations are not validated versus the physical experiments, and are only presented as a preliminary research. Four regular wave states are tested, their characteristics are shown in Table 9. For each simulation heave response, incident wave and water flow inside the tube are measured. Heave and incident wave signals are analyzed through zero up-crossing procedure, then their medium values are calculated. Furthermore spectral analysis of the signal is done in order to identify reflection from the boundary and its related frequency. Medium value of water discharge is calculated by means of integral mean value of the flow signal over five wave periods. In the following plots, results are shown.
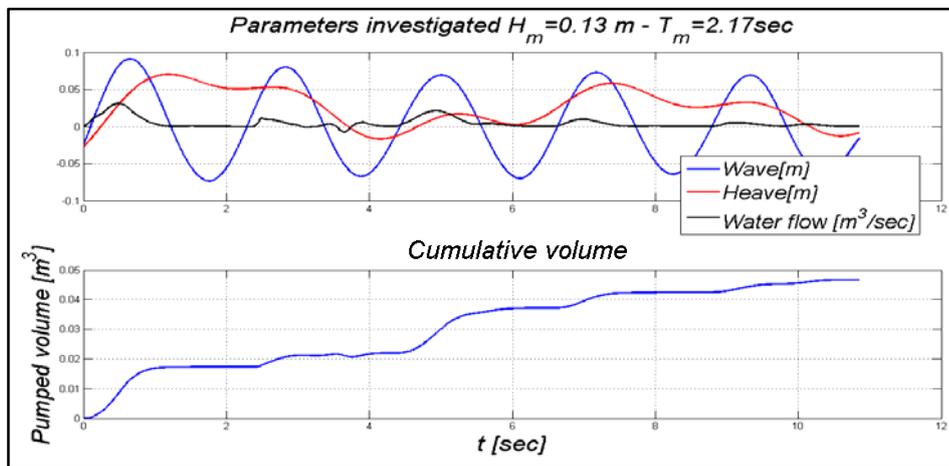
Figure 101: Wave, Heave, Water flow and cumulative pumped volumes for O_1.
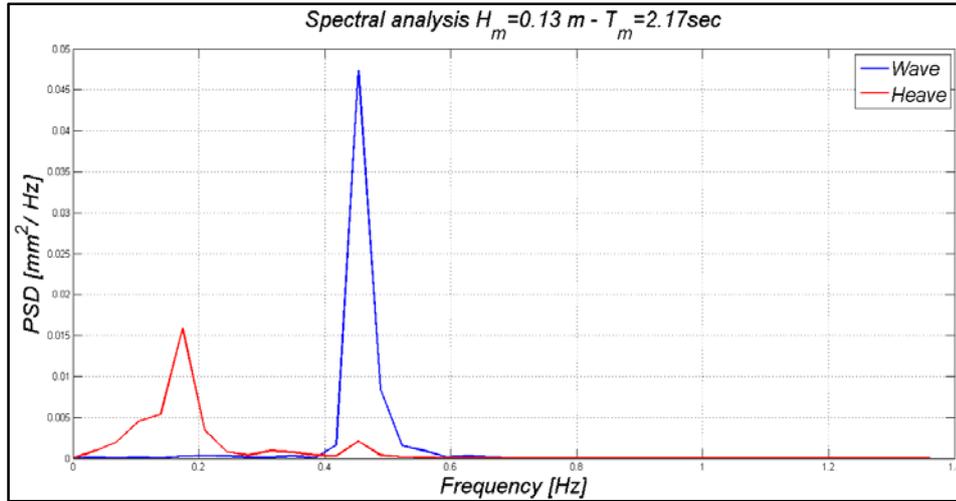
Figure 102: Spectral analysis for O_1.
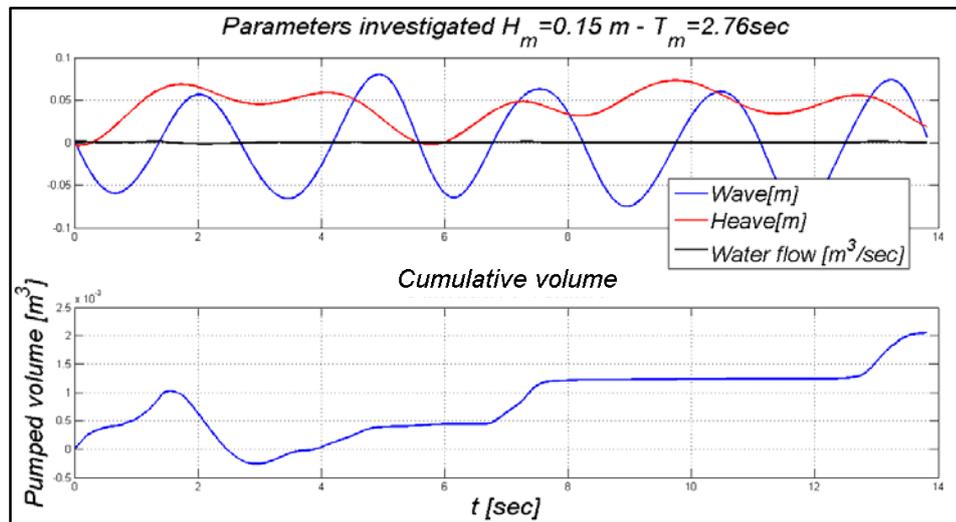
Figure 103: Wave, Heave, Water flow and cumulative pumped volumes for O_2.
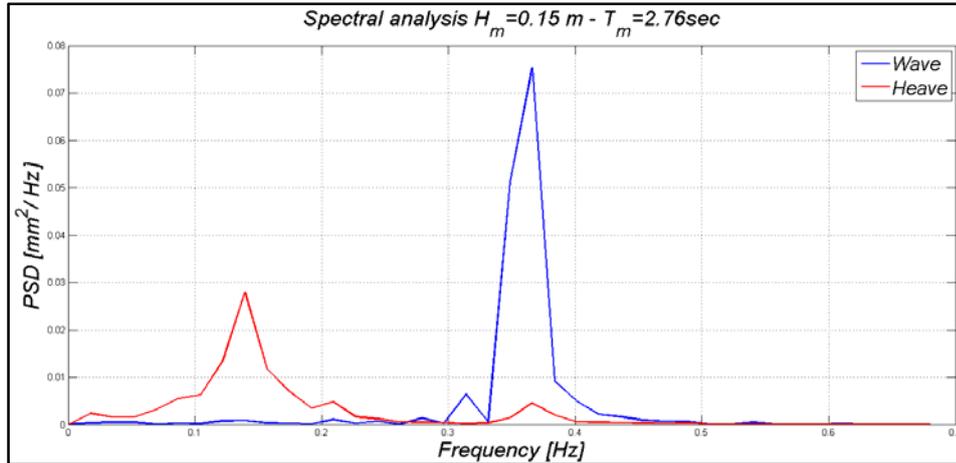
Figure 104: Spectral analysis for O_2.
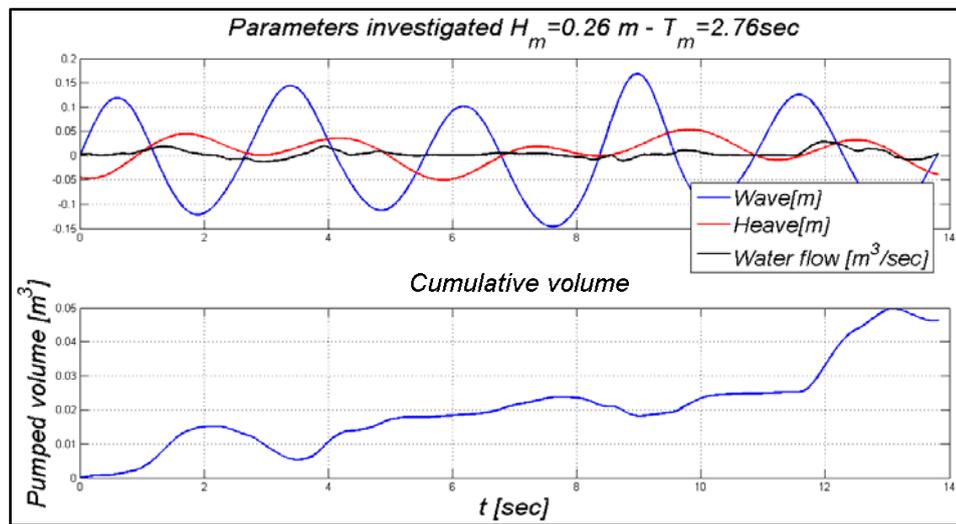
Figure 105: Wave, Heave, Water flow and cumulative pumped volumes for O_3.
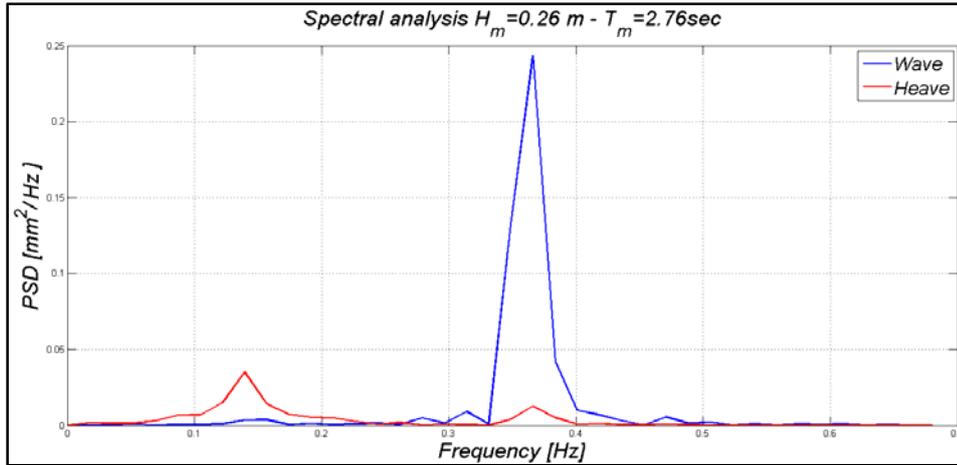
Figure 106: Spectral analysis for O_3.
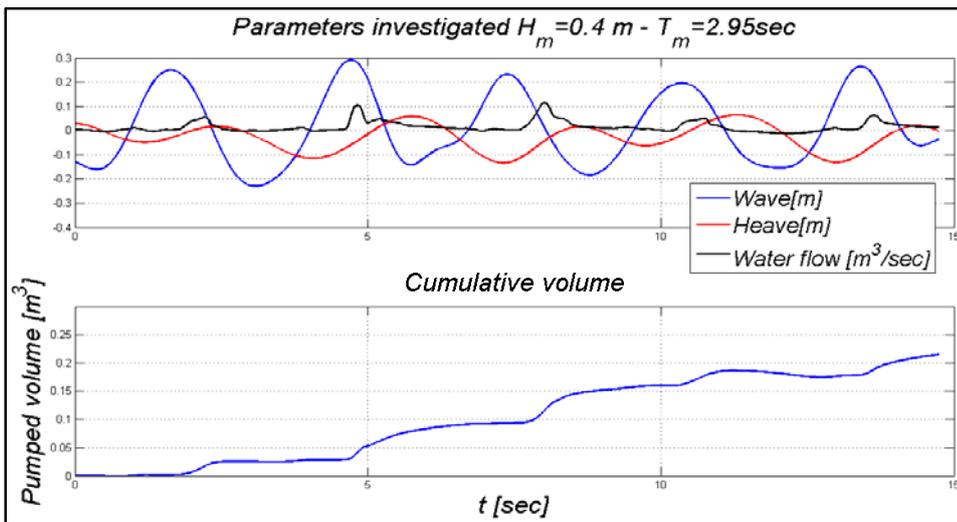
Figure 107: Wave, Heave, Water flow and cumulative pumped volumes for O_4.
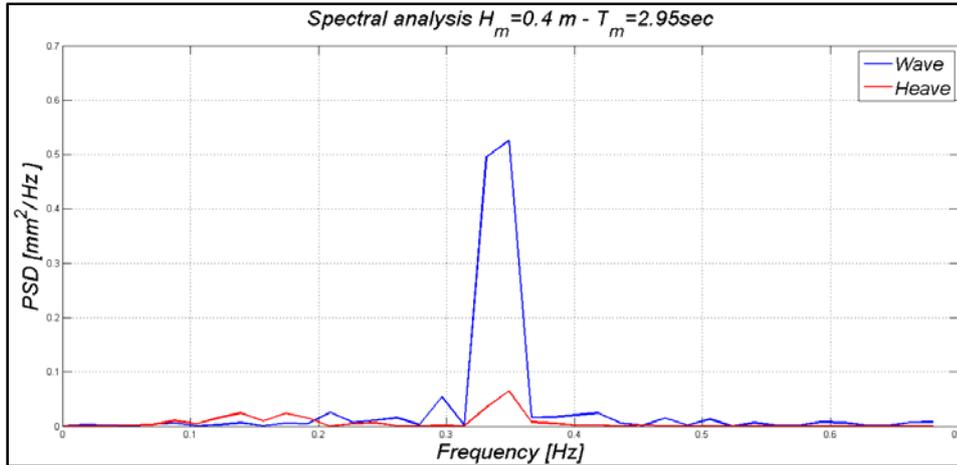
Figure 108: Spectral analysis for O_4.

Table 9: Regular wave states simulated.

Wave	Depth [m]	Hm [m]	Tm [sec]	Qm [l/sec]
O_1	7.00	0.13	2.21	4.2467
O_2	7.00	0.15	2.73	0.149
O_3	7.00	0.26	2.73	3.3972
O_4	7.00	0.40	2.87	14.5705

Spectral analysis presented in Figure 102, Figure 104, Figure 106 and Figure 108 clearly show problems due to reflection, since a low frequency appears. Such phenomena clearly vitiate the results related to the displacement. However, the order of magnitude of the mean discharge flow can be considered right, demonstrating STAR-CCM+ can be the suitable tool to describe OXYFLUX's operation under an appropriate configuration.

Overset mesh technique

This section describes method and results relative to the final numerical modelling of the OXUFLUX. To do this, an overset mesh is used to discretize the computational domain

whit two different meshes that overlap each other in an arbitrary manner. Such mesh approach is the most useful in problems with moving bodies like this. Numerical modelling of the OXYFLUX through the overset mesh involves a background region enclosing the entire domain and a smaller region within the domain containing the body Figure 109. In a domain discretized by means of overset mesh, cells are grouped into active, inactive, or acceptor cells. Within active cells, discretized governing equations are solved. Within inactive cells, no equation is solved, however, these cells can become active if the overset region is moving. Acceptor cells separate active and inactive cells in the background region and are attached to the overset boundary in the overset region. Acceptor cells are used to couple solutions on the two overlapping grids, Figure 110. Variable values at donor cells of one mesh express variable values at acceptor cells in the other mesh, through interpolation. The donor cells are the active cells from the other mesh that are nearest the acceptor cell. The solution is computed for all active cells in all regions simultaneously, that is, the meshes are implicitly coupled.
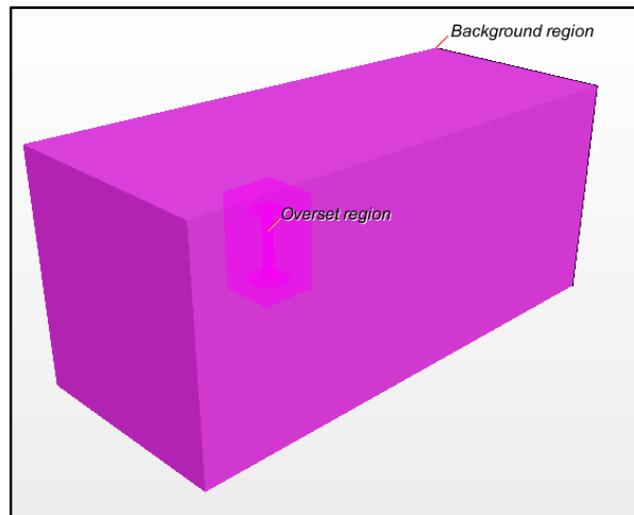
Figure 109: Schematic representation of the region used to discretized the domain.
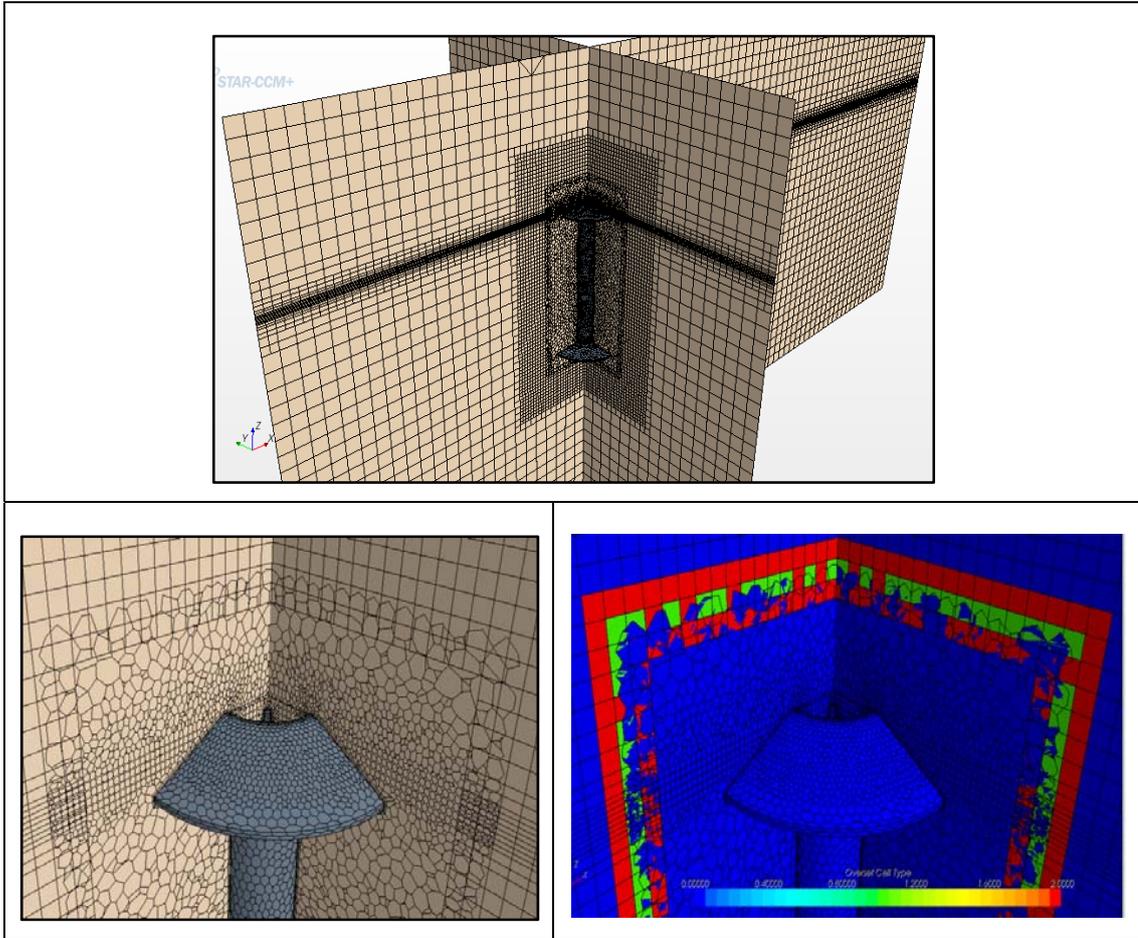
Figure 110: Screenshots of the used overset mesh. Representation of the cell type used in the coupling of the two regions, *(blue inactive cells , green donor, red intermediate cell layer used by the hole cutting process).*

Using overset mesh involves the same approximations used for all active cells as in the case of regular, single meshes. The difference arises from the substitution of the variable value at an acceptor cell by interpolation involving 3 (in 2D) or 4 (in 3D) donor cells in the overlapping region. Three interpolation methods are available in STAR-CCM+; the present simulations have been conducted by means of linear interpolation using shape functions spanning a tetrahedron defined by centroids of the donor cells. This option is more accurate but also more expensive. It is important in simulations involving moving meshes as it ensures that interpolation elements do not overlap. The choice of donor cells is not unique since the available donor cell centroids that enclose the acceptor cell

142

centroid can define more than one tetrahedron. This way the interpolation is continuous as the acceptor cell centroid passes from one interpolation element to the next. The interpolation function is built directly into the coefficient matrix of the algebraic equation system. This approach ensures implicit coupling of the overset meshes. The coefficient matrix of each equation solved is updated accordingly to ensure that equations can be solved up to the round-off level of residuals, more details on this procedure are available in [93].

Domain and boundary conditions

Simulations presented in this work are conducted on the whole OXYFLUX and domain geometry, then no symmetry planes are used to describe them. The computational domain is divided in two main regions: background and overset region. Length of the background region is variable with the wave length $(-\frac{\lambda}{2} \leq x \leq \frac{3}{2}\lambda)$, 9.00 m wide (-4.5.00 $\leq y \leq$ 4.5.00) and 12.00 m high (-3.5.00 $\leq z \leq$ 8.5.00), while overset region is represented with square-section parallelepiped which has height equal to 7.00 m (-6.00 $\leq z \leq$ 1.00), and side equal to 4.00 m (-2.00 $\leq x$; $y \leq$ 2.00), Figure 111 . The geometry of the device is placed in order to have its vertical axis of revolution passeing through $x=y$ =0.00. Such configuration of the domain ensures suitable overlap of the two regions and adequate gap from the background's boundaries to the overset region. Furthermore it allows to keep, at least, four layers of cell from device surface to overset boundaries, Figure 113. The seabed was given at 7.00 m below mean water surface, and a 1st order wave velocity profile is specified at the up-wave, lateral, bottom and top boundaries, Figure 113. The pressure outlet is implemented at the down-wave boundary, where pressure field due to a calm plane of water is imposed in order to use VOF Wave damping layer. This means that a VOF wave is damped in the vicinity of outlet boundary to reduce wave oscillation

143

near it, Figure 114. Such operation introduces vertical resistance to the vertical water motion in the selected area of domain [130], [93]. Simulations are carried out using a length of the wave damping zone equal to the simulated wave length, thus ensuring a gap of one half length between the dumped zone and the device. An additional artificial interface is generated at the top of the floater in order to measure flow and velocity due to wave overtopping, Figure 112.
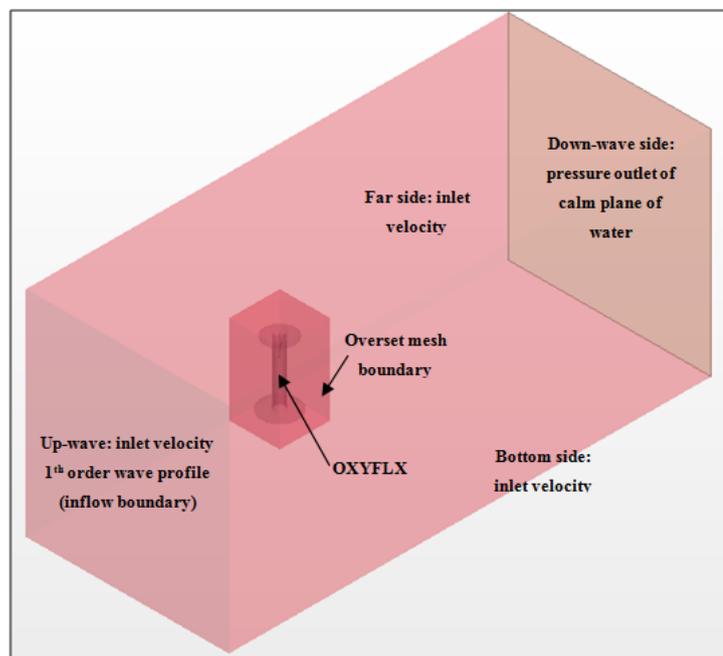
Figure 111: Domain and boundary conditions.
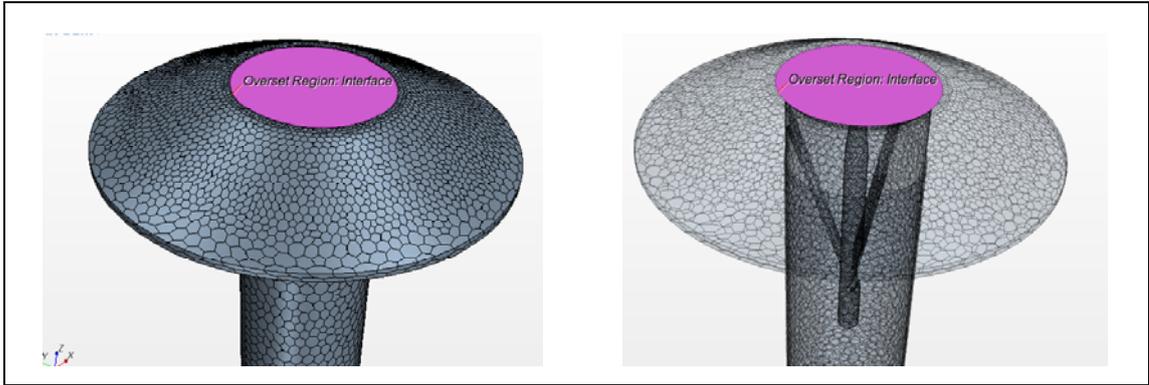
Figure 112: Generated interface at the top of the floater.
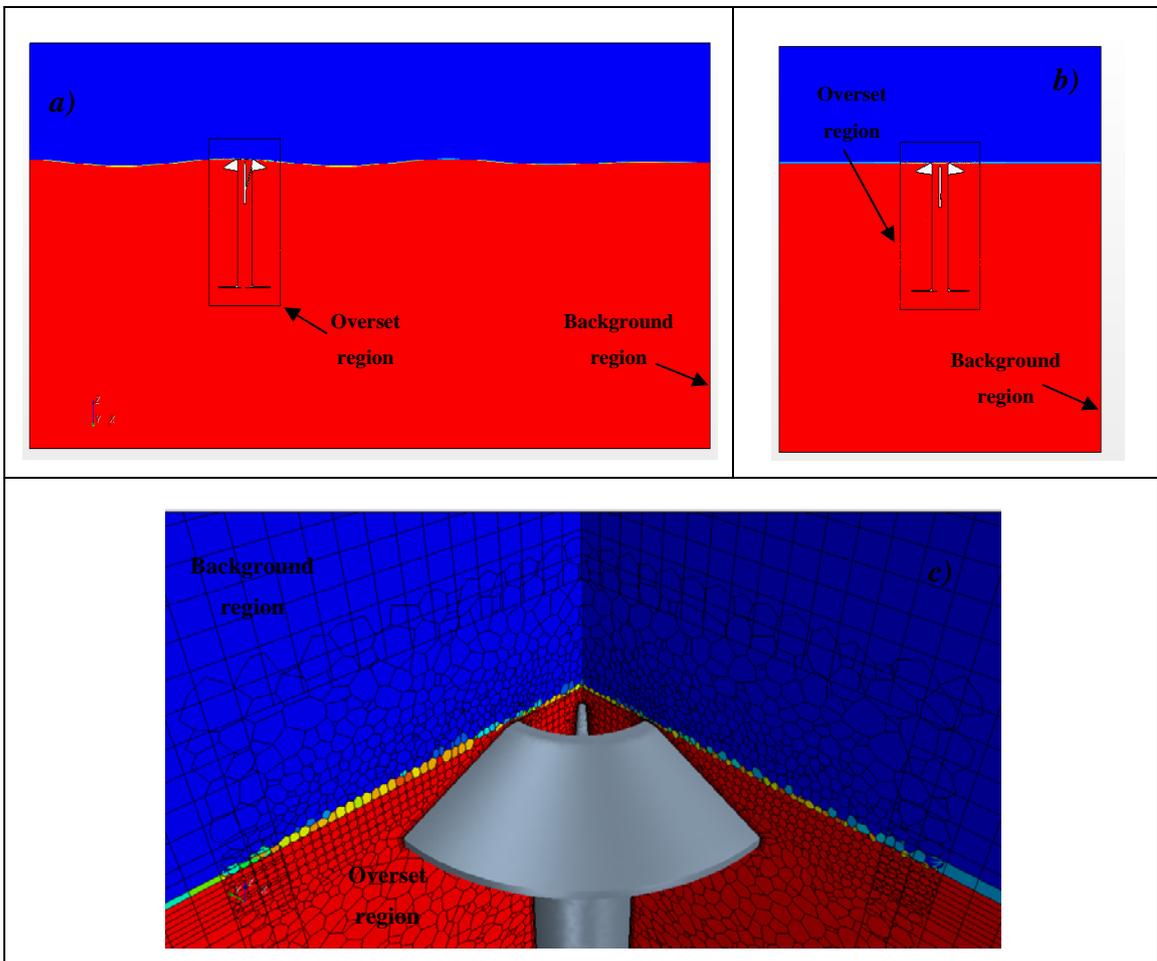
Figure 113: *a*) Section view *x-z*, *b*) section view *y-z*, c) 3D view of the overset mesh.

Four boundary conditions have been used to describe the fluid field at the bounds of the domain. They involve wall, velocity inlet, pressure outlet and overset mesh condition. Wall boundary condition represents an impenetrable, no-slip condition for viscous flow simulation. For no-slip walls, the tangential velocity is explicitly set either to zero (for the case of no wall motion) or to a specified value, while the pressure at the boundary is extrapolated from the adjacent cell using reconstruction gradients. A velocity inlet boundary represents the inlet of the domain at which the flow velocity is known, in this investigation it represents the wave maker of the numerical wave flume, where the inlet face velocity vector is specified directly according to the required wave profile. The boundary face pressure is extrapolated from the adjacent cell using reconstruction gradients. A pressure outlet boundary is a flow outlet boundary for which the pressure is specified. The boundary face velocity is extrapolated from the interior using reconstruction gradients, while boundary pressure can have two different calculation methods. If inflow occurs, pressure is defined by the following equation:

$$p = p_{specified} - \frac{1}{2} \cdot \rho \cdot |\boldsymbol{v}_n|^2 \qquad\qquad (42)$$

While if no inflow occurs the boundary pressure is kept equal to the specified one. The overset mesh is created using the overset mesh boundary, which is the outer boundary of the overset region that is expected to be coupled with the background mesh by means of the overset mesh interface. All boundary conditions mentioned above, except for the overset mesh boundary, involve some specified values, constant or variable during the simulation; these values are given to the model by means of field function. Such functions are automatically developed during the selection of the physical model.
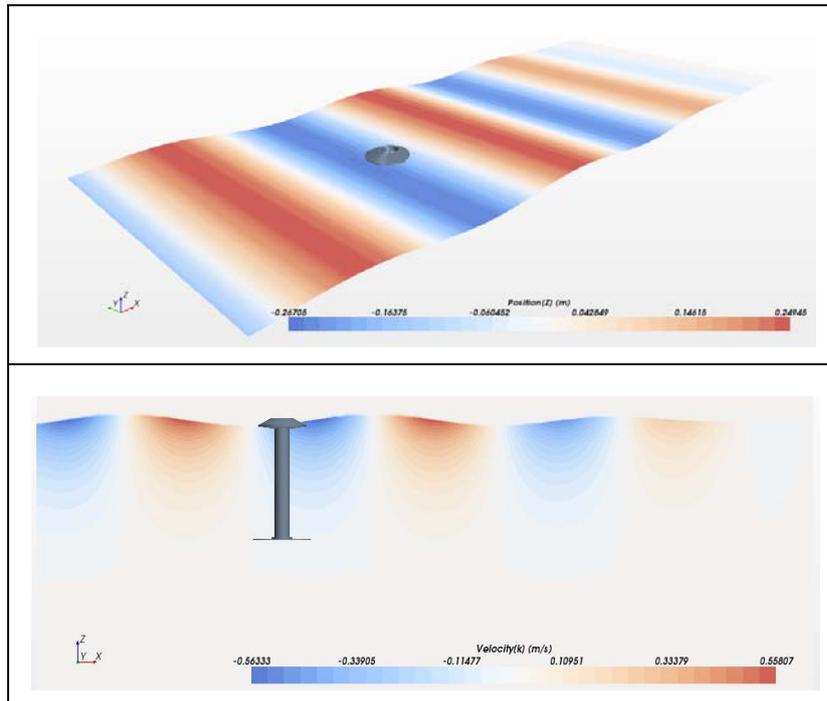
Figure 114: Effects of the VOF Wave damping on the free surface and on the water vertical velocity.

Mesh and time step selection

The mesh is created using the STAR-CCM+ grid generation utility. Figure 97 shows the grid resolution around the OXYFLUX model. The grid resolution is finer near the free surface and around the OXYFLUX to capture both the wave dynamics and the details of the flow around the device, Figure 115. Furthermore a thicker zone is created in order to have cells in the overlapping region of similar size on both the background and overset meshes. Moreover, prism-layer cells are placed along the OXYFLUX surface, Figure 116.
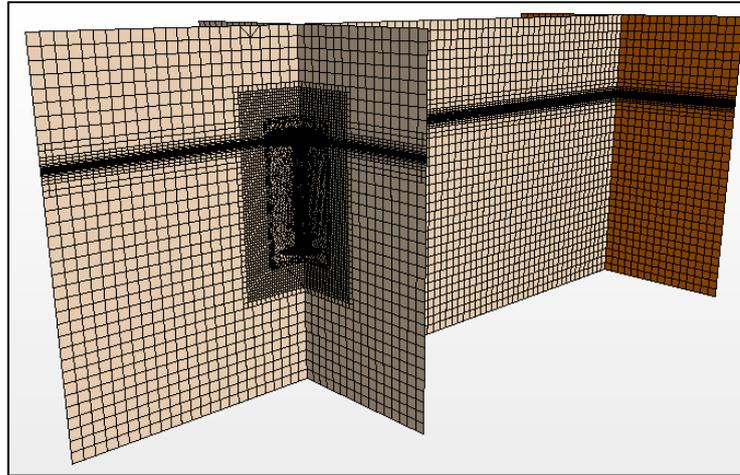
Figure 115: Section views of the overset mesh.

Such layers of cells near the body surface are responsible to generate the grid which is used to solve the closure problem. Relatively coarse mesh are used near the boundaries; the lower part of the boundary layer, namely the viscous sub-layer and part of the buffer, is not resolved. The centre point (*P*) of the wall-adjacent cell is placed inside the buffer or logarithmic layer and flow parameters are modelled by blended wall functions, [93], [129]. Typically, during the simulations, y^+ values of the wall-adjacent cell between 5 and 300 are recognized so that *P* is located in the buffer or logarithmic region, Figure 117. A all-y^+ wall treatment is used in order to not impose a more sever wall treatment, like high-y^+ wall treatment and then solve both buffer and logarithmic layer. The all y^+ wall treatment is a hybrid model. It provides a more realistic modeling than either the high-Re treatments when the wall-cell centroid falls in the buffer region. This treatment uses damping functions for the source terms in the transport equation, but the source terms of the model in the wall cell are modified using the blended wall laws.

148
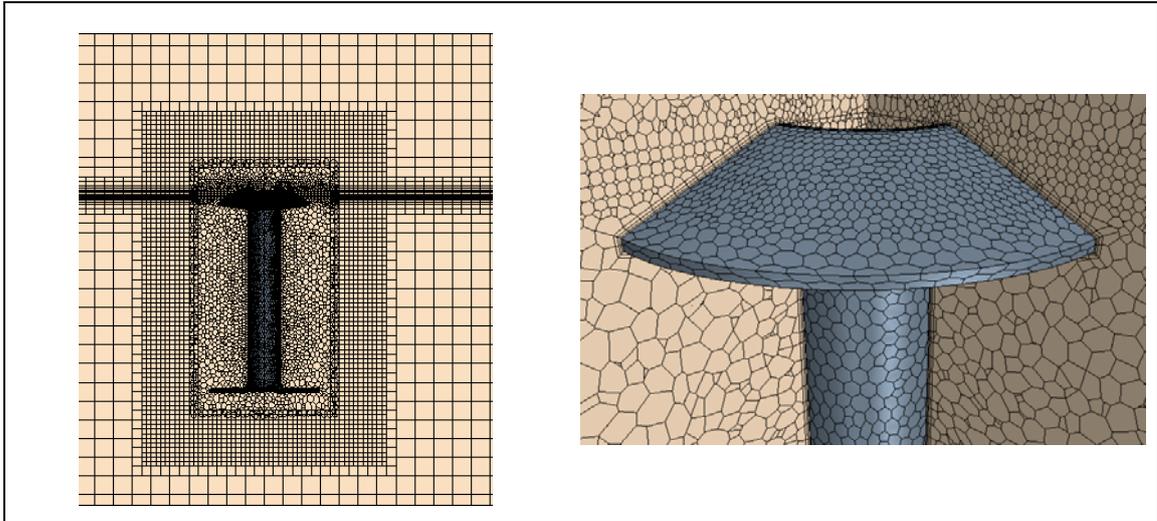
Figure 116: Thicker zone around the overset region, and boundary layer.
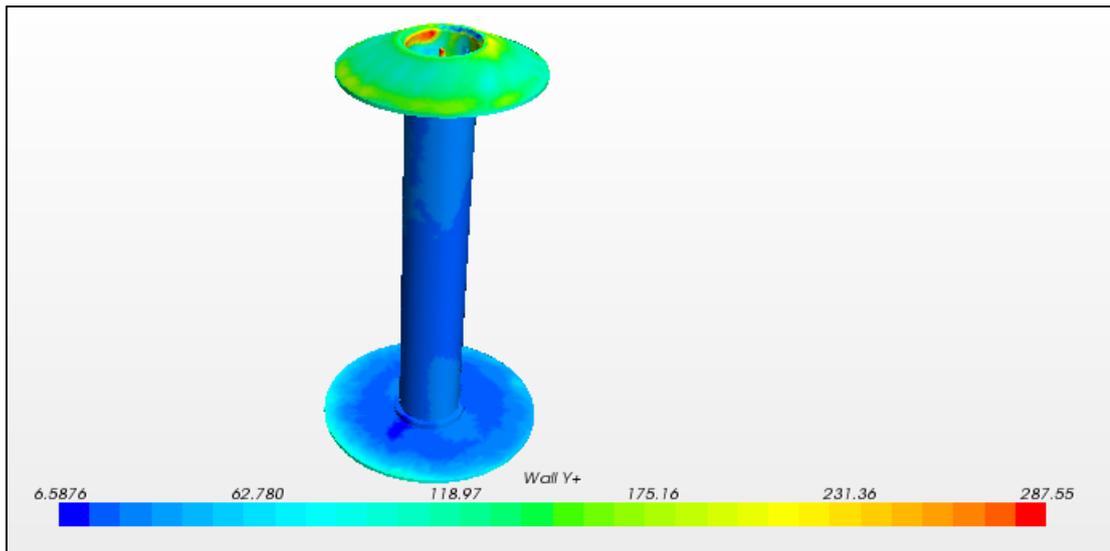
Figure 117: Distribution of the y^+ values on the OXYFLUX surface.

Background region is discretized by regular hexahedral cells, 0.50 m is selected as a target size, while three thinner areas are used to capture free surface action and device dynamic. In order to describe waves structure interaction two volumetric controls (V_{B1} and V_{B2}) are proposed across the free surface for the entire domain. Their thicknesses are

equal to the simulated wave height for the thickest (V_{B2}) and 50% more than simulated wave height for the highest one (V_{B1}). Grid size (Δx and Δz) for these elements is determined by the incident wave length λ, concerning the wave propagation direction (Δx), while the vertical direction (Δz) is adjusted according to the incident wave height, H. Third volumetric control (V_{BO}) aims to better describe the body dynamic and then, also to allow to have cells in the overlapping region of similar size on both the background and overset meshes. Overset region is discretized by irregular polyhedral cells, 0.125 m is selected as a target size ($O_{B.S.}$), while one thinner area is used to capture free surface action. Volumetric control used in the overset region (V_O) has the same planar dimensions of the region and a thickness equal to the incident wave height. Particular attention to the size of the cell had to be paid in the generation of volumetric controls in the overlapping zone. It is critical to have the same size in all three directions in the overlapping layer in order to avoid error in the interpolation. Above it is made use of Δx for both planar dimensions of the grid cell, so in the following Δx will refer to both the dimensions.
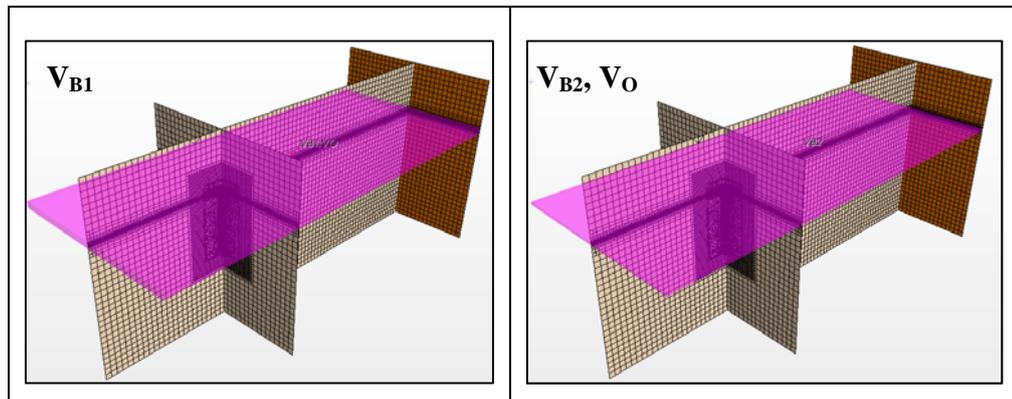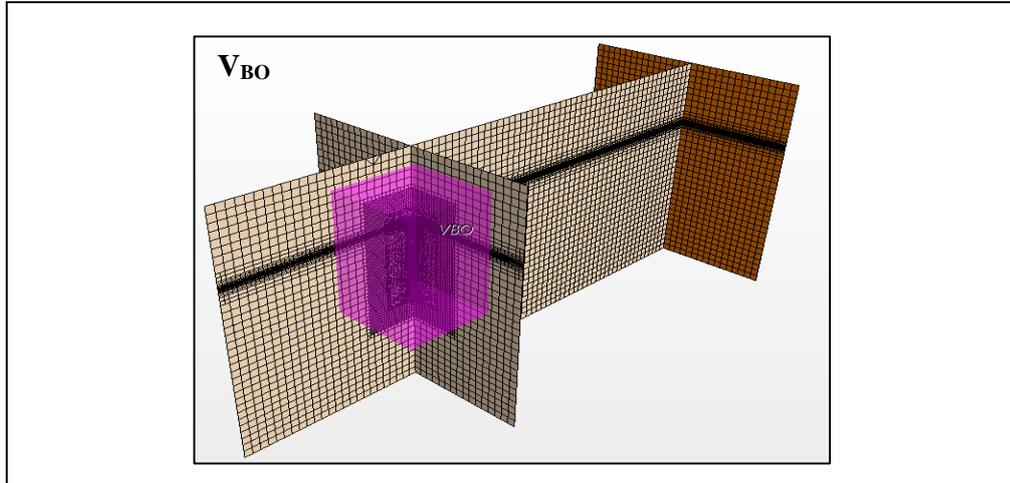
Figure 118: Volumetric controls used to describe water surface (UPPER, VB1, VB2, VO), and to ensure the same grid size in the overlapping region.

According to Yi-Hsiang [124] a series of numerical wave tank tests has been conducted to determine the appropriate grid resolution needed to model the waves-surface and body dynamics. To study the appropriate grid resolution around the OXYFLUX model and domain characteristic dimensions, nine grids with different resolutions, sidewall distances and V_{BO} dimensions have been generated. In order to do this an incident wave profile with a height of 0.29 m and a period of 2.80 sec has been used. Characteristics of each grid are summarized in Table 10. The normalized heave response is used as a tool to analyze the effects of grid resolution and the domain dimensions on the hydrodynamics of the device model, Figure 119. The domain width study indicated that the effect of the sidewall distance is not significant, particularly if compared with that of grid size used to discretize the wave. Then smaller sidewall is selected in order to reduce number of cells used, Figure 120.

Table 10: grid characteristics.

Grid n°	n° cells	Sidewall [m]	V_{B1}		V_{B2}		V_{B0}			V_0	$O_{B.S.}$	Computed time	RAO
			Δx	Δz	Δx	Δz	$\Delta x = \Delta y = \Delta z$	height [m]	side [m]	size [m]	size [m]	10 waves [h]	[heave/H_m]
1	680489	6.500	0.250	0.125	0.250	0.044	0.125	9.000	6.000	0.044	0.125	186	0.335
2	630664	6.000	0.250	0.125	0.250	0.044	0.125	9.000	6.000	0.044	0.125	175	0.348
3	602824	4.500	0.250	0.125	0.250	0.044	0.125	9.000	6.000	0.044	0.125	167	0.350
4	845525	4.500	0.250	0.125	0.250	0.031	0.125	9.000	6.000	0.031	0.125	211	0.297
5	524531	4.500	0.250	0.125	0.250	0.044	0.125	8.000	5.000	0.044	0.125	160	0.360
6	741139	4.500	0.250	0.125	0.200	0.044	0.125	8.250	5.250	0.044	0.125	197	0.303
7	1300326	4.500	0.250	0.125	0.200	0.025	0.125	8.250	5.250	0.025	0.125	228	0.291
8	1414146	4.500	0.250	0.125	0.150	0.025	0.125	8.250	5.250	0.025	0.125	240	0.299
9	2043861	4.500	0.250	0.125	0.150	0.020	0.125	8.250	5.250	0.020	0.125	273	0.285
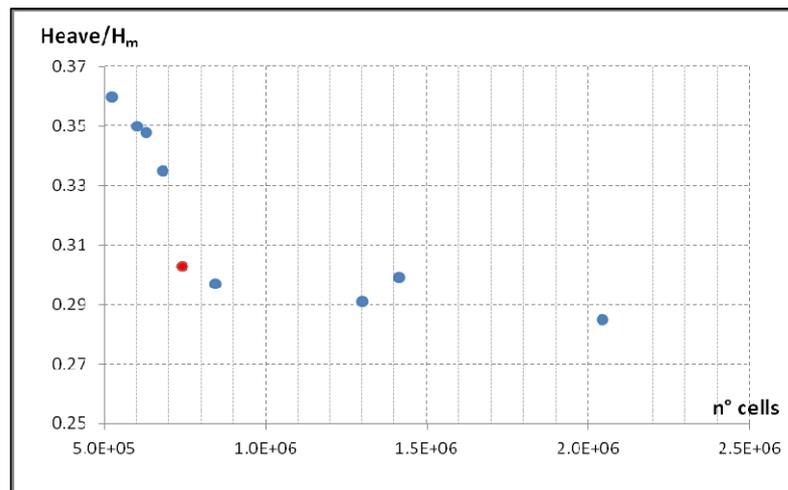
Figure 119: Effects of grid resolution on heave response, red dot is the value used for the simulations
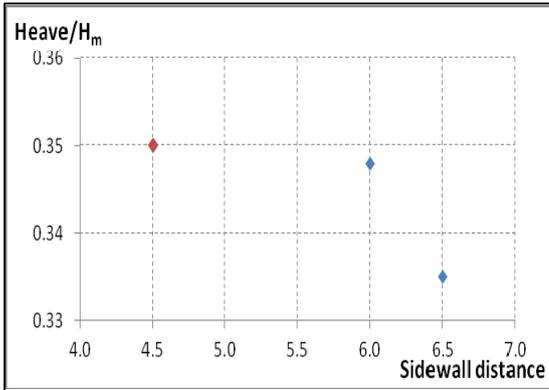
Figure 120: Effects of sidewall distance on heave response, red diamond is the value used for the simulations
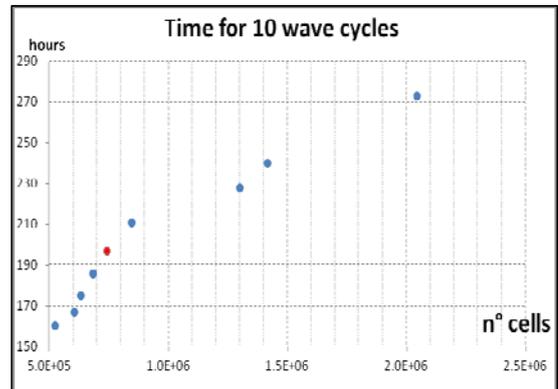
Figure 121: Effects of grid resolution on computed time, red dot is the value used for the simulations
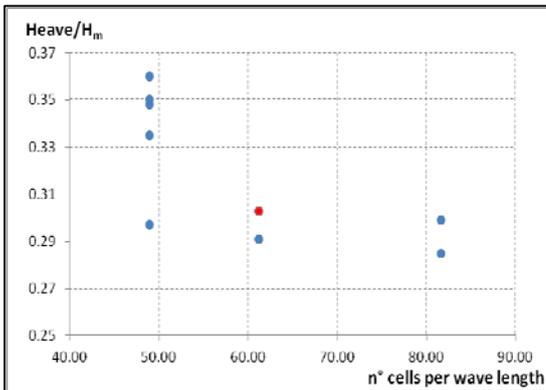
Figure 122: Effects of wave length discretization on heave response, red dot is the value used for the simulations
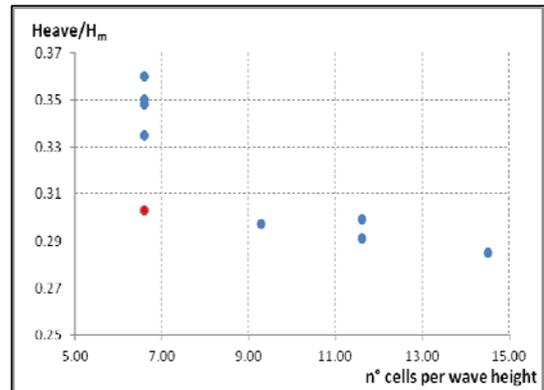
Figure 123: Effects of wave height discretization on heave response, red dot is the value used for the simulations

Further, the local grid resolution around the overset region has shown little effect on the prediction of the amplitude of the heave response. It has been observed that a gap able to ensure four cell layers between the overset region and the V_{BO} is enough to guarantee the convergence if the cell size between the two regions has the same order of magnitude. The local grid resolution between the free surface showed large effect on the prediction of the heave response and on the computational time required. For these parameters a compromise has to be taken between required time for a simulation and accuracy. In this

regard, it was decide to use $\Delta x = \Delta y = \lambda/60$ and $\Delta z = H/7.50$; such values contribute to generate a grid with a number cells variable from $7.5 \cdot 10^5$ to $1.4 \cdot 10^6$ according with the wave characteristics. *Grid 6* in Table 10, is selected to carry out all the simulations. It should be taken into account that, if the device model is allowed to move in surge mode, the viscous damping effect caused by those shed vortices around the body might have been more significant and retain the motion. In that case, additional details of the flow need to be resolved, and a higher resolution grid may be required. To keep Courant number small to preserve numerical stability, a small time step of T/800 was utilized in the study, where T is the incident wave period.

Results and model validation

Validation of the model is carried out by comparing vertical displacements measured in the wave flume and those evaluated within the numerical tank. Furthermore a calm water test is completed in STAR-CCM+ in order to identify the natural period of the floating body. This parameter is used as a mean to evaluate the accuracy of the numerical model in describing the dynamic behavior of the OXYFLUX. A numerical calm water test is performed in a squared section computational domain having side equal to 6.00 m and height equal to 7.00 m, while the grid used is *grid 6*. A damping layer zone is placed in front of all the far field boundaries to absorb outgoing waves. To perform the decay test, the OXYFLUX has been immersed with an initial displacement of -0.15 m. Upper plot in Figure 125 shows a comparison between heave decay time history obtained from STAR-CCM+ simulation and experimental measurements, while the lower one shows spectral analysis from both the simulations. Numerical results agreed with experimental data, and the natural decay period has been found to be around 4.00 sec in full scale, i.e. around 1.00 sec in model scale. Although both results agree, some small discrepancies appear in the natural period of the body. A period equal to 4.02 sec is detected for physical calm water test while 4.10 sec is calculated for the numerical test. Furthermore the numerical

simulation seems to be affected by a larger damping than physical test that shows its effects also through smaller amplitude oscillations. It can be argued that the mesh could be thinner near the OXYFLUX boundaries in order to describe better the local small scale turbulence that affects the body, but since the simulations, with these characteristics, already required a long computational time, an error of almost 2.00 % between numerical and experimental result was considered to be acceptable.
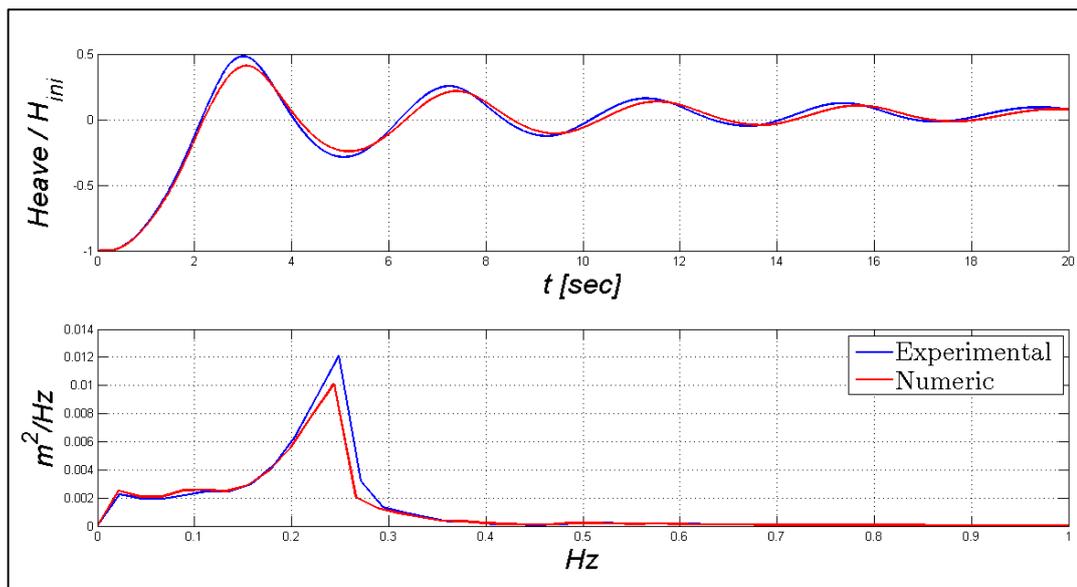
Figure 124: Calm water tests from STAR-CCM+ and experimental measurement.

A series of simulations has been performed to investigate nonlinear effects of the interaction between waves and the device under regular waves. Used wave states and their characteristics can be seen in Table 11. The simulations aimed to investigate the dynamic response of the whole device and its pumping capacity.

Table 11: Regular wave states simulated in numerical tank.

Wave n°	depth	H	T	s %	RAO	Q_m l/sec
1	7.00	0.24	3.20	1.51%	0.37	21.69
38	7.00	0.48	2.80	3.93%	0.35	44.70
39	7.00	0.59	2.80	4.83%	0.34	35.62
44	7.00	0.48	3.00	3.43%	0.35	38.71
C	7.00	0.18	2.80	1.47%	0.31	4.25
T	7.00	0.29	2.80	1.83%	0.30	27.58
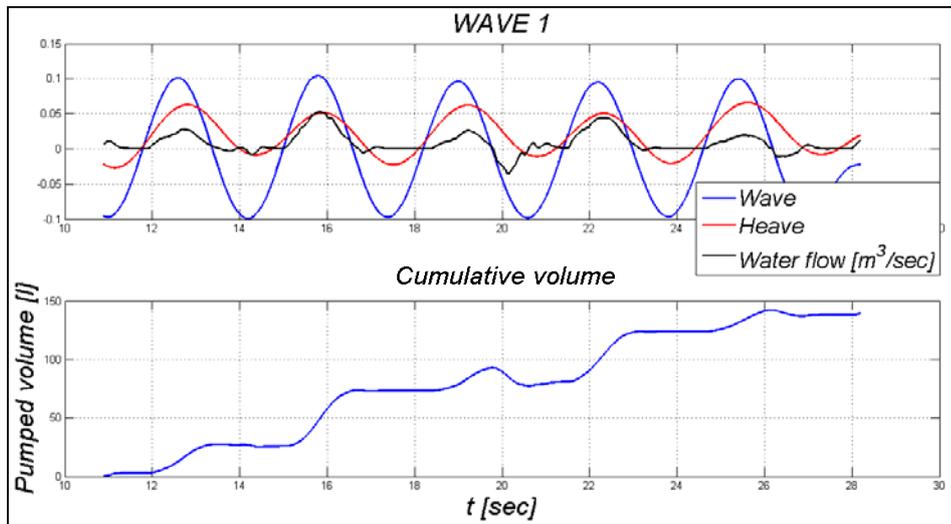
Figure 125: Heave response of the device, water flow inside the tube and cumulative pumped volume for WAVE 1.

156
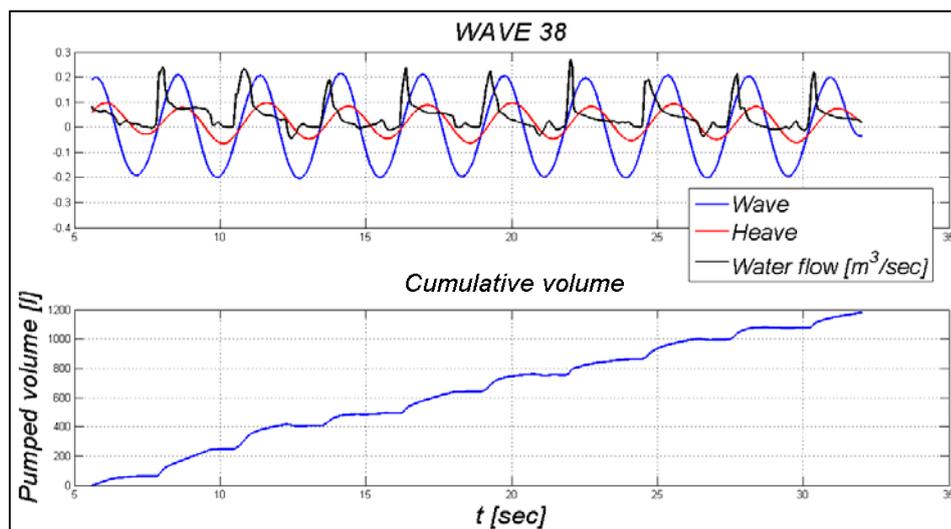
Figure 126: Heave response of the device, water flow inside the tube and cumulative pumped volume for WAVE 38.
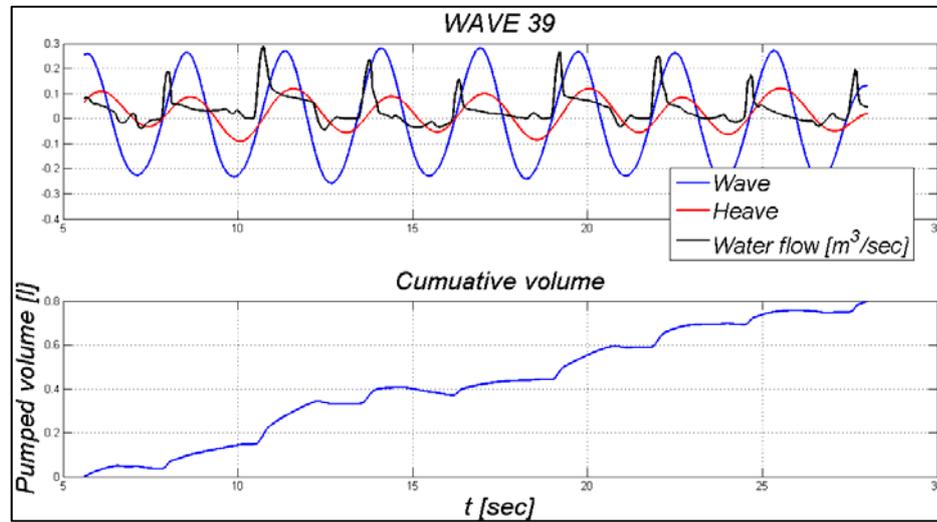
Figure 127: Heave response of the device, water flow inside the tube and cumulative pumped volume for WAVE 39.
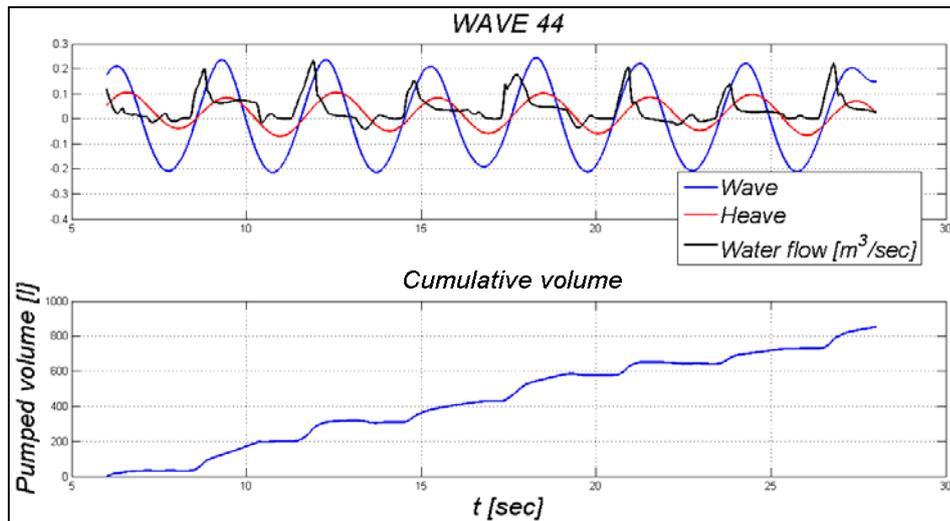
Figure 128: Heave response of the device, water flow inside the tube and cumulative pumped volume for WAVE 44.
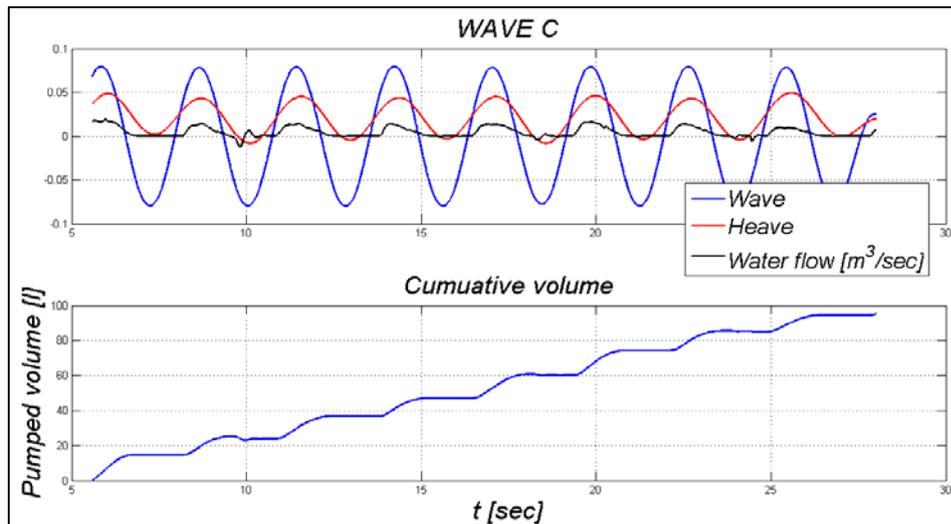
Figure 129: Heave response of the device, water flow inside the tube and cumulative pumped volume for WAVE C.
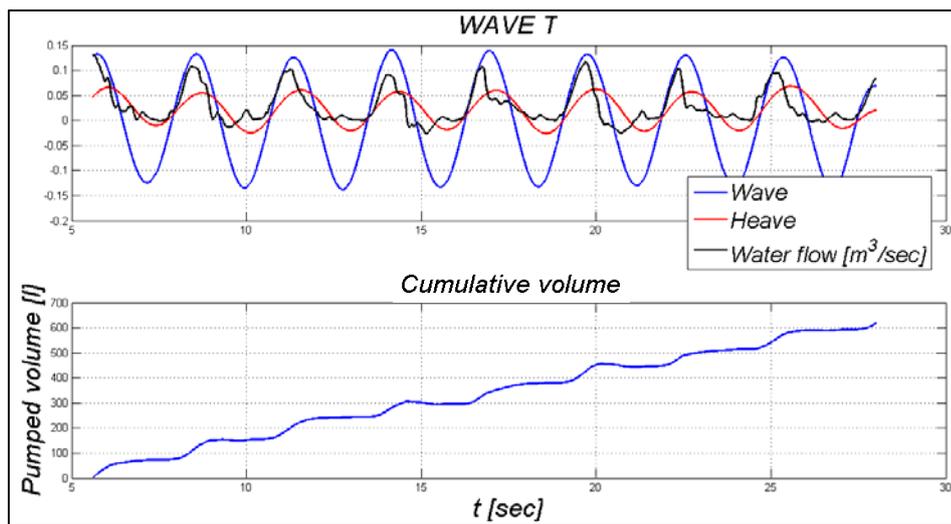
Figure 130: Heave response of the device, water flow inside the tube and cumulative pumped volume for WAVE T.

Series from Figure 125 to Figure 130 shows the main results coming from the numerical simulations conducted in STAR-CCM+. In the upper part of the above figures, time series of incident wave, heave response and values of the real-time flow overtopping the floater are plotted, while in the lower part the cumulative overtopped volume is represented. Time integration of the flow signal allows to calculate the volume of

158

overtopped water at each single instant. Since the pumping mechanism is driven by incoming waves it is clearly visible as the cumulative volume increases for each wave cycle.
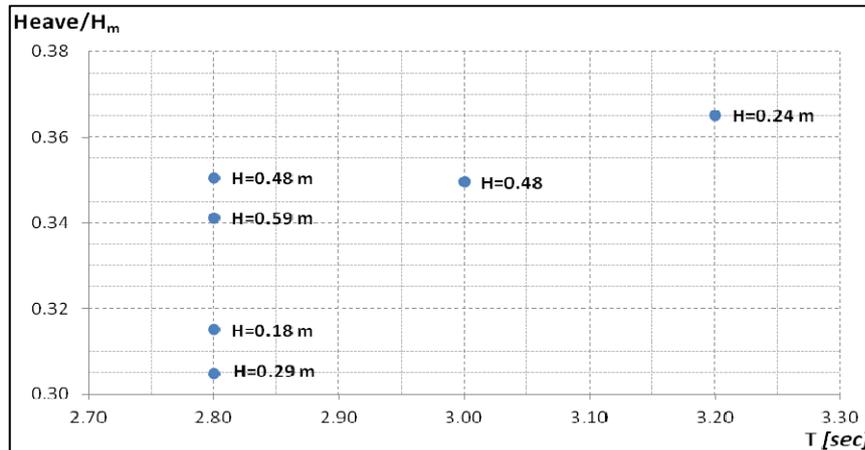
Figure 131: OXYFLUX's heave response

Comparing Figure 126 Figure 127 Figure 129 and Figure 130, in which equal period waves are plotted, it can be noted how the phase shift increases with the increasing of wave height. It can be argued that such shift in the heave response is mainly due to the larger damping that affects the device for higher wave heights. Therefore, nonlinear effects can be more significant, particularly in scenarios concerning greater wave-heights, Figure 131. Nonlinear effects of wave and floating-body interaction introduce additional damping forces that reduce the response amplitude and shift heave response. Results of the heave response are compared with the experimental ones in order to be validated, Figure 132. Numerical simulations are carried out in order to investigate OXYFLUX's behavior under the action of short waves, since the device has been developed to work with breeze waves or comparable sea states. Investigation of larger periods is not conducted here since it requires a larger domain and computational time. Heave response analysis and decay test study which have been conducted by comparing RANS solutions to experimental results, indicates that the mesh and specified numerical settings and algorithms are sufficient and capable to model OXYFLUX's dynamic.
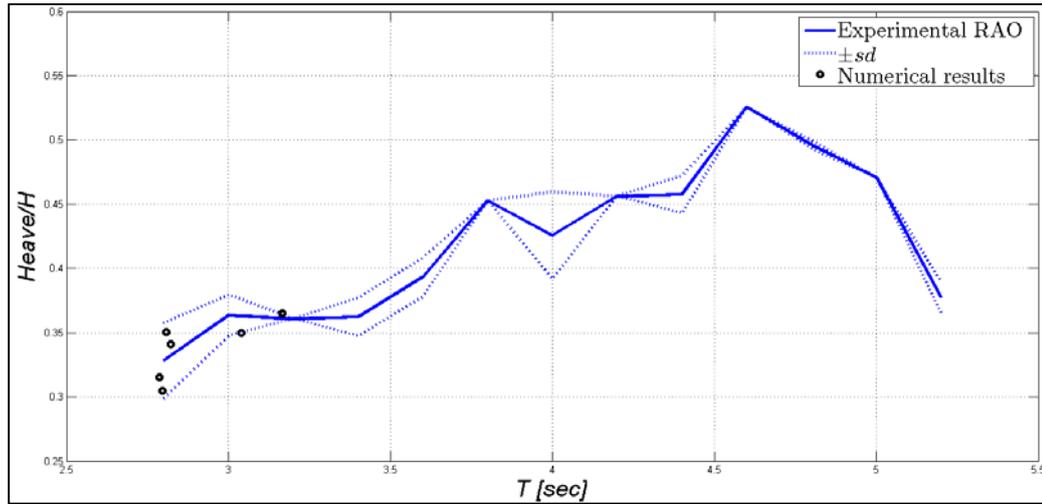
Figure 132: Comparison of experimental and numerical heave response.

The flow inside the tube is mainly driven by the waves that overtop the floater. Such phenomena, jointly with the heave displacement, lead to a cyclic flux with a period comparable to the incident wave's one. Relevant peaks relative to higher frequencies appear in the downward flux signal, and are mainly due to two factors One is the pitch movement of the device, that affects the capacity of the wave to go inside the floater. Since the pitch mode generates a rigid rotation of the floater it affects the capacity of the wave to run on the conical surface and fall into the tube. The second factor that generates higher frequency response in the flow signal is due to the wave crest action on the back side of the mouth of the floater. Once the wave crest meets the frontal region of the floater it is divided in two parts that start to run around the circular shape of the floater and then hit, on the back side, one with each other generating a second overtopping wave. This phenomenon originates from the jointly action of the pitch mode and incident wave crest, generating an additional contribution to the downward flux. Some other phenomena characterized by a frequency higher than the incident wave are present in the signal, especially for highest waves. Such components of the signal are largely caused by the sloshing of the water surface inside the floater. Since the flow is measured by means of an artificial interface generated at the top of the floater some of those oscillations can be

evaluated like overtopping water. Since this component has average value equal to zero its effect on the final medium flow can be neglected.

Solution time 0.125 sec

Position(Z) (m)
-0.20607   -0.13338   -0.060695   0.011993   0.084680   0.15737

Solution time 0.25 sec

Position(Z) (m)
-0.14450   -0.083379   -0.022256   0.038868   0.099991   0.16111

Solution time 0.375 sec

Position(Z) (m)
-0.14457   -0.073319   -0.0020673   0.069184   0.14044   0.21169

Solution time 0.50 sec

Position(Z) (m)
-0.14468   -0.072148   0.00038247   0.072912   0.14544   0.21797

Solution time 0.625 sec

Position(Z) (m)
-0.14464   -0.065663   0.0073136   0.083291   0.15927   0.23524

Solution time 0.75 sec

Position(Z) (m)
-0.14467   -0.065153   0.014368   0.093890   0.17341   0.25293

Figure 133: Images sequence of wave crest meeting the floater.

Through integral mean for each wave state the mean values over 5 waves cycles have been calculated. The discharged flow is largely affected by the wave height. As it clearly appears from Figure 134, for wave states characterized by a period equal to 2.80 sec, the more the wave height increases, the more the mean discharge flow increases. An exception can be noticed for the wave height equal to 0.59 m, when the maximum downward flow appears to be smaller than the one that occurred for a wave height of 0.48 m. Such circumstance is due to the depression that the wave, above certain values of height, generates going over the floater but not into it. Such process has been also observed in the physical investigation of the OXYFLUX but, since only waves with height smaller than 0.75 m have been model numerically, effects of the depression at the top of the floater are not strong enough to divert the flow field inside the tube.
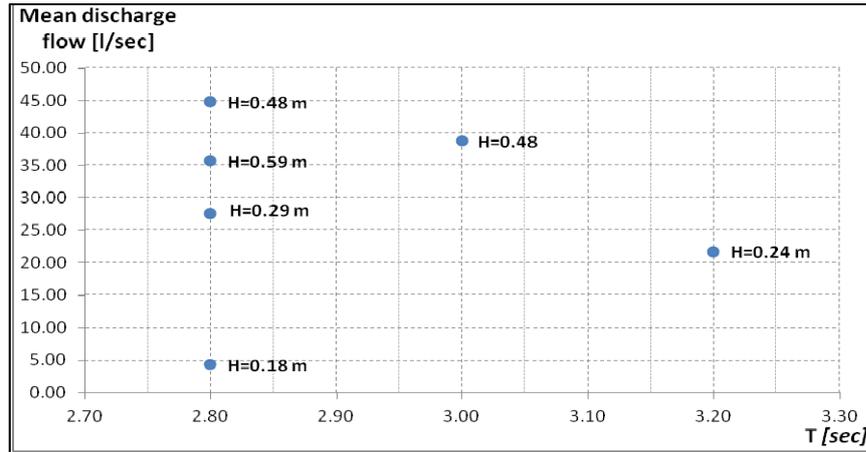
Figure 134: OXYFLUX's mean pumped flow.

Results of the mean flow are compared with the experimental ones in order to be validated, Figure 135Figure 132. Experimental velocity values compared with the RANS solutions indicate that the mesh and specified numerical settings and algorithms are sufficient and capable to model the OXYFLUX's pumping mechanism.
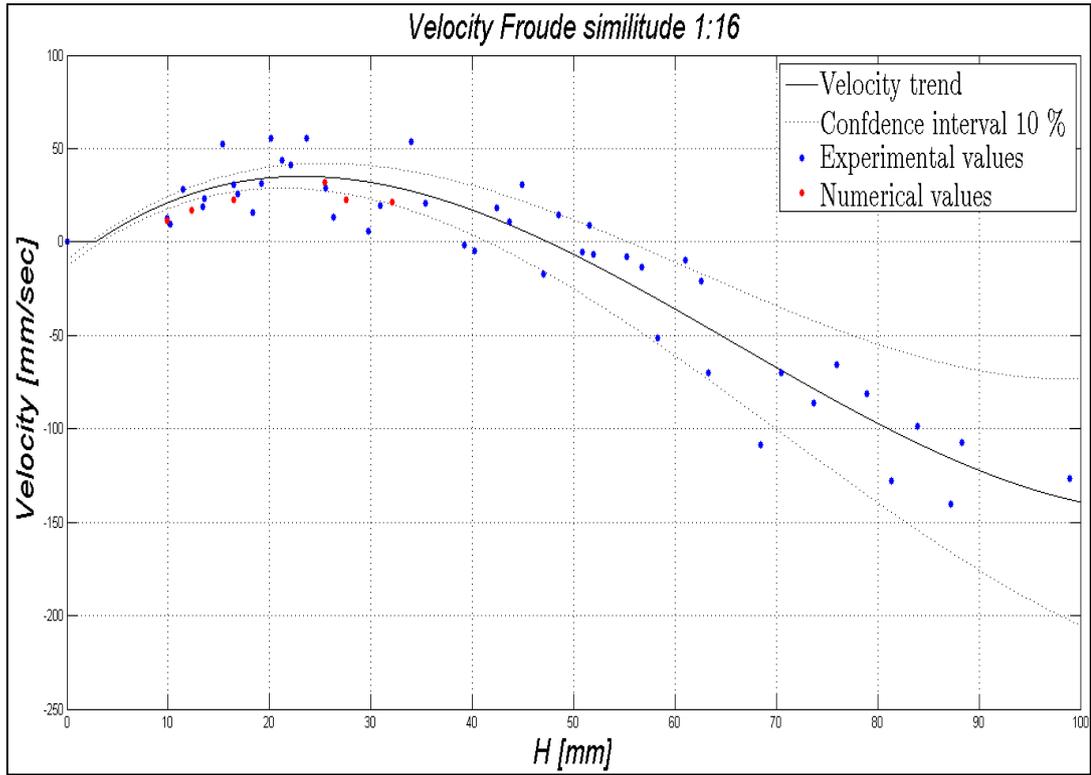
Figure 135: Comparison of experimental and numerical mean downward flux.

CHAPTER VI: DEVELOPMENT AND NUMERICAL MODELLING OF THE NEW GEOMETRY

The geometry of the device presented in this chapter, from here on called *Geometry 2*, derives from the results of the analysis described in the preceding chapters. The first shape of the device, from here on called *Geometry 1*, is characterized by three behaviors according to the incident wave height and presenting some limits as concerns the amount of water pumped down. The inability of this shape to take advantage of the phase shift between incident wave and heave response is mainly due to the geometry of the floater, which is designed to benefit to the maximum from the overtopping of the wave crest in its classical form, as defined by Kofoed, [62]. In this chapter, in order to obtain maximum efficiency from the intermediate, lowest wave heights, an already known profile is used to model the floater surface. Lazzari's profile [145], is used to design a new shape of floater (*Geometry 2*). Such a kind of application has never been tested in a physical or numerical model before since its main application concerns spillways used in artificial lakes. The principal difference with the traditional application concerns the conditions in which the spillway is going to work. In artificial lakes, the common applications of Lazzari's profile regards a base fixed concrete structure posed in a way that the increasing level of the water brings the free surface to surround and finally overtop the whole structure. The adaptation of such a fixed system to a movable floating structure interacting with the incident wave is proposed here. *Geometry 2* aims to catch as much water as possible from the wave crest during the emersion of the floater under the water surface. In the following the main parts of *Geometry 2* and the results from the numerical model will be described and compared with the ones of *Geometry 1*.

.

Figure 136: Example of spillway designed according Lazzari's profile, [131]

Figure 137: Spillway during common operation time, [131]

Three main parts constitute *Geometry 2,* and each of them has the same function as in *Geometry 1*. In the following, only the new shape of the floater will be described since the other two parts are not going to change. The new floater will ensure the buoyancy of the whole structure. The following paragraphs focus on the design of the new shape which will be used for numerical simulations, thus dimensions will be in real scale.
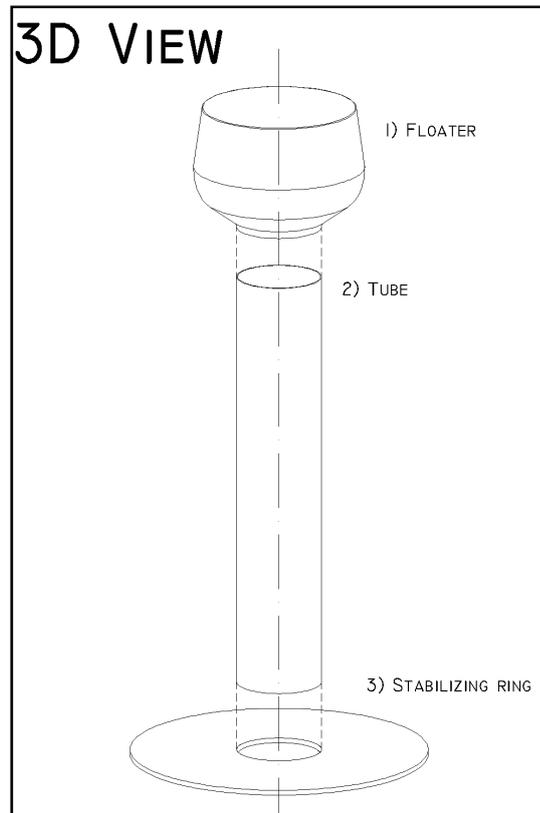
Figure 138: Components of *Geometry 2* used in numerical model.

Floater of *Geometry 2*

In order to define the shape of the floater, i.e. of its median section, reference has been made to the curve that describes the lower profile of freely fluid flux going out from a circular thin-walled spillway. This curve has been moved forward in order to guarantee the complete adhesion of the fluid to the wall and a constant pressure on the spillway surface as suggested by Creager, [105].
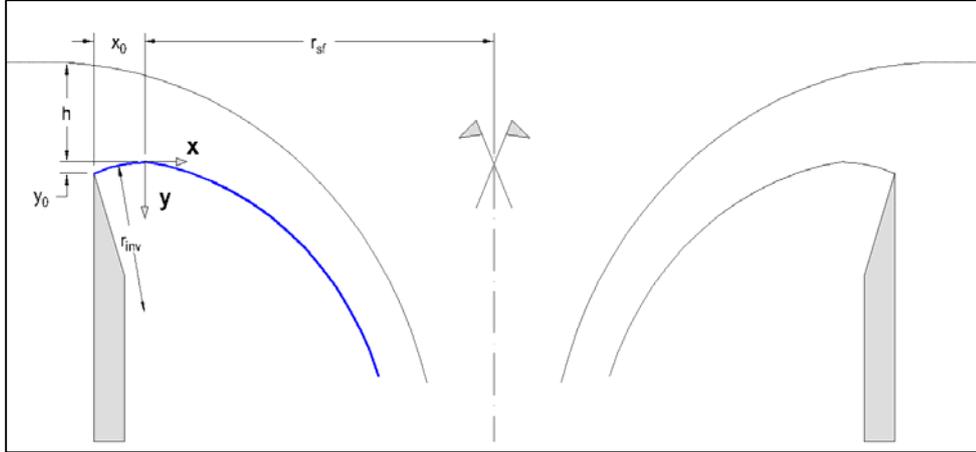
Figure 139: Reference system used to define Lazzari's profile.

x_0 and y_0 are the distances of the origin of reference system used to describe the parabolic profile from the external wall of the spillway, and are defined as,[132]:

$$\begin{cases} x_0 = 0.144 \cdot (h + y_0) + 0.011 \cdot \left(r_{sf} + x_0\right) \\ y_0 = 0.055 \cdot (h + y_0) + 0.030 \cdot \left(\dfrac{(h + y_0)^2}{r_{sf} + x_0}\right) \end{cases} \qquad 0.1 \le \dfrac{h + y_0}{r_{sf} + x_0} \le 0.5 \qquad (43)$$

The equation of the parabolic profile is:

$$\frac{y}{h + y_0} = 0.608 \cdot \left(\frac{x}{h + y_0}\right)^{1.8} \qquad\qquad (44)$$

Assuming a circular shape of the connection used to move forward the origin of the parabolic profile, its radius is described as:

$$r_{inv} = \frac{x_0^2 + y_0^2}{y_0} \qquad\qquad (45)$$

Geometry 2 has been calculated starting from the dimension of the internal radius of the cylinder connected to the floater; such a dimension has been kept equal to *Geometry 1* i.e. 0.40 m. The values of the above mentioned variables are estimated by means of an iterative procedure developed by Matlab under the hypothesis of a total head equal to

0.13 m. This value is in accordance with the smallest wave height able to activate the pumping mechanism.

Table 12: Geometric parameters used for *Geometry 2*.

h [m]	x_0 [m]	y_0 [m]	r_{sf} [m]	r_{inv} [m]	$(h+y_0)/(r_{sf}+x_0)$
0.13	0.028	0.0315	0.4	0.0282	0.3774

Such a procedure allows to define the internal surface of the floater, while the external one has been designed in order to keep the body floating and to guarantee floatation of the device even after the inevitable weight gain due to biofouling growth in a real sea environment. In order to compare the two geometries and their efficiencies, the percentage of buoyancy reserve force will be the same for both, i.e. 7.0 % of the total force that, for *Geometry 2,* is equal to 14400.00 N. The result of the design process is a goblet shaped floater with a volume of 1.05 m³, corresponding to a weight of 520 N. Its maximum diameter is equal to 1.65 m while its height is 1.21 m. The central opening is directly connected to the outlet side and it has a diameter of 0.40 m. See Appendix B for all the details of the structure.
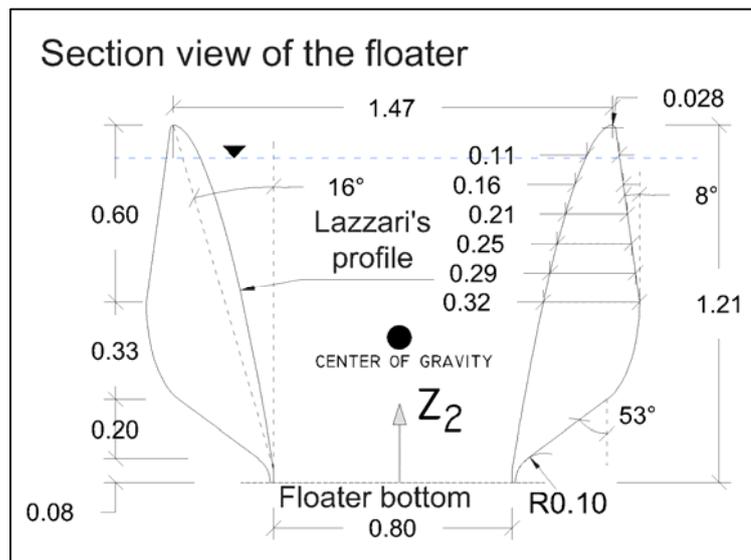
Figure 140: Details of the floater, all lengths are in m.

Table 13: Hydrodynamics parameters of the *Geometry 2* floater.

Floater *Geometry 2*			
Center of gravity (respect z_2 [m])	Radii of Gyration [m]		Mass moment of inertia (respec center of gravity [m^2·kg])
0.56	R_{xx}	3.683312	18790
	R_{yy}	3.683312	18790
	R_{zz}	0.744171	767

As already mentioned geometry and the characteristic of the tube and stabilizing ring do not change from *Geometry 1*. Their description is omitted since it is available in Chapter 3.

The total length of the device described in this chapter is equal to 5.36 m from the top of the floater to the stabilizing ring (*Froude similitude 1:16: 335.00 mm*), the position of the center of gravity is largely affected by the difference in the different density of the components, and it is located at 4.59 m (*Froude similitude 1:16: 287.00 mm*) below mean water level when the device is at rest i.e. 0.56 m (*Froude similitude 1:16: 35.00 mm*) above the lowest surface of the stabilizing ring, Figure 142. Such a position for the center of gravity, below the center of buoyancy, was chosen in order to improve the stability of the device under the action of waves. The total weight of the device is 13392.00 N (*Froude similitude 1:16: 3.26 N*) while the maximum buoyancy force is 14400.00 N (*Froude similitude 1:16 3.51 N*) ensuring a buoyancy reserve force of 1008.00 N (*Froude similitude 1:16 0.24 N*), 7 % of the total buoyancy force. 13392.00 N corresponds to a free-board crest equal to 0.21 m (*Froude similitude 1:16: 13.12 mm*), Figure 142Figure 39. This buoyancy reserve was chosen in order to guarantee, the floatation of the device even after the inevitable weight gain due to biofouling growth in a real sea environment.

Figure 141: Trend of the buoyancy force for both geometries, the weight has been chosen in order to have the same buoyancy reserve force for both geometries.
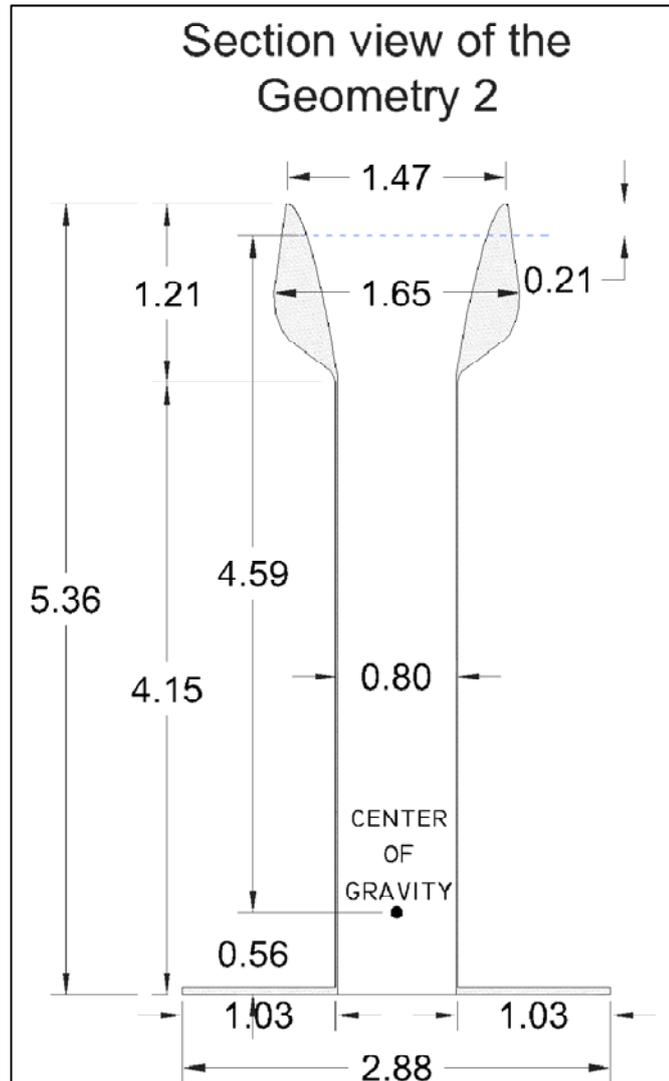
Figure 142: Details of the *Geometry 2*.

Numerical modelling and results of *Geometry 2*

In this paragraph numerical modelling results of *Geometry 2* will be presented. The set-up, the domain and the mesh used are not described, since the settings of the model are the same as used for *Geometry 1*. The model presented in chapter 5 has shown good compliance with physical model results, thus it is can be assumed valid for the simulation

of the new geometry, too. No mesh sensitivity has been carried out. Simulations for *Geometry 2* are also conducted on the whole OXYFLUX and domain geometry; no symmetry planes are used to describe them. The computational domain is divided into two main regions: background and overset region. The length of the background region varies with the wave length $(-\frac{\lambda}{2} \leq x \leq \frac{3}{2}\lambda)$, 9.00 m wide (-4.5.00 $\leq y \leq$ 4.5.00) and 12.00 m high (-3.5.00 $\leq z \leq$ 8.5.00), while the overset region is represented with a square-section parallelepiped which is 7.00 m high (-6.00 $\leq z \leq$ 1.00), and 4.00 m large (-2.00 $\leq x$; $y \leq$ 2.00). Device geometry is placed in order to have its vertical axis of revolution passing through $x=y$ =0.00. Such a configuration of the domain ensures suitable overlap of the two regions and an adequate gap from the background boundaries to the overset region. Furthermore it allows to keep, at least, four layers of cell from device surface to overset boundaries, Figure 143Figure 143: 3D view of the overset mesh used to simulate *Geometry 2*.Figure 113.
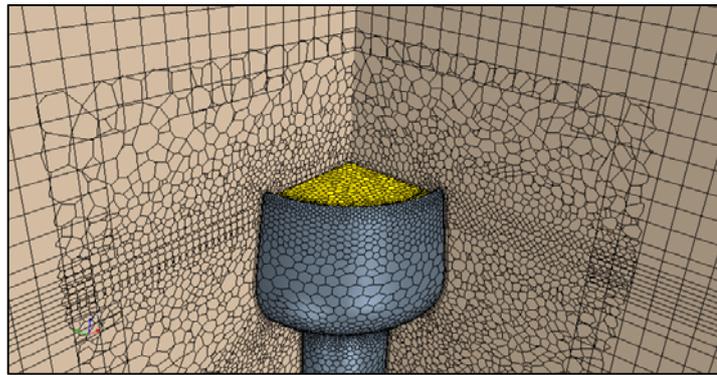
Figure 143: 3D view of the overset mesh used to simulate *Geometry 2*.

The seabed was positioned at 7.00 m below the mean water surface, and a first order wave velocity profile is specified at the up-wave, lateral, bottom and top boundaries. The pressure outlet is implemented at the down-wave boundary, where the pressure field due to a calm plane of water is imposed in order to use VOF Wave damping layer. This means that a VOF wave is damped in the vicinity of outlet boundary to reduce wave oscillation near it. Simulations are carried out using a length of the wave damping zone

equal to the simulated wave length. This ensures a gap of one half length between the damped zone and the device. An additional artificial interface is generated in order to measure the flow and the velocity of the water at the top of the floater due to wave overtopping, (yellow surface in Figure 143). *Grid 6* is chosen, and three volumetric controls are placed in the domain. Two of them are used to better describe interface water-air, and the third one is used to generate a zone in which the grid size of the overset region and background is the same, as widely explained in chapter 5. The time step is selected according to the settings of the previous simulation and it is equal to T/800, where T is the period of the incident wave.

Results

As previously done, a series of simulations has been performed in order to investigate the nonlinear effects of the interaction between waves and the device under regular waves. Used wave states and their characteristics can be seen in Table 14. The simulations are aimed at investigating the dynamic response of the whole device and its pumping capacity.

Table 14: Regular wave states simulated in numerical tank and results for *Geometry 2*.

Wave n°	depth	H	T	s %	RAO	Q_m l/sec
1	7.00	0.24	3.20	1.51%	0.38	2.85
38	7.00	0.48	2.80	3.93%	0.34	65.80
39	7.00	0.59	2.80	4.83%	0.31	79.55
44	7.00	0.48	3.00	3.43%	0.36	61.23
C	7.00	0.18	2.80	1.47%	0.27	0.00
T	7.00	0.29	2.80	1.83%	0.26	5.65
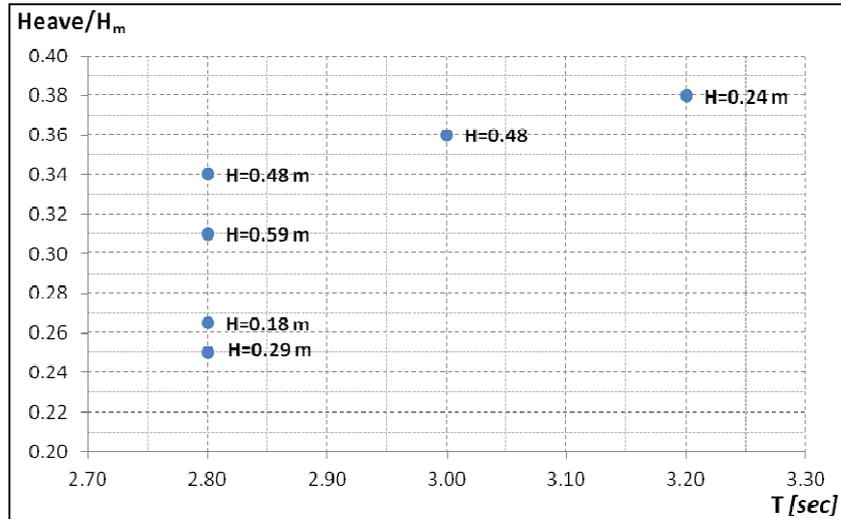
Figure 144: OXYFLUX's response in heave for *Geometry 2*.

Numerical simulations are carried out in order to investigate OXYFLUX's behavior under the action of short waves, since the device has been developed to work with breeze waves or comparable sea states. Investigation of larger periods is not conducted in this work, since it requires larger domain and computational time. Through integral mean for each wave state the mean values over 5 waves cycles have been calculated according to the procedure used for *Geometry 1*.
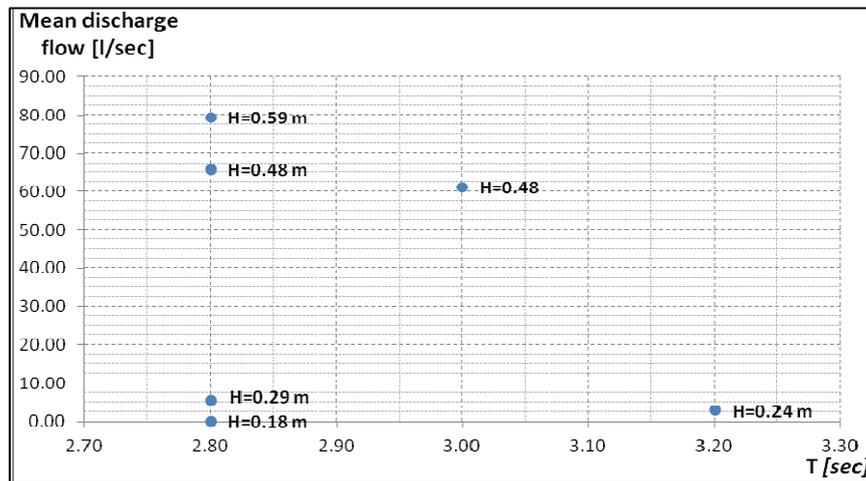
Figure 145: OXYFLUX's mean pumped flow for *Geometry 2*.

Geometry 2 shows a different dynamic behavior and pumping capacity to *Geometry 1*. The dynamic response, described here by means of the RAO, shows lower values for all the wave states characterized by a period equal to 2.8 sec, that increases as the period increases and comes closer to the resonant period. As for *Geometry 1*, simulations with periods greater than 3.20 sec have not been conducted since this work only aims to investigate the efficiency of the OXYFLUX under the action of short waves that, in the majority of cases, are common during summer when anoxia tends to develop. As expected, the water velocity inside the device is affected by the floater device, furthermore no overtopping occurs for the lowest wave heights, those waves that mostly characterize anoxic areas, while the more the wave height increases, the more the device takes in water from the wave crest to pump it downward. A significant increase can be noted for the values of mean discharge flow in correspondence to the highest wave heights for *Geometry 2*, even though such an increase occurs for wave states that can already mix the water column and then oxygenate the bottom.

CHAPTER VII: DISCUSSION

As an aid to the reader, this chapter of the dissertation provides a brief overview of the study, including an introduction to the problem and the major methods involved. The main part of the chapter is, however, devoted to the summary and discussion of the physical and numerical modelling results of the OXYFLUX. Furthermore, limitations and possible future in-depth analysis of the device will be evaluated at the end of the chapter.

The main aim of this dissertation is to identify the geometry, the shape, and the working mechanism of a device able to counteract hypoxia at the bottom sea layers. A device able to take advantage of wave energy has been proposed, and its capacity to pump water down to the bottom has been demonstrated by means of physical and numerical simulations. Results from both investigations, point out the device capacity to pump water, identifying a range of mean discharge flow from 0 to 80.00 l/sec according to the incident wave characteristics and to the shape of the floater.

Physical modelling was carried out in two phases. The first one was the preliminary investigation. Since then, no results or evidence of the functioning mechanism were known. Such a series of tests was completed under the action of four wave states characteristic of the Northern Adriatic Sea and gave an idea of the feasibility and applicability of the device, highlighting the capacity of the device to pump or draw water from the surface to the bottom layers. At the later stage a series of ninety-eight tests was completed in order to deduce the dynamic and pumping mechanism of the device and identify the effects of the mooring system. This later series of tests underline three main operating ranges, in accordance with the incident wave height and mooring system used. During such an investigation the main difficulty was relative to the measurement of the flow inside the device, since the environment, where the transducer worked, was very noisy. This phenomenon affected the measurements, as the trend of the mean water velocity shows, and gave some uncertainties during its estimation. Although such

uncertainties appear, the method developed allows to identify the functioning mechanism of the device and the main parameters which affect it, Figure 146. The image analysis procedure developed proved to be an optimum solution to monitor the displacement of the device, since it does not affect the body motion, since any contact with the surface of the device was absent. Furthermore, it proved to be extremely efficient for what concerns the time needed to elaborate the test results.
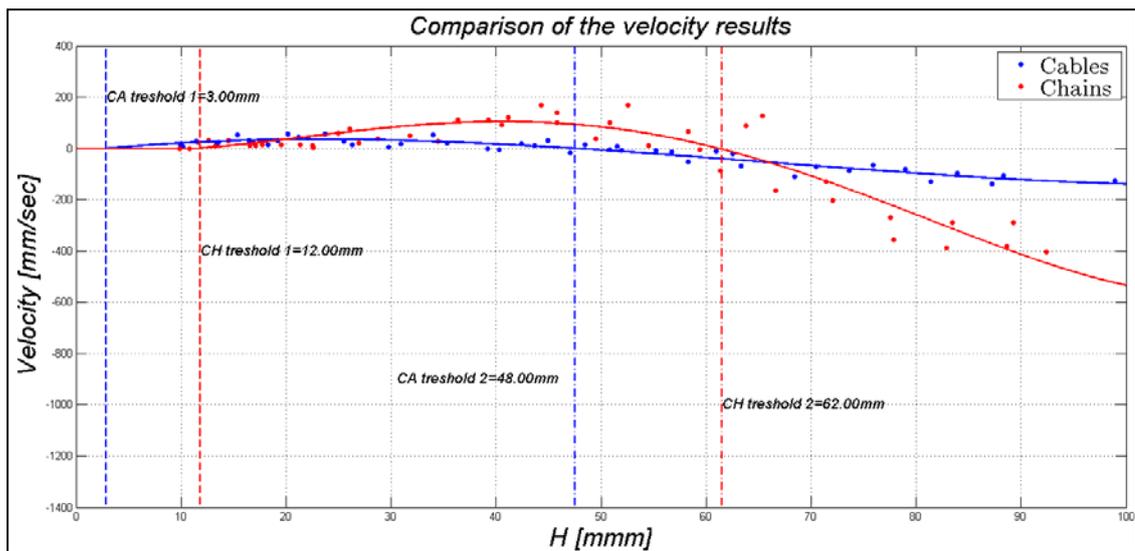
Figure 146: Comparison of water velocity results and fitting for both the mooring systems used

Numerical modelling carried out during this study was aimed at investigating the behavior of the OXYFLUX during modest energetic wave states, and to identify a second geometry able to take into account the limits of the first one and to improve its efficiency. The capacity of the numerical model to simulate the dynamic performance and the pumping efficiency has been validated by the comparison of the numerical results and the physical ones carried out with the cables as mooring system. It has been noted that the numerical model cannot describe the exact dynamic of the floating body, as shown by the comparison plot of the calm water test. A discrepancy between the natural period identified by means of numerical and physical modelling emerged, likely due to the too coarse mesh used to discretize the fluid domain around the OXYFLUX surface; this

discrepancy is around 2.00 % of the natural period identified, Figure 147. Such inaccuracy has been evaluated to be reasonable and then the results are acceptable. A second validation test has been done, with the aim to compare the mean flow discharged. This validation procedure was accomplished only for the operating range "*field 2*". The results showed good compliance between numerical and physical results, so the numerical model developed can be considered capable of describing the entire behavior of the OXYFLUX for the operating range called *field 2*.
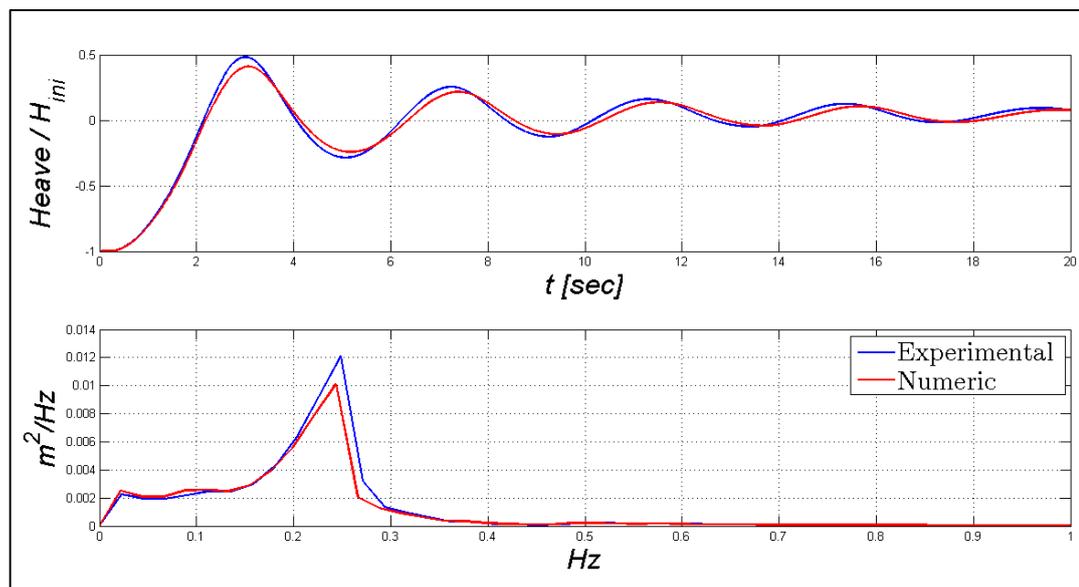
Figure 147: Calm water test from STAR-CCM+ and experimental measurement.

The second geometry tested, called *Geometry 2,* has a shape based on Lazzari's profile; the results coming from these series of simulations presented an increase in the minimum wave height capable of generating downward water flux as well as a growth in the mean water velocity for middle wave heights. Such an increase in the mean velocity has been registered for wave heights outside the range of interest, since for the shortest wave height used in the simulations the device designed with *Geometry 2* did not present any overtopping phenomenon. All these considerations lead to reject this new shape, since it does not show any relevant increase in the pumped water flow for the wave states characteristic of the period when hypoxia and anoxia develop. The comparison of the

results coming from both the tested geometries, can be considered valid since both the shapes were designed considering the same buoyancy reserve force, i.e. 7.00 % of the total buoyancy.
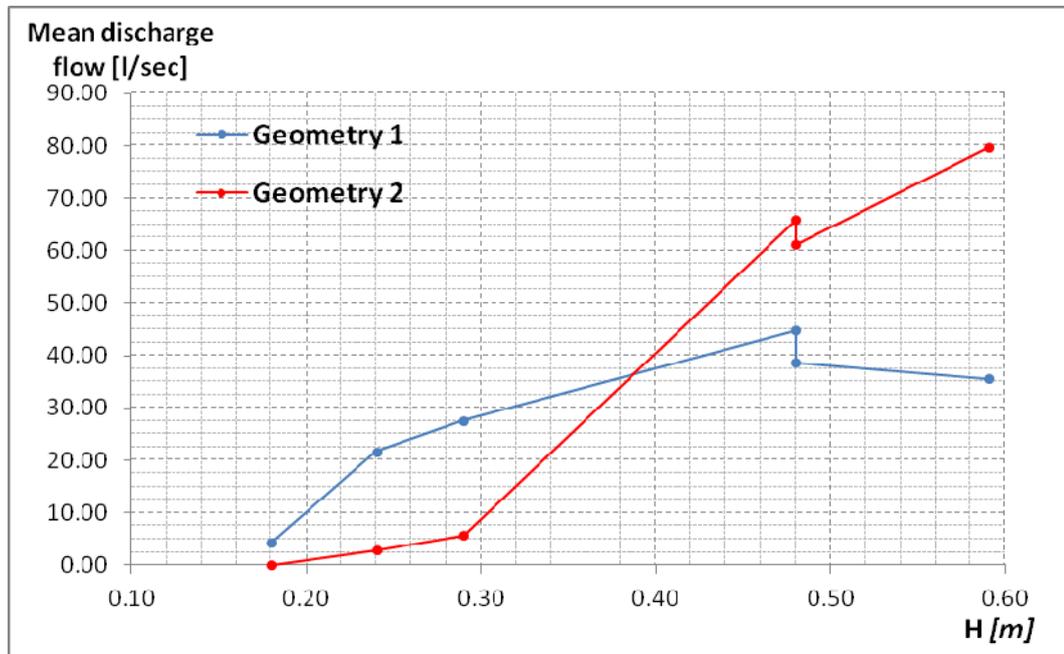
Figure 148: Comparison of the mean pumped water flow for *Geometry 1* and *Geometry 2*.

The findings of this study cannot give the final design of the OXYFLUX, since the tested geometries show two extreme behavior of the device. *Geometry 1* showed its capacity to generate a downward water flux for whole wave states dataset used. The values of the flow are relatively small in perspective to absolute value but this kind of device can work for most of the summer, since a minimum sea surface agitation is always present also in summer. On the other hand, *Geometry 2* showed a relatively large increase in the pumped flow but only for wave heights that are not common during hypoxic development periods; furthermore it is characterized by a complex shape that requires a more accurate and complex production process which is not justifiable with this increase in the efficiency of the device. Therefore, the findings of this study are expected to be useful for the inventors or developers of new devices to counteract oxygen depletion at the bottom layers as well as for all the public authorities involved in managing eutrophic, hypoxic

and anoxic coastal areas, introducing a new concept of device. Such a new concept will take on importance, since the only other device able to counteract oxygen depletion described and published at the present day has been designed to work in deeper waters and presents a main wave direction for its functioning. OXYFLUX removes these problems and presents a new concept of device, that does not require large wave heights to work as well as a preferred wave direction.

It can be argued that the optimum configuration of the device might be a middle ground between the tested geometries, but in this thesis it has not been possible to simulate it, considering the computational time required to complete each simulation. This new geometry can be tested in the future through physical or numerical models, in order to evaluate its efficiency. Furthermore, a more extensive numerical analysis would be of interest, in order to evaluate the dynamics of the OXYFLUX for a range of incident wave periods closer to the natural one. Such investigations would not aim much in the analysis of the mean water discharge, but rather in the analysis of maximum displacement under such wave conditions.

The modest values of pumped water produced by the device suggest the installation of little farms of OXYFLUX in environments such as little fjords or little gulfs where aquaculture is an important business to contrast the risk of eutrophication due to the pollutants produced by such activities.

CHAPTER VIII: CONCLUSION

This chapter presents the conclusions of the studies conducted during three years of PhD studies.

The problems of eutrophication, hypoxia and anoxia are discussed. Locations, reasons and the consequences of such common problems are described in order to identify the global scale of eutrophication in coastal areas. The abnormal enrichment of nutrients transported by river run-off appears to be, along with specific environmental and physical conditions, the main reason for the development of such phenomenon. It is evident, from existing knowledge, that additional investigations aimed to design a direct method to counteract or at least mitigate hypoxia in coastal areas needs to be conducted. From this point of view a critical review of wave energy converter devices has been conducted in order to analyze their strengths and weaknesses and their possible application to counteract over enrichment of sea waters from nutrients. The main failure causes for wave energy converters appeared to be related to electro-mechanic components or to the mooring system, that has to guarantee the safe behavior of large and heavy structures, both during normal and extreme wave events. On these bases a floating device called "*OXYFLUX*", devoid of any electro-mechanic part and characterized by a simple geometry and realization process, has been designed and tested through physical and numerical models. The proof of concept that drives the pumping mechanism has been described, as well as the hydrodynamic response of the floating structure. Since the results showed low values of pumped water, a second geometry for the floater of the OXYFLUX has been proposed and analyzed by means of a numerical model. This second geometry, as expected, shows an increase in the mean values of pumped water, but it still encounters difficulties in producing a downward flux for wave heights typical of summer wave climate. It can be argued that the optimal shape of the floater of the device, in order to guarantee downward flux for low wave heights and at the same time

maximize the amount of overtopped water for middle waves, should take into account both the geometries tested in this study.

After the brief general description proposed above, the main conclusions for both physical and numerical modeling will be presented below, along with outlines for further research and final remarks.

Physical Modelling: Conclusions

In chapter 4 physical modelling of the OXYFLUX is described and the set-up of the laboratory, measuring methods and results are given in order to let the reader understand the workflow that was followed during this work. Such an investigation was developed in two phases; the first regarded a preliminary test and the second regarded more a detailed analysis of the dynamics and pumping mechanism of the device. 49 regular waves have been generated in order to have a set of waves which covers a range of wave steepness between 1% and 5%. Moreover, in order to identify the effects of the moorings, two different systems have been tested. The schemes used consisted of two pretention nylon cables and four chains, respectively. The dynamic response of the device was characterized by means of calm water tests and response amplitude operator (RAO). The natural period of the structure was identified as being around 1.10 sec. RAO showed the high non linear dynamics of the structure, since the effects of the viscous dissipations due to the stabilizing ring became dominant for the heave mode with the increase in wave height. The mooring system also affects the dynamic response, chains generate a second main component for the heave response. The main results coming from water velocity measurements gave the proof of concept of the pumping mechanism, since three fields are identified by means of wave height thresholds. The values of the thresholds vary according to the mooring system used. The results coming from the configuration which takes into account the nylon cables shows the following fields: *Field 1* for wave heights

smaller than 3.00 mm in Froude similitude 1:16 (*real scale 0.05 m*) where no overtopping occurs, **Field 2** for wave heights between 3.00 mm and 48.00 mm (*real scale 0.77 m*) where overtopping of incoming wave generates a downward flow as a consequence of the higher head of the water column inside the device with respect to the surrounding wave field and **Field 3** for wave heights between 48.00 mm and 100.00 mm (*real scale 1.60 m*) where water flux reverses its direction and water flows from the bottom to the surface. Results coming from the configuration which takes into account the chains highlight as the chains let the floater free to ride the waves and then increase the minimum threshold value to allow overtopping of the floater. Both threshold values increase but the main trend can be recognized even for this mooring system. So we can distinguish **Field 1** for wave heights smaller than 12.00 mm in Froude similitude 1:16 (*real scale 0.19 m*) where no overtopping occurs, **Field 2** for wave heights between 12.00 mm and 62.00 mm (*real scale 0.99 m*) where overtopping of incoming wave generates a downward flow as a consequence of the higher head of the water column inside the device with respect to the surrounding wave field and **Field 3** for wave heights between 62.00 mm and 100.00 mm (*real scale 1.60 m*) where water flux reverses its direction and water flows from the bottom to the surface. Chains let the device ride the waves generating higher values of velocity that can be reached only for wave heights greater than 12.00 mm (*real scale 0.19 m*). The aim of the investigated device is to induce vertical water flux during the summer season when strong vertical stratification presents its effects and available wave energy is generally rare. A lower value of the first threshold should be preferred in order to guarantee a constant flux during all kind of wave states.

Numerical Modelling: Conclusions

In chapter 5 CFD software was validated by modelling a calm water test and the interaction of the OXYFLUX with regular waves. Only wave states belonging to **Field 2** have been modelled, since the modelling of wave characterized by a period larger than 3.20 sec needed a larger numerical domain which involved a longer computational time. It was shown that the CFD software was well capable of predicting the dynamic response

of the device as well as the overtopping mean discharge. The validated numerical model was applied to 1:1 OXYFLUX design. Nine simulations were performed to investigate the effects of the model selection and the grid resolution. It was shown that the CFD code is very sensitive to the type of mesh used and to its size. In order to avoid any relevant phenomenon of wave reflection from the outlet boundary, which is mainly due to the resolution of the interface air-water with inappropriate mesh size moves according to body displacement, an overset mesh has been used. Selected size grid was chosen making a compromise between accuracy and computational time required for a single simulation, as shown by a discrepancy equal to 2 % of the value of natural period computed with the numerical model with respect to the physical model. Since the modelling has been considered appropriate to model all the processes that affect the wave-OXYFLUX interaction, a second geometry of the floater, based on Lazzari's profile was tested only by means of a numerical model in order to determine its pumping efficiency. This second type of floater increases the mean discharged water but ,at the same time, it is not able to produce a downward flux for the lowest wave heights tested.

Further research

It can be argued that the optimum configuration of the device would be a middle ground of the two tested geometries, that in this thesis could not be simulated due to the time required to complete each simulation. This new geometry can be tested in the future through physical or numerical models, in order to evaluate its efficiency. Furthermore, a more extensive numerical analysis would be of interest, in order to evaluate the dynamics of the OXYFLUX for a range of incident wave periods closer to the natural one. Such investigations would not aim much in the analysis of the mean water discharge, but rather in the analysis of maximum displacement under such wave conditions. The knowledge of the dynamics of the body under the action of the extreme waves is essential in order to

design a prototype installation and avoid problems due to contact of the OXYFLUX with surrounding structures.

No results, or analysis have been carried out in this study regarding the biochemical effects generated by the OXYFLUX in real seas. Since the difficulty of modelling such processes, the only way to evaluate how the concentration of oxygen changes, and how biological species react to a flux of surface water pumped to the bottom, is the installation of a prototype in real environments. This kind of test is expensive and could represent the final step of the research that was started in these three years of this PhD study.

Final remarks

Despite some gaps which still exist in the general knowledge of devices to counteract eutrophication, the conclusion can be reached that a new concept of device has been developed and tested, which shows its capacity to generate a downward flux of well oxygenated surface water to the bottom. The modest values of pumped water produced by the device suggest the installation of little farms of OXYFLUX in environments such as little fjords or little gulfs where aquaculture is an important business to contrast the risk of eutrophication due to the pollutants produced by such activities. This thesis does not claim to give the final design of a device that can stop the worldwide problem of the depletion of oxygen in coastal waters, but, because of its innovative slant it can represent a base study for the development of a direct approach that can mitigate the eutrophication of such kinds of water.

REFERENCES

[1] R. J. Diaz, "Overview of Hypoxia around the World," *Journal of Environmental Quality,* vol. 30, no. 2, pp. 275 - 281, 2001.

[2] E. E. Agency, "European rivers and lakes," Copenaghen, 1994.

[3] O. Catani and G. Vitali, "Effetti degli adattamenti biochimici alla carenza di ossigeno degli organismi marini sulle comunità bentoniche di aree eutrofizzate. Il caso dell'Adriatico nordoccidentle.," in *Evoluzione dello stato trofico in Adriatico: analisi degli interventi attuati e future linee di intervento*, Bologna, 1995.

[4] D. Degobbis, S. Fonda-Umani, P. Franco, A. Malej, R. Precali and N. Smodlaka, "Changes in the Northern Adriatic ecosystem and appearance of hypertrophic gelatinous aggregates," *The Science of the Total Environment,* vol. 165, pp. 43 - 58, 1995.

[5] F. Sangiorgi and T. H. Donders, "Reconstructing 150 years of eutrophication in the north-western Adriatic Sea (Italy) using dinoflagellate cysts, pollen and spores," vol. 60, pp. 69 - 79, 2004.

[6] OSPAR Commission, "OSPAR integrated report 2003 on the eutrophication status," London, 2003.

[7] W. Longstaff, A. Dennison, K. Jones, C. Boicourt and Woerner, "Effects of Nutrient Enrichment in the Nation's Estuaries: A Decade of Change.," Silver Spring, 2007.

[8] M. Selman, S. GreenHalgh, R. Diaz and Z. Sugg, "Eutrophication and hypoxia in

coastal areas: a global assessment of the state of knowledge," Waashignton D.C., 2008.

[9] R. Howart and K. Ramakrrshna, "Nutrient Management," in *Ecosystems and human wellbeing: Policy respone*, vol. 3, Washington, Island Press, 2005.

[10] National Oceanic and Atmospheric Administration, "Global Warning: Frequently asked question," NOAA, 2008.

[11] J. Galloway, J. Aber, J. Erisman, S. Seitzinger, R. Howarth, E. Cowling and B. Cosby, "The nitrogen cascade," *Bioscience,* vol. 53, no. 4, pp. 341 - 356, 2003.

[12] United Nation, "Risks, Untreated Sewage Threatens Seas, Coastal Population," *Edition, UN Chronicle Online,* vol. I , 2003.

[13] S. Lu and I. Hodgkiss, "Harmful algal bloom causative collected from Hong Kong waters," *Hydrobiologia,* vol. 512, no. 1 - 3, pp. 231 - 238, 2004.

[14] R. Diaz, J. Nestlerode and M. Diaz, "A global perspective on the effects of eutrophication and hypoxia on aquatic biota," in *7th International Symposium on Fish Physiology, Toxicology, and Water Quality*, Tallin, 2003.

[15] R. Diaz and A. Solow, "Ecological and Economic Consequences of Hypoxia," 1999.

[16] R. Howarth, B. G., S. D., T. A., J. N., L. K., D. J.A., E. R., C. N., J. T., B. F., F. J., K. V., M. P. and Z.-L. Z., "Regional nitrogen budgets and reverine N & P fluxes for the drainage to the North Atlantic Ocean: Natural and human influences," *Biogeochemistry ,* vol. 35, pp. 75-139, 1996.

[17] L. Spokes and T. Jickells, "Is the atmosphere really an important source of reactive

nitrogen to coastal waters?," *Continental Shelf Research,* vol. 25, pp. 2022-2035, 2005.

[18] J. Candy, "Toward a comparative evaluation of human impacts on fishery ecosystems of enclosed and semi-enclosed seas.," *Reviews in Fisheries Science,* vol. 1, pp. 57-96, 1993.

[19] S. Nixon, "Coastal marine eutrophication: A definition, social causes, and future concerns.," *Ophelia,* vol. 41, pp. 199-219, 1995.

[20] R. Diaz and R. Rosenburg, "Marine benthic hypoxia: a review of its ecological effects and the behavioural responses of benthic macrofauna," *Oceanography and Marine Biology,* vol. 33, pp. 245-303, 1995.

[21] A. F. Falcao, "Wave energy utilization: A review of the technologies," *Renewable and Sustainable Energy Reviews,* vol. 14, pp. 899 - 918, 2010.

[22] M. McCormick, Ocean wave energy conversion, New York: Wiley, 1981.

[23] D. Ross, Power from sea waves, Oxford: Oxford University Press, 1995.

[24] Y. Masuda, "Wave-activated generator," in *International Colloquium on the Expoxition of the Ocean*, Bordeaux, 1971.

[25] Y. Masuda, "Experimental full-scale results of wave power machine Kaimei," in *irst Symp Wave Energy Utilization*, Gothenburg, 1978.

[26] Y. Masuda and M. McCormick, "Experiences in pneumatic wave energy conversion in Japan," New York, ASCE, 1987, pp. 1 - 33.

[27] Y. Masuda, L. Xianguang and G. Xiangfan, "High performance of cylinder float

backward bent duct buoy (BBDB) and its use in European seas," in *First European Wave Energy Symposium*, Edinburgh, 1993.

[28] Y. Masuda, H. Kimura, X. Liang, X. Gao, R. Mogensen and T. Andersen, "Regarding BBDB wave power generation plant," in *2nd European Wave Power Conference*, Lisbon, 1995.

[29] S. Salter, "Wave power," *Nature,* vol. 249, pp. 720 - 724, 1974.

[30] T. Whittaker, S. McIlwaine and S. Raghunathan, "A review of the Islay shoreline," in *First European Wave Energy Symposium*, Edinburgh, 1993.

[31] H. Ohneda, S. Igarashi, O. Shinbo and S. Sekihara, "Construction procedure of a wave power extracting caisson breakwater," Tokyo, 1991.

[32] M. Ravindran and P. Koola, "Energy from sea waves the Indian wave energy," *Current Science,* vol. 60, pp. 676 - 756, 1991.

[33] R. Bedard, M. Previsic, G. Hagerman, B. Polagye, W. Musia and j. Klure, "North American ocean energy status," in *7th European Wave Tidal Energy Conference; ,* Porto, 2007.

[34] M. Previsic, A. Moreno, R. Bedard, B. Polagye, C. Collar and D. Lockard, "Hydrokinetic energy in the United States resources, challenges and opportunities.," in *8th European Wave Tidal Energy Conference*, Uppsala, 2009.

[35] J. Chozas, "Wave energy consultancy," 2013. [Online]. Available: http://www.juliafchozas.com/wave-energy/why-wave-energy/. [Accessed 3 1 2014].

[36] O. Langhamer, K. Haikonen and J. Sundberg, "Wave power—Sustainable energy

or environmentally costly? A review with special emphasis on linear wave energy converters," *Renewable and Sustainable Energy Reviews,* vol. 14, p. 1329–1335, 2010.

[37] M. Previsic and S. Kourosh, "Cost Reduction Pathways for Wave Energy," in *10th European Wave and Tidal Energy Conference Series*, Aalborg, 2013.

[38] K. Rinkesh, "Conserve Energy Future," 2009. [Online]. Available: http://www.conserve-energy-future.com/Advantages_Disadvantages_WaveEnergy.php. [Accessed 3 1 2014].

[39] E. Callaway, "To catch a wave," *Nature,* vol. 450, pp. 156 - 165, 2007.

[40] A. Artegiani, D. Bregant, E. Paschini, N. Pinardi, G. Raicich and A. Russo, "The Adriatic Sea General Circulation. Part I: Air–Sea Interactions and Water Mass Structure," *JOURNAL OF PHYSICAL OCEANOGRAPHY,* vol. 27, pp. 1492 - 1514, 1997.

[41] A. Artegiani, D. Bregant, E. Paschini, N. Pinardi, G. Raicich and A. Russo, "The Adriatic Sea General Circulation. Part II: Baroclinic Circulation Structure," *Journal of Physical Oceanography,* vol. 27, pp. 1515- 1532, 1997.

[42] R. Marchetti, A. Provini and G. Crosa, "Nutrient load carried by the River Po into the Adriatic Sea," *Marine Pollution Bulletin ,* vol. 20, pp. 168 - 172, 1989.

[43] P.-. Giordani, D. Hammond, W. Berelson, G. Montanari, R. Poletti, A. Milandri, M. Frignani, L. Langone, M. Ravaioli, G. Rovatti and E. Rabbi, "Benthic fluxes and nutrient budget for sediments in the Northern Adriatic Sea: burial and recycling efficiencies," in *Marine Coastal Eutrophication*, Amsterdam, Elsevier, 1992, pp. 251 - 275.

[44] D. Justic, "Long term eutrophication of the Northern Adriatic Sea," *Marine Pollution Bulletin ,* vol. 18, pp. 281 - 284, 1987.

[45] D. Degobbis, "Increased eutrophication of the Northern Adriatic Sea," *Marine Pollution Bulletin ,* vol. 20, pp. 452 - 457, 1989.

[46] M. Zavatarelli, F. Raicich, D. Bregant, A. Russo and A. Artegiani, "Climatological biogeochemical characteristics of the Adriatic Sea," *Journal of Marine Systems ,* vol. 18, pp. 227 - 263, 1998.

[47] M. Gilmartin and N. Revelante, "Observations on particulate organic carbon and nitrogen in the northern Adriatic Sea," *Thalassia Jugoslavica,* vol. 23, pp. 39 - 49, 1991.

[48] A. Boldrin, M. Juracic, L. Vitturi, S. Rabitti and G. Rampazzo, "Geochemical considerations on trace element distributions in suspended matter and sediments at the river-sea interface, Adige river mouth, northern Adriatic sea," *Applied Geochemistry,* vol. 4, pp. 409 - 421, 1989.

[49] M. Giani, A. Boldrin, G. Matteucci, F. Frascari, M. Gismondi and S. Rabitti, "Downward fluxes of particulate carbon, nitrogen and phosphorus in the north-western Adriatic Sea," *The Science of the Total Environment,* vol. 266, pp. 125 - 134, 2001.

[50] A. Russo, S. Maccaferri, T. Djakovac, R. Precali, D. Degobbis, M. Deserti, E. Paschini and D. M. Lyons, "Meteorological and oceanographic conditions in the northern Adriatic Sea during the period June 1999–July 2002: Influence on the mucilage phenomenon," *Science of the Total Environment,* vol. 353, pp. 24 - 38, 2005.

[51] P. Poulain, V. Kourafalou and B. Cushman-Roisin, "Northern Adriatic Sea," in *Physical oceanography of the Adriatic Sea Past, present and future*, Dordrecht, Kluwe Academic Publ., 2001, pp. 143 - 208.

[52] P. Franco and M. A., "Northern Adriatic Sea: oceanography of the basin proper and of the western coastal zone," *Science of the Total Environment,* vol. 35, pp. 35-97, 1992.

[53] d. Degobbis, R. Precali, C. Ferrari, T. Djakovac, A. Rinaldi and I. Ivanc, "Changes of nutrient concentrations and ratios during mucilage events in the period 1999–2002.," *Science of the Total Environment,* vol. 353, pp. 103 - 117, 2005.

[54] A. S. A. Leder N. and V. I., "Extreme values of surface wave heights in the Northern Adriatic," *GEOFIZIKA ,* vol. VOL. 15 , pp. 1 - 13, 1998.

[55] J. Parunov, M. Corak and M. Pmsa, "Wave height statistics for seakeeping assessment of ships in the Adriatic Sea," *Ocean Engineering,* vol. 38, p. 1323–1330, 2011.

[56] C. Guedes Soares, "Assessment of the uncertainty in visual observations of wave height," *Ocean Engineering ,* vol. 13, no. 1, pp. 37 - 56, 1986.

[57] C. Guedes Soares, "On the definition of rule requirements for wave induced vertical bending moments," *Marine Structures ,* vol. 9, pp. 409 - 425, 1996.

[58] D. Vicinanza, L. Cappietti, V. Ferrante and P. Contestabile, "Estimation of the wave energy in the Italian offshore," *Journal of Coastal Research,* vol. SPEC. ISSUE 64, pp. 613 - 617, 2011.

[59] Envirtech, "Technologies for a wonderful word - Italian Data Buoy Network,"

Envirtech, 2013. [Online]. Available: http://www.envirtech.org/ron.htm. [Accessed 3 1 2014].

[60] Earth-vision.biz, "Maritime Journal," 1 Jun 2007. [Online]. Available: http://www.maritimejournal.com/news101/marine-civils/port,-harbour-and-marine-construction/wave_dragon_will_fire_marine_construction. [Accessed 11 1 2014].

[61] J. W. Van der Meer, M. R. A. van Gent, B. Pozueta, H. Verhaeghe, G.-J. Steendam and J. Medina, "Applications of a neural network to predict wave overtopping at coastal structures," in *ICE, Coastlines, Structures and Breakwaters*, London, 2005.

[62] J. P. Kofoed, "Wave overtopping of Marine Structures - Utilization of wve energy," Aalborg, 2002.

[63] T. Pullen, N. Allsop, T. Bruce, A. Korthenaus, S. H. and J. van deer Meer, "Wave Overtopping of Sea Defences," Environment Agency, (UK); Expertise Netwerk Waterkeren, (NL); Kuratorium für Forschung im Küsteningenieurwesen, (DE), 2007.

[64] M. Owen, "Design of seawalls allowing for wave overtopping.," HR Wallingford, 1980.

[65] M. W. Owen, " Overtopping of Sea Defences.," in *International Conference on the Hydraulic*, Coventry, 1982.

[66] Bradbury, A. P.; Allsop, N. W. H, "Hydraulic performance of breakwater crown walls," HR Wallingford, 1988.

[67] P. L. Aminti and L. Franco, "Wave overtopping on rubble mound breakwaters.," in *Int. Conf. on Coastal Engng*, Torremolinos, 1988.

[68] J. Ahrens and M. Heimbaugh, "IRREGULAR WAVE RUNUP ON RIPRAP REVETMENTS," *Journal of Waterway, Port, Coastal and Ocean Engineering,* vol. 114, no. 4, pp. 524 - 530, 1988.

[69] J. Pedersen and H. F. Burcharth, "Wave forces on crown walls," in *Int. Conf. on Coastal Engineering*, Venice, 1992.

[70] J. W. Van der Meer and J. P. F. M. Janssen, "Wave run-up and wave overtopping at dikes," in *Wave Forces on Inclined and Vertical Wall Structures*, New York, ASCE, 1995, p. 1 – 26.

[71] L. Franco and M. v. d. M. J. de Gerloni, "Wave overtopping on vertical and composite breakwaters," in *Coastal Engineering Conference*, Kobe, 1995.

[72] M. Hebsgaard, P. Sloth and J. Juhl, "Wave overtopping of rubble mound breakwaters," in *International Conference on Coastal Engineering*, Copenhagen, 1998.

[73] H. Schüttrumpf, J. Möller, H. Oumeraci, J. Grüne and W. R., "Effects of Natural Sea States on Wave Overtopping of Seadikes," in *Waves Conference* , San Francisco, 2001.

[74] H. Burcharth and S. Hughes, in *Coastal Engineering Manual*, Vicksburg, Engineering Research Center, Waterways Experiment Station, US Army Corps of Engineers, 2000, p. Chapter 5.

[75] S. Douglass, "Review and Comparison of Methods for Estimating Irregular Wave Overtopping Rates," U. S. Army Corps of Engineering, 1986.

[76] H. Stommel, A. B. Arons and D. Blanchard, "An oceanographic curiosity: the

perpetual salt fountain.," *Deep-Sea. Res.,* vol. 3, pp. 152 - 153, 1956.

[77] Veronis, G. , "Evolution of Physical Oceanography," MTI Press, Cambridge, 1981.

[78] H. E. Huppert and J. S. Turner, "Double diffusive convection," *Journal of Fluid mechanics,* vol. 106, pp. 299 - 329, 1981.

[79] S. K. Maruyama, K. Tsubaki, T. Sakai and S. Sakai, "Artificial upwelling of seep seawater using the perpetual salt fountain for cultivation of ocean desert.," *Journal of oceanography,* vol. 60, pp. 563 - 568, 2004.

[80] K. Kenyon, "Upwelling by a Wave Pump," *Journal of oceanography,* vol. 63, pp. 327 - 331, 2007.

[81] J. D. Isaacs, C. D. and G. Wick, "Utilization of the energy in ocean waves," *Ocean Engineering ,* vol. 3, no. 4, pp. 175 - 187, 1976.

[82] C. K. Liu and Q. Jin, "Artificial upwlling in regular and random waves," *Ocean Engineering,* vol. 22, pp. 337 - 350, 1995.

[83] B. Nam, S. Shin, K. Hong and S. Hong, "Numerical Simulation of Wave Flow over the Spiral-Reef Overtopping Device," in *ISOPE International Society of Offshore and Polar Engineers*, Bangkok, 2008.

[84] A. Antonini, M. G. Gaeta and A. Lamberti, "Wave - induced devices for the oxygenation of deep layer: a physical investigation," in *International Conference on Coastal Engineering*, Santander, 2012.

[85] C. Carstens, *Hydrodynamic Capacity Study of the Wave-Energized Baltic Aeration Pump,* R. I. o. T. (KTH), Ed., STOCKHOLM: Department of Land and Water Resources Engineering, 2008.

[86] L. Margheritini, S. Parmeggiani, J. Kofoed and A. Sumila, "Proof of concept: Wave Energized Baltic Aeration Pump (WEBAP)," University of Aalborg, Aalborg, 2010.

[87] L. Margheritini and L. Claeson, "An Innovative Way of Utilizing Wave Energy to Counteract Eutrophication and Hypoxia," in *EWTEC-European Wave and Tidal Energy Conference*, Southampton, 2011.

[88] A. Nielsen and J. Kofoed, *The Wave Dragon – evaluation of a wave energy converter,* Aalborg: Aalborg University, 1997.

[89] Disconzi; F., "accettabilitasociale.com," [Online]. Available: http://www.accettabilitasociale.com/pagine/moto-ondoso/. [Accessed 13 1 2014].

[90] L. Margheritini, D. Vicinanza and P. Freigaard, "SSG wave energy converter: Design, reliability and hydraulic performance of an innovative overtopping device," *Rebewable Energy,* vol. 34, p. 1371 – 1380, 2009.

[91] L. Margheritini, D. Vicinanza and P. Frigaard, "Sea Slot Cone Generator overtopping performance in 3D conditions," in *International Offshore and Polar Engineering Conference*, Vancouver, 2008.

[92] D. Vicinanza, F. Ciardulli, M. Buccino, M. Calabrese and J. Koefed, "Wave loadings acting on an innovative breakwater for energy production," *Journal of Coastal Research,* vol. Issue SPEC, no. ISSUE 64, pp. 608 - 612, 2011.

[93] C. ADAPCO, *Star-CCM+ 8.04 User Manual,* CD ADAPCO, 2013.

[94] ANSYS, *FLUENT 14.5 User's Guide,* ANSYS, 2014.

[95] J. P. Kofoed, "Vertical Distribution of Wave Overtopping for Design of Multi Level Overtopping Based Wave Energy Converters," in *30th International Conference on Coastal Engineering*, San Diego, 2007.

[96] D. Vicinanza, L. Margheritini, J. Kofoed and M. Buccino, "The SSG Wave Energy Converter: Performance, Status and Recent Developments," *Energies,* vol. 5, pp. 193 - 226, 2012.

[97] "O2 gruppen," [Online]. Available: http://www.o2gruppen.se/. [Accessed 14 1 2014].

[98] European Union, "Environmental Life Program," 2010. [Online]. Available: http://ec.europa.eu/environment/life/project/Projects/index.cfm. [Accessed 14 1 2014].

[99] USACE, Shore Protection Manual., Department of the U.S. Army Corps of Engineers, 1977.

[100] C. Baresel, "Wave Energized Baltic Aeration Pump," WEBAP, 2010. [Online]. Available: http://webap.ivl.se/1.html. [Accessed 14 1 2014].

[101] C. Baresel, "Short version of the WEBAP project's final report," LIFE project WEBAP, 2013.

[102] A. Stigebrandt and B. Gustafsson, "Improvement of Baltic proper water quality using large-scale ecological engineering," *A Journal of the Human Environment,* Vols. 2 - 3, pp. 280-286, 2007.

[103] N. Fofonoff and J. Milard, "Algoritms for computation of foundamental properties of seawater," Division of Marine Sciences , Paris, 1983.

[104] K. Pijush, M. Ira and H. Howard, Fluid Mechanics, San Diego: Academic Press, 2011.

[105] D. Citrini and G. Noseda, Idraulica, Ambrosiana.

[106] B. McCormick, Aerodynamics, Aeronautics, and Flight Mechanics., New York: John Wiley & Sons, Inc., , 1979.

[107] National Aeronautics and Space Administrator, "Shape Effects and Drag," [Online]. Available: http://www.grc.nasa.gov/WWW/k-12/airplane/shaped.html. [Accessed 19 2 2014].

[108] J. Serra, Image analysis and mathematical morphology, Academic Press, 1988.

[109] M. McCormick, Ocean Engineering Mechanics with Applications, New York: Cambridge University Press, 2010.

[110] J. Westphalen, D. Greaves, C. Williams, A. Hunt-Raby and J. Zang, "Focused wave and wave-strucutre interaction in a numerical waave tank," *Ocean Engineering,* vol. 45, pp. 9 - 21, 2012.

[111] T. Sarpkaya and M. Issacson, Mechanics of wave forces on offshore structures, New York: Van Nostrand Reinhold, 1981.

[112] J. Newman and C. Lee, "Boundary element method in off-shore structures analysis," *Journal of Offshore Mechanics and Arctic Engineering,* vol. 124, pp. 81 - 89, 2002.

[113] E. Agamloh, A. Wallace and A. Von Juanne, "Application of fluid-structure interaction simulation of an ocean wave energy extraction device," *Rebewabe*

energy, vol. 33, pp. 748 - 757, 2008.

[114] M. Bhinder, C. Mingham, D. Causon, M. Rahmati, G. Aggidis and R. Chaplin, "A joint numerical and experimental study of a surging point absorbing wave energy converter (WRASPA).," in *28th International conference on ocean,offshore and arctic engineering, OMAE*, Honolulu, 2009.

[115] CD-Adapco, "USER GUIDE STAR-CCM+ Version 8.04," London, 2013.

[116] M. Bozorgnia, *Computational fluid dynamic analysis of highway bridge superstructures exposed to hurricane waves,* Los Angeles: UNIVERSITY OF SOUTHERN CALIFORNIA, 2012.

[117] B. Balinga and S. Pantakar, "A new finite-volume formulation for convection-diffusion problems.," *Numerical heat transfert ,* vol. A 3, pp. 393 - 409 , 1980.

[118] C. M. Rhie and W. Chow, "Numerical Study of the Turbulent Flow Past an Airfoil with Trailing Edge Separation," *AIAA J.,* vol. 21, p. 1523–1532, 1983.

[119] H. Versteeg and W. Malalasekera, An introduction to computational fluid dynamics: the finite volume method, NewYork: Longman Scientific&Technical , 2007.

[120] S. Mozaferija and M. Peric, "Computation of free surface flows using interface tracking and inteface-capturing methods," in *Computational Mechanics Publications*, 1998.

[121] B. Leonard, "Bounded highe-order upwind multidimensional finite volume convection-diffusion algorithms," in *Advances in Numerical Heat Transfer*, 1997, pp. 1 - 57.

[122] D. Wilcox, Turbulence Modeling for CFD, DCW Industries, Inc., 1998..

[123] F. Menter, "Two-equation eddy-viscosity turbulence modeling for engineering applications," *AIAA Journal,* vol. 32, no. 8, pp. 1598 - 1605, 1994.

[124] Y. Yi-Hsiang and Y. L., "Reynolds-Averaged Navier–Stokes simulation of the heave performance of a two-body floating-point absorber wave energy system," *Computers & Fluids,* vol. 73, pp. 104 - 114, 2013.

[125] P. Ruponen, P. Queutey, M. Kraskowski, R. Jalonen and E. Guilmineau, "On the calculation of cross-flooding time," *Ocean Engineering,* vol. 40 , p. 27–39, 2012.

[126] M. Muliawan, Z. Gao, T. Moan and A. Babarit, "Analysis of a two-body floating wave energy converter with particular focus on the effects of power take off and mooring systems on energy capture," in *30th International conference on ocean, offshore and arctic engineering, OMAE,* , Rotterdam, 2011.

[127] J. Ferziger and M. Peric, Computational Methods for Fluid Dynamics, Berlin: Springer-Verlag, 2002.

[128] J. Supamusdisukul, Experimental investigation of wing-fuselage integration geometries including CFD analyses, Ann Arbor: ProQuest, UMI Dissertation Publishing, 2012.

[129] H. Reichardt, "Vollstaendige Darstellung der turbulenten Geschwindigkeitsverteilung in glatten Leitungen," *Journal of Applied Mathematics and Mechanics,* vol. 31, no. 7, pp. 208 - 219, 1951.

[130] C. Junwoo and S. Bum Yoon, "Numerical simulations using momentum source wave-maker applied to RANS equation model," *Coastal engineering,* vol. 56, no.

10, pp. 1043 - 1060, 2009.

[131] E. Del Tedesco, "ProgettoDighe," 2005. [Online]. Available: http://www.progettodighe.it/main/le-dighe/article/pontesei. [Accessed 10 2 2014].

[132] E. Lazzari, "Ricerca sperimentale sugli sfioratori a calice : comunicazione presentata al 6," in *Convegno italiano di idraulica e costruzioni idrauliche*, Padova, 1959.

[133] I. Glendenning, "Energy from waves," in *Oceanology International* , London, 1978.

[134] M. Gilmartin and N. Revelante, "The phytoplankton of the Adriatic Sea: standing crop and primary production," *Thalassia Jugoslavica,* vol. 19 , pp. 173 - 188, 1983.

[135] G. Montanari, R. A., P. N., S. S. and G. L., I quaderni di arpa, in The currents of Emilia-Romagna coastal, Bologna: Agenzia Regionale Prevenzione e Ambiente (ARPA), 2006.

[136] H. Verhaeghe, J. van der Meer, G.-J. Steendam, P. Besley, L. Franco and M. R. A. van Gent, "Wave overtopping database as the starting point for a neural network prediction," in *Coastal Structures 2003,*, Portland, 2003.

[137] M. E. Stern, "The "salt fountain" and thermohaline convection," *Tellus,* vol. 12, pp. 172 - 175, 1960.

[138] D. Vicinanza and P. Frigaard, "Wave pressure acting on a seawave slot-cone generator," *Coastal Engineering,* vol. 55, pp. 553 - 568, 2008.

[139] Y. Ma, S. Soatto, J. Kosecha and S. Shankar, An invitation to 3D Vision. From Images to Geometric Models, Berlin: Springer, 2004.

[140] L. Shapiro and G. Stockman, Computer vision, Prentice Hall, 2001.

[141] R. Tsai, "A versatile camera calibration technique for high-accuracy 3D machine vision metrology using off-the-shelf TV cameras and lenses," *Journal of Robotics and Automation RA ,* vol. 3, p. 323 – 344, 1987.

[142] G. Iglesias, O. Ibanez, A. CCastro, J. Rabunal and J. Dorado, "Computer vision applied to wave flume measurements," *Ocean Engineering,* vol. 36, pp. 1073 - 1079, 2009.

[143] J. Zelt and E. Skjelbreia, "Estimating Incident and Reflected Wave Fields Using an Arbitrary Number of Wave Gauges," in *International conference on Coastal Engineering ,* Venice, 1992.

[144] G. De Haan and E. Bellers, "Deinterlacing—an overview," in *IEEE*, 1998.

[145] H. Kalmus, "Electronic Flowmeter System," *The review of the scientific instrument,* vol. 25, no. 3, pp. 201 - 206, 1954.

[146] D. Baker and H. F. l. Stegal, "Transcutaneous doppler flow detection as a nondestructive technique," *Journal of Applied Physiology,* vol. 21, no. 2, pp. 554 - 566, 1966.

[147] Y. Takeda, "Velocity profile measurment by ultrasound doppler shift method," *Int. Journal of Heat Fluid Flow,* vol. 7, p. 313, 1986.

[148] Signal Processing S.A., Switzerland, *DOP 2000 User's Manual,,* Signal Processing S.A., Switzerland.

[149] Nanopartikel,   "Nanopartikel,"   [Online].   Available:

http://www.nanopartikel.info/cms/lang/en/Wissensbasis/Titandioxid. [Accessed 31 1 2014].

[150] S. Longo, D. Liang, L. Chiapponi and L. Jiménez, "urbulent flow structure in experimental laboratory wind-generated gravity waves," *Costal Engineering,* vol. 64, pp. 1 - 15, 2012.

[151] O. Groupen, "O2 Groupen," [Online]. Available: http://www.o2gruppen.se/eng.html. [Accessed 20 4 2012].

[152] Y. Yu and Y. Li, "Reynolds-Averaged Navier–Stokes simulation of the heave performance of a two-body floating-point absorber wave energy system," *Computer & Fluid,* vol. 73, pp. 104 - 114, 2013.

[153] M. Ariff and S. C. S. Saim, "Wall y+ approach for dealing with turbulent flow over a surface mounted cube: part 2 – high reynolds number," in *7th International Conference on CFD in the Minerals and Process Industries*, Melbourne, 2009.

[154] M. Messer, *Pulsed ultrasonic doppler velocimetry for measurement of velocity profiles in small channels and cappilaries,* Georgia Institute of Technology, 2005.

Appendix A

APPENDIX A.pdf

Appendix B

APPENDIX B.pdf

APPENDIX A

Physical model of OXYFLUX

Geometry 1 (Froude similitude 1:16)

WAVE DRIVEN DEVICES FOR THE OXYGENATION
OF BOTTOM LAYERS

Alessandro Antonini

Section view of the wave flume and Geometry 1

Wave flume 500x700 mm

Top aluminum clamping ring

Top plastic ring

Floater polystyrene

Tube

Top aluminum clamping ring

Bottom aluminum clamping ring

Stabilizing aluminum ring

m.w.l.

SCALA 1:2.5

- 160.0
- 175.0
- 335.00
- 65.0
- 50.0
- 50.0
- 50.0
- 50.0
- 65.0
- 297.8
- 175.0
- 160.0
- 74
- 400
- 300
- 700
- 500

3D View

Top aluminum clamping ring

Top plastic ring

Floater polystyrene

Stabilizing aluminum ring

Bottom aluminum clamping ring

Tube

Top view

Thickness 3.00 mm
Surface 23263 mmq

- 51.6
- 180.0

SCALE 1:2.5

---

(1) Top aluminum clamping ring

Top view

- 50.0
- 54.6
- 10°

Section view

- 54.6
- 50.0
- 50.0
- 13.0

SCALE 1:2.5

SCALE 1:1

---

(2) Top plastic ring

Top view

- 53.1
- 55.8
- 64.9
- 85.3

Section view

- 25°
- 4.6°
- 10°
- 53.1
- 85.3
- 5.0
- 4.6°

SCALE 1:2.5

SCALE 1:1

---

(3) Floater polystyrene

Top view

- 50.0
- 53.1
- 85.3
- 150.0

Section view

- 10°
- 25°
- 8°
- 10°
- 50.0
- 53.1
- 16.1
- 16.1
- 50.0
- 150.0
- 150.0
- 50.0
- 25.0
- 16.0
- 15.0
- 7.0
- 13.0
- 7.0

SCALE 1:2.5

SCALE 1:1

---

(4) Nylon for tube

- 350.0
- 340.0
- 177.0
- 157.0
- 10.0
- 10 mm to ensure the positioning
- 20 mm required for the welding
- Thickness 0.5 mm
- 20.0

SCALE 1:2.5

---

(4) Rigid tube

Section view

- 350.0
- 50.0
- 2.0
- 50.0
- 58.2
- 12.0

Top view

- 50.0
- 54.2

SCALE 1:2.5

SCALE 1:1

---

(6) Bottom aluminum clamping ring

Section view

- 10°
- 50.0
- 54.2
- 12.0

Top view

- 50.0
- 54.2

SCALE 1:1

---

(5) Stabilizing aluminum ring

Section view

- 10°
- 52.6
- 51.6
- 180.0
- 180.0
- 3.0

SCALE 1:1

APPENDIX B
Prototype of OXYFLUX
Geometry 2 (Real scale)

WAVE DRIVEN DEVICES FOR THE OXYGENATION OF BOTTOM LAYERS

Alessandro Antonini

3D view, Scale 1:25

Section view, Scale 1:25

CENTER OF GRAVITY

4.15
1.21
4.59
0.80
0.56
1.03
2.88
1.03
1.47
1.65
0.21
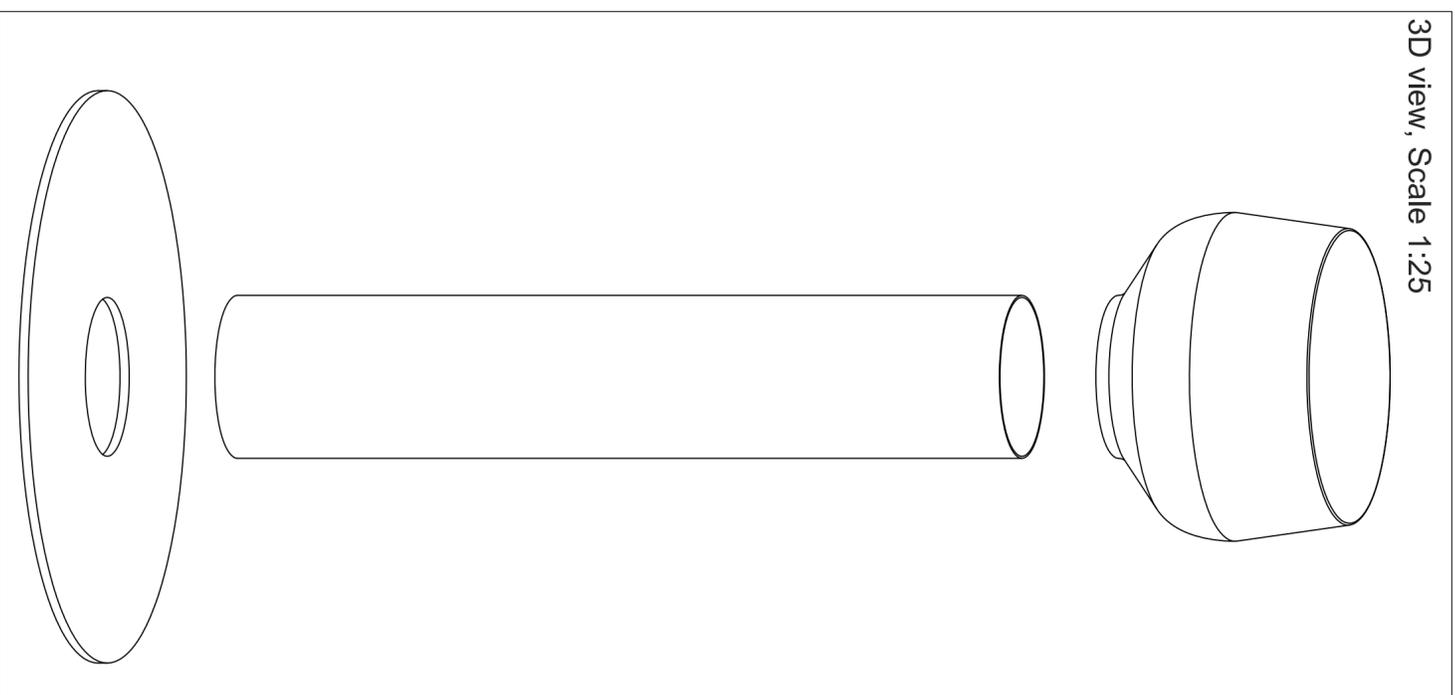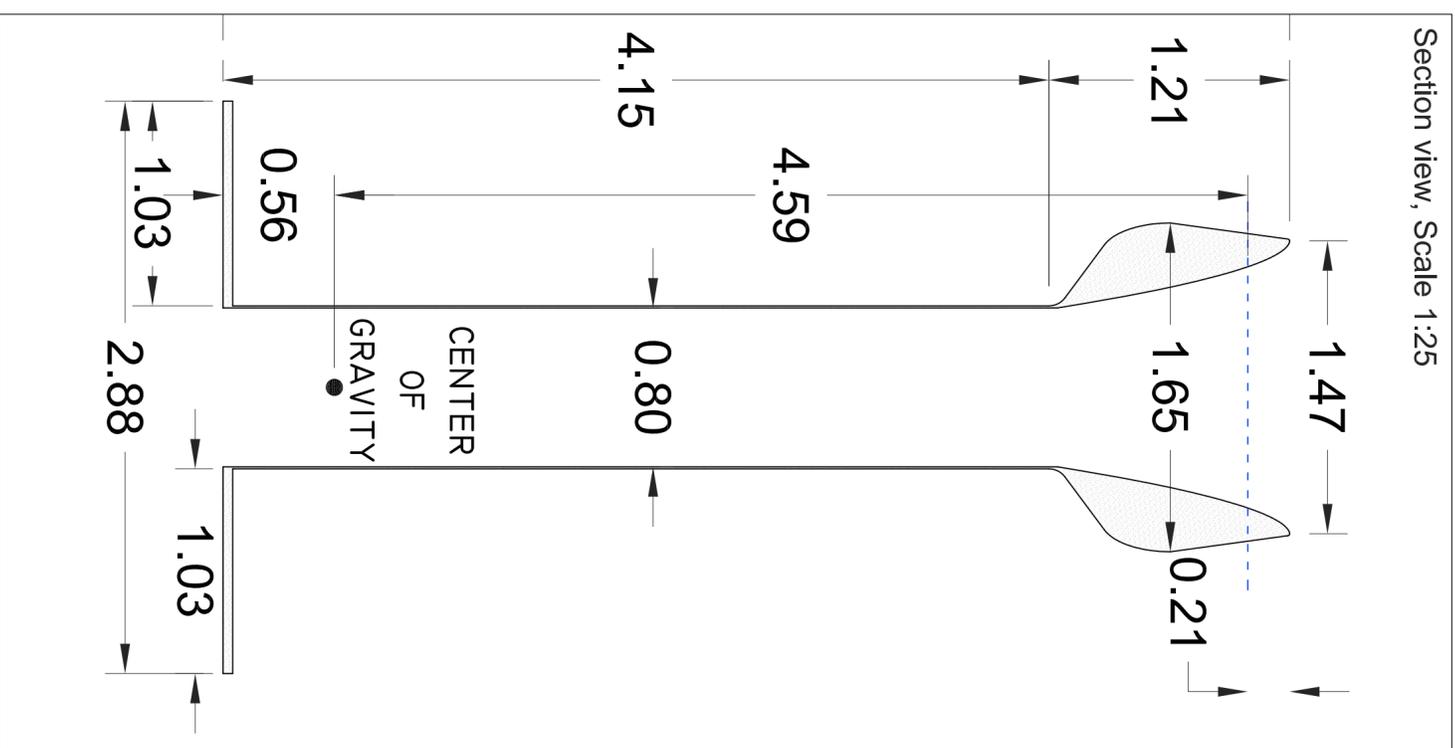
Floater section view, Scale 1:10

0.08
0.20
0.33
0.60
16°
Lazzari's profile
CENTER OF GRAVITY
0.11
0.16
0.21
0.25
0.29
0.32
1.47
Z₂
Floater bottom 0.80
R0.10
53°
8°
1.21
0.028